Retrieval of methane and carbon monoxide using near infrared spectra recorded by SCIAMACHY onboard ENVISAT

Algorithm development and data analysis

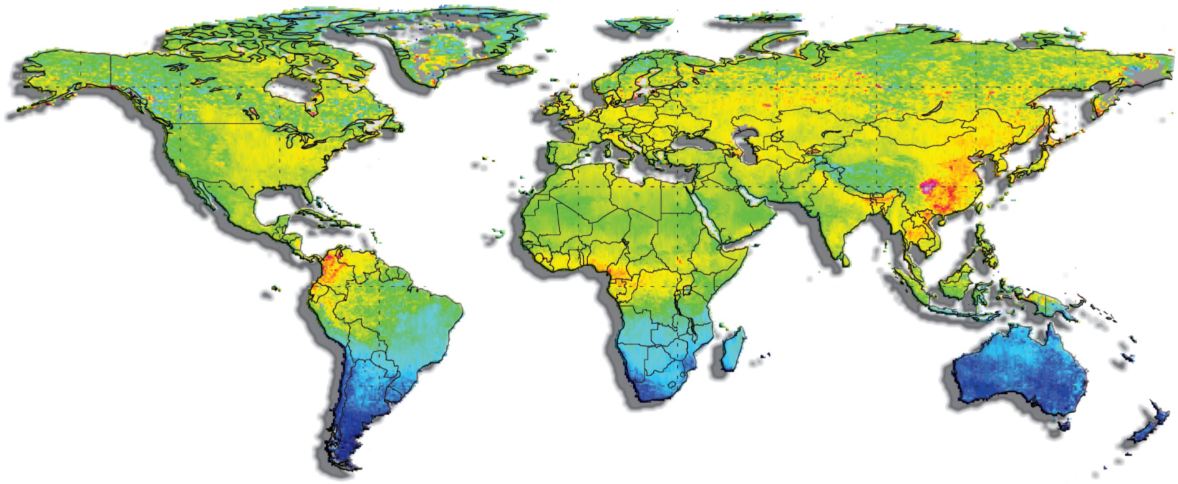

Christian Frankenberg

INAUGURAL - DISSERTATION
zur
Erlangung der Doktorwürde
der
Naturwissenschaftlich-Mathematischen
Gesamtfakultät
der
Ruprecht-Karls-Universität
Heidelberg

vorgelegt von
Diplom-Geoökologe Christian Frankenberg
geboren in Bad Honnef

Tag der mündlichen Prüfung: 16. November, 2005

Retrieval of methane and carbon monoxide using near infrared spectra recorded by SCIAMACHY onboard ENVISAT

Algorithm development and data analysis

Referees: Prof. Dr. Ulrich Platt
Prof. Dr. Jos Lelieveld

Kurzzusammenfassung

In der Nacht vom 28 Februar auf den 1 März 2002 wurde von der europäischen Raumfahrtbehörde ESA der Umweltsatellit ENVISAT mit einer Ariane 5 Rakete in eine Erdumlaufbahn in 800km Höhe gebracht. Als Nutzlast an Bord befindet sich unter anderem das Instrument SCIAMACHY, welches erstmals in der Geschichte der satellitengestützten Erdbeobachtung mit Spektrometern ausgestattet ist, die, in Ergänzung zu Messungen im ultravioletten und sichtbaren Spektralbereich, im Nahinfraroten (1-2.4µm) das von der Erdoberfläche und Atmosphäre zurückgestreute Sonnenlicht messen.

Im Gegensatz zu Spektrometern im thermischen Infrarot erlauben diese Nahinfrarotspektrometer erstmals eine globale Bestimmung der klimarelevanten Gase Methan, Kohlendioxid und Kohlenmonoxid mit hoher Sensitivität für bodennahe Luftmassen. In dieser Arbeit wurde ein Algorithmus auf Basis der differentiellen optischen Absorptionspektroskopie (DOAS) entwickelt, welcher die Besonderheiten der Bestimmung starker Absorber im Nahinfarotbereich berücksichtigt und eine präzise Bestimmung der Säulendichten der jeweiligen Spurengase erlaubt. Es wurde gezeigt, dass nichtlineare iterative Verfahren notwendig sind, um Sättigungseffekte zu berücksichtigen und Wechselwirkungen zwischen spektral überlappenden starken Absorbern zu vermeiden. Basierend auf dem entwickelten *nichtlinearen maximum a Posteriori* Algorithmus *(IMAP-DOAS)* wurden die Messungen von SCIAMACHY ausgewertet und interpretiert. Da SCIAMACHY nicht als dediziertes Nahinfrarotspektrometer sondern mehr als Prototyp betrachtet werden kann, mussten zuvor eine Reihe von instrumentell bedingten Problemen gelöst werden. Mit einer intensiven Betrachtung dieser Effekte wurden Auswertungen von Kohlenmonoxid und Methan ermöglicht.

Erhöhungen von Kohlenmonoxid in Gebieten mit Biomasseverbrennung konnten klar identifiziert werden. Weiterhin wurden die saisonalen räumlichen Muster typischer Brandregionen beobachtet. Nur in den Industriegebieten Chinas wurden durchgehend hohe Kohlenmonoxidvorkommen über das Jahr bestimmt.

Die weltweit ersten globalen Messungen des Gesamtsäulengehaltes von Methan mit hoher Präzision wurden ermöglicht, indem Messungen von dem relativ gleichverteilten Kohlendioxid als Indikator für den Lichtweg der gemessenen Photonen verwendet wurde. Es zeigte sich, daß die gemessenen Methanvorkommen in weiten Teilen der Erde sehr gut mit simulierten Werten des Chemie–Transportmodells TM3 übereinstimmen. Herausstechend waren stark erhöhte Methankonzentrationen über Reisanbaugebieten in Südostasien. Diese Messungen können daher als direkter Beweis für großräumige Methanemissionen von Reisfeldern angesehen werden.

Für den Zeitraum August bis November 2003 wurden weiterhin starke Diskrepanzen zwischen den Messungen und simulierten Werten über tropischen Waldgebieten entdeckt. Messungen von SCIAMACHY über diesen Gebieten zeigten durchgehend signifikant höhere Vorkommen. Diese Beobachtung ließ den Schluss zu, daß die derzeitigen Emissionsinventare der Methanemissionen die Tropen als Quelle deutlich unterschätzen. Ob eine bislang unbekannte Quelle oder nur eine Unterschätzung bereits bekannter Methanquellen verantwortlich zu machen ist verbleibt unklar. Neueste Studien zeigen in der Tat, daß eine bislang unbekannte Methanquelle, nämlich die direkte Emission von Pflanzen, für diese Diskrepanzen verantwortlich sein könnten. Sollten sich diese Indizien durch Validationsstudien verhärten wäre eine Neubewertung des globalen Methanhaushaltes erforderlich.

Eine Ausweitung der Analysen auf die Jahre 2003 und 2004 zeigte, dass die Diskrepanzen jeweils in den Monaten August bis Oktober am höchsten sind. Weiterhin konnten im Zweijahresmittel die höchsten Methanvorkommen im roten Becken in China beobachtet werden. Die Präzision der Messungen erlaubt nun, sie in Inversionsmodellen zu verwenden um die zeitliche und geographische Verteilung der Methanquellen zu quantifizieren. Da Methan als zweitstärkstes anthropogenes Treibhausgas im Rahmen des Kyotoprotokols gehandelt wird, ist eine genaue Bestimmung der Quellstärken unabdingbar, und diese Arbeit ist ein wichtiger Schritt im Hinblick auf die Verwendung von Satellitendaten zur Quellstärkenbestimmung von Treibhausgasen.

Short summary

On the night of 28 February/1 March 2002 the European Space Agency (ESA) launched the environmental satellite ENVISAT on an Ariane 5 rocket from the European spaceport in Kourou. Onboard is, amongst others, the instrument SCIAMACHY that, for the first time in the history of space-borne remote sensing, features near infrared spectrometers measuring sunlight reflected and scattered back from the earth's surface and atmosphere.

In contrast to thermal emission sounders, the near infrared spectrometers enable the global retrieval of methane, carbon dioxide and carbon monoxide for the first time with high sensitivity to near-ground atmospheric layers. In this thesis, an algorithm was developed based on the principles of differential optical absorption spectroscopy (DOAS), that deals with the peculiarities of retrieving strong absorbers in the near infrared, thus allowing a precise retrieval of the respective trace gases. It was shown that nonlinear iterative schemes are necessary to account for saturation effects and to avoid interdependencies of spectrally overlapping strong absorbers. The resulting *nonlinear maximum a Posteriori* algorithm *(IMAP-DOAS)* was applied to spectra recorded by SCIAMACHY and the retrieved total columns of methane and carbon monoxide were analyzed and interpreted. Since SCIAMACHY cannot be considered a dedicated greenhouse gas mission but a prototype with respect to near infrared spectroscopy, several instrumental shortcomings had to be solved. An extensive analysis of these effects enabled the retrieval of methane and carbon monoxide.

Enhancements of carbon monoxide in biomass-burning regions could be clearly identified. In addition, the seasonal and geographical patterns of typical biomass burning regions could be observed. Only in the industrial regions of China, high carbon monoxide abundances were found to be persistent over the year.

The worldwide first global measurements of the total columns of methane with high precision were made possible by use of concurrent retrievals of the relatively homogenously distributed carbon dioxide as proxy for the light path of the recorded photons. It was shown that the retrieved methane abundances show a very good agreement with modeled abundances from the chemistry-transport model TM3. The highest abundances were found over areas of rice cultivation in South-East Asia and can be considered a direct proof of large scale methane emissions in Asia.

In the time-period from August through November 2003, large discrepancies between measurements and model were discovered over tropical rainforest areas. Measured abundances showed persistently higher abundances than those predicted by the model. This led to the conclusion that the tropical regions as methane source have been hitherto underestimated in current emissions inventories. Whether the discrepancies are attributable to a so far unknown methane source or to simply an underestimation of already known sources remains unclear. Recent studies suggest that there might indeed be a yet unknown source, namely the in-situ formation of methane in plants. If these findings can be supported by validation studies, a reassessment of the global methane budget should be indispensable.

An extension of the analysis to the years 2003 and 2004 showed that the discrepancies are highest during the months of August through October. In addition, the highest methane abundances averaged over 2 years are found in the red basin in China. The precision of these measurements now allows their use in inversion models to quantify the temporal and geographical distribution of methane sources. Since methane, as second strongest anthropogenic greenhouse gas, is subject to the Kyoto-Protocol, a precise determination of its source strengths is indispensable. Thus, this work can be considered an important step towards greenhouse gas source inversions using space based retrievals.

Contents

Chapter 1

Introduction

1.1 Foreword and Thesis Outline

The objective of this thesis was the global retrieval of methane, carbon dioxide and carbon monoxide from the SCIAMACHY[1] instrument onboard the European research satellite ENVISAT. In this work, several factors required detailed investigations in a hitherto scarcely explored scientific field, viz. space borne near infrared spectroscopy. First, a new algorithm had to be developed since already existing retrieval algorithms that have been proven successful in the UV and visible spectral region cannot be applied in the near infrared where absorption spectroscopy is highly non-linear. Second, methane and carbon dioxide are long-lived trace gases exhibiting very small variations in the atmosphere. Thus, the precision requirements for a meaningful retrieval from space are unprecedented. Third, when SCIAMACHY was designed, no appropriate near infrared detectors were available (*Buchwitz et al.*, 2005b). The near infrared InGaAs detectors were a special development for SCIAMACHY, albeit now outdated compared to state of the art technology.

In the introductory part, I will give a brief overview of the SCIAMACHY instrument before explaining the peculiarities of the near infrared spectral region and the necessity of substantial modifications to the classical Differential Optical Absorption Spectroscopy (DOAS, *Platt* (1994)) algorithm. Further, instrumental problems and their implications are introduced before I explain the general obstacles in retrieving total column amounts of trace gases with a precision of 1-2%.

In addition to these more technical issues, the importance of global measurements of methane and carbon monoxide is described, confining the scientific interpretation of the results mainly to the publications (chapters 2 to 5 (*Frankenberg et al.*, 2005a,b,c,d)) and the discussion part of this thesis.

The core of this thesis is comprised of 4 scientific publications. Chapter 2, published in Atmospheric Chemistry and Physics (*Frankenberg et al.*, 2005a), is a technical paper that deals with the development of a new retrieval algorithm optimized for the near infrared spectral

---

[1] **SC**anning **I**maging **A**bsorption Spectro**M**eter for **A**tmospheric **CH**artograph**Y**, Greek word for the activity of fighting or arguing against imaginary opponents, literally for *fighting shadows*: Greek skiamakhia: skia=shadow; makhe=fight.

region. Based on the algorithm elaborated in chapter 2, chapter 3, published in Atmospheric Chemistry and Physics (*Frankenberg et al.*, 2005b), shows first intensive studies of retrievals of carbon monoxide and the solution to instrumental difficulties. Chapter 4, published in Science (*Frankenberg et al.*, 2005c), elaborates the retrieval of methane and introduces the application of concurrent CO_2 total column retrievals to convert total columns of methane to column averaged mixing ratios. A comparison with the atmospheric transport model TM3 (*Dentener et al.*, 2003) revealed that methane emissions in the tropics are hitherto vastly underestimated. The analysis in chapter 4 is further refined in chapter 5, submitted in a revised version to the Journal of Geophysical Research (*Frankenberg et al.*, 2005d)).

Chapter 6 briefly summarizes this thesis and discusses the latest results as well as the future potential of the work elaborated in this thesis.

In the appendix, more technical issues related to this work are presented.

Please note that the introductory part of this thesis is more a guideline for the publications and all but a complete introduction to the scientific fields under investigation. The basic purpose of the introductory part is to illustrate the different topics of the publications using simplified examples.

1.2 The SCIAMACHY instrument

On the night of 28 February/1 March 2002 the European Space Agency (ESA) launched the environmental satellite ENVISAT on an Ariane 5 rocket from the European spaceport in Kourou. Ever since, ENVISAT has been operating in a near polar, sun-synchronous orbit at an altitude of about 800 km. Amongst various instruments onboard designed for the observation of the earth's surface and atmosphere is SCIAMACHY (**SC**anning **I**maging **A**bsorption spectro**M**eter for **A**tmospheric **CH**artograph**Y**), a grating spectrometer measuring solar radiation reflected at the earth's surface or scattered within the atmosphere. SCIAMACHY is a superset of its predecessor GOME (Global Ozone Monitoring Experiment) onboard ERS-2. Both GOME and SCIAMACHY are equipped with UV/Vis spectrometers, enabling global detection of NO_2, BrO, OClO, H_2O, SO_2, O_3, CH_2O, O_2 and O_4 as well as providing information on clouds and aerosols (*Burrows et al.*, 1999; *Wagner et al.*, 2002).

The instrument alternates between limb and nadir measurement modes. In the latter mode a swath of 960 km gives full global coverage every six days (14 orbits everyday; see Fig. 1.2 for an example of an orbit and the swath). The typical ground pixel size of SCIAMACHY is 30 km (along track, i.e. approx. north-south) times 60 to 120 km (across track, i.e. approx. east-west). In this study only nadir measurements are used, i.e. the instrument points down almost perpendicular to the earth's surface, detecting reflected sunlight.

In addition to GOME, SCIAMACHY features three near infrared spectrometers (channel 6: 1000-1750 nm, ch. 7: 1940-2040 nm, and ch. 8: 2265-2380 nm). Methane (CH_4), carbon dioxide (CO_2), nitrous oxide (N_2O) as well as carbon monoxide (CO) exhibit spectral lines due to vibrational-rotational transitions in this wavelength range. Thermal emission from the earth can be neglected compared to solar radiation in the near infrared. Thus, trace gases can be measured by means of differential optical absorption spectroscopy (DOAS) (*Platt*, 1994). However, retrieval algorithms developed for the UV and visible spectral region cannot be directly

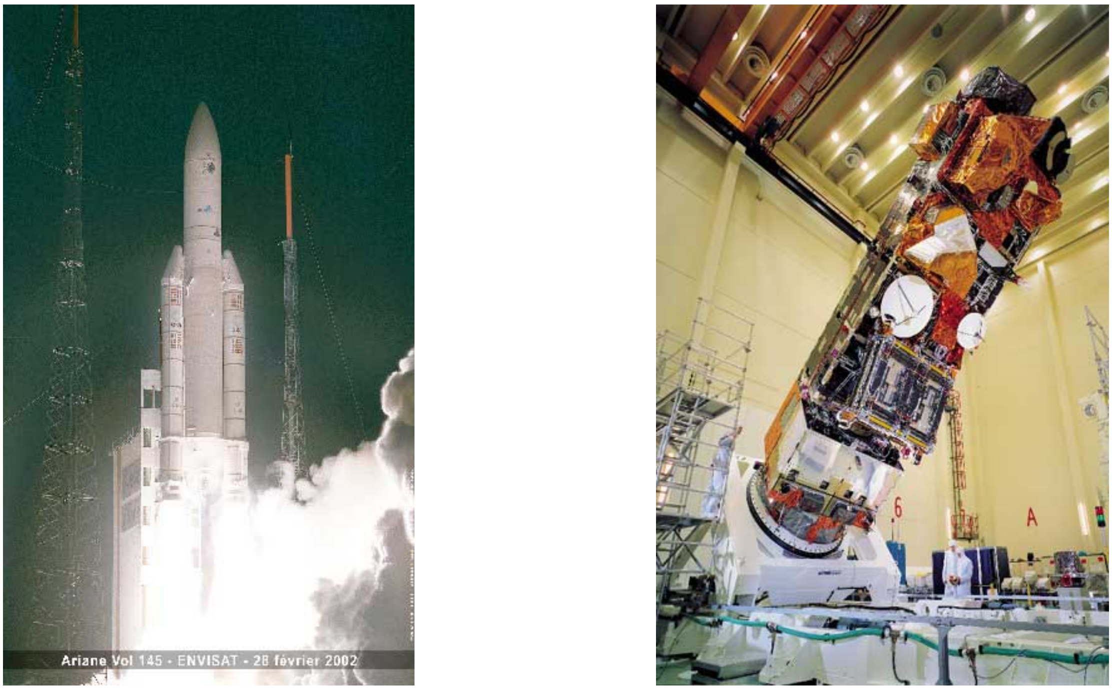

(a) Launch of the Ariane 5 rocket

(b) The ENVISAT satellite

Figure 1.1: The European research satellite ENVISAT and its launch on the Ariane 5 rocket at Kourou (©ESA).

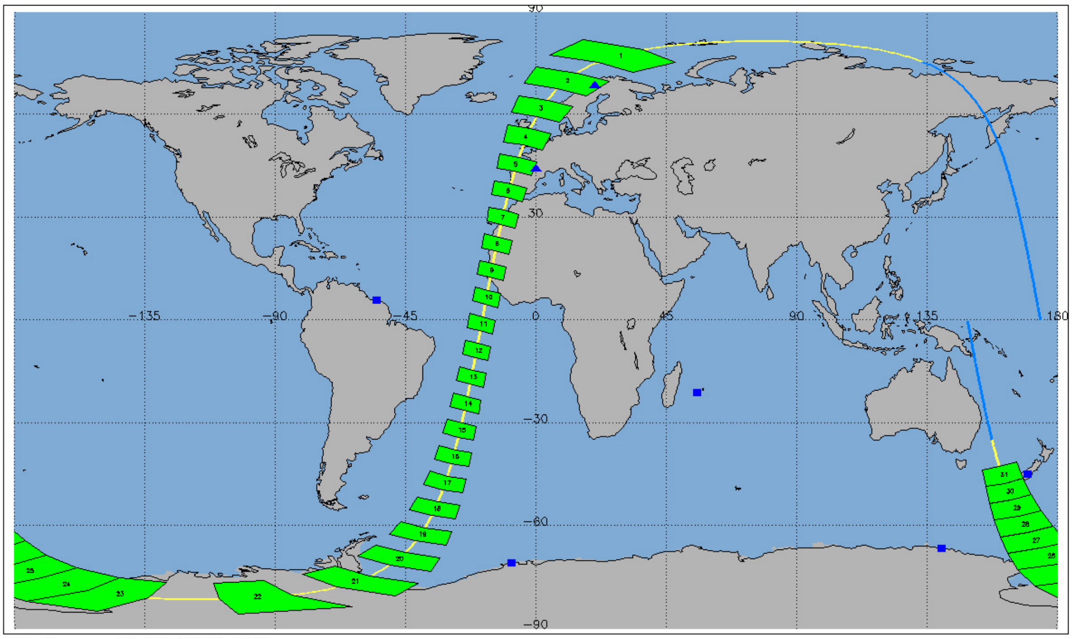

Figure 1.2: Example of SCIAMACHY nadir orbit (taken from the Sciamachy Operations Support Team (SOST) website: http://atmos.af.op.dlr.de/projects/scops/)

applied in the near infrared. Hence, a retrieval algorithm customized for the near infrared is indispensable for the retrieval of global abundances of carbon monoxide and methane.

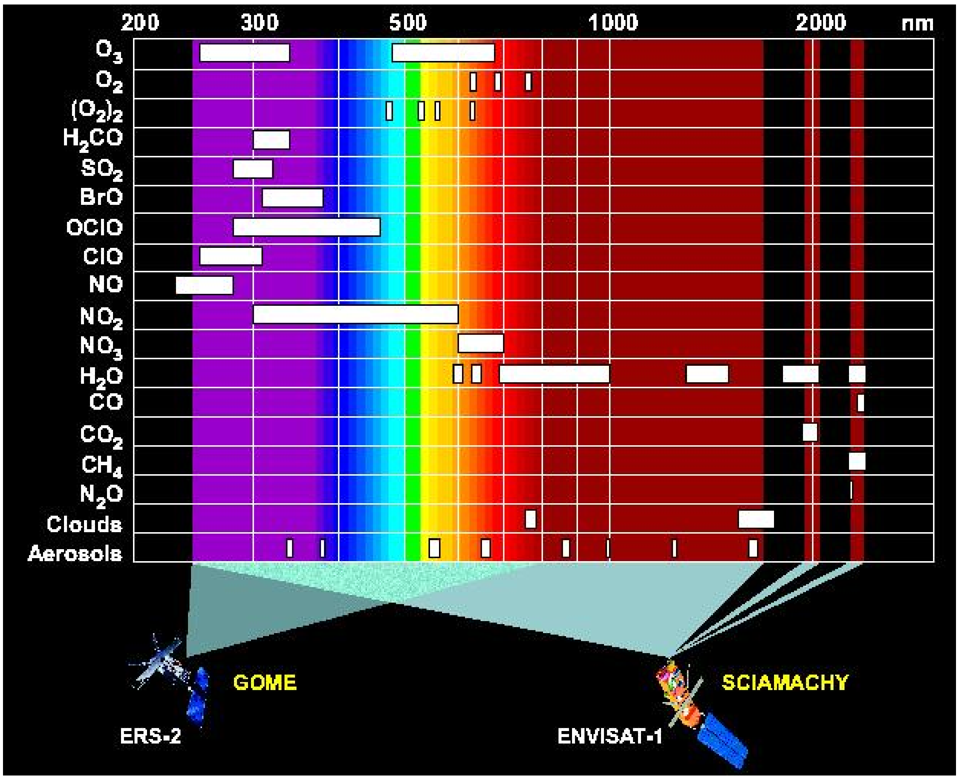

Figure 1.3: The spectral range of GOME and SCIAMACHY (©IUP, University of Bremen).

1.3 Absorption spectroscopy in the near infrared

The infrared spectrum lies between the visible and the microwave regions of the electromagnetic spectrum. In this study, we consider only a small fraction of the infrared region, viz. the part where thermal (blackbody at approx. 285K) emission from the earth's surface and atmosphere can be neglected while the tail of the solar spectrum (blackbody at 5800K) still provides enough photons to be recorded by SCIAMACHY.

The infrared region covered by SCIAMACHY ranges from 0.7 to 2.4 µm. Literature definitions of this spectral region vary widely, one being the near infrared (NIR). According to the German Institute for Standardization (DIN), the near infrared ranges only from 0.7 to 1.4 µm while the region from 1.4 to 3 µm is denoted short wave infrared (SWIR). However, for the sake of consistency the term *near infrared* is used throughout this study for the entire spectral from 0.7 to 3 µm.

In the near infrared, interactions between radiation and molecules in the atmosphere are mainly due to rotational and vibrational transitions, while electronic transitions are rarely involved. Especially the greenhouse gases carbon dioxide (CO_2), methane (CH_4) and water vapor (H_2O) exhibit not only strong absorption lines in the mid infrared (absorbing thermal emission from the earth's surface and atmosphere) but also in the near infrared. The absorption lines are very narrow and often so strong that the transmission drops to almost zero (see Fig. 1.5).

Absorption spectroscopy, such as the method of Differential Optical Absorption Spectroscopy

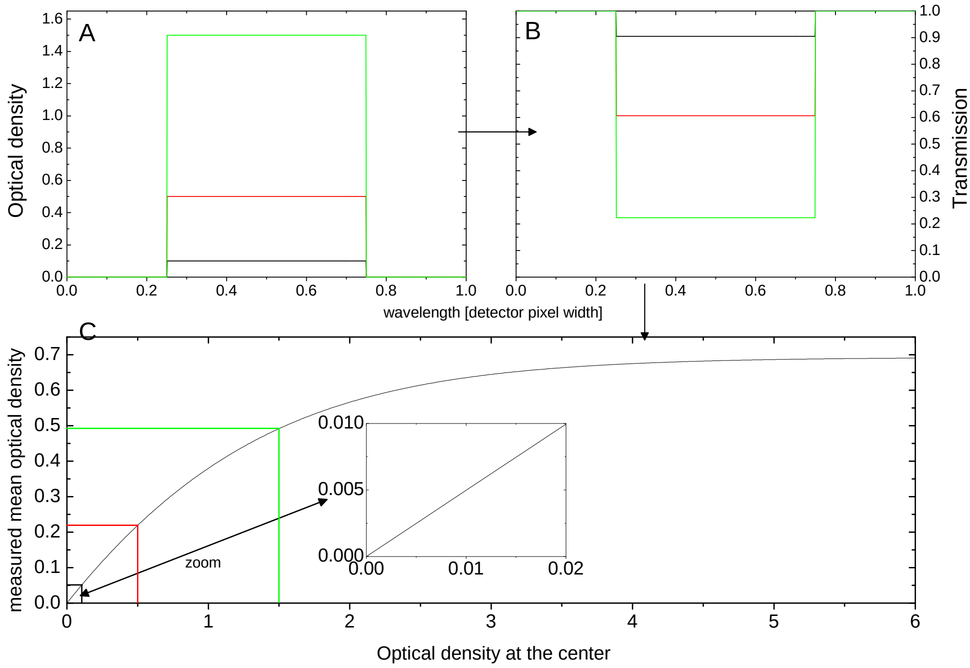

Figure 1.4: Saturation effect. Artificial measurements of an absorber with a box-like line shape (upper left panel, x-axis in units of detector width) and a detector with a spectral resolution that is twice the width of the line shape are shown. The corresponding optical depth measured by this detector is plotted against the actual optical depth of the absorber (at line center).

(DOAS) (*Platt*, 1994), is based on the Lambert Beer Law (cf. Sect. A.1)

$$\frac{I}{I_0} = \exp(-\sigma \cdot S)\,, \tag{1.1}$$

where the logarithm of the measured intensity (I) divided by the incident intensity (I_0) is strictly proportional to the number concentration of the respective absorber integrated along the light path (S denotes the slant column density and σ the cross section of the respective trace gas for a given wavelength).

Strictly speaking, the Lambert Beer law is only valid for monochromatic light, i.e. when spectrometers can fully resolve individual absorption lines. In our case, however, we are dealing with moderate spectral resolution, i.e. the spectrometer detects light convolved with an instrumental function that is broader than individual absorption lines. Thereby, always a blend of different wavelengths with very different transmissions is recorded. For weak absorbers, the Lambert Beer law is still valid, but in the near infrared, where optical densities are often large, there is no linear relationship between the measured (i.e. convolved) optical density and the trace gas column density any more. This nonlinearity is not to be confused with nonlinearities due to disturbances in the population of the lower rotational and vibrational levels (cf. Sect. C.1).

A simple but illustrative example is given in Fig. 1.4 where an artificial absorber with a box line profile is measured by a spectrometer with a box-shaped instrumental function. In panel A, the optical density of the absorber (with 3 different concentrations) is shown as a function of the width of a detector pixel. The absorption line is only half as broad as the pixel while the instrumental function is supposed to be a box with the same width as the detector pixel. The resulting transmission is depicted in panel B while the mean transmission ($\bar{T}$) with respect to the entire detector pixel is given by

$$\bar{T} = \underbrace{0.5 \cdot 1}_{T_1} + \underbrace{0.5 \cdot \exp(-\tau)}_{T_2} . \tag{1.2}$$

It is obvious that at least half the incident light is always transmitted (T_1) since the artificial absorber can at most attenuate the other half (T_2). Taking the negative logarithm of the mean transmission measured by the detector pixel (expressed as measured mean optical density), there is a fundamental difference from the mean optical density (i.e. half the optical density at the line center). This can be seen in panel C where the linear relationship is valid at very small optical densities (see zoom-box) but where saturation effects eventually come into play. For $\tau \rightarrow \infty$, the measured optical density approaches $-\log(0.5) \approx 0.69$.

Although this example is largely contrived, it underlines the problem that arises when the actual width of strong absorption lines is not fully resolved by the spectrometer. The relations become nonlinear causing the classical DOAS algorithm (*Platt*, 1994) to fail. Hence, a non-linear iterative algorithm was developed in *Frankenberg et al.* (2005a). The simple example stresses another important factor, namely that, for strong absorbers, the sensitivity depends on the width of the actual absorption line. Consequently, broader absorption lines absorb more efficiently than narrow ones[2] that might be closer to saturation. In the atmosphere, pressure is one of the main factors governing the actual shape of absorption lines (*Goody and Yung*, 1989) (cf. Sec. C.2). In the lower atmosphere, the width of the absorption line is proportional to pressure. Hence, at high pressure the line wings contribute more to the absorption process while the line center might already be saturated. Consequently, absorption is more effective in lower parts of the atmosphere and, in turn, the sensitivity of the measurement depends on height. This complication is thoroughly investigated in chapter 2 (*Frankenberg et al.*, 2005a) and 5 (*Frankenberg et al.*, 2005d) where the effect of this height sensitivity with respect to a comparison with atmospheric models is analyzed.

Another complication in the retrieval will arise if the absorption lines of strong absorbers overlap. In this case, the involved species cannot be treated independently any more. The retrieval of minor absorbers can then be severely hindered, as explained in Appendix A.4. This holds especially for the CO retrieval in this study since its weak absorptions are overlapped by strong water vapor and methane absorption lines. The iterative retrieval algorithm elaborated in chapter 2 effectively avoids the effects of overlapping absorbers and thereby enables the retrieval of carbon monoxide as shown in chapter 4.

A detailed description of the theory behind the shape of absorption lines is far beyond the scope of this thesis. A good general overview can be found in *Goody and Yung* (1989), *Thomas and Stamnes* (1999) or in a freely available community text (FACTs) by C. Zender (http://dust.ess.uci.edu/facts/). More detailed information can be found in *Dicke* (1953); *Ma and Tipping* (1999); *Clough et al.* (1989); *Strow and Reuter* (1988); *Pine* (1997).

---

[2] In the same way, pressure broadening influences the effectiveness of greenhouse gases absorbing thermal infrared radiation emitted by the earth. Interestingly, this is one of the reasons for the extraordinary strong greenhouse effect of Venus, where the air pressure with its main constituent $\mathsf{CO_2}$ is 91 times the Earth's surface atmospheric pressure.

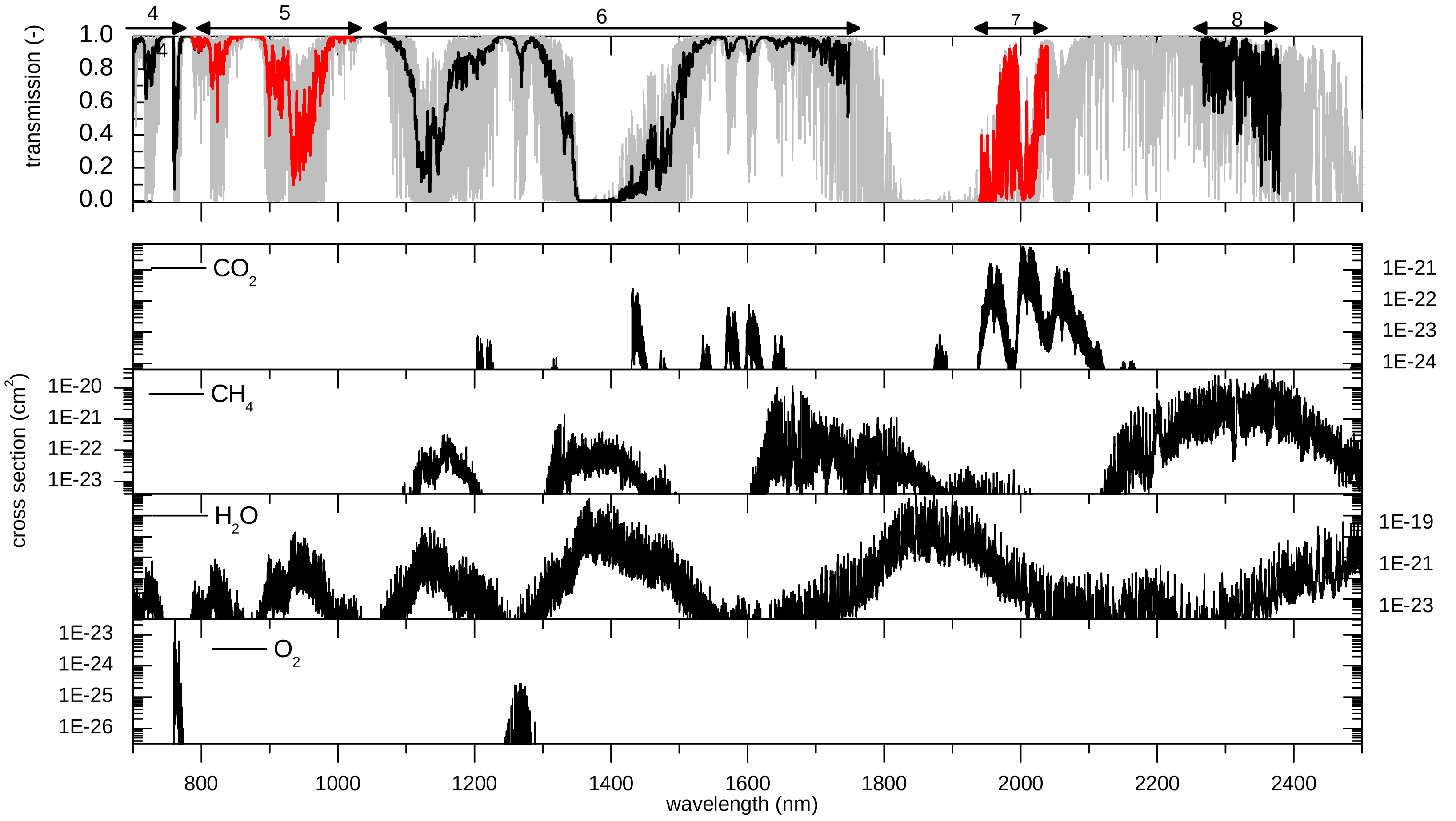

Figure 1.5: Transmission spectra of an artificial SCIAMACHY measurement. The upper panel shows a highly resolved transmission spectrum from space considering the gases CO_2,H_2O,CH_4 and O_2. The theoretical SCIAMACHY measurements of channels 4 (FWHM=0.48 nm),5 (FWHM=0.54 nm),6 (FWHM=1.35 nm),7 (FWHM=0.22 nm) and 8 (FWHM=0.24 nm) are shown in the alternating colors black and red. For the gases the US-Standard profiles are taken and the slant column density (SCD) is chosen to be exactly twice the vertical column density (VCD). The lower panels show the cross sections of the respective gases at 288K and 1013hPa.

1.4 The SCIAMACHY near infrared detectors

From a technological viewpoint, spectrometry (using image arrays) in the near infrared is a challenging task. At the time SCIAMACHY was planned, the now common detector material Indium Gallium Arsenide (InGaAs) was still very experimental and especially the extension of the wavelength range to nearly 2.4 µm was very difficult. Compared to classical silicon detectors used in the UV and visible, the major drawbacks of the SCIAMACHY InGaAs detector pixels are a substantially higher pixel-to-pixel variability in quantum efficiency and a more predominant dark (leakage) current. Further, an increasing number of pixels are developing defects and the build-up of an ice layer on channels 7 and 8 deteriorates throughput and alters the instrumental line-shape. All these factors were not considered in the development of operational calibration tools. Hence, the correction for dark current as well as the identification of dead or bad pixels had to be implemented in the retrieval scheme of this work.

Figure 1.6 depicts a typical SCIAMACHY measurement. The upper panels show the raw readouts of all detector pixels before any dead or bad pixels have been removed. After this correction (second panel-row of the figure), the total raw readouts are composed of the actual signal (red area) and the dark current (black area). Following the idea of Buchwitz and de Beek (personal communication), the dark current is corrected by directly subtracting the actual dark current measurements (now performed every night when the sun is eclipsed by the earth) corresponding to the pixel exposure time of the measurement under consideration. The dark current itself consists of fixed pattern noise and leakage current. For channel 6, most of the dark current consists of fixed pattern noise whereas channel 8 exhibits high leakage current. In the example spectra, nearly half the signal stems from dark current. For the retrieval, not as much the absolute magnitude as the uncertainty in dark current is of importance. The third row depicts the standard deviation of the respective dark current measurements at eclipse. Within channel 6, there is a change in the detector material with a substantially increased dark current variability at higher wavelengths.

Given this measurement, the signal to noise ratio (only considering the noise of the dark current) is shown in the lowermost panels (note the different scales for the channels). While for channel 6 dark current might not be the major source of noise, it certainly plays an important role in channel 8. Due to the decline in quantum efficiency, the signal to noise ratio in channel 8 steadily decreases with increasing wavelength. This is one of the reasons for the choice of the fitting window for CO in chapter 3.

A good characterization of the uncertainty of each pixel readout is necessary for a proper retrieval. However, DOAS retrievals are performed in the log-space, i.e. the original measurement of I/I_0 is transformed via the logarithm. Thus, also the associated errors of the original measurements (denoted by $\sigma(I/I_0)$) have to be transformed to the log-space

$$\sigma(\log(I/I_0)) \approx \frac{I_0}{I} \cdot \sigma(I/I_0)\,. \tag{1.3}$$

In an optically thin medium, variations of I/I_0 are small and the associated transformed errors strongly resemble the errors in the actual measurement, the transformation having no major effect on the weighting of the individual pixels. If, however, strong absorbers result in high pixel to pixels variations of I/I_0, Eq. (1.3) has to be applied.

In channels 7 and 8, an additional problem occurs. It has been found that water vapor has

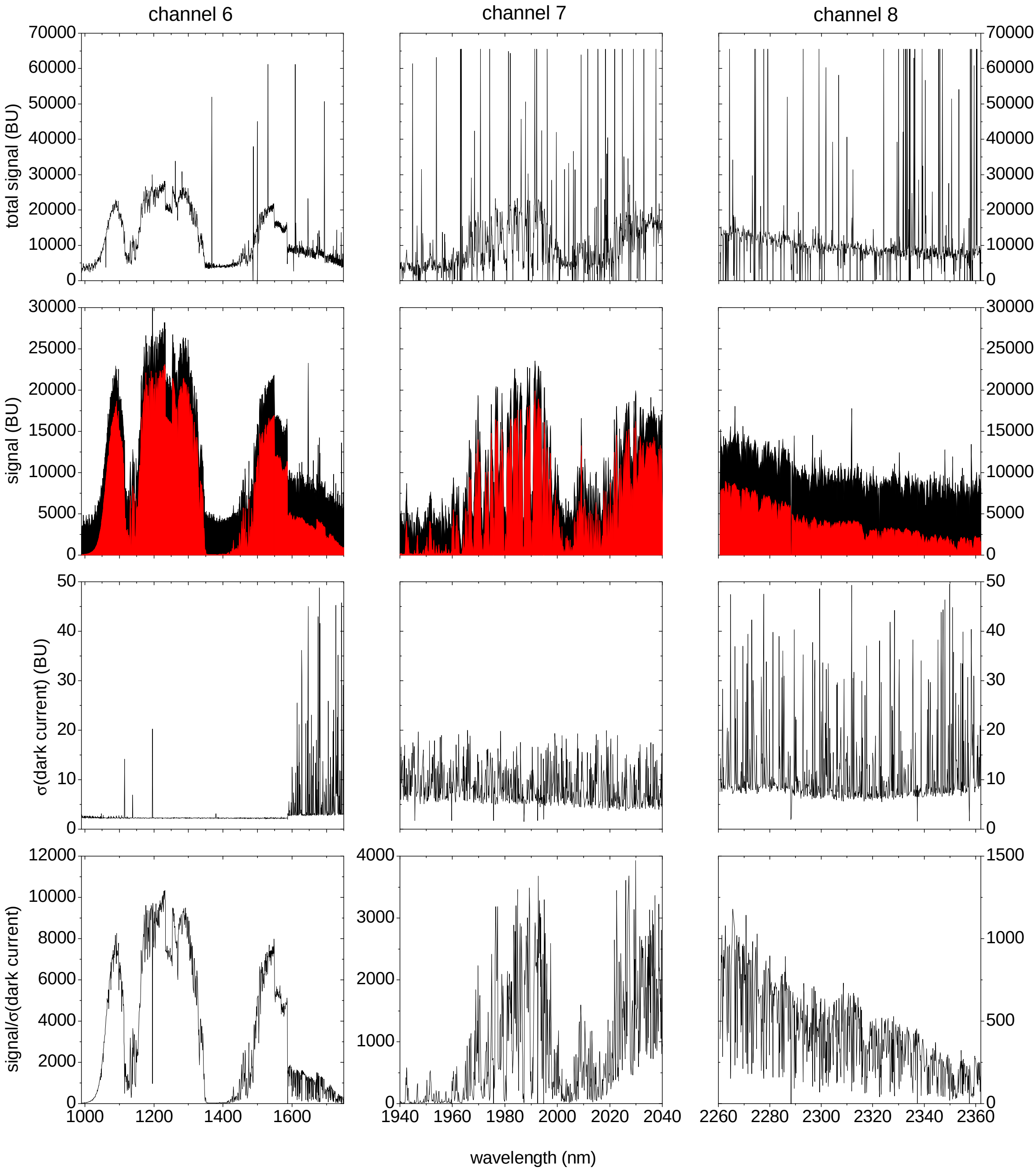

Figure 1.6: Exemplary SCIAMACHY measurements over the Sahara at the 20th of May 2005 (Orbit 11613, latitude: 21.55°, longitude: 13.45°). The upper panels show the raw detector readouts of channels 6,7 and 8, respectively. In the second row, pixels marked as dead or bad are masked out and the individual contribution of the dark current (black area) and actual signal (red area) are shown. The third row depicts the standard deviation of the dark current measurements performed at the night side of orbit 11613. The bottom panels show the signal to noise ratio of this measurement assuming that the standard deviation of the dark current is the only and limiting noise term.

somehow infiltrated the satellite. Since channels 7 and 8 are the coolest elements (150K) of the SCIAMACHY instrument, the water vapor resublimation occurs on the surfaces of these detectors. This ice layer has two impacts, first it reduces the transmission and second, it alters the instrumental line-shape and the dark current as photons are scattered within the ice layer (see *Gloudemans et al.* (2005) and references therein). From time to time, SCIAMACHY is heated in order to get rid of the ice layer. However, after these decontamination periods, the ice layer starts to rebuild once the detectors are at nominal temperature. Thus, the problem of transmission and line-shape distortion depends strongly on time. For the retrieval of carbon monoxide, there is no way to circumvent this problem since strong absorption lines are only present in channel 8. However, both methane and carbon dioxide exhibit absorption lines in channel 6 as well. To avoid these instrumental problems for the methane and carbon dioxide retrieval, channel 6 has been chosen for the retrieval whereas only CO is being retrieved using channel 8 spectra.

1.5 Atmospheric methane

Methane ($\mathsf{CH_4}$) is the most abundant hydrocarbon in the atmosphere and plays an important role in the context of radiative forcing (*Lelieveld et al.*, 1998; *IPCC*, 2001) and atmospheric chemistry. Methane is, after carbon dioxide, the second most important anthropogenic greenhouse gas, directly contributing $0.48\,\mathsf{Wm^{-2}}$ to the total anthropogenic radiative forcing of $2.43\,\mathsf{Wm^{-2}}$ by well-mixed greenhouse gases (*IPCC*, 2001). In addition, it exhibits an indirect effect of about $0.13\,\mathsf{Wm^{2}}$ through formation of other absorbing gases, most notably tropospheric ozone and stratospheric water vapor (*Lelieveld et al.*, 1998). Recent studies by *Shindell et al.* (2005) and *Hansen et al.* (2005) show that the overall impact (direct and indirect) of methane is even slightly higher than the aforementioned estimates, namely $+0.8\ \mathsf{Wm^{-2}}$, which is more than half of the forcing by $\mathsf{CO_2}$.

Since the beginning of industrialization, atmospheric methane abundances have more than doubled (*Etheridge et al.*, 1998) albeit with decreasing growth rate (*Dlugokencky et al.*, 1998) during the past two decades. Further, $\mathsf{CH_4}$ shows considerable inter-annual variations (*Dlugokencky et al.*, 2001). As *Hansen et al.* (2000) point out, if sources of $\mathsf{CH_4}$ and other $\mathsf{O_3}$ precursors were reduced in the future, the change in climate forcing by non-$\mathsf{CO_2}$ greenhouse gases in the next 50 years could be near zero.

This underlines the necessity of understanding and quantifying the methane budget properly, a goal that is, as shown in chapter 4 (*Frankenberg et al.*, 2005c), currently only partially achieved.

According to current knowledge, the origin of methane in the atmosphere is mainly biogenic, caused by bacteria that already produced methane in the early history of the planet earth, viz. the Archean (4.0–2.5 billion years ago). These methane-forming bacteria, called methanogens, belong to the kingdom of Archaebacteria and share, apart from the formation of methane in their respiratory system, the feature of being strictly anaerobic (see *Ehrlich* (1990) and references therein). In the simplest case, the metabolism uses hydrogen as energy source and reduces $\mathsf{CO_2}$ to methane.

$$4\mathsf{H_2} + \mathsf{CO_2} \rightarrow \mathsf{CH_4} + 2\mathsf{H_2O}\,. \tag{R1.1}$$

Apart from $\mathsf{CO_2}$, acetic acid, methanol or methylamines act as electron acceptor. In the presence of alternative electron acceptors (such as $\mathsf{NO_3^-}, \mathsf{Fe(III)}, \mathsf{Mn(IV)}$), methane production is often suppressed.

It is supposed that, before the incidence of oxygen in the archean atmosphere, methane was the most abundant greenhouse gas at a level of 1000 parts per million (*Kasting*, 1993; *Kasting and Siefert*, 2002). Since the sun was considerably dimmer at that time, the additional greenhouse effect of methane might have kept the earth from freezing (*Pavlov et al.*, 2000; *Kasting and Siefert*, 2002).

Even today, methanogens are supposed to account for the majority of methane emissions into the atmosphere. This holds not only for emissions from wetlands where methanogens find the optimal breeding ground but also for ruminants which bear methanogens in their gestative organs. Also in landfills, methanogens are responsible for the production of methane. Hence, it is often difficult to distinguish natural from anthropogenic emissions. Rice paddies are one example where an anaerobic environment is artificially created by waterlogging (about 4 months a year). Methane produced by soil methanogens is then released through the stems of the plants growing in it (called plant-mediated transport). Only recently, the archaeal group of microorganisms that plays a key role in CH_4 production from plant-derived carbon has been isolated (*Lu and Conrad*, 2005). In nature, most of the methane thus produced is subsequently oxidized by a group of aerobic bacteria, the so-called methanotrophs. Due to the competition of methanogens and methanotrophs, the magnitude of local methane emission depends on many natural factors such as water table, redox potential, pH and temperature.

Table 1.1 summarizes the emission estimates given in *IPCC* (2001). Next to biogenic emissions, the energy sector (natural gas, coal mines) and biomass burning contributes most to the overall source of methane.

Table 1.1: Range of IPCC (2001) methane emission estimates

Category	Methane source strength (Tg/year)
Natural	
Wetlands	115–237
Termites	20
Ocean	10–15
Hydrates	5–10
Anthropogenic	
Energy	75–110
Landfills	35–73
Ruminants	80-115
Waste treatment	14–25
Rice agriculture	25–100
Biomass burning	23–55
Total	500–600

Currently, the annual source strength is estimated to be 550 (±50) Tg. Although the individual source strengths and their geographic variations are not well known (see Table 1.1), the total source strength is relatively well constrained by the predominant sink, viz. oxidation by OH radicals. Further constraints on individual source strengths for separate emission processes

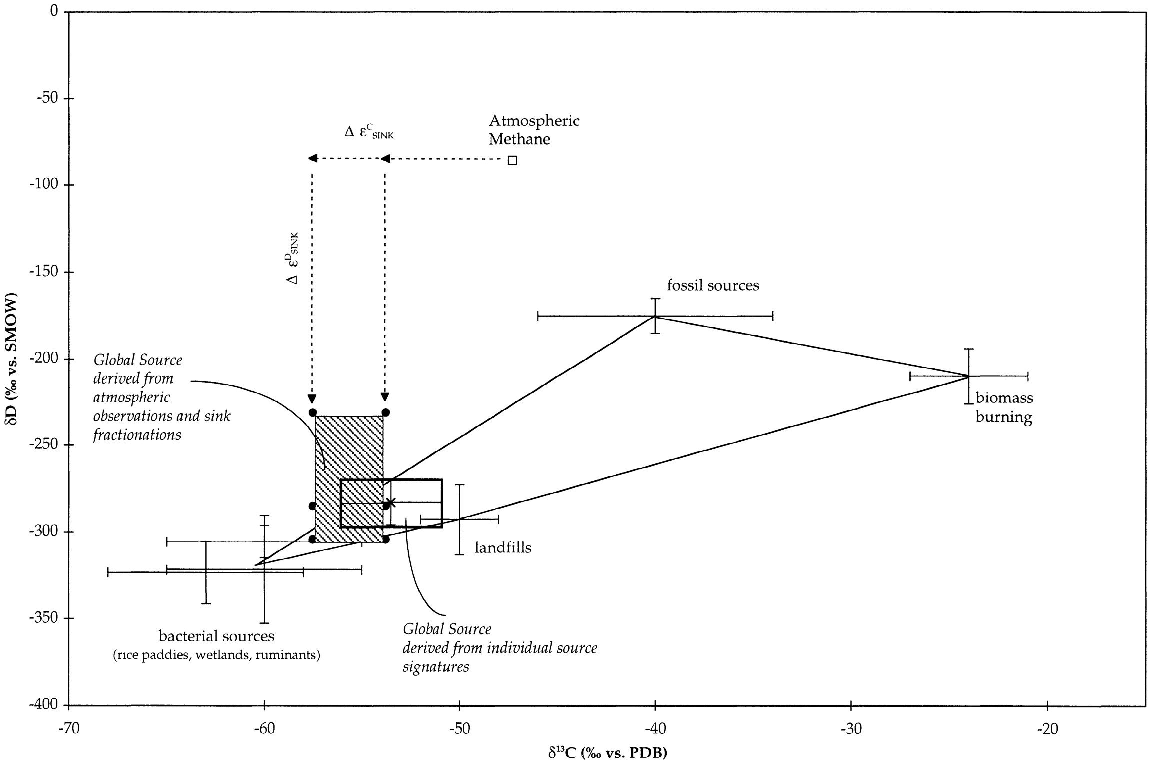

Figure 1.7: Isotopic fractionation of methane. Image courtesy: American Geophysical Union, *Snover et al.* (2000). Original Figure caption: Mixing diagram for the global CH_4 source. The δD and $\delta^{13}C$ of the major CH_4 sources define the possible combinations of δD and $\delta^{13}C$ isotopic composition for the global CH_4 source, i.e., the outline triangle (using a δD and $\delta^{13}C$ for the mean bacterial source of -318 and -61‰, respectively). Combining the strengths and isotopic compositions of the CH_4 sources results in a global CH_4 source with $\delta D = -283 \pm 12‰$ and $\delta^{13}C = -53.5 \pm 2.6‰$ (bolded box). The δD and $\delta^{13}C$ of the global source can also be determined by adjusting the observed δD and $\delta^{13}C$ of atmospheric CH_4 (open square) for the isotopic fractionations associated with CH_4 loss, $\Delta\epsilon_{sink}$, assuming steady state. This yields the area depicted by the cross-hatched rectangle. The solid circles represent the isotopic composition of the CH_4 source derived in this manner using the hydrogen and carbon fractionations during CH_4 loss to OH determined by *deMore* (1993), *Gierczak et al.* (1997) and *Xiao et al.* (1997) ($\Delta\epsilon^{D}_{sink}$ top to bottom) and *Gupta et al.* (1997) and *Cantrell et al.* (1990) ($\Delta\epsilon^{C}_{sink}$ left to right), respectively, in the calculation of $\Delta\epsilon_{sink}$.

can be given by the isotopic fractionation in atmospheric methane abundances (cf. *Snover et al.* (2000) and references therein). Measurements of isotopes provide a powerful tool to discriminate source processes (see Fig. 1.7) but operational global measurements are so far limited. In this work isotopes are not considered separately since the precision of SCIAMACHY does not allow the discrimination of isotope fractionation in a per mil range.

The mean global loss rate of atmospheric CH_4 is dominated by its reaction with OH in the troposphere (*Jacob*, 1999):

$$CH_4 + OH \rightarrow CH_3 + H_2O \qquad \text{(R1.2)}$$

$$CH_3 + O_2 + M \rightarrow CH_3O_2 + M \qquad \text{(R1.3)}$$

The methylperoxy radical (CH_3O_2) is analogous to the HO_2 radical and its main sinks are reaction with either HO_2 or NO:

$$CH_3O_2 + HO_2 \rightarrow CH_3OOH + O_2 \tag{R1.4}$$

$$CH_3O_2 + NO \rightarrow CH_3O + NO_2 \tag{R1.5}$$

Methylhydroperoxide (CH_3OOH) and the methoxy radical (CH_3O) are further oxidised to formaldehyde (CH_2O), carbon monoxide (CO), subsequently forming carbon dioxide (CO_2) (*Jacob*, 1999). Depending on the availability of NO_x, OH and ozone are produced (high-NO_x case) or OH is consumed (low-NO_x case) (*Jacob*, 1999; *Houweling*, 1999). This underlines both, the importance of methane influencing the global abundance of the OH radical as well as being a source of formaldehyde and carbon monoxide.

Apart from oxidation by the OH radical, methane can also react with the Cl radical produced in the marine boundary layer (see *Platt et al.* (2004) and references therein):

$$CH_4 + Cl \rightarrow CH_3 + HCl \tag{R1.6}$$

Compared to OH, this sink is supposed to be relatively small (≈ 19 $Tgyr^{-1}$).

For the sake of completeness, it has to be mentioned that CH_4 can also be photolyzed in the upper stratosphere and mesosphere (*Brasseur and Solomon*, 1996).

1.5.1 Simple methane box model

Assuming a total atmospheric burden of 4950 Tg(CH_4) (roughly corresponding to an average mixing ratio of 1750ppm), a very simple box model of the atmosphere can be constructed. In the simplest form, we can regard the entire atmosphere as one box. If the reaction rate of (R1.2) is $k = 1/\tau$ with a lifetime τ of 9 years, the mass balance equation can be written as

$$\frac{d[CH_4]}{dt} = -k_{R1.2} \cdot [CH_4] + \sum_i S_i \,, \tag{1.4}$$

where S_i denotes the individual sources and $[CH_4]$ the atmospheric burden of CH_4 in Tg. In steady state, $\frac{d[CH_4]}{dt}$ is zero and one can easily solve for $\sum_i S_i$:

$$\sum_i S_i = k \cdot [CH_4] = \frac{[CH_4]}{\tau} \,. \tag{1.5}$$

Using realistic numbers, we find an annual source strength of 4950Tg/9yr = 550Tg/yr. Due to various reasons (like uncertainties in the OH distribution and rate constants), the lifetime is known with a precision of approximately 10%, directly translating to an uncertainty in the annual source strength of 10%. This example is probably the simplest form of a source strength inversion. Only the measurement of the average methane burden and its time evolution has to be known to infer the overall source.

The example can be extended to a 2-box model, describing the atmosphere in 2 boxes, one for each hemisphere (*NH* for northern hemisphere and *SH* for southern hemisphere). Now we also have to consider the transport between both boxes, which can be described by the interhemispheric exchange coefficient $k_{IH} \approx 1yr^{-1}$ (see Fig. 1.8). The mass balance equation

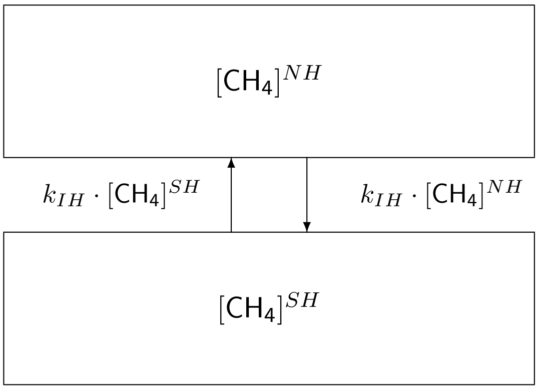

Figure 1.8: Simple methane 2 box model

of both boxes now reads

$$\frac{d[\mathsf{CH_4}]^{NH}}{dt} = -k_{R1.2} \cdot [\mathsf{CH_4}]^{NH} + \sum_i (S_i^{NH}) - k_{IH} \cdot [\mathsf{CH_4}]^{NH} + k_{IH} \cdot [\mathsf{CH_4}]^{SH} \tag{1.6}$$

$$\frac{d[\mathsf{CH_4}]^{SH}}{dt} = -k_{R1.2} \cdot [\mathsf{CH_4}]^{SH} + \sum_i (S_i^{SH}) + k_{IH} \cdot [\mathsf{CH_4}]^{NH} - k_{IH} \cdot [\mathsf{CH_4}]^{SH}\,. \tag{1.7}$$

We can now study, for instance, how the interhemispheric gradient of methane depends on the unequal distribution of sources (and sinks) with regard to both hemispheres. Figure 1.9 depicts the dependence of the interhemispheric methane gradient (%) as a function of the southern hemispheric source strength (given a total source of 550Tg/yr). Assuming an interhemispheric mixing time of 1 year and that 25% of the total source is located in the southern hemisphere, we infer a methane gradient of approximately 6% which is close to the actually observed one.

However, the individual contributions of the separate sources S_i can still not be inferred from these simple models. The models described here should only give an impression on what even simple models can achieve and that models are necessary to translate measurements of the abundances of atmospheric trace gases to actual emission rates. Modern complex models divide the earth into 3-dimensional boxes and use wind fields and parameterizations for exchange coefficients to simulate abundances of trace gases in the atmosphere. In this thesis, modeled methane abundances from the TM3 model (*Dentener et al.*, 2003) are compared with SCIAMACHY retrievals (see chapters 4 and 5).

Figure 1.10 shows an example of modeled (TM3) and retrieved methane abundances. The synoptic variations of atmospheric methane are unusually large during the two days that are shown. In most cases, the SCIAMACHY retrieval captures high abundances predicted by the model. The figure further illustrates the different spatial resolutions of model and measurement as well as the gaps between the SCIAMACHY retrievals, which are due to the alternate nadir limb viewing geometry.

In chapters 4 and 5, the model is mainly used to compare retrievals by SCIAMACHY with modeled methane abundances. The applied model incorporates current knowledge on the distribution, strength and time dependence of individual sources. Any significant deviation from measurements is thus an indicator to erroneous input parameters in the model. Since methane is so well mixed within the atmosphere, local gradients are fairly small, with rare

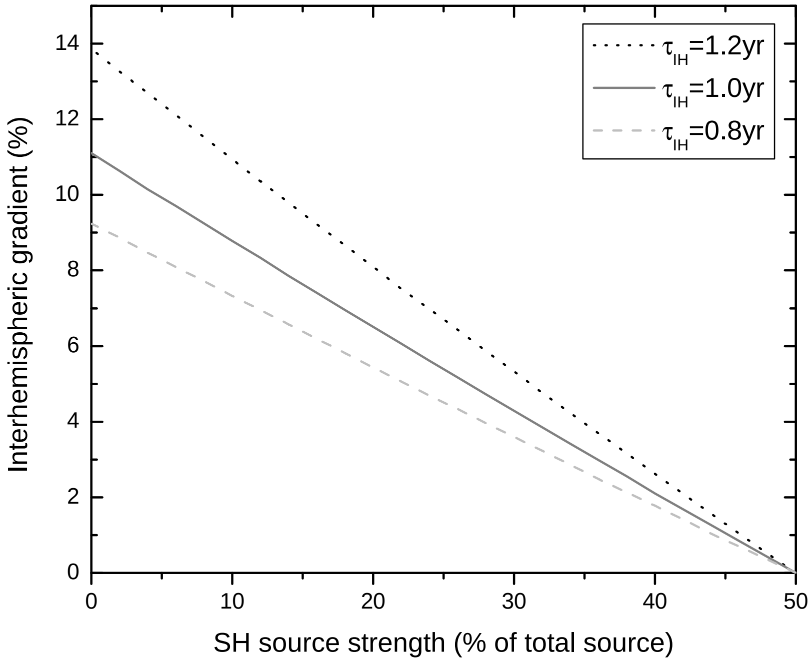

Figure 1.9: Interhemispheric gradient as a function of an unequal source distribution.

exceptions as shown in Figure 1.10. Inversion methods, however, strongly rely on the existence of these gradients. Thus, precision requirements are unprecedented for total column retrievals from space.

1.5.2 Precision requirements for space based retrievals

Sensitivity studies suggest that methane column abundances have to be measured with a precision of 1-2% in order to be useful for inversion schemes. Although Rayleigh scattering within the atmosphere can be neglected in the near infrared, aerosols and partial cloud cover alter the light path of the recorded photons such that a proxy for the light path is necessary in order to meet the stringent precision requirement. Furthermore, atmospheric pressure variations induce uncertainties in the total mass of the probed atmosphere. Total column measurements of an inert reference gas are thus ideal to serve as proxy for both light path and total mass[3].

The application of O_2 measurements as proxy turned out to be suitable to only a limited extent. The main problem arises when radiative transfer properties in the fitting windows (spectral windows in which the column amounts of the trace gases are fitted to the measurements) of the species of interest (such as CH_4) and the proxy (such as O_2) differ largely and thereby render the proxy inappropriate. Unfortunately, this is the case for O_2 retrievals (performed at 765 nm) if applied as proxy for CH_4 (retrieved at about 1650 nm or at about 2300 nm) measurements. However, as will be shown in chapter 4 (*Frankenberg et al.*, 2005c), CO_2 retrieved

---

[3] In principle, the total mass of the measured volume depends on both, pressure and variations in the light path

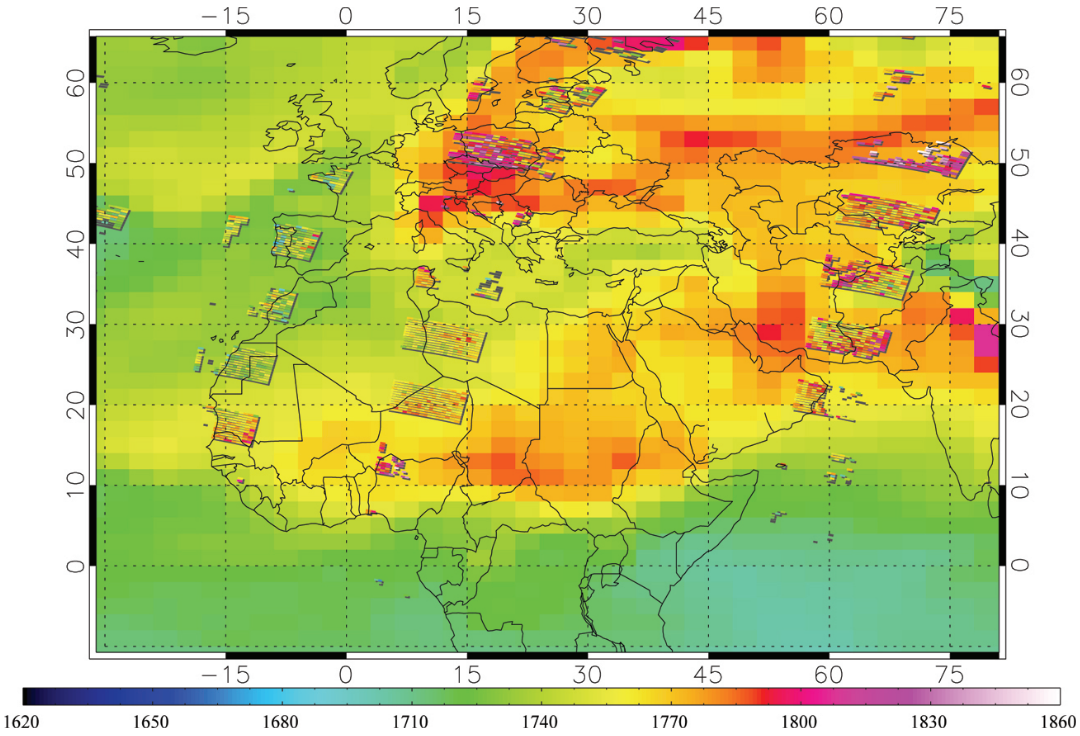

(a) 01.08.2003

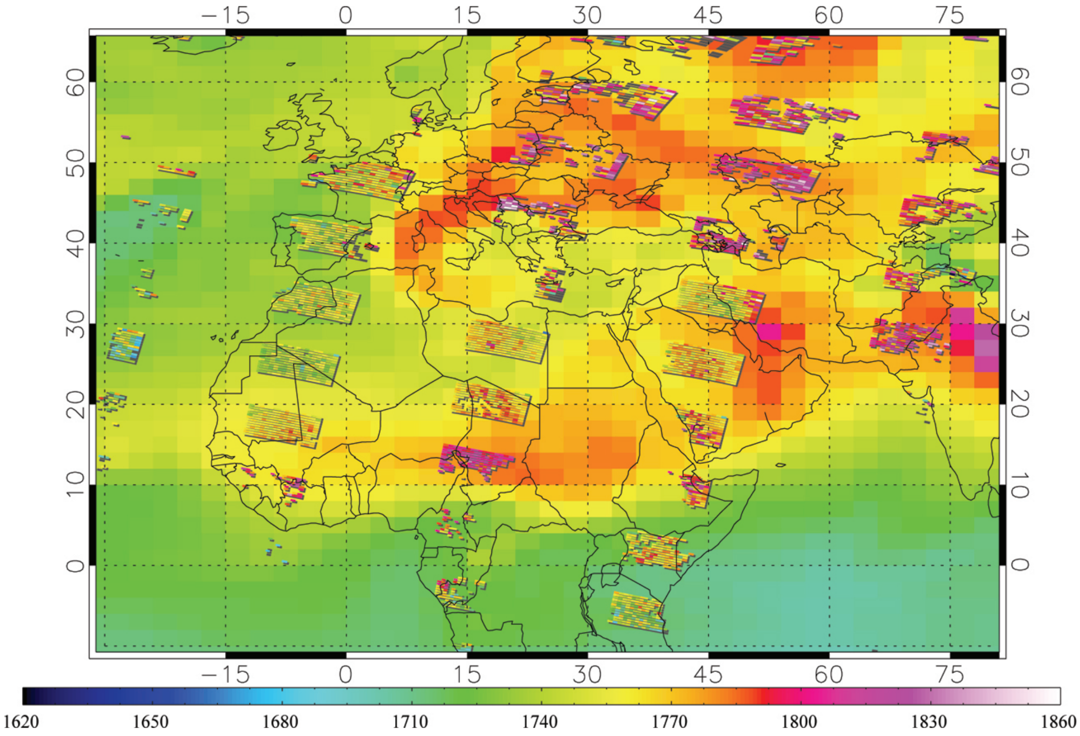

(b) 02.08.2003

Figure 1.10: Comparison of measurements and modeled abundances on a daily basis. The SCIAMACHY measurements are overlaid over the TM3 model values (SCIAMACHY ground pixels exhibit a slight shadow to be more easily visible).

at about 1570 nm can be used as proxy for the light path since its fitting window is in spectral proximity and its variations in the atmosphere are far smaller than those in methane. Since

CO_2 itself exhibits, on seasonal timescales, variations of the order of the precision requirement, modeled CO_2 column abundances are required in order to minimize any possible artificial bias (elaborated in chapter 5, (*Frankenberg et al.*, 2005d)).

1.6 Atmospheric carbon monoxide

As *Holloway et al.* (2000) puts it, the global distribution of carbon monoxide (CO) holds interest from several perspectives: as a primary and secondary determinant of air quality, as the leading sink of hydroxyl radicals, and as an atmospheric tracer with a relatively long lifetime, that is, an indicator of how transport redistributes pollutants on a global scale. High CO concentrations can directly affect human health. Indirectly, CO plays a role in the catalytic production and destruction of ozone. In case of high NO_x abundance, CO oxidation by OH radicals leads to ozone production (*Holloway et al.*, 2000, and references therein):

$$CO + OH \rightarrow H + CO_2 \tag{R1.7}$$

$$H + O_2 + M \rightarrow HO_2 + M \tag{R1.8}$$

$$HO_2 + NO \rightarrow NO_2 + OH \tag{R1.9}$$

$$NO_2 \xrightarrow{h\nu(\lambda<420\,nm)} NO + O \tag{R1.10}$$

$$O + O_2 + M \rightarrow O_3 + M \tag{R1.11}$$

$$CO + 2O_2 \rightarrow O_3 + CO_2 \tag{R1.12}$$

In clean air (low NO_x abundance), however, ozone and OH are destroyed:

$$2CO + 2OH \rightarrow 2H + 2CO_2 \tag{R1.13}$$

$$2H + 2O_2 + 2M \rightarrow 2HO_2 + 2M \tag{R1.14}$$

$$HO_2 + O_3 \rightarrow 2O_2 + OH \tag{R1.15}$$

$$2CO + O_3 + OH \rightarrow HO_2 + 2CO_2 \tag{R1.16}$$

Depending on the amount of available OH radicals, the lifetime of CO varies between 2 weeks and one year. Thus, its variation also depends strongly on the seasonal variations of OH abundances. As for the sources, table 1.2 shows the emission estimates given by *IPCC* (2001). While methane oxidation as one of the largest contributors is a relatively homogenously distributed source, biomass burning, for instance, can be considered as a point source. Hence, atmospheric CO exhibits a latitudinally dependent background mixing ratio overlaid with strong local variations due to point sources. Thus, it serves very well as an indicator of OH oxidation rate, atmospheric transport and biomass burning.

For a more detailed overview of the global CO budget and its implication see *IPCC* (2001); *Holloway et al.* (2000); *Bergamaschi et al.* (2000b,a) and references therein.

Table 1.2: IPCC (2001) carbon monoxide emission estimates

Category	Carbon monoxide source strength (Tg/year)
Sources	
Oxidation of CH_4	800
Oxidation of Isoprene	270
Oxidation of industrial NMHC	110
Oxidation of biomass NMHC	30
Oxidation of Acetone	20
Sub-total in situ oxidation	**1230**
Vegetation	150
Oceans	50
Biomass burning	700
Fossil & domestic fuel	650
Sub-total direct emissions	**1550**
Total sources	**2780**
Sinks	
Surface deposition	200-640
OH reaction	1500-2700

Publications

Iterative maximum a posteriori (IMAP)-DOAS for retrieval of strongly absorbing trace gases: Model studies for CH_4 and CO_2 retrieval from near infrared spectra of SCIAMACHY onboard ENVISAT

C. Frankenberg, U. Platt, and T. Wagner

Institute of Environmental Physics, Heidelberg, Germany

Journal: Atmospheric Chemistry and Physics, Atmos. Chem. Phys, Volume 5, pp. 9-22, 2005.
Status: Received: 2 August 2004
Published in Atmos. Chem. Phys. Discuss.: 29 September 2004
Revised: 17 December 2004
Accepted: 23 December 2004
Published: 12 January 2005
URL: `http://www.copernicus.org/EGU/acp/acp/5/9/acp-5-9.htm`

Chapter 2

Iterative maximum a posteriori (IMAP)-DOAS for retrieval of strongly absorbing trace gases: Model studies for CH_4 and CO_2 retrieval from near infrared spectra of SCIAMACHY onboard ENVISAT

C. Frankenberg, U. Platt, and T. Wagner

In the past, differential optical absorption spectroscopy (DOAS) has mostly been employed for atmospheric trace gas retrieval in the UV/Vis spectral region. New spectrometers such as SCIAMACHY onboard ENVISAT also provide near infrared channels and thus allow for the detection of greenhouse gases like CH_4, CO_2, or N_2O. However, modifications of the classical DOAS algorithm are necessary to account for the idiosyncrasies of this spectral region, i.e. the temperature and pressure dependence of the high resolution absorption lines. Furthermore, understanding the sensitivity of the measurement of these high resolution, strong absorption lines by means of a non-ideal device, i.e. having finite spectral resolution, is of special importance. This applies not only in the NIR, but can also prove to be an issue for the UV/Vis spectral region.

This paper presents a modified iterative maximum a posteriori -DOAS (IMAP-DOAS) algorithm based on optimal estimation theory introduced to the remote sensing community by *Rodgers* (1976). This method directly iterates the vertical column densities of the absorbers of interest until the modeled total optical density fits the measurement. Although the discussion in this paper lays emphasis on satellite retrieval, the basic principles of the algorithm also hold for arbitrary measurement geometries.

For a quantitative test of this new approach and a comparison with classical algorithms, it is applied to modeled spectra based on a comprehensive set of atmospheric temperature and pressure profiles. This analysis reveals that the sensitivity of measurement strongly depends on the prevailing pressure-height. The IMAP-DOAS algorithm properly accounts for the sensitivity of measurement on pressure due to pressure broadening of the absorption lines. Thus, biases in the retrieved vertical columns that would arise in classical algorithms, are obviated.

Here, we analyse and quantify these systematic biases as well as errors due to variations in the temperature and pressure profiles, which is indispensable for the understanding of measurement precision and accuracy in the near infrared as well as for future intercomparisons of retrieval algorithms.

2.1 Introduction

Absorption spectroscopy in the UV/Vis spectral region has been widely and successfully employed as a method for determining total column densities of several trace gases in the atmosphere (cf. *Platt*, 1994; *Wagner and Platt*, 1999). Satellite borne measurement devices such as GOME or SCIAMACHY use solar radiation reflected from the earth's surface and scattered within the earth's atmosphere as light source.

In addition to UV/Vis channels, SCIAMACHY onboard ENVISAT provides 3 near infrared channels covering wavelengths from 1–1.75 μm, 1.94–2.04 μm and 2.26–2.38 μm with moderate spectral resolution (*Bovensmann et al.*, 1999). Among the absorbers in these regions are the greenhouse gases CO_2, CH_4, N_2O and H_2O as well as CO. SCIAMACHY thereby paves the way for the first global measurements of tropospheric CO_2 and CH_4 from space. Since these greenhouse gases are longlived, their spatial and temporal variations are fairly low, posing the problem of measuring small deviations from a large background total column. Thus, high measurement precision is needed in order to gain information in addition to the existing sparse but precise ground based measurements (*Tans et al.*, 1996; *Rayner and O'Brien*, 2001; *Levin et al.*, 2002; *Olsen and Randerson*, 2004b). Furthermore, the retrieval has to be bias-free which will be one of the main issues addressed in this paper.

Some authors have already noticed the drawbacks of the classical DOAS algorithm under certain conditions. *Maurellis et al.* (2000) parameterised the DOAS algorithm for highly structured spectra, while *Solomon et al.* (1998) and *Volkamer et al.* (1998) analysed the interference between different absorbers. A more general approach was introduced by *Buchwitz et al.* (2000) in the form of a new weighting function based modified DOAS approach for retrieval in the near infrared. This work firstly implemented the use of linearisation points in the classical DOAS approach which is vitally important for the retrieval of strongly absorbing gases. Also *Schrijver* (1999) focussed on retrieval in the near infrared and first results from SCIAMACHY are available from both groups (*Buchwitz et al.*, 2004, 2005a; *Gloudemans et al.*, 2004). Especially for the precise retrieval of long-lived gases, some progress has been made on quantifying the influence of clouds and aerosols on the retrieval (*Buchwitz et al.*, 2000; *O'Brien and Rayner*, 2002; *Rayner et al.*, 2002).

The major focus of this work is the general treatment of strong absorbers, interferences between different absorbers and the characteristic features of the near infrared spectral region, viz. the shape of the spectral absorption lines and how they determine the sensitivity of the measurement in spite of often not being fully resolved by the spectrometer. This issue is hence analyzed in conjunction with instrumental lineshape issues, in particular with respect to measurement devices having moderate spectral resolution. This encompasses the influence of the actual atmospheric state on the retrieval and the effect of the nonlinearity of the forward model. Till date, only few climatological profiles have been used in other studies to analyze this effect. Our study makes use of a comprehensive set of atmospheric profiles to cover a realistic set of atmospheric states.

2.2 Basic Theory

The classical DOAS approach (*Platt*, 1994) uses the Lambert-Beer law to obtain a linear system of equations where the column density to be retrieved is directly proportional to the measured differential optical density:

$$I(\nu) = I_0(\nu) \exp\left(- \int \sigma(\nu, p, T) c(s) ds \right) \tag{2.1}$$

$$\vec{\tau} = \ln\left(\frac{I_0(\nu)}{I(\nu)} \right) \approx \sigma(\nu, \bar{p}, \bar{T}) \cdot \int c(s) ds = \sigma(\nu, \bar{p}, \bar{T}) \cdot S \, , \tag{2.2}$$

where S denotes the slant column density, which is defined as the path integral of the concentration of the respective absorber along the actual lightpath. The ratio of the slant column density S and the vertical column density (VCD or simply V, the integral of the concentration along the vertical from the surface to the top of atmosphere) is called airmass factor (A) and depends on many factors such as measurement geometry, albedo, wavelength and concentration profile. Neglecting scattering, the airmass factor can be approximated by simple geometric considerations of the slant light path. If aerosols and clouds are absent, this is a reasonable approximation in the near infrared and assumed in this study. However, airmass factors calculated by means of a radiative transfer model taking consideration of multiple scattering, refraction and spherical geometry can be directly used in the IMAP-DOAS algorithm.

Since absorption in the NIR is only due to rotational and vibrational transitions, the respective absorption lines are rather narrow and strongly temperature and pressure dependent. Thus, the integral in Eq. (2.1) cannot be simplified since $\sigma(\nu, p, T)$ is not constant along the light path ds. The total vertical optical densities of the respective absorbers therefore have to be calculated as the sum of the vertical optical densities of several height layers, each having nearly constant pressure and temperature.

Except for longpath-systems with reasonably well defined T and P, the simplification of Eq. (2.1) is generally only a rough approximation and almost all cross sections of species measured show a certain T-dependence. This also holds for the UV/Vis, where we have electronic transitions as well but where this dependence often plays only a minor role in the DOAS retrieval. However, we have to distinguish between a temperature effect which changes also the line intensity and is thus also important for weak absorbers, and pressure broadening which alters merely the lineshape and is thus only important if we are dealing with strong absorbers. As will be shown later, the importance of the actual lineshape will increase with the nonlinearity of the problem. Since most DOAS measurements in the UV/Vis deal only with weak absorbers which can be described by a linear problem, these issues have largely been neglected in the past.

2.2.1 Spectral line shape

In the case of Local Thermodynamic Equilibrium the absorption cross section of a single transition line $\sigma_i(\nu)$ can be written as the product of the line intensity S_i (not to be confused with the slant column density) and a frequency dependent part determining the line shape $\Phi_i(\nu)$ (*Thomas and Stamnes*, 1999):

$$\sigma_i(\nu) = S_i \Phi_i(\nu)\,. \tag{2.3}$$

The line shape is mainly determined by doppler (Gaussian shape) and pressure broadening (Lorentzian shape). If both processes are assumed to be independent of each other, the resulting Voigt profile is a convolution of a Gaussian and a Lorentzian line shape (*Goody and Yung*, 1989):

$$\Phi(a,b) = \frac{b}{\pi^{3/2}\gamma_D} \int_{-\infty}^{\infty} \frac{\exp(-t^2)}{(a-t)^2 + b^2} dt\,, \tag{2.4}$$

with b denoting the ratio of the Lorentzian and the Gaussian halfwidth γ_L/γ_D and a the distance from the line center in units of the Gaussian halfwidth ($a{=}(\nu{-}\nu_0)/\gamma_D$). The Lorentzian halfwidth, γ_L, is directly proportional to the pressure p while γ_D is independent of p. All parameters used in this study have been taken from the latest release of the HITRAN database (*Rothman et al.*, 2003). The Voigt function is computed in an efficient way as demonstrated by *Kuntz* (1997).

The total absorption cross section of a single molecule $\sigma_{tot}(\nu)$, or simply $\sigma(\nu)$, considering all transitions can then be described as the sum of the cross sections of all individual transitions:

$$\sigma(\nu) = \sum_i \sigma_i(\nu)\,. \tag{2.5}$$

Strictly speaking, Eq. (C.2) is only valid when each transition can be treated separately (i.e. as an isolated line). If lines of different transitions overlap, e.g. due to pressure broadening, the wave functions of different rotational energy levels are no longer independent and simple summation is no more valid, since Eqs. (2.3) and (C.5) were based on the assumption of independence of rotational levels (*Goody and Yung*, 1989). This effect, called line-mixing, can alter the line shape and thus also the sensitivity of the measurements (*Strow and Reuter*, 1988) as it has a narrowing effect on the linewidths. Apart from line-mixing, the behavior of the line wings of a single transition could differ from a classical Lorentz shape (*Goody and Yung*, 1989). This deviation from the classical Lorentz theory is more likely for vigorously interacting molecules such as H_2O with the known problems of continuum absorption (*Clough et al.*, 1989; *Ma and Tipping*, 1999). However, *Pine* (1997) found deviations from the Voigt profile as well as line mixing in the ν_3 band of CH_4 at about 3300 nm (3000 cm^{-1}). So far, these effects have been neglected for the model analysis of CO_2 and CH_4 presented in this paper.

2.2.2 Instrumental line shape

For grating spectrometers such as SCIAMACHY, a convolution of the high resolution structure of the incoming light with the instrumental slit function constitutes the actually recorded spectra. Dealing with narrow lines exhibiting relatively strong absorptions (optical densities

>0.1) and moderate spectral resolution of the spectrometer (in our case 0.2–1.5 nm) is a crucial aspect in the NIR spectral region: the actual shape of the absorption lines cannot be fully resolved by the spectrometer. In order to account for all spectral features, the transmission has to be calculated using a fine wavelength grid before convolution with the instrumental function. This convolution has to be performed in the intensity space. Hence, the direct convolution of the optical densities, τ, or cross sections, often used as a reasonable approximation for weak absorbers in the DOAS approach, is inappropriate in this case:

$$< \vec{I_0} \exp(-\vec{\tau}) > \neq < \vec{I_0} > \exp(< -\vec{\tau} >)\,, \tag{2.6}$$

where $\vec{I_0}$ is the Fraunhofer spectrum and $< \cdot >$ denotes the convolution with the (normalised) instrumental function $\phi_I(\lambda)$:

$$< I(\lambda) >= \int_{-\infty}^{\infty} I(\lambda') \cdot \phi_I(\lambda - \lambda') d\lambda' \tag{2.7}$$

2.2.3 Sensitivity of the measurement

Since convolution and logarithm are not associative and we are dealing with strong, non-resolved absorption lines, the sensitivity of the measurement with respect to a perturbation in τ decreases with increasing τ and Eq. (2.2) is not valid any more. Pressure broadening decreases the maximum values of τ and therefore increases the sensitivity. In other words, the line wings contribute most to the sensitivity of strong absorption lines. However, since the shape of the line wings is generally less well known and cannot be always treated as a Voigt shape (*Goody and Yung*, 1989), this uncertainty could introduce further errors.

In the case of a moderate spectral resolution, the measured optical density is thus no longer linearly dependent on the vertical column density of the respective absorbers. Ignoring scattering, the theoretically measured slant optical density of a single absorber can be written as

$$\vec{\tau}_\lambda^{meas}(x) = -\ln\left(< \exp(-x \cdot A \cdot \vec{\tau}_\lambda^{ref}) >\right)\,. \tag{2.8}$$

where
x = retrieved scaling factor for V (V/V^{ref})
$\vec{\tau}_\lambda^{ref}$ = total vertical optical density
A = Airmass factor (A=S/V).

Figure 2.1 shows an idealized case, where the transmission through a medium with constant pressure and temperature and with a column density of $7{\cdot}10^{19}$ molec/cm^2 CH_4 is computed at two different pressures. In panels (b1) and (b2) the high resolution transmission as well as their convolution with the instrumental slit function is shown. The width of the slit function is far larger than the actual width of the absorption lines. One can see that the resulting apparent optical densities, which would theoretically be measured by an instrument with the given slit function, in Fig. 2.1c differ for both pressures although the column density is the same. The medium with higher ambient pressure clearly exhibits a stronger apparent optical density due to the broader absorption lines as shown in the cross sections in panels (a1) and (a2).

Assuming an inhomogeneous path, the total vertical optical density $\vec{\tau}_\lambda^{ref}$ of the respective species is computed numerically from the integral $\vec{\tau}_\lambda^{ref} = \int_0^{z_T} \sigma_\lambda\left(p(z), T(z)\right) c(z) dz$ where $c(z)$

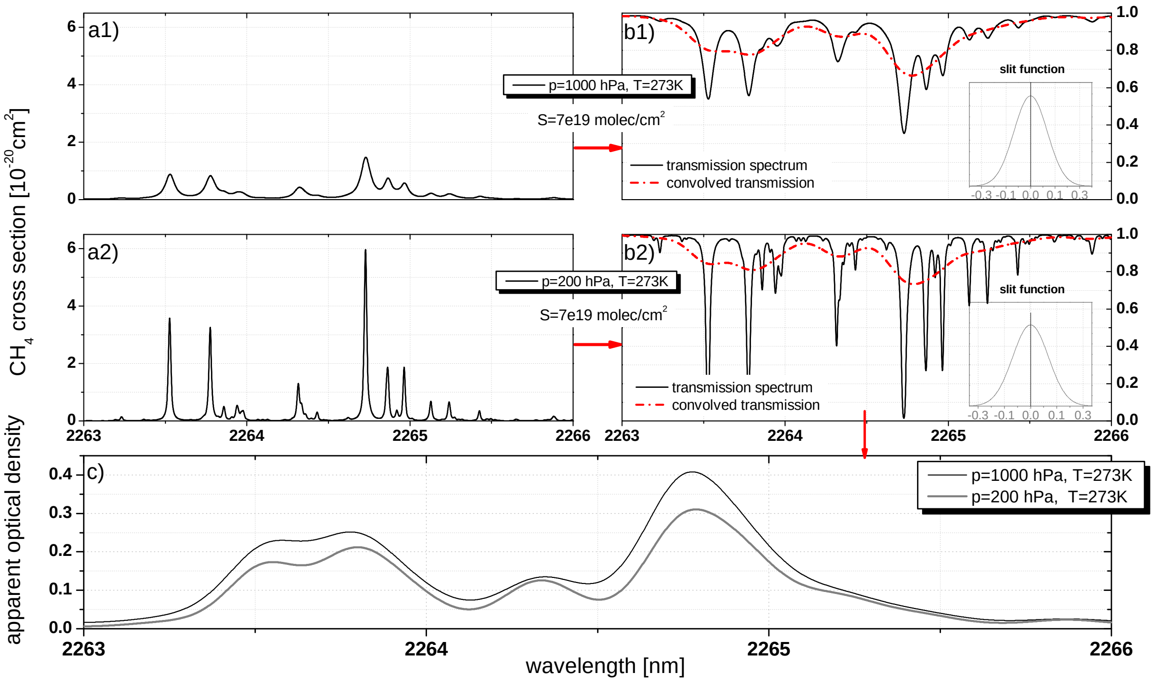

Figure 2.1: Panel **(a1)** and **(a2)** show the cross sections of methane for two different ambient pressures. From these cross sections, the theoretical transmissions through a column of $7{\cdot}10^{19}$ molec cm^{-2} CH$_4$ are depicted in panels **(b1)** and **(b2)**. Also shown are the convolutions of the high resolution transmission with the instrumental slit function (FWHM=0.24 nm). Panel **(c)** then shows the negative logarithm of the convolved transmissions.

is the volume number concentration of the respective species and z_T the top of atmosphere. In our algorithm, typically 40–60 height layers are chosen in order to account for the changes in temperature and pressure.

Figure A.2 shows the theoretically measured (apparent) optical density due to CH$_4$ absorptions at a given wavelength where the (unconvolved) vertical optical density of methane is rather high (about 1.7 for a reference vertical column density of $3.6{\cdot}10^{19}$ molec cm^{-2}). One can clearly see that the measured optical density is not linearly dependent on the slant column density of CH$_4$. Furthermore, the nonlinearity decreases with decreasing FWHM of the slit function but is still present even for a FWHM of 0.1 nm. The degree of nonlinearity also depends on the actual slant optical density itself. Thus, a classical DOAS approach which assumes strict linearity is not well applicable in the near infrared spectral region in particular and for strong absorbers in general.

2.2.4 Linearisation points and derivatives

Buchwitz et al. (2000) introduced the concept of weighting functions to the classical DOAS approach. The basic idea is to linearise the problem about a linearisation point in S, the expected slant column density derived using climatological profiles of meteorological parameters such as pressure, temperature and vertical profiles of all absorbers. This has been an important step in adjusting the DOAS algorithm to meet the needs of the near infrared spectral region. However, this approach does not treat different height layers separately, which can result in systematic biases as will be shown in the following. If the actual atmospheric state deviates

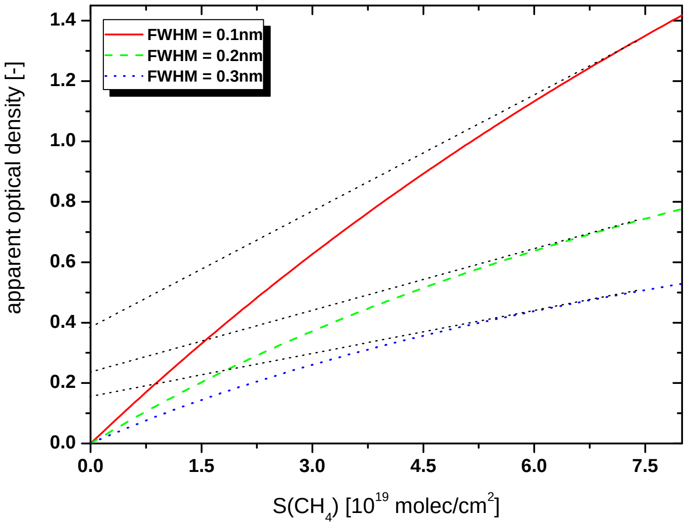

Figure 2.2: Curve of growth for $\mathsf{CH_4}$. Depicted is the apparent slant optical density at one single detector pixel (at about 2328 nm) due to $\mathsf{CH_4}$ absorptions modeled with a gaussian slit function with different Full Width at Half Maximum. For the sake of simplicity, the air mass factor was chosen to be 2 (i.e. S=2·V). The weighting functions at S=7.5 molec cm^{-2} are indicated by the black, dotted lines (strictly speaking by the slope of these lines).

strongly from the first a priori assumption (e.g. due to the highly variable amount of water vapour or clouds shielding significant parts of the atmosphere), further iterations are necessary in order to yield unbiased results. This can be seen in Fig. A.2, where the actual slope of each curve depends on the slant column density S of $\mathsf{CH_4}$, indicating that the sensitivity of the measurement decreases with an increase in the slant column density. Thus, the linearisation point has to be close to the actual state which is only possible by means of iterations. A generalised and comprehensive approach to nonlinear and linear inverse problems for atmospheric remote sounding is given by *Rodgers* (2000).

Given a linearisation point, the derivatives of the measured optical density with respect to perturbations of the respective trace gas columns in different height layers, to temperature changes and other affecting factors can be calculated.

The general concept is a linearisation of the forward model $\mathbf{F}(\mathbf{x})$ at $\mathbf{x_0}$ (nomenclature according to

The derivatives $\mathbf{K}_0 = \left.\frac{\partial \vec{F}(\vec{x})}{\partial \vec{x}}\right|_{\vec{x}_0}$ can be represented as a Jacobian Matrix where each column is the derivative vector of the measurement with respect to an element of the state vector. The forward model also has to include the instrumental function which is of special interest in the NIR spectral region.

Thus, we can combine the Beer-Lambert law consisting of a low order polynomial accounting for broadband absorption structures and the instrumental function to obtain the resulting simplified forward model, i.e.

$$\frac{\vec{I}^{lr}}{\vec{I}_0^{lr}} = <\vec{T}^{hr}>, \tag{2.9}$$

or with $\vec{I}_0$ correction (cf. *Aliwell et al.* (2002) and Sect. 2.4.2):

$$\frac{\vec{I}^{lr}}{\vec{I}_0^{lr}} = \frac{<\vec{I}_0^{hr}\cdot\vec{T}^{hr}>}{<\vec{I}_0^{hr}>}, \tag{2.10}$$

where the indices lr and hr denote low resolution (instrument resolution) and high resolution (resolution high enough to account for all spectral features; for this study we used 0.001 nm). $\vec{I}_0^{hr}$ is a high resolution Fraunhofer spectrum (in our case taken from *Livingston and Wallace*, 1991) and $\vec{T}^{hr}$ the high resolution modeled transmission:

$$\vec{T}^{hr} = \exp\left(-\sum_j A\cdot\frac{\vec{\tau}_j^{ref}}{V_j^{ref}}V_j - \sum_k a_k\cdot\lambda^k\right). \tag{2.11}$$

We can now regard the ratio of the vertical column to be retrieved and the reference vertical column as x^j:

$$x^j = \frac{V_j}{V_j^{ref}}. \tag{2.12}$$

Neglecting the $\vec{I}_0$-effect (cf. Sec. 2.4.2), the derivatives of $\vec{F}(\vec{x})$ at $\vec{x}_0$ with respect to x^j can be easily deduced:

$$\begin{aligned}\left.\frac{\partial\vec{F}(\vec{x})}{\partial x^j}\right|_{\vec{x}_0} &= \left.\frac{\partial\ln\left(<\vec{T}^{hr}(\vec{x})>\right)}{\partial x^j}\right|_{\vec{x}_0}\\ &= \frac{1}{<\vec{T}^{hr}(\vec{x}_0)>}\left.\frac{\partial<\vec{T}^{hr}(\vec{x})>}{\partial x^j}\right|_{\vec{x}_0}\\ &= \frac{1}{<\vec{T}^{hr}(\vec{x}_0)>}<-\vec{T}^{hr}(\vec{x}_0)\cdot A\cdot\vec{\tau}_i^{ref}>.\end{aligned} \tag{2.13}$$

For the computation of the linearisation point, we include an $\vec{I}_0$ correction:

$$\vec{F}(\vec{x}_0) = \ln\left(\frac{\vec{I}^{lr}}{\vec{I}_0^{lr}}\right) = \ln\left(\frac{<\vec{I}_0^{hr}\cdot\vec{T}^{hr}(\vec{x}_0)>}{<\vec{I}_0^{hr}>}\right). \tag{2.14}$$

Figures 2.3a and b show the vertical optical densities $\vec{\tau}^{ref}$ of CH_4 and H_2O at about 2.3 μm. The derivatives with respect to change in CH_4 column densities in different height layers as well as the derivative with respect to the total vertical column of CH_4 at different VCD's of H_2O are depicted in Figs. 2.3d and e. It can clearly be seen that the derivatives with respect to CH_4 column density depend on the height at which the actual perturbation takes place. This dependence on height can be readily explained as a result of different mean ambient temperatures and different line-shapes at the respective pressure levels.

Thus, the sensitivity to a perturbation taking place in lower parts of the atmosphere is almost always higher since the pressure broadened line wings contribute most to the sensitivity. The opposite holds for upper parts of the atmosphere where rather narrow lines exhibit less sensitivity. However, this effect strongly depends on the actual optical density and the slit function of

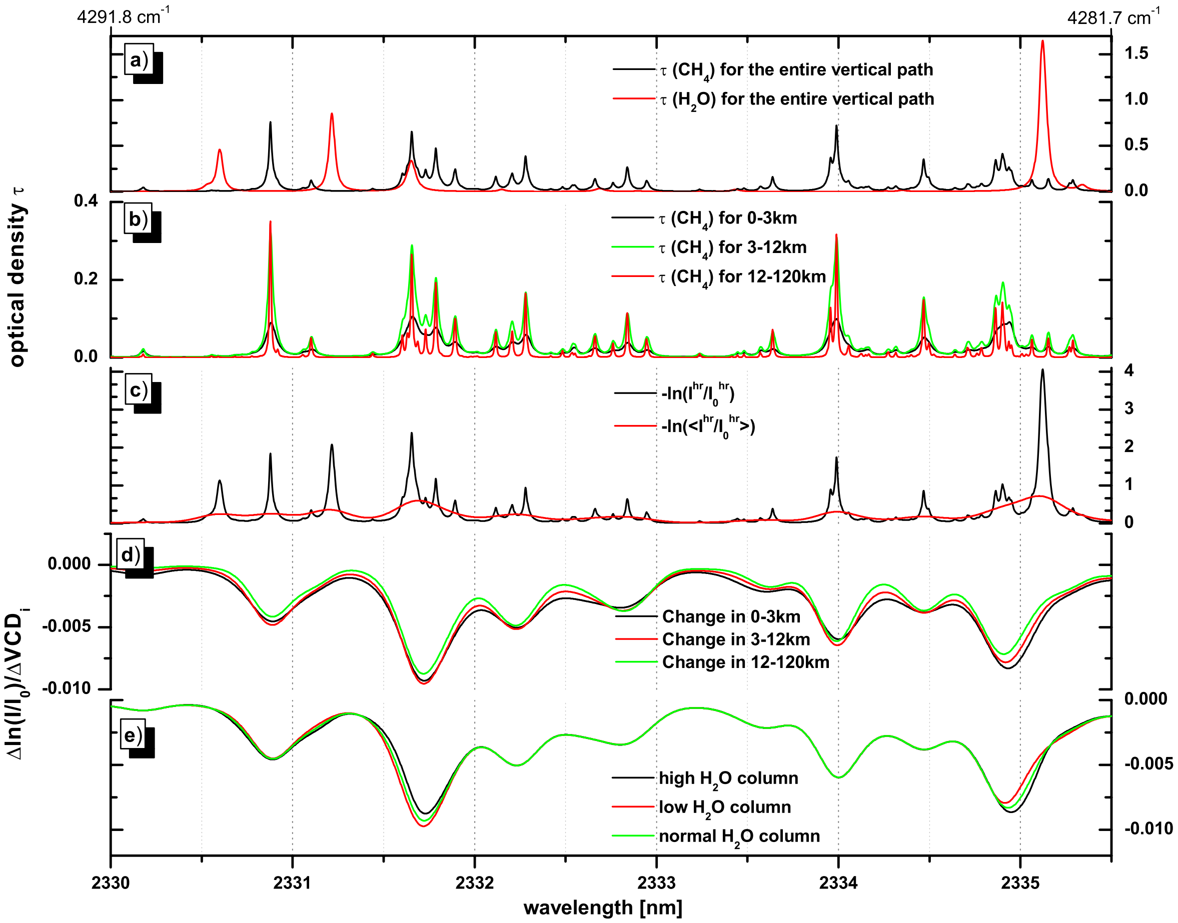

Figure 2.3: Panel **(a)** shows the spectrally fully resolved total optical densities for a vertical path for CH_4 (V=3.6·10^{19} molec cm^{-2}) and H_2O (V=6.5·10^{22} molec cm^{-2}) while panel **(b)** depicts the vertical optical densities of CH_4 for different height layers in the atmosphere. The expected total slant optical density (here for A=2.41) is now shown in panel **(c)**. Shown is the high resolution optical density and the convolved one that is seen by the instrument, i.e. convolved with ϕ_I (here: SCIAMACHY slit function in channel 8: Gaussian, FWHM=0.24 nm). Starting from this linearisation point, the effect of a change in the vertical column density of CH_4 of +10^{18} molec cm^2 (i.e. ≈3% of the total column) in different height layers is shown in panel **(d)**. Panel **(e)** shows the derivatives (also with respect to CH_4 perturbations) for different linearisation points, viz. for different water vapour columns (1.3, 6.5 and 32.5·10^{22} molec cm^{-2}, respectively). The optical densities in (a) and (b) are not convolved.

the instrument. The high sensitivity close to the surface can be seen as an advantage, since the boundary layer is of special importance for atmospheric chemistry and atmosphere-geosphere exchange processes.

Interestingly, Fig. 2.3e shows that the derivatives also depend on the amount of water vapour present. In the case of direct overlapping of the absorption lines, this is obvious because it increases the degree of saturation, and thereby reducing the sensitivity (e.g. at about 2331.75 nm). However, even distinct absorption lines can influence each other if they are close enough to lie within the width of the instrumental function. This can be seen, for instance, at about 2335 nm where enhanced water vapour increases the sensitivity with respect to $\mathsf{CH_4}$ perturbations. In principle, this effect is similar to the well known I_0 effect (*Aliwell et al.*, 2002) differing in that the interfering strong absorption lines are not constant as in case of Fraunhofer lines. This implies that different absorbers cannot be treated separately any more as in the classical DOAS approach.

All these effects are due to the following inequality with respect to convolution:

$$< \vec{I_0} \cdot e^{-\vec{\tau}_a} \cdot e^{-\vec{\tau}_b} > \neq < \vec{I_0} > \cdot < e^{-\vec{\tau}_a} > \cdot < e^{-\vec{\tau}_b} > \tag{2.15}$$

Implementation of Optimal Estimation

We have seen that we are dealing with a nonlinear problem, i.e. the derivatives of the forward model with respect to the column densities of strong absorbers depend on the actual state. Thus, we need an iterative scheme for retrieving the state vector. Further constraints are also necessary since we are dealing with moderate spectral resolution and thus the derivatives at different height layers for the same species are nearly linearly dependent. Thus, the information content of the measurement is not high enough to discriminate between different height layers. In our case, the linear system of equations would be badly conditioned and necessary constraints have to be introduced by the covariance matrix $\mathbf{S}_a$, i.e. by the expected covariances of the a priori state vector before any measurement has been made. Assuming the elements of the state vector to have gaussian distributions, the state vector maximising the a posteriori probability density function of a nonlinear problem can then be written by means of Newtonian iteration (*Rodgers*, 2000)

$$\vec{x}_{i+1} = \vec{x}_a + \left(\mathbf{K}_i^T \mathbf{S}_\epsilon^{-1} \mathbf{K}_i + \mathbf{S}_a^{-1}\right)^{-1} \mathbf{K}_i^T \mathbf{S}_\epsilon^{-1} \cdot \left[\vec{y} - \vec{F}(\vec{x}_i) + \mathbf{K}_i(\vec{x}_i - \vec{x}_a)\right] , \tag{2.16}$$

where

$\vec{x}_a$ = a priori state vector,
$\vec{x}_i$ = state vector at the i-th iteration,
$\mathbf{S}_\epsilon$ = (pixel) error covariance matrix,
$\mathbf{S}_a$ = a priori covariance matrix,
$\vec{F}(\vec{x}_i)$ = forward model evaluated at $\mathbf{x}_i$,
$\mathbf{K}_i$ = Jacobian of the forward model at $\vec{x}_i$.

Optimal estimation according to (2.16) is applied with a state vector that is comprised of the scaling factors for the vertical columns of the respective trace gases in different height layers, a climatological index for temperature change in the atmosphere (see next Section), polynomial coefficients accounting for low frequency absorptions and scattering. In the following, this implementation of optimal estimation is referred to as IMAP-DOAS (iterative maximum a posteriori DOAS). Shift and squeeze, a procedure often used in DOAS to account for any slight spectral mismatch between the expected and the actual wavelengths attributed to each detector pixel, can also be easily implemented in this scheme. The Jacobian matrix $\mathbf{K}_i$ is evaluated in each iteration i by computing T^{hr} with $\mathbf{x}_{i-1}$ as input values. At every iteration, several convolutions are involved. Since the numerical computation of a convolution is rather time consuming, neat and fast methods are indispensable. Fast Fourier Transform can in general be used to perform a fast convolution with all kinds of slit functions (*Press et al.*, 2002). Multi-grid binomial filters further decrease the computation time for slit functions having Gaussian shape (cf. *Jähne* (2002) and references therein).

Allowing only for small variances in $\mathbf{S}_a$ for the scaling factors of the VCD's of higher atmospheric layers, the fit can be constrained to changes in the lower atmosphere where the variance is expected to be high. In case of long lived trace gases like $\mathsf{CO_2}$, this is a reasonable assumption since the stratospheric variations are negligible. $\mathbf{S}_\epsilon$ is usually a diagonal matrix whose elements represents the expected errors (variances, e.g. due to shot-noise or uncertainties in the dark current) of $\mathbf{y}$. Each diagonal element of $\mathbf{S}_\epsilon$ shows a different value, since the variance (in the intensity space) of a particular detector pixel depends on the intensity itself (for shot-noise) transformed via the logarithm (*Jähne*, 2002). Especially in the near infrared the uncertainties of the dark current can also vary from pixel to pixel which can be accounted for in a proper choice of $\mathbf{S}_\epsilon$.

Temperature derivatives

Since the temperature determines the population of the lower state of each transition, the optical densities also depend on temperature, which therefore has to be taken into account. The temperature derivative can be chosen as the derivative of $\vec{F}(\vec{x})$ with respect to temperature. Theoretically, we would have to consider these derivatives for each height layer separately but this would lead to an under-determined linear system of equations. *Buchwitz et al.* (2000) computed this derivative by assuming a constant temperature change at all height layers. For our study, we choose the temperature difference at each height layer to correspond to a typical difference between two distinct climatologies. This means that we compute the difference quotient $\Delta\vec{F}(\vec{x})/\Delta(T,p)$, where $\Delta(T,p)$ is chosen to correspond to the differences between both climatologies. This method is used throughout this study. $\Delta(T,p)$ can be regarded as the deviation of the pressure and temperature profile from the a priori climatology toward another climatological standard profile, e.g. a deviation from the US standard atmosphere toward a standard mid-latitude winter climatology.

Using this method allows not only for different temperature changes in each height layer, but also changes in the scale height of the atmosphere. $\Delta(T,p)$ can be scaled by a scalar entity C_I (here climatological index). The climatological indices are then part of the state vector and the derivatives are computed for each strong absorber separately, water vapour almost always exhibiting the strongest sensitivity to temperature change. Since water vapour content is highly variable, the temperature (or climatological) derivative should not be directly coupled to, e.g., the temperature derivative of $\mathsf{CH_4}$ or $\mathsf{CO_2}$. However, a covariance of these elements can be assumed and represented in $\mathbf{S}_a$.

The derivative with respect to a climatological index can be computed as the difference of the vertical optical densities of each absorber for different climatologies (the VCD has, of course, to be scaled to a common value), e.g.

$$\Delta\vec{\tau}_i = \vec{\tau}_i^{clima_1} - \vec{\tau}_i^{clima2} \tag{2.17}$$

Here, we have chosen the difference between the US standard atmosphere (a priori climatology) and a mid-latitude winter atmosphere (profiles taken from *Kneizys et al.*, 1996). If scattering is ignored, the derivative can be written analytically as

$$\frac{\partial\vec{F}(\vec{x})}{\partial C_I} = \frac{1}{<\vec{T}^{hr}>}\frac{\partial<\vec{T}^{hr}>}{\partial C_I}$$

$$= \frac{1}{< \vec{T}^{hr} >} < -\vec{T}^{hr} \cdot A \cdot \Delta \vec{\tau}_i > \ .$$

Even though this method presumes linear sensitivity with respect to perturbations in the actual pressure/temperature profile, it turned out to yield reasonably precise results.

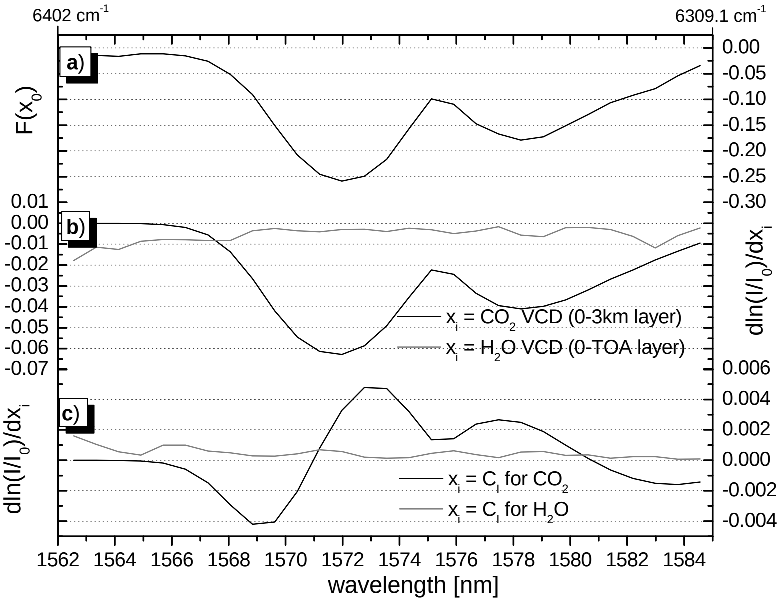

Figure 2.4: Example of $\mathbf{F}(\mathbf{x_0})$ and temperature derivatives (SZA=60°, $V(\mathsf{CO_2})$=7.75·10^{21} molec cm^{-2}, $V(\mathsf{H_2O})$=6.5·10^{22} molec cm^{-2}) for a typical SCIAMACHY CO_2 retrieval with poor spectral resolution (FWHM=1.33 nm).

If computational time were not an issue, vertical optical densities could be computed for each scan using more realistic temperature and pressure profiles, for instance from actual meteorological forecasts or infrared sounders. However, computation of the optical densities is still considerably time consuming, due to which such an approach would not be feasible for the analysis of millions of spectra. Fig. 2.4, for example, shows $\mathbf{F}(\mathbf{x_0})$ (i.e. the expected $\ln(< \vec{I}/\vec{I}_0 >)$) in panel (a) and the derivatives of $\mathbf{F}(\mathbf{x_0})$ with respect to perturbation in the CO_2 and H_2O columns in panel (b). Panel (c) depicts the derivative with respect to a change in climatology, separately for CO_2 and H_2O. One can clearly see that this derivative for CO_2 leads to reduced as well as enhanced optical densities in different spectral regions. This facilitates the discrimination of a change in total column from a temperature change.

2.3 Simulated retrieval

2.3.1 Standard profiles

In order to analyze the effect of atmospheric pressure and temperature variability on the retrieval, a comprehensive set of 2000 (for the CH_4 retrieval) and 5000 (for CO_2) ECMWF vertical profiles of temperature (see Fig. 2.5), pressure and water vapour (*Chevallier*, 2001)

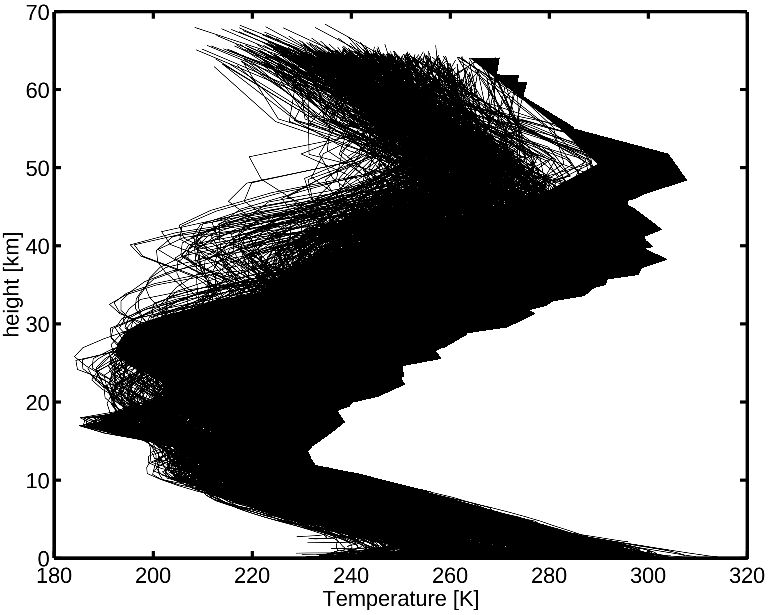

Figure 2.5: Range of ECMWF temperature profiles used for the simulation of the retrieval.

was used to compute optical densities of the absorbers of interest. For CO_2 and CH_4 the profiles were taken from *Kneizys et al.* (1996) and scaled to actual mixing ratios (tropospheric mixing ratios of 370 ppm for CO_2 and 1.7 ppm for CH_4, corresponding to vertical column densities of $7.75 \cdot 10^{21}$ and $3.6 \cdot 10^{19}$, respectively).

Starting from these optical densities, theoretical measurements of $\ln(\vec{I}/\vec{I}_0)$ with the spectral resolution of SCIAMACHY were simulated (scattering as well as instrumental noise were neglected and a solar zenith angle of 45° was chosen). These simulated measurements then were used as input parameters for different versions of the retrieval algorithm. Since the set of profiles also includes surface elevation and was chosen especially to cover a wide range of possible atmospheric states, a comprehensive and realistic simulation could be performed.

The following retrieval schemes were used for the simulation:

a1. For all species of interest, the vertical column density of the entire atmosphere was used in the state vector. Thus, the whole column was scaled with a single factor without accounting for where the change actually takes place. No temperature derivative was included in the state vector. Thus, the state vector only included the total vertical columns of each absorber.

a2. Same as a1) but a climatological index *CI* accounting for changes in temperature was introduced (U.S. standard atmosphere – mid-latitude winter, cf. Sect. 2.2.4) as an additional entry in the state vector.

b. A full IMAP fit was used: the state vector comprises a climatological index as well as *VCD*'s of strong absorbers divided into different height layers (0–3 km, 3–12 km, 12–120 km). The fit was confined to the lowermost layer (0–3 km) by setting the variance of higher layers close to zero.

Table 4.1 shows the fit windows for CO_2 and CH_4 chosen to represent very different instrumental

Table 2.1: Fit windows used for the ECMWF simulated retrieval

	FWHM [nm]	spectral range [nm]	SZA [°]
CH_4	0.24	2261–2277	45
CO_2	1.3	1562–1585	45

resolutions (given as Full Width at Half Maximum FWHM of the slit function).

For all retrievals, the a priori temperature and pressure profile was the US-standard atmosphere and no surface elevation was included, i.e. the surface pressure was 1013 hPa.

Retrieval results

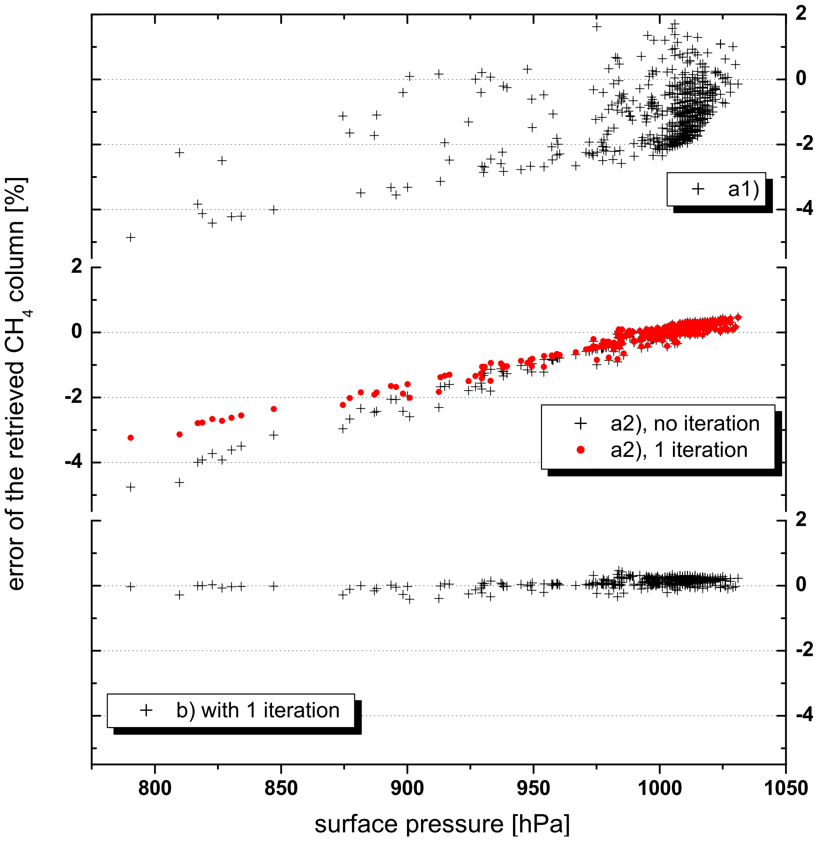

Figure 2.6: Error of the retrieved CH_4 vertical column for different ECMWF profiles and retrieval methods (see text for the explanation of **(a1)**, **(a2)** and **(b)**) in a latitude band of −60° to 45°. Only method (b) avoids huge errors due the atmospheric variability of temperature and pressure (dominant in (a1)) and the systematic bias dominant in (a2)).

Figure 2.6 shows the theoretical errors of a methane fit in a typical SCIAMACHY fit window (see Table 4.1) plotted against the actual surface pressure. The error is given as the percentage deviation from the true vertical column density $\Delta V_{rel}=\frac{V_{meas}-V_{true}}{V_{true}}\cdot 100\%$. The upper panel shows a retrieval which does not include a temperature derivative in the fit. It can be clearly seen that the errors are far larger than desired for long-lived trace gases although only

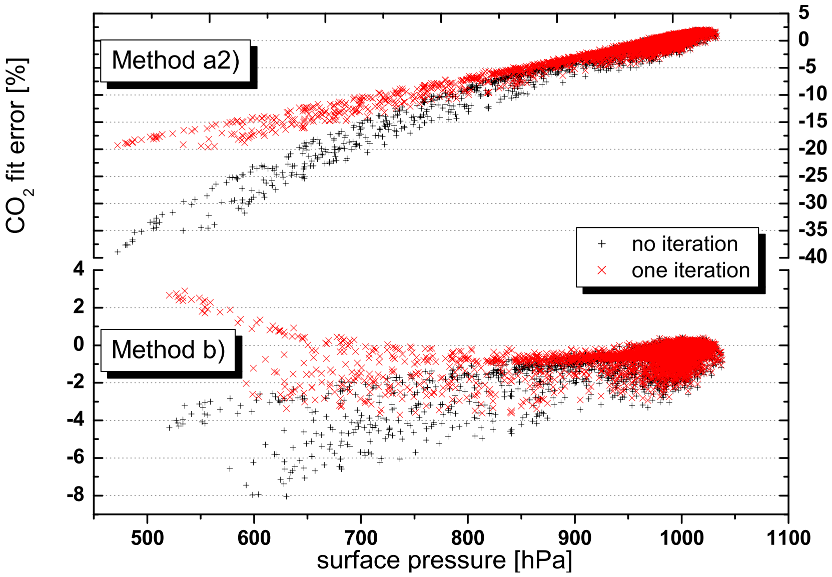

Figure 2.7: Error of the retrieved CO_2 vertical column for different ECMWF profiles. Please note the different scale for both panels. A second iteration would yield nearly identical results as using only one iteration for both algorithms.

ECMWF profiles within a latitude band between −60° to 45° were considered. The errors for latitudes above 45° were slightly larger. Thus, a derivative of the forward model with respect to temperature is indispensable if high precision is desired. Having analysed a small sample of climatological profiles, *Buchwitz et al.* (2000) also came to the conclusion that this derivative has to be included in most cases.

The fit window should be chosen such that the absorption lines exhibit a wide variety of lower state energies and thus different responses to temperature changes. In this case, a change in temperature can be well distinguished from an actual change in concentration. Another solution would be to choose only absorption lines with a negligible temperature dependence.

Water vapour, in general, poses a more severe problem due to the predominantly higher values of the lower state energies, which implies a stronger temperature dependence of the absorption line. Furthermore, the actual water vapour profile can vary considerably and thus vary in concentration in layers of different sensitivities inducing systematic errors. This could be of great significance in, e.g., a precise water vapour retrieval with moderate spectral resolution where no height information can be extracted from the spectra.

Also, it can be seen that scaling the entire column (method a2) creates an artificial bias in the retrieved column and would lead to averaging kernels above unity in the lower parts of the atmosphere. As mentioned before, this problem can be alleviated by including surface elevation in the a priori (i.e. when the a priori optical density is not computed from z=0 to the top of atmosphere but from z=surface elevation to the top of atmosphere). On the other hand, the nonlinearity is also not negligible on scales of actual meteorological surface pressure changes (±≈30 hPa). Confining the fit to the lower atmosphere circumvents these problems, since it properly accounts for the higher sensitivity to the boundary layer. In order to account for, for instance, seasonal changes in CO_2 column which occur throughout the troposphere, the fit could be extended to encompass the entire troposphere (e.g. by using a height layer of 0–10 km instead of only 0–3 km or by setting higher variances in $\mathbf{S_a}$ for height layers above

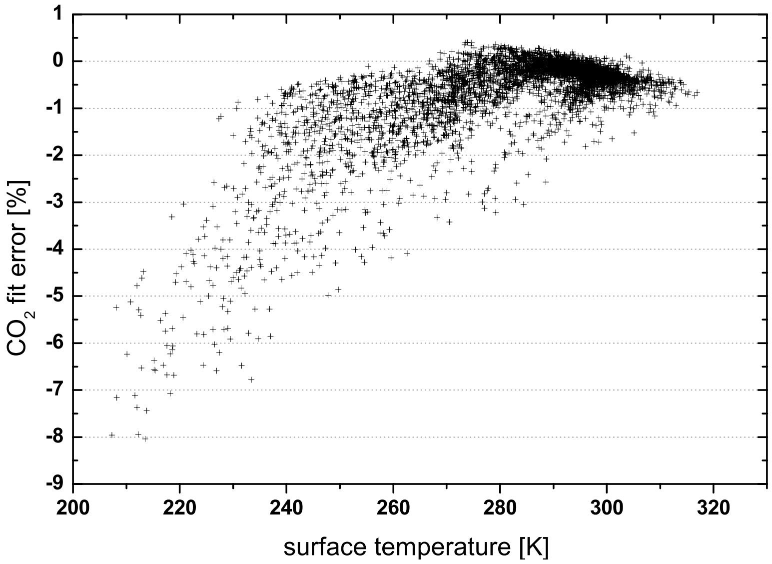

Figure 2.8: Error of the retrieved CO_2 vertical column for different ECMWF profiles with respect to surface temperature. Profiles with a surface elevation of more than 200 m have been excluded.

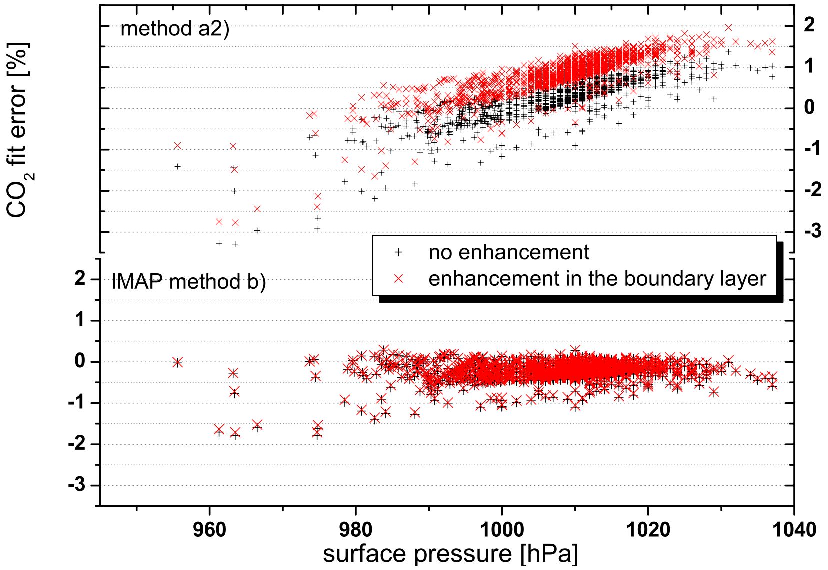

Figure 2.9: Error of the retrieved CO_2 vertical column for different ECMWF profiles with and without enhancement of 50 ppm CO_2 in the lowermost kilometer. Profiles with a surface elevation higher than 200 m and a surface temperature lower than 270 K have been discarded.

3 km and below 10 km).

As already pointed out, the impact of nonlinearity becomes substantial when either the actual state deviates strongly from the a priori state (e.g. when clouds shield most parts of the lower atmosphere or mountains are present) or the state vector is not properly chosen (e.g. scaling the whole column instead of only the lower atmosphere). Figure 2.7 underlines this effect in several ways: Without iteration, an additional bias is introduced at low surface pressures. This effect could be only partly obviated by a more accurate a priori estimation of the surface pressure (e.g. an elevation database). Moreover, scaling the entire column creates an artificial bias of up to 20% because the actual change in concentration takes place in the lower atmosphere whereas the fit algorithm scales the whole column. The slope of this bias depends on the degree of saturation, and thereby also on the slit function and the air mass factor.

To summarise, it can be said that Fig. 2.7 shows two different types of biases, one induced by different sensitivities in different height layers (the slope of the upper panel using one iteration, avoided by the IMAP-DOAS algorithm in the lower panel), and the other induced by the general nonlinearity of the problem (see curve of growth in Fig. A.2), which explains the differences of both methods using no and one iteration. Furthermore, it reveals a source of error, namely the uncertainty in pressure and temperature profiles leading to a scatter of up to 1–2% of the retrieved column.

The IMAP algorithm in the lower panel (using one iteration) starts to overestimate the total column when the surface pressure drops below values corresponding to a height of 3 km since the height layer between 0–3 km has been used as entry in the state vector (which does not exist any more since this layer has been clipped by mountains). This is prevented by supplying a priori information about the surface elevation, e.g. by setting the lower level of the lowest height layer to the actual surface elevation.

Figure 2.8 shows that the errors caused by the IMAP fit increase with decreasing surface temperature. This is mainly because the a priori has been based on the US-standard atmosphere. In most cases, this is a fair approximation, in extremely cold atmospheres, though, a more appropriate a priori profile needs to be adopted in order to yield more precise results.

2.3.2 Simulating enhanced CO_2 in the boundary layer

The short term variability of long-lived trace gases is expected to be highest in the boundary layer, close to the surface where the sources and sinks (*Olsen and Randerson*, 2004b) are located. If the algorithm does not properly account for this additional information, the retrieved column will be biased.

To quantify this effect, artificial measurements (see Sect. 2.3.1) with an enhancement of 50 ppm CO_2 in a boundary layer of 1 km vertical extent have been simulated and retrieved by different algorithms. The results of two methods, viz. a2 and b, are depicted in Fig. 2.9. Using method a2, the bias produced receives an additional offset of about 0.6% while the IMAP-DOAS algorithm remains unaffected by this change in concentration profile (lower panel).

2.4 Other parameters influencing the retrieval

2.4.1 Radiative transfer

Effect of atmospheric scattering

In the near infrared spectral region, Rayleigh scattering is nearly negligible and plays only a minor role. However, aerosols and clouds can significantly alter the distribution of the light paths. Thick clouds alter the light path dramatically and often render measurements useless. However, they are far easier to detect than aerosols or thin cirrus clouds, serving to generate a mask according to which measurements can be discarded. As *O'Brien and Rayner*

(2002) pointed out, also thin cirrus can significantly shorten the light path, thus also biasing the retrieved column by up to a few percent. Depending on their optical properties, surface reflectance and other parameters, aerosols can shorten as well as enhance the light path by up to a few percent (see e.g. *O'Brien and Rayner* (2002), *Dufour and Breon* (2003) or *Buchwitz and Burrows* (2003)). To alleviate the difficulties posed by these factors in the estimation of the actual light path distribution, O_2 can be used as a proxy for the light path distribution (*Pfeilsticker et al.*, 1998a; *Pfeilsticker*, 1999). *O'Brien and Rayner* (2002) proposed the nearby 1.27 μm region for the retrieval of O_2 since the scattering properties of the spectral retrieval window of the proxy species have to be as similar as possible to that of the retrieval windows of the target species.

Using a proxy for the light path primarily requires an unbiased spectral analysis of both species, e.g. O_2 and CO_2. Being outside the scope of this paper, a comprehensive analysis of the influence of single and multiple scattering will not be given. It should be mentioned that especially the O_2 A-band at 765 nm which is often used for the determination of airmass factors, exhibits very strong absorptions, thus also strong height-dependence of the sensitivity. Neglecting the issues addressed in this paper would lead to systematic biases in the retrieved airmass factor and subsequently also in the target species.

Effect of surface elevation and albedo

When the footprint of a measurement is relatively coarse (e.g. 30×60 km for SCIAMACHY), cross-correlations between the surface altitude and surface albedo can introduce systematic errors. If, for instance, 50% of the ground pixel has a height of 500 m and an albedo of 0.02 and the other 50% a height of 200 m and an albedo of 0.2, the systematic error would be about 1.5% in the total column (for an nearly equally distributed gas such as CH_4 or CO_2). Especially snow covered areas above a certain altitude with a low albedo in the NIR can create cross-correlations between the surface altitude and albedo.

One could use broadband measurements with a finer spatial resolution to provide a more accurate weighting for different areas of a given ground-pixel or exclude pixels with a surface altitude variance higher than a predefined threshold. SCIAMACHY provides broadband detectors having higher spatial resolution that can be used to derive this information. In using proxies such as O_2, care has to be taken that the albedos for the O_2 retrieval are similar to the retrieval window used for, e.g., CO_2.

2.4.2 Spectroscopical aspects

$\vec{I_0}$ effect

Although the density of the Fraunhofer lines in the near infrared is not as pronounced as in the UV/Vis, the spectral structure of the incoming solar radiation $\vec{I_0}$ and their undersampling may introduce errors (*Aliwell et al.*, 2002). This effect is similar to the effect of overlapping strong absorbers as in Fig. 2.3d. The $\vec{I_0}$ corrected slant optical density can be written as

$$\vec{\tau}_\lambda^{corr}(x) = -\ln\left(\frac{<\vec{I_0}\exp(-x\cdot A\cdot\vec{\tau}_\lambda^{ref})>}{<\vec{I_0}>}\right). \quad (2.18)$$

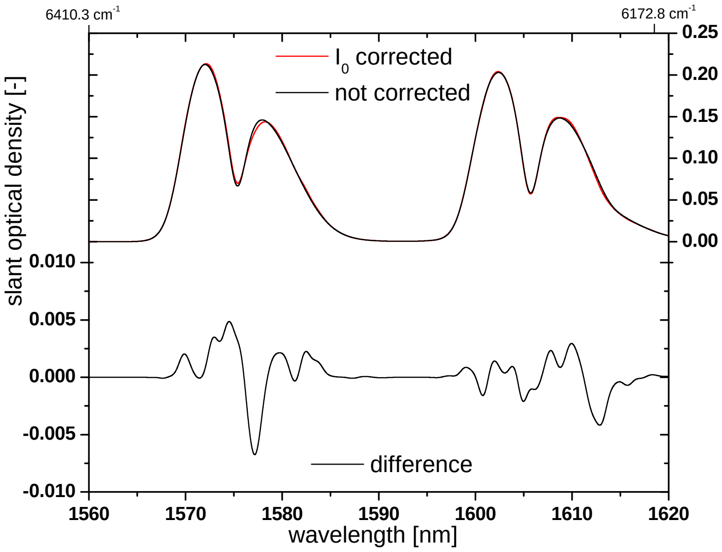

Figure 2.10: Slant optical densities of CO_2 with and without I_0 correction (AMF=3, FWHM=1.3 nm). The lower panel shows the difference of the I_0 corrected and the uncorrected slant optical density.

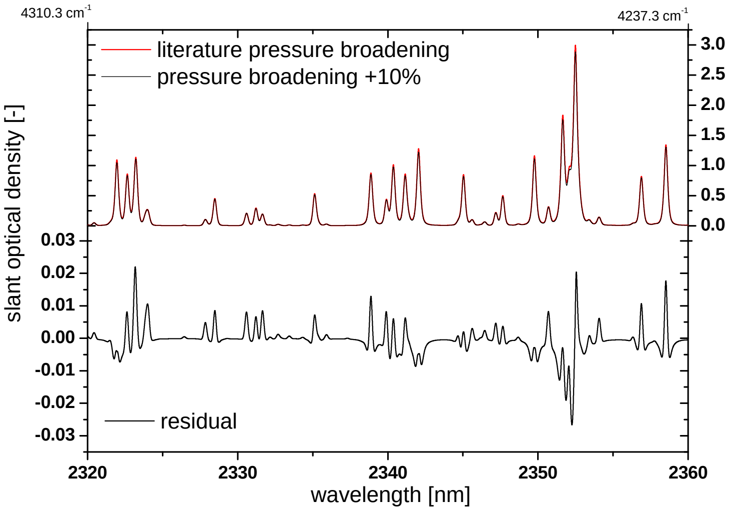

Figure 2.11: Influence of the pressure broadening coefficient γ_L^{air} on the apparent differential slant optical densities of H_2O. The remaining residual of a linear fit of both is shown in the lower panel.

The $\vec{I_0}$ effect is implemented in the evaluation of the forward model $\vec{F}(\vec{x})$ and is thus properly corrected. The highly resolved solar atlas used in this study was obtained from *Livingston and Wallace* (1991).

As can be seen in Fig. 2.10, the I_0 effect can have a relatively strong influence on the slant optical densities. Especially the absorption bands at about 1575 nm that are used for CO_2 retrieval from SCIAMACHY show a strong effect.

Effect of the uncertainty of broadening parameters

As already stated, the actual shapes of the absorption lines are important for the retrieval of strong absorbers. Thus, if the broadening coefficients are larger than given in the literature, the sensitivity of $\ln(\vec{I}/\vec{I}_0)$ with respect to concentration changes of the respective absorber will be underestimated and vice versa. This is due to the reduced degree of saturation of broader lines. However, wrong broadening parameters not only introduce systematic errors in the total columns of strong absorbers but also systematic residuals in the fit which can become stronger than spectral structures of some weak absorbers of interest.

According to *Rothman et al.* (2003), the effective pressure broadened halfwidth $\gamma_L(p,T)$ of a molecule with a partial pressure far lower than the actual pressure p [atm] is calculated as

$$\gamma_L(p,T) = \left(\frac{T_{ref}}{T}\right)^n \gamma_L^{air}(p_{ref}, T_{ref}) \cdot p\,, \tag{2.19}$$

where n is the coefficient of temperature dependence of γ_L. Especially for water vapour the line parameters exhibit large uncertainties and the absorptions in many areas in the near infrared are very strong (optical density in the line centre >10).

Figure 2.11 shows the effect of a change of 10% in γ_L^{air} for $\mathsf{H_2O}$ at US standard atmosphere concentrations and an air mass factor of 3 (corresponding to a solar zenith angle of 60°). The upper panel depicts the two optical densities at SCIAMACHY resolution (FWHM=0.24 nm) for the same vertical column density. If the actual value of γ_L^{air} would be 10% higher than expected, the total column would be overestimated by approximately 4%. It would also introduce a stable residual which is shown in the lower panel of Fig. 2.11. *Washenfelder et al.* (2003), for instance, found wrong broadening parameters for $\mathsf{CH_4}$ at about 1680 nm which lies in a wavelength region of special importance for the $\mathsf{CH_4}$ retrieval with SCIAMACHY.

Since the influence of an error in γ_L^{air} depends on the strength of the absorption lines, it also depends on the solar zenith angle. Thus, the systematic bias introduced by a wrong value of γ_L^{air} also depends on the solar zenith angle. Hence, a simple correction factor cannot be applied.

2.5 Conclusions

We have investigated several important aspects that can complicate the spectroscopic analysis of atmospheric trace gases in the presence of strong absorbers. The nonlinearity of the classical DOAS approach in situations where non-resolved lines prevail, e.g. in the near infrared spectral region, was analysed and a new IMAP-DOAS algorithm based on optimal estimation was implemented to account for the peculiarities of this spectral region.

The nonlinearity of the problem requires the use of iterations which are implemented in the IMAP-DOAS algorithm. In the iterative procedure, the vertical column densities are directly fitted such that the total slant optical density of all absorbers matches the measurement. By using convolutions with the instrumental slit function in every iteration, any interference between different absorbers or with the Fraunhofer spectrum that may occur in the classical DOAS approach is resolved. This is of importance in all cases where strong absorbers have to be retrieved (e.g. CO_2, CH_4 or O_2) or when strong absorbers interfere with the target species to be retrieved (e.g. O_3 interferences with SO_2).

Furthermore, we showed that for strong absorbers in the near infrared, the sensitivity of $\ln(\vec{I}^{lr}/\vec{I}_0^{lr})$ with respect to perturbations in concentration mostly increases with increasing ambient pressure due to pressure broadening of the absorption lines. This effect can lead to a strong systematic bias, if the whole atmosphere is scaled with a single factor as is often done in conventional DOAS algorithms. The IMAP-DOAS method circumvents this problem by confining the fit to the lowermost layers of the atmosphere.

The analysis also shows that a further derivative for changes in the temperature profile is indispensable. In Absence of this derivative, errors of up to several percent in the total column may arise.

Although spectrometers with moderate spectral resolution cannot fully resolve the absorption lines, it has been shown that the actual lineshape is of special importance since it determines the sensitivity of the measurement. Thus, an accurate knowledge of the lineshape, especially the broadening parameters, is necessary to avoid further biases.

The techniques elaborated in this paper are applicable to all cases where non-resolved strong spectral structures are encountered.

Acknowledgements

Although this study has not yet focussed on actual results of the analysis of SCIAMACHY spectra, the authors wish to thank all people involved in the SCIAMACHY and ENVISAT mission, especially ESA/ESTEC, DLR, SRON and of course the IUP Bremen team of J. P. Burrows without whom SCIAMACHY would not have been possible.

For very helpful comments we would like to thank G. C. Toon and H. Bösch from Jet Propulsion Laboratory as well as K. Pfeilsticker from IUP Heidelberg.

Retrieval of CO from SCIAMACHY onboard ENVISAT Detection of strongly polluted areas and seasonal patterns in global CO abundances

C. Frankenberg, U. Platt, and T. Wagner

Institute of Environmental Physics, Heidelberg, Germany

Journal: Atmospheric Chemistry and Physics, Atmos. Chem. Phys, Volume 5, pp. 1639-1644, 2005.
Status: Received: 2 November 2004
Published in Atmos. Chem. Phys. Discuss.: 20 December 2004
Revised: 29 March 2005
Accepted: 9 May 2005
Published: 27 June 2005
URL: `http://www.cosis.net/members/journals/df/abstract.php?a_id=2294`

Chapter 3

Retrieval of CO from SCIAMACHY onboard ENVISAT Detection of strongly polluted areas and seasonal patterns in global CO abundances

C. Frankenberg, U. Platt, and T. Wagner

SCIAMACHY onboard the European environmental research satellite ENVISAT is an UV/visible/near-infrared spectrometer providing 3 near infrared channels covering wavelengths from 1-1.75 μm, 1.94-2.04 μm and 2.26-2.38 μm with moderate spectral resolution (0.22-1.5 nm). From their structured absorption in these spectral regions, we can quantitatively determine the total column densities of the greenhouse gases CO_2, CH_4, N_2O and H_2O as well as of CO. A modified DOAS algorithm based on optimal estimation (IMAP-DOAS) has been developed at the University of Heidelberg to account for the peculiarities of these absorbers. CO is a relatively weak absorber whose spectral signature is overlapped by strong CH_4 and H_2O absorptions. Hence, retrieval of CO from SCIAMACHY spectra (within 2.26-2.38 μm) is a challenging task. Therefore, the calibration of the raw spectra with respect to dark current issues and nonlinearity were analysed in detail and substantially improved to enable reasonable retrieval of CO. This paper focusses on first results of the CO retrieval where various sources like biomass burning events and their seasonal variability can be clearly identified.

3.1 Introduction

CO is one of the most important pollutants in the troposphere and although CO itself is not a greenhouse gas, it has an indirect effect on climate as sink for the OH radical, thus leading to longer lifetime of direct greenhouse gases such as CH_4 (*IPCC*, 2001). The main sources are presumed to be biomass burning, oxidation of hydrocarbons and methane as well as fossil fuel use (*Holloway et al.*, 2000). It has already been measured by spaceborne instruments, namely by MAPS (Measurement of Air Pollution from Satellite) onboard space shuttles in 1981, 1984, and 1994 (*Reichle Jr. et al.*, 1999) and by the Interferometric Monitor for Greenhouse gases (IMG) onboard ADEOS from August 1996 to June 1997 (*Kobayashi et al.*, 1999). MOPITT onboard EOS-TERRA since 1999 (*Deeter et al.*, 2003) is still in orbit measuring global CO abundances using the gas correlation technique in the thermal infrared.

SCIAMACHY is the first instrument that allows retrieval of CO by measuring absorption in the near infrared, i.e. observing reflected and scattered sunlight instead of thermal emission (*Buchwitz et al.*, 2004). Thus, the integrated concentration of CO along the light path (the slant column density, SCD) can be inferred from the ratio of nadir radiance and solar irradiance spectra using the DOAS method (*Platt*, 1994). The near infrared spectral region has the advantage that there is little scattering within the atmosphere, thus most of the measured photons are directly reflected from the earth's surface (for cloud-free scenes and sufficiently high surface albedo). Thus, CO measurements by SCIAMACHY are, in contrast to thermal emission sounders, highly sensitive to lower layers of the troposphere where the sources are located and the bulk of the CO SCD is usually found. This is of special importance for the detection of enhanced CO abundances in the boundary layer, thus particularly of interest for human health issues.

3.2 The SCIAMACHY instrument and data analysis

SCIAMACHY onboard the European Space Agencies environmental research satellite ENVISAT consists of 8 grating spectrometers measuring in the ultraviolet, visible and near infrared wavelength region (240 nm–2380 nm) (*Bovensmann et al.*, 1999). The satellite operates in a near polar, sun-synchronous orbit at an altitude of 800 km and a local equator crossing time at approximately 10:00 am. In each orbit, a swath width of 960 km across track with a maximum pixel resolution of 26 km x 15 km is covered, thus being a substantial improvement to the large footprint of the predecessor instrument GOME onboard ERS-2. Global coverage is achieved every six days. For the CO retrieval, the typical ground pixel size is 30 km (along track) times 120 km (across track).

SCIAMACHY is designed to measure sunlight that is either transmitted, reflected or scattered by the earth's atmosphere or surface. For this purpose it has 3 viewing geometries, Nadir, Limb and Occultation. This work focusses only on Nadir spectra because they yield detailed information on the tropospheric CO abundance. We discuss instrument calibration issues, the development of a new algorithm and results of the CO retrieval.

3.2.1 Retrieval algorithm

In contrast to the UV/Vis spectral region, the near infrared exhibit peculiarities that render classical DOAS algorithms for CO retrieval unsuitable: First, there is a strong sensitivity to temperature and pressure of the strong and narrow absorption lines that are not fully resolved by the spectral resolution of the instrument, thus making the retrieval nonlinear. Second, the weak CO absorptions are overlapped by strong methane and water vapour lines whose interferences are stronger than the CO absorption itself. *Buchwitz et al.* (2000) were the first to focus on the near infrared and introduced the concept of weighting function modified (WFM)-DOAS. To account for the general nonlinearity of the problem and to avoid interferences between strong absorbers, we developed a new iterative maximum a posteriori DOAS (*IMAP*-DOAS) (*Frankenberg et al.*, 2005a) at the University of Heidelberg. The algorithm is based on optimal estimation theory introduced to the remote sensing community by *Rodgers* (1976). This method directly iterates the vertical column densities of the absorbers of interest until the expected spectral signature of the total optical density fits the measurement. It accounts for nonlinearities due to spectrally non-resolved strong absorptions and considers sensitivity to pressure and temperature changes in the atmospheric profile. This algorithm minimises systematic biases that would occur in classical DOAS algorithms. A detailed description of the algorithm can be found in *Frankenberg et al.* (2005a). Other research groups, e.g. *Schrijver* (1999), also developed modified algorithms for the near infrared spectral region and some preliminary results are shown by *Buchwitz et al.* (2004) and *Gloudemans et al.* (2004).

The CO retrieval turned out not only to be a challenging task from a spectroscopic point of view, but also due to instrumental issues: An ice layer on the near infrared detectors affects dark current and the instrumental function. These are important issues and have to be analysed and corrected in detail.

3.2.2 Spectral calibration, dark current and nonlinearity

The near infrared channels exhibit a substantially higher dark current than the UV/Vis channels of SCIAMACHY. In addition to this complication, the leakage current (the time dependent part of the dark current) and the fixed pattern noise are not a smooth function but show strong variations over the entire detector array. Due to the variable ice deposition on the detectors, the dark current and even the slit function show time dependent behaviour (*Kleipool*, 2004). Thus, a simple correction is not possible and the expected operational correction algorithms (*Slijkhuis*, 2001) have not yet solved the problem.

Due to these crucial problems, a reasonable retrieval of CO is not possible without application of sophisticated calibration methods. A first correction scheme has been implemented in the current *IMAP*-DOAS algorithm using daily readouts of the dark current to correct the raw spectra with the respective pixel exposure times (as initially proposed by the instrument PI, J. Burrows, see technote by *Kleipool* (2003a)). Furthermore, the standard deviations of the daily dark current readouts are used in the algorithm to generate a daily dead/bad pixel mask and for the weighting of the available pixels in the weighted least squares fit according to their dark current stability. Since the dark current can also vary over the orbit (*Kleipool*, 2004), a first order dark current offset correction has been implemented as the fit factor in our algorithm. In addition to these complications, the detector pixels exhibit a nonlinearity (*Kleipool*, 2003b) that has not yet been considered in the operational calibration tools (*Slijkhuis*, 2001). The proposed correction by *Kleipool* (2003b), which treats even and odd detector pixels separately, has been implemented in our correction scheme. These modifications substantially improved the CO retrieval in channel 8 of SCIAMACHY.

3.2.3 Spectral fitting

For the retrieval of CO, a fit window between 2324 and 2335 nm was chosen. Due to the decline of instrument sensitivity towards larger wavelengths, this has been found to be an optimal fitting window with respect to signal to noise ratio. CO is a relatively weak absorber whose absorption lines are superposed by strong absorptions by CH_4 and H_2O. The root mean square (RMS) of the (not-weighted) residual of the fit in this wavelength range is typically about 0.9% (see Fig. 3.2). Considering this residual only as noise in the spectra, an upper limit of the statistical errors (standard deviation) in the CO column is about $3{\cdot}10^{17}$molec/cm^2. All outliers in the retrievals are masked by using only fits where the root mean square of the residual is below 1.7% and the statistical error of the CO vertical column density is below 30%.

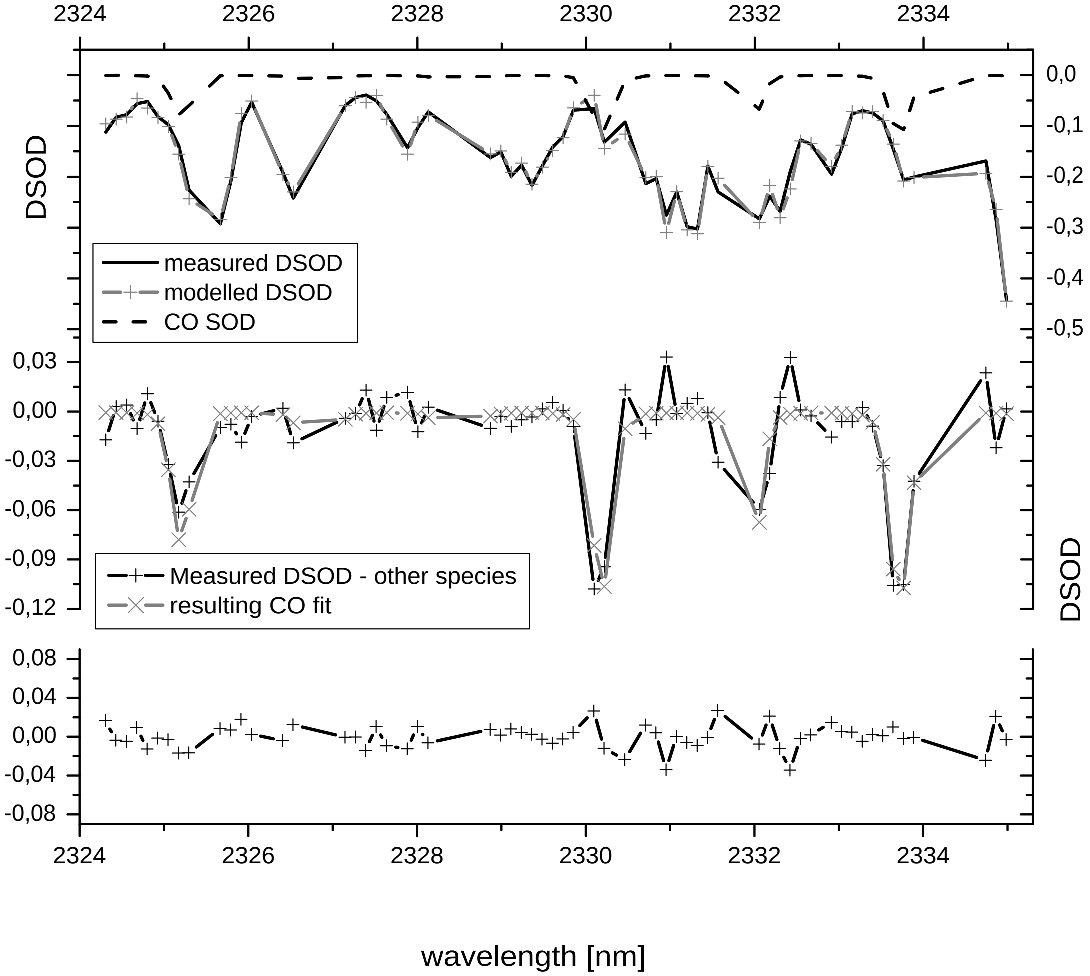

Figure 3.1: Example of a CO fit with relatively strong CO absorptions ($VCD \approx 8{\cdot}10^{18}$molec/cm^2). The upper panel shows the differential slant optical density (DSOD) of all absorbers (CH_4, H_2O and CO) as well as that of CO separated (dashed line). The centre panel shows the measured slant optical density with the slant optical density of CH_4 and H_2O subtracted in order to depict only the absorption structures of CO. The lower panel shows the residual of the fit (please note the different scale).

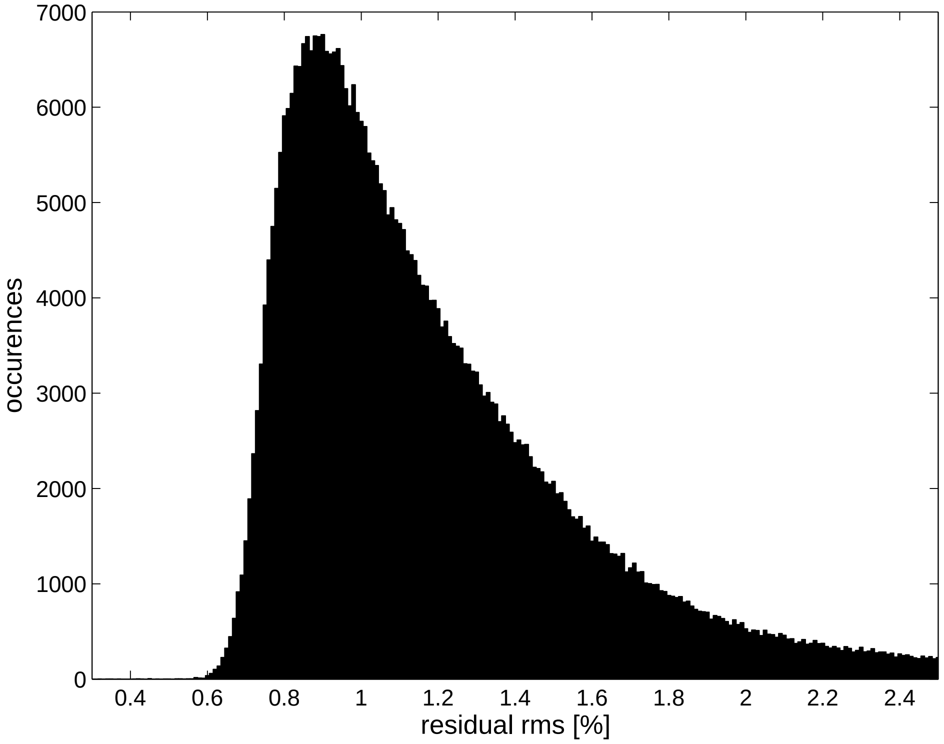

Figure 3.2: Histogram of the RMS of the fit residual for the CO retrieval in channel 8 during July 2004.

This subset of appropriate retrievals can then be used for the analysis of the global distribution and variations of CO vertical column densities.

3.2.4 Aims

The aim of the CO retrieval is to detect global patterns and variations in the total column abundances of CO. Although the highest mixing ratios are expected in the boundary layer, which is sometimes shielded from satellite observations by clouds, a substantial amount of CO can also be present above the clouds. Thus, all observations have been taken into account for the analysis and cloud-covered pixels have not been masked out.

However, in order to account for clouds and other processes that can artificially diminish the retrieved total column, global pictures of CO for a certain time period are depicted as described in the following. Pixels (meeting the criteria described in Sec. 3.2.3) with higher VCD's are displayed above pixels with lower VCD's. This procedure unveils the patterns of maximum CO abundances. Since clouds usually diminish the retrieved columns, this method also hides measurements that might be artificially reduced. Nevertheless, in some areas no cloud free conditions might have occurred within the given time periods, biasing the observed maximum values. Future work will take more sophisticated cloud algorithms into account, using information on cloud top-height and cloud cover.

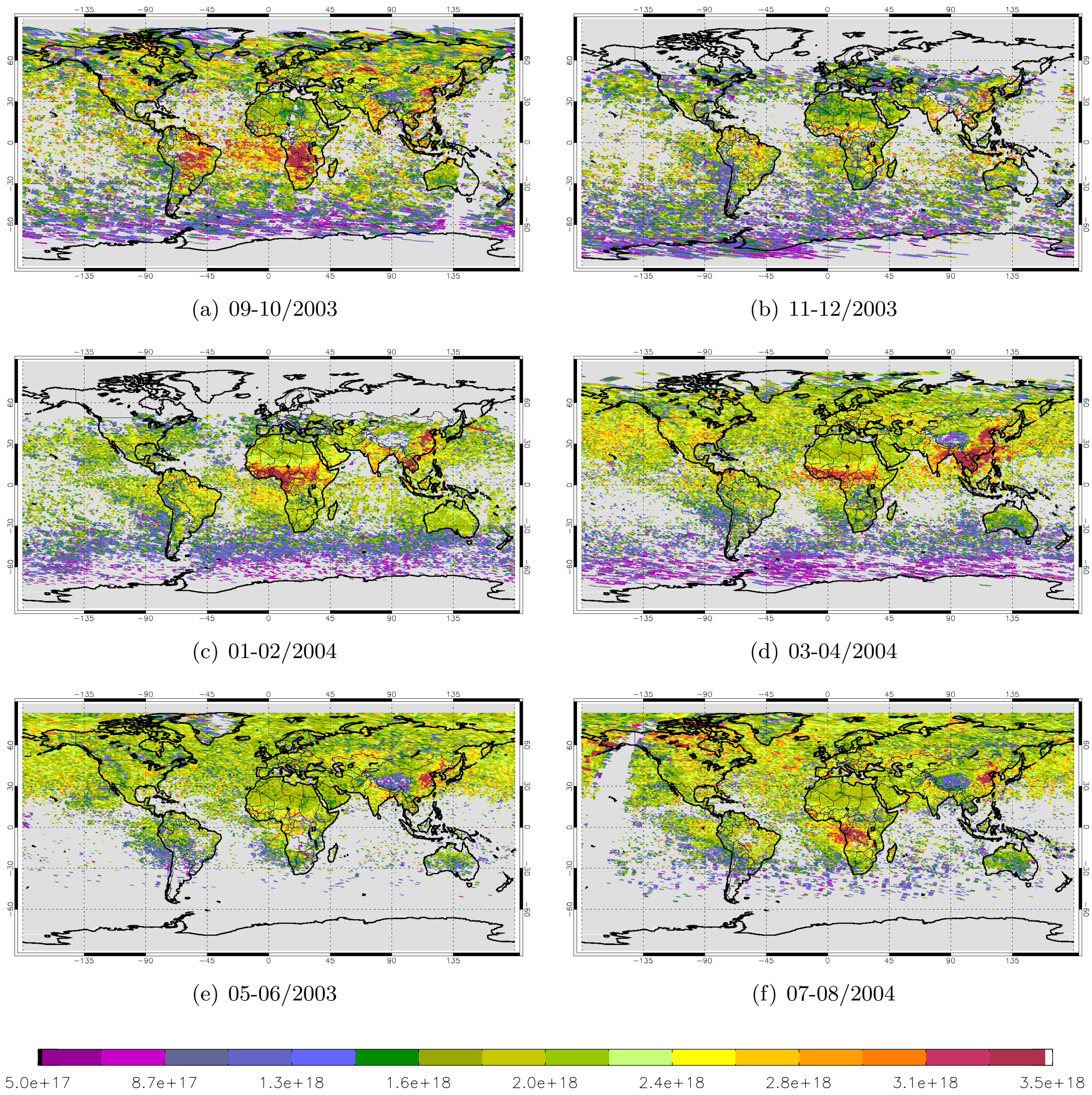

(a) 09-10/2003

(b) 11-12/2003

(c) 01-02/2004

(d) 03-04/2004

(e) 05-06/2003

(f) 07-08/2004

Figure 3.3: Maximum observed CO vertical column density [molec/cm^2] in six two-month periods from September 2003 to August 2004. $1 \cdot 10^{18}$ molec/cm^2 correspond roughly to an column-averaged CO mixing ratio of 50ppbv. Enhancements due to seasonal variations of biomass burning (e.g. in Africa), constant anthropogenic sources (e.g. China) or sporadic fires (e.g Alaska in July/August 2004) can be observed (see text). Although the CO columns are not averaged over the given time periods, the patterns of enhancements appear rather smooth, proving the good fit quality and the absence of outliers. Over certain areas (gray), no suitable measurements are available due to very low surface albedo (e.g. over the ocean) or too high solar zenith angles.

3.3 Results

Monthly maps created as described above are a useful method to show the general patterns of CO abundance and their seasonal variations. Figure 3.3 depicts the maximum CO VCD for a whole year divided into bimonthly periods ranging from September 2003 to August 2004. Since most CO sources are located in the northern hemisphere, a clear north-south gradient can be identified. This finding substantiates that even low column abundances can be measured by SCIAMACHY.

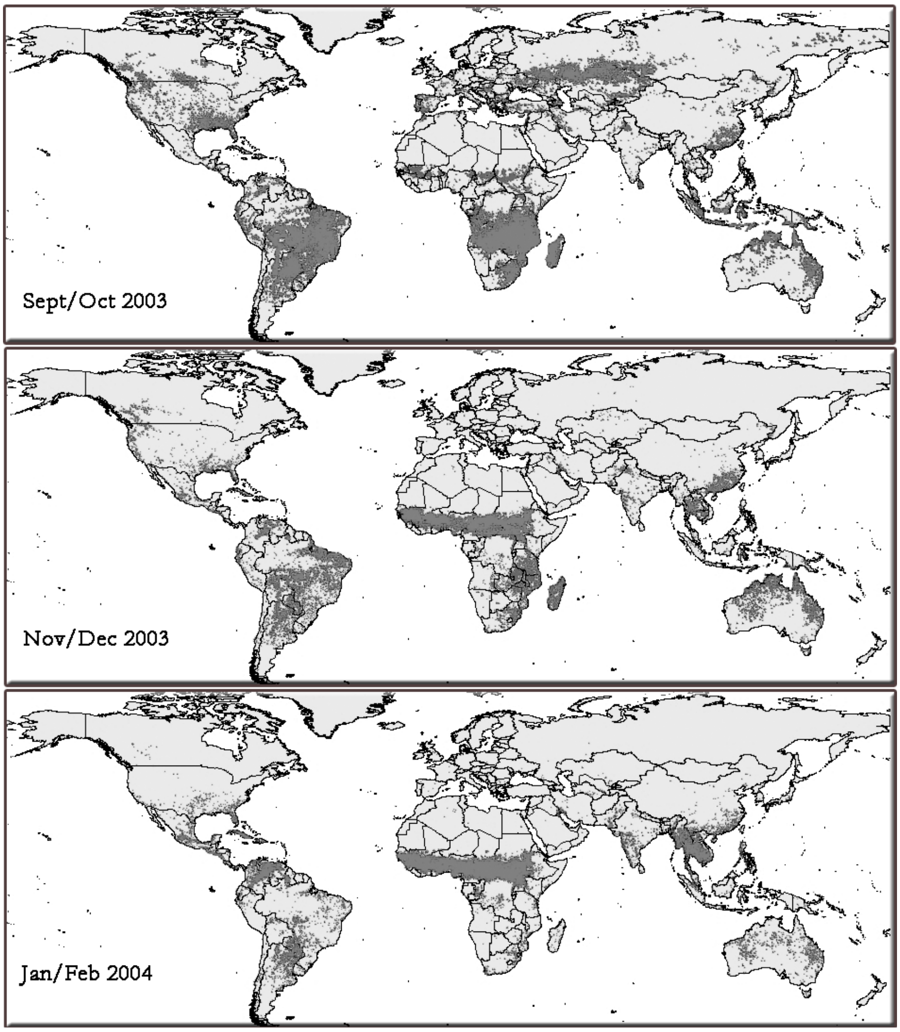

Figure 3.4: Bimonthly fire distributions from September 2003 through February 2004. Displayed are fire counts measured by MODIS aboard Terra. At the time of publication, no newer data than February 2004 were available.

Further, large-scale CO enhancements with seasonal variations can also be clearly identified in Africa, South America and Southeast Asia. In March and April, we retrieved vertical columns in Thailand and India with values of up to $6.5 \cdot 10^{18}$ molec/cm^2. Biomass burning is presumed to mostly contribute to these seasonal patterns of strong enhancements in CO. The seasonal variations of the global distribution of biomass burning events can be well observed by MODIS (Moderate Resolution Imaging Spectroradiometer) aboard Terra. Figure 3.4 shows fire counts made by MODIS from September 2003 through February 2004. The areas with high fire frequencies correlate well with high abundances of CO, substantiating the assumption that the CO enhancements stem from biomass burning. Also striking are the enhanced CO concentrations in South-America in September/October 2003, coinciding with the typical period of fires in this region. In this context it has to be noted that, particularly in the tropics, oxidation of hydrocarbons can also be a substantial source of CO.

However, there are also patterns of CO enhancements that do not exhibit strong seasonality: The region around Bejing in China shows high CO abundances over the whole time period and can be associated with high industrial activities. These values also peaked at about $7 \cdot 10^{18}$ molec/cm^2 in March/April 2004.

In addition to these seasonal and constant sources, there are CO enhancements due to occasionally occurring fires, such as in Alaska and northern Canada (July/August 2004, forest fires) or Kazakhstan in September and October 2003.

3.4 Conclusions

For the retrieval of CO from SCIAMACHY near infrared spectra, we implemented several important spectral calibration procedures and applied our newly developed *IMAP*-DOAS algorithm (*Frankenberg et al.*, 2005a) to account for the peculiarities of the near infrared and the CO retrieval in particular. We have demonstrated that SCIAMACHY can perform global measurements of the CO total column density with high sensitivity even to the boundary layer. Although the calibration of the spectra and the slit function posed some serious problems the solutions to which have yet to be perfected, first results are very encouraging and demonstrate that SCIAMACHY is able to detect CO globally with sufficient accuracy. We observed seasonal variations of biomass burning events as well as enhancements due to anthropogenic activities such as in China. Furthermore, we detected sporadic biomass burning events in various regions on earth. Thus, our observations provide important information on tropospheric chemistry issues on a global scale.

More efforts in the calibration of the spectra and a diminishing ice deposition on the detectors will further improve fit quality and retrieval results. Using longer time periods, will enable us to analyse the correlation of industrial activities and biomass burning with CO in more detail.

Acknowledgements

The authors wish to thank all people involved in the SCIAMACHY and ENVISAT mission, especially ESA/ESTEC, DLR, SRON, KNMI and of course the IUP Bremen team, especially J.P. Burrows without whom SCIAMACHY would not have been possible. We are also very grateful to Ankie Piters and John van de Vegte from KNMI for their immense help in handling SCIAMACHY data.

Assessing methane emissions from global space-borne observations

C. Frankenberg[1], **J.F. Meirink**[2], **M. van Weele**[2], **U. Platt**[1], **and T. Wagner**[1]

[1]Institute of Environmental Physics, University of Heidelberg, INF 229, 69120 Heidelberg, Germany

[2]Royal Netherlands Meteorological Institute, Section of Atmospheric Composition, P.O.Box 201, 3730 AE De Bilt, The Netherlands

Journal: Science, Volume 308, Number 5724, Issue of 13 May 2005, pp. 1010-1014.
Status: Submitted: 22 October 2004
Accepted: 9 March 2005
Published online in Science Express: 17 March 2005
Published: 13 May 2005
URL: Full text: `http://www.sciencemag.org/cgi/content/full/308/5724/1010`
Supporting online material (incl. movie): `http://www.sciencemag.org/cgi/content/full/1106644/DC1`

Chapter 4

Assessing methane emissions from global space-borne observations

C. Frankenberg, J.F. Meirink, M. van Weele, U. Platt, and T. Wagner

In the past two centuries, atmospheric methane has more than doubled and now constitutes 20% of the anthropogenic climate forcing by greenhouse gases. Yet its sources are not well quantified, introducing uncertainties in its global budget. We retrieved the global methane distribution using space-borne near-infrared absorption spectroscopy. In addition to the expected latitudinal gradient, we detect large-scale patterns of anthropogenic and natural methane emissions. Furthermore, we observe unexpectedly high methane concentrations over tropical rainforests revealing that emission inventories considerably underestimate methane sources in these regions during the time period of investigation (August-November 2003).

4.1 Introduction

Methane (CH_4) is, after carbon dioxide (CO_2), the second most important anthropogenic greenhouse gas (*IPCC*, 2001). It also has an indirect effect on the climate through chemical feedbacks (*IPCC*, 2001; *Lelieveld et al.*, 1998). More than 50% of present-day global methane emissions are anthropogenic, the largest contributors being fossil fuel production, ruminants, rice cultivation and waste handling (*Olivier and Berdowski*, 2001). The natural source strength of CH_4, mainly constituted by wetlands, is particularly uncertain since these emissions vary considerably in time and space (*Morrissey and Livingston*, 1992; *Walter and Heimann*, 2000) and available ground-based measurements are sparse, albeit precise, and limitedly representative at larger scales. Better knowledge of the methane distribution and emissions is indispensable for a correct assessment of its impact on global change (*IPCC*, 2001). Observations from space now allow the global detection of spatial and temporal variations in atmospheric methane concentrations, thereby enabling identification of known sources and discovery of new ones, particularly in regions that are poorly sampled by existing surface measurement networks.

4.2 The SCIAMACHY instrument

The SCIAMACHY (SCanning Imaging Absorption spectroMeter for Atmospheric CHartographY) instrument (*Bovensmann et al.*, 1999) onboard ESA's European environmental research satellite ENVISAT records the intensity of solar radiation, reflected from the earth surface or the atmosphere, in more than 8000 spectral channels between 240-2390 nm. From these measurements, atmospheric trace gas concentrations (e.g. BrO, $OClO$, H_2O, SO_2, NO_2, CH_2O, O_3, N_2O, CO, CH_4 or CO_2) can be derived (*Burrows et al.*, 1999; *Wagner et al.*, 2002). The near infrared spectrometers are employed for global measurement of total columns of carbon monoxide and greenhouse gases carbon dioxide and methane. ENVISAT operates in a nearly polar, sun-synchronous orbit at an altitude of 800 km, crossing the equator at 10:00 AM local time. SCIAMACHY offers a variety of measurement geometries. For column retrievals, we choose the nadir mode in which the instrument points down almost perpendicular to the earth's surface, detecting reflected sunlight. The spatial extent of the ground pixels considered in this study is 60 km (east-west) by 30 km (north-south). Global coverage is achieved every six days.

4.3 Retrieval Algorithm

CO_2 and CH_4 not only absorb thermal radiation from the earth system causing radiative forcing, but also solar radiation in the near infrared. Hence, these molecules can be measured by means of the proven method of differential optical absorption spectroscopy (*Platt*, 1994) (DOAS). To account for peculiarities of spectrometry in the near infrared (*Buchwitz et al.*, 2000; *O'Brien and Rayner*, 2002), we implemented a new modified iterative algorithm (IMAP-DOAS) (*Frankenberg et al.*, 2005a) that enables precise and unbiased determination of vertical column densities (VCD, the vertically integrated concentration from surface to top of atmosphere) of methane and carbon dioxide. The negligibility of Rayleigh scattering proves to be a major advantage in the near infrared: In the absence of clouds and aerosols, most photons recorded by the instrument have thus been reflected at the earth's surface, thereby having traversed the entire atmospheric column twice. This renders the measurements sensitive to the lower troposphere, which is a prerequisite for the detection of near ground methane sources. In contrast, thermal-infrared sounders, which have also been employed to measure CH_4 (*Clerbaux et al.*, 2003), exhibit a lack of sensitivity near the ground. However, they could derive methane abundances in the free troposphere and stratosphere, thus yielding more accurate information about the lower troposphere when synergistically combined with near-infrared retrievals.

Two main points affecting the retrieval in the near infrared have to be considered: First, the VCD of a well-mixed gas scales linearly with the total column of all atmospheric constituents, thus with surface pressure. Hence, we need a proxy for surface pressure to convert columns into mixing ratios. Second, clouds and aerosols can substantially alter the light path of the recorded photons. CO_2 exhibits only very small variations in its total columns and the retrieval window (1562-1585 nm) is spectrally close to the CH_4 retrieval window (1630-1670 nm). Thus,

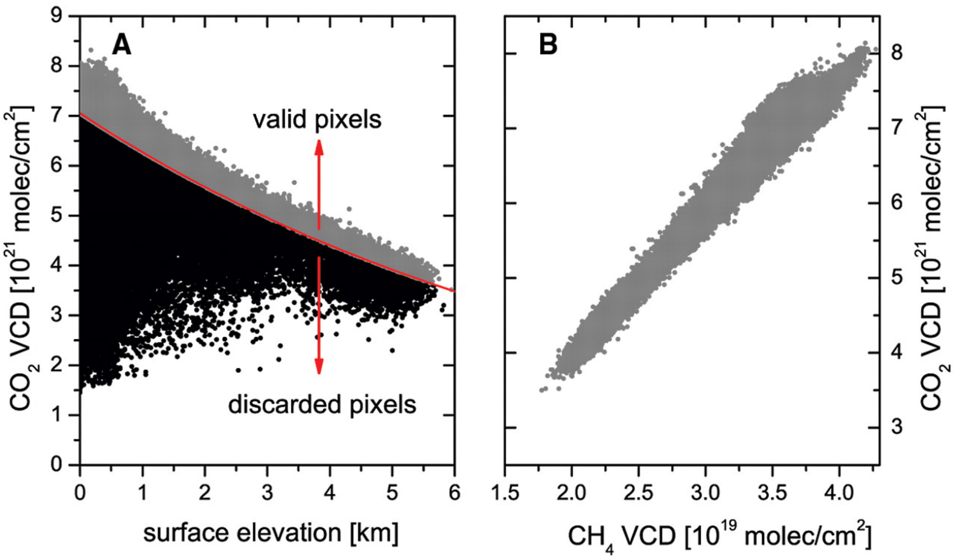

Figure 4.1: **(A)** A scatter plot of the retrieved CO_2 VCDs versus surface altitude (August to September 2003). For further evaluations, only pixels above the threshold indicated by the red line are considered (corresponding to an effective cloud top height of 1 km). **(B)** A scatter plot of the retrieved vertical column densities of CH_4 and CO_2 for all valid pixels. The slight deviations from the strictly linear correlation between both VCDs can be mostly explained by variations in the CH_4 VMRs.

it is well suited as a proxy for both, surface pressure (or, in the presence of clouds, cloud top pressure) and changes in the light path due to partial cloud cover and aerosols. Consequently, we can derive the column-averaged dry (no water vapour included) volume mixing ratio (VMR) of CH_4 in the atmosphere from the ratio of the CH_4 VCD (V_{CH_4}) and the CO_2 VCD (V_{CO_2}), scaled by the global and annual mean of the CO_2 column-averaged mixing ratio (370 ppm), i.e. $VMR(CH_4 \approx V_{CH_4}/V_{CO_2} \cdot \overline{VMR}(CO_2)$. Care should be taken not to confuse column-averaged VMRs with surface VMRs. Surface VMRs have a stronger response to emissions, while column averaged mixing ratios exhibit less variation and are slightly lower due to reduced methane VMRs in the stratosphere.

A retrieval bias is introduced by assuming a constant column-averaged VMR(CO_2), whereas in reality it varies globally and seasonally over a range (minimum to maximum) of about 11 ppmv or 3% (*Olsen and Randerson*, 2004a). This bias will be largest in Eurasia and North America north of 40°N. However, south of 40°N the bias can be assumed to be within 1.5% (*Olsen and Randerson*, 2004a). Note that methane enhancements may be masked by our method, in case of sources leading to similar relative enhancements of and (e.g., biomass burning for certain fire types).

In the next step, we discard all measurements exhibiting substantial cloud cover at altitudes significantly above the ground since we are primarily interested in variations in the lower troposphere. Fig. 4.1a demonstrates how we extract appropriate measurements: highest CO_2 column observations show strong anti-correlation with surface altitude, illustrating the sensitivity to the boundary layer and being a first proof of the quality of the measurements. Strongly reduced column retrievals can be attributed to the shielding effect of clouds. We use a lower threshold of (red line) to obtain a suitable subset of measurements (grey pixels) representing the lower troposphere. A scatter-plot of and underlines the excellent correlation of both measurements in this subset (see Fig. 4.1b). The deviations from the strictly linear correlation bear the actual information, i.e. the variations of the CH_4 column with respect to the CO_2 column, which is determined by the length of the light path and an only slightly varying CO_2 VMR.

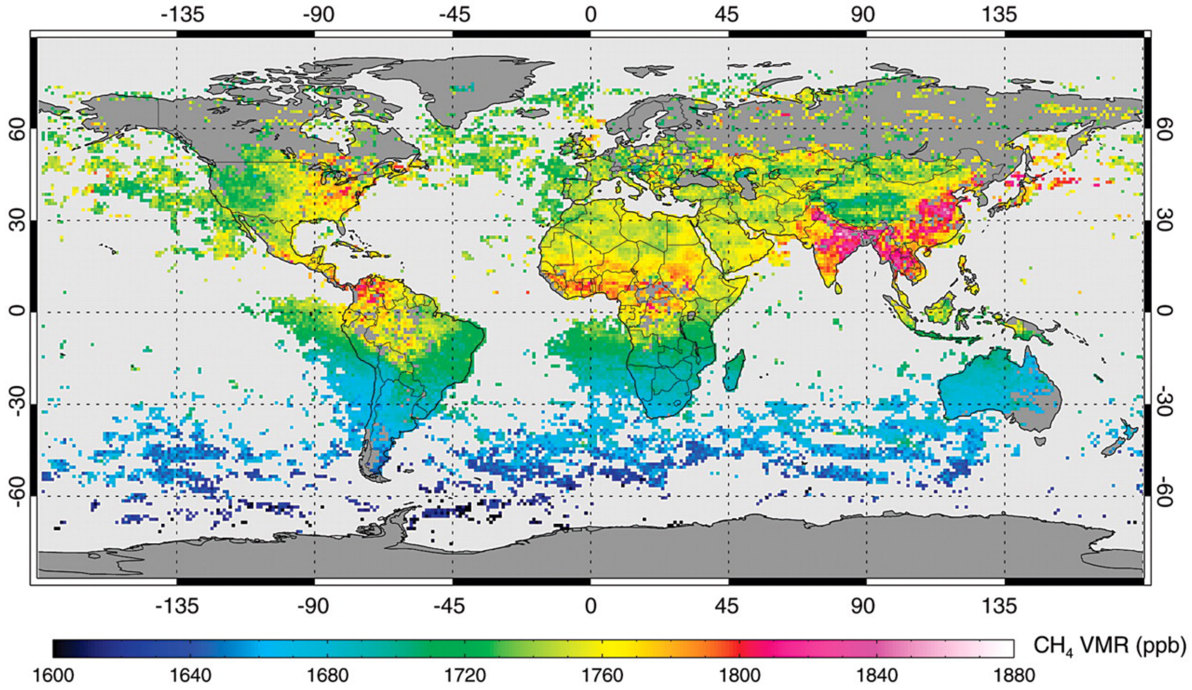

Figure 4.2: SCIAMACHY measurements of column-averaged methane VMR in units of parts per billion. The measurements are averaged over the time period of August through November 2003 on a 1°x1°horizontal grid. At least 5 (and up to 150) measurements are taken for each grid cell. Only few observations are available over the ocean, since low ocean reflectivity substantially reduces the quality of the retrieval, leading in turn, to unreliable measurements (standard deviation of the fit residual above 0.5%) that are discarded. Occasionally, sun glint or clouds at low altitudes allow measurement over the ocean.

4.4 Results

Using only the aforementioned measurement subset, we averaged the CH_4 VMRs from August through November 2003 on a horizontal grid (1°x1°) as shown in Fig. 4.2. The latitudinal gradient in the methane VMRs can be seen, with strongest gradients, as expected, across the Intertropical Convergence Zone (ITCZ). Apart from this gradient, large scale and strong methane enhancements are observed in various parts of the world. The largest abundances are found in the Gangetic plains of India, South-East Asia and parts of China. According to current emission inventories (see Fig. 4.4) (*Olivier and Berdowski*, 2001), the sources can be mostly attributed to rice cultivation in this time period, and to a lesser extent, to domestic ruminants. Wetlands presumably cause the observed high abundances in central Africa and Manchuria in China. Fossil fuel production can be associated with enhanced CH_4 VMRs over the industrialised Yellow-river basin in China and the Appalachian basin (coal mining) in the eastern USA. Waste-treatment related emissions are likely to add to these in populated areas.

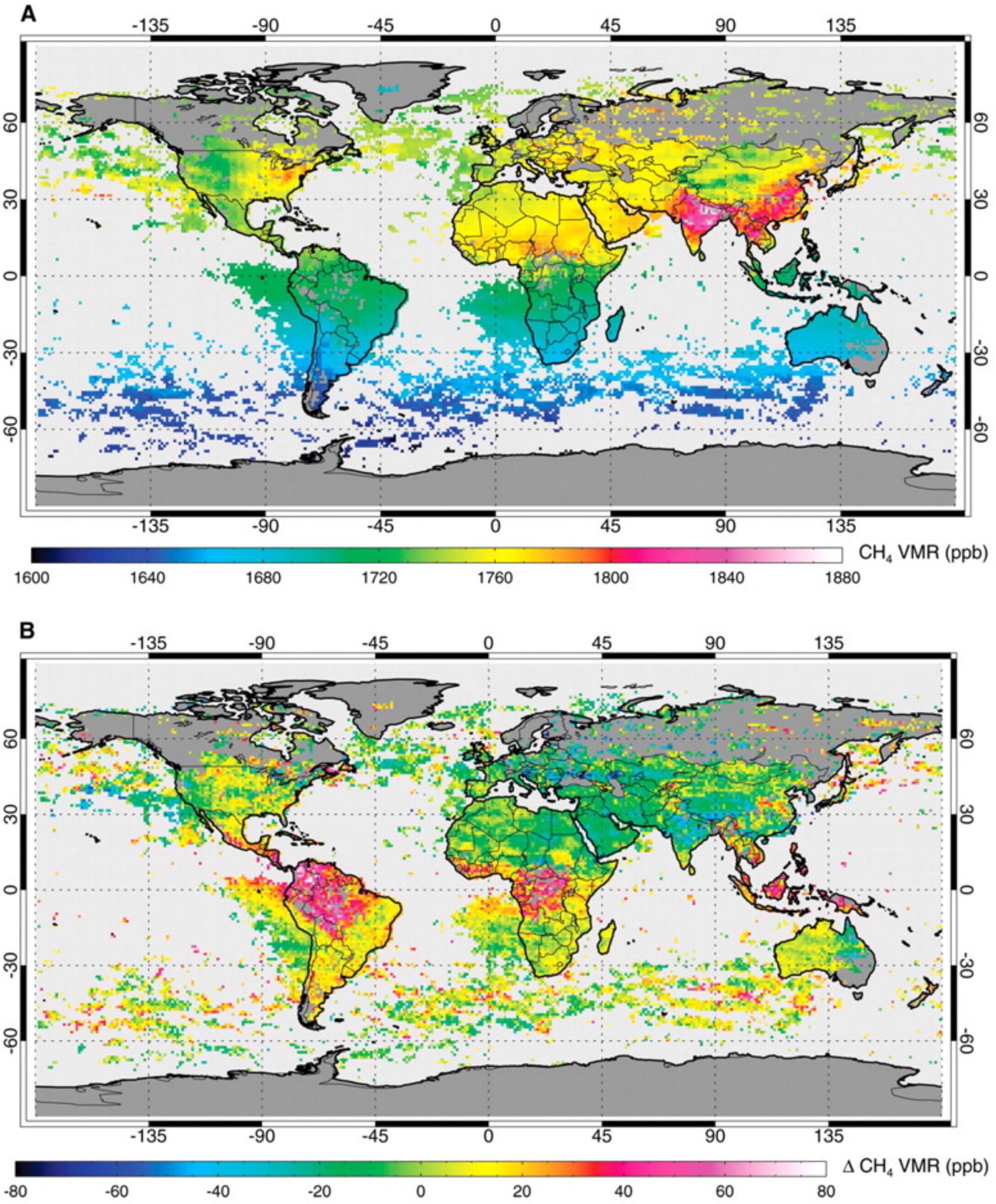

Figure 4.3: **(A)** The TM3 model results of the column-averaged methane VMR in ppb for the time period of August through November 2003. Only modeled values that are colocated in space and time with the respective SCIAMACHY measurements are used for the averaging. **(B)** The difference between the SCIAMACHY measurements and the TM3 model results (Δ). The results are displayed in ppb, ranging in most pixels from −20 to 20 `ppb` (±1% relative difference). The largest discrepancies can be seen over tropical broadleaf evergreen forests in South America, central Africa, and Indonesia. In these areas, measured values are persistently higher than predicted by the model. Prevailing wind directions cause transport of these discrepant concentrations over the oceans (e.g., northwest of South America or west of Africa).

To substantiate our findings, we compared the measurements with methane concentration fields simulated using a global chemistry-transport model (TM3) (*Dentener et al.*, 2003) that takes current emission inventories (*Houweling et al.*, 2000; *Van Aardenne et al.*, 2001) into account (see also Fig. 4.4). The modelled enhancements in the USA and Asia as well as the north-south gradient (Fig. 4.3) strongly resemble the methane VMRs retrieved by SCIAMACHY in magnitude and spatial extent (Fig. 4.2). Additionally, persistent long-range transport features are observed, most clearly over the Pacific, east of Japan (see Movie S1 ; see online SOM)) and Fig. 4.2). In principle, the model enables discrimination of emissions and transport, e.g. evident in November 2003, with Africa strongly influenced by methane transported from South-Asia (Movie S1; see online SOM).

Although the general agreement between the measurements and the model is very good (see Fig. 4.5), there are discrepancies in India and in the tropics (Fig. 4.3b). The measured abundances over India are lower than simulated by the model. This indicates that the rice emissions used in our model runs (amounting to 80 Tg per year) are probably overestimated. In contrast, SCIAMACHY retrievals in the tropics are up to 4% (70 ppb) higher than predicted by the model.

We verified that this discrepancy cannot be attributed to a retrieval error dependent on solar zenith angle, light-path changes or albedo (see supporting text). A model bias, such as an underestimation of the stratospheric methane abundances or large errors in the modelled distribution of OH radicals, can also be excluded (see supporting text). The higher methane VMRs of the measurement compared to the model can thus be explained either by tropical methane emissions not considered in the model, a regional CO_2 depression relative to the annual global mean, or some combination of both. Although CO_2 flux estimates in the tropical landmasses are uncertain (*Gurney et al.*, 2002), the required depression in the CO_2 column (3-4%) would be of an improbably high magnitude (*Olsen and Randerson*, 2004a). Hence, we conclude that tropical CH_4 sources in our model are underestimated.

The underestimation may be related to biogenic methane emissions since there is a strong spatial correlation between the discrepancies and the presence of broadleaf evergreen forest (Fig. 4.6) (*DeFries and Townshend*, 1994). Model simulations indicate that an additional tropical methane source of around 30 Tg over the considered time period (August-November) is needed if the discrepancy is fully assigned to methane sources. For comparison: the tropical source in our model is 45 Tg (see Table 4.1). Potential candidates for the enhanced source include wetlands, biomass burning, termites, cattle breeding in pastures, or a hitherto unknown methane source that might be directly related to the broadleaf evergreen forest. Wetland emissions, in particular in the Amazon, appear to be underestimated in our model (e.g. *Melack et al.* (2004) estimate an annual source of 29 Tg CH_4 for the Amazon, while we used 8 Tg), but the investigated period coincides with the dry season in most of the tropics, when wetland emissions are supposed to be lowest (*Melack et al.*, 2004; *Devol et al.*, 1990). However, in the dry season also unaccounted biomass burning can contribute to the discrepancy. Tropical fires are characterized by a molar CH_4/CO_2 ratio (*Andreae and Merlet*, 2001) that is more than twice the ratio of their respective background concentrations. Hence, our measurements are sensitive to these fires. Finally, termites constitute a significant but poorly constrained tropical methane source (*Sanderson*, 1996). Further validation measurements and process-based investigations for the considered season in the evergreen forests of tropical South America, Africa and Indonesia are needed to conclude which source type is responsible for the observed discrepancy and to what extent this discrepancy is due to an underestimated or hitherto unknown methane source. In addition, investigations of satellite data for longer time periods are necessary to estimate the annual methane excess and to constrain the source attribution.

An additional methane source of 30 Tg in four month is large but can be accommodated by the uncertainty in the global budget, which is estimated to be 50-100 Tgyr^{-1} (*IPCC*, 2001). Further, it is important to note that surface observations (Climate Monitoring and Diagnostics Network (CMDL), http://www.cmdl.noaa.gov/ccg/) are not in disagreement with a large additional tropical source. Methane emitted in the tropics is generally rapidly uplifted by convection, so that the surface stations, which are located in remote ocean sites, are sensitive to these emissions only to a limited extent. Inverse modelling studies based on ground-based measurements (*Hein et al.*, 1997; *Houweling et al.*, 1999) have also indicated higher tropical emissions than estimated from bottom-up inventories. However, this evidence has been rather indirect and uncertain. The present satellite measurements over the tropical landmasses are sensitive to the entire atmospheric column, thus directly reflecting enhancement patterns.

4.5 Discussion

Global measurement from space has, for the first time, proven feasible for detection of CH_4 emissions. The satellite's ability to sense sources globally is unique and opens a new window for the analysis of the biogeochemical cycle of methane and anthropogenic impacts. With SCIAMACHY hopefully in operation for several years to come, we should be able to examine the temporal and spatial variations of CH_4 over longer time periods. The integration of these measurements with atmospheric models and precise ground-based observations should greatly reduce uncertainties in the methane source strength, helping draw a consistent picture of the global methane budget. This will be of high priority for climate research.

4.6 Supporting Online Material

4.6.1 Materials and Methods

Our iterative maximum a posteriori (IMAP) DOAS algorithm (*Frankenberg et al.*, 2005a) is based on optimal estimation (*Rodgers*, 1976, 2000) and uses the depth of the absorption structures of the respective trace gases to deduce their abundances (see Fig. 4.7). Spectral parameters are taken from the HITRAN database (*Rothman et al.*, 2003) with modifications for CH_4 line broadening parameters (*Washenfelder et al.*, 2003) and CO_2 line strengths (*O'Brien and Rayner*, 2002). In brief, the algorithm iterates the slant column densities (SCD, concentration integrated along the light path) of all absorbers until their overall optical density best matches the measured optical density. Supposing that no clouds or aerosols in the atmosphere lead to enhanced scattering (*Pfeilsticker et al.*, 1998b), we can exactly derive the desired vertical column densities by dividing the retrieved SCD by the geometric air mass factor (AMF, the ratio of the length of the actual and the vertical light path). For our retrieval, we use a spectral window of 1630-1670 nm for CH_4 and 1562-1585 nm for CO_2. The precision errors in a single set of CH_4 and CO_2 VCD retrievals due to uncertainties in the fit are approximately 1.5% and 1%, respectively. Errors induced by clouds and aerosols in the field of view are far larger. However, rationing by CO_2 eliminates this source of error since the retrieved CO_2 VCD can be used as proxy for the light-path, analogous to O_2 or O_4 in other applications (*O'Brien and Rayner*, 2002). Not only their spectral proximity but also their similar optical densities at high spectral resolution assure very similar light-path lengths whose errors can be assumed to be below 0.5% (*O'Brien and Rayner*, 2002). Due to the relatively coarse spatial resolution (60x30 km), we often encounter partially clouded pixels that might have the strongest influence on the light-path distribution. However, due to the spectral proximity of both retrieval windows, the cloud and surface albedo can be assumed to be the same resulting in equal light-paths even in the presence of partial cloud cover. Due to uncertainties in the instrumental slit function, the accuracy is currently estimated to be 10% but will improve in the future. We hitherto scaled our retrieved CH_4 VMR by 0.93 to adjust the measurements to column VMRs from the model that, in turn, is in close agreement with ground-based measurements of surface VMRs from the NOAA/CMDL network (*Dlugokencky et al.*, 2003, 1998). The systematic bias in the satellite observations is most probably related to uncertainties in the width of the instrumental slit function. Nevertheless, the bias does not affect the spatial variations shown in this paper.

Usually, measurements of oxygen (O_2 or O_4) (*Pfeilsticker et al.*, 1998b; *Wagner et al.*, 2003) are used for the determination of column averaged mixing ratios (*Buchwitz et al.*, 2005a) since the O_2 VMR is known exactly. However, the spectral retrieval window for suitable O_2 detection (about 765 nm) is not near those of CO_2 or CH_4, creating larger uncertainties due to differences in the respective photon paths, especially in the presence of partial cloud cover or large aerosol loading in the field of view.

For the determination of the threshold line in Fig. 4.1a, we used a CO_2 VCD that corresponds to an effective cloud top height of approx. 1 km. This theoretical value was computed using a scale height of 8.5 km, which results in a maximum reduction of the expected CO_2 column (also computed with a scale height of 8.5 km) of 11%. This ensures that we probe the largest part of the atmospheric column (89%) and still use a reasonable fraction of available measurements (in our case approx. 20%).

The global chemistry-transport model TM3 (*Dentener et al.*, 2003) is used in this study at a spatial resolution of 2.5º x 2.5º with 31 vertical layers up to the 10-hPa pressure level. Six-hourly meteorological fields from the European Centre for Medium Range Weather Forecast (ECMWF) operational data are employed. These fields include global distributions for horizontal wind, surface pressure, temperature, humidity, liquid and ice water content, cloud cover and precipitation. Key processes included are mass-conserved tracer advection, convective tracer transport, boundary-layer diffusion, photolysis, dry and wet deposition as well as tropospheric chemistry including non-methane hydrocarbons to account for chemical loss by reaction with OH (*Houweling et al.*, 1998). Methane emissions closely follow (*Houweling et al.*, 2000) (see also Figures 4.4, Table 4.1). Other emission distributions are based on the inventories from EDGAR (Emission Database for Global Atmospheric Research) (*Van Aardenne et al.*, 2001). $\mathsf{CH_4}$ concentrations at the highest model level are nudged to the monthly-mean zonal HALOE/CLAES climatology from UARS (Upper Atmosphere Research Satellite; $\mathsf{CH_4}$ climatology: http://haloedata.larc.nasa.gov.

4.6.2 Supporting Text

To examine the discrepancy between model and measurements over the tropical rainforest, we analyzed several possible influencing factors. The first possibility, a systematic error in the measured ratios, can be excluded. No correlation of the retrieval with albedo was found. Further, a possible retrieval bias dependent on solar zenith angle would lead to a strictly latitudinal dependence, whereas Fig. 4.3b shows considerable longitudinal variability in the tropics. Strong aerosol loading have also proven not to influence the ratio: Even in the presence of dust storms over the Sahara with very coarse aerosols that alter the light path also in the near infrared substantially, we found exactly the same light-path change (indicated by a change in the retrieved column) for both retrievals. This is mainly because the phase function and the optical density of the aerosols do not differ much between the two retrieval windows. Furthermore, both $\mathsf{CH_4}$ and $\mathsf{CO_2}$ exhibit similar optical densities, causing similar path-lengths even if aerosol scattering leads to a light-path distribution that depends on the optical density itself.

The second possibility, a systematic error in the model, can also be excluded. An underestimation of stratospheric methane concentrations would also result in a bias that mainly varies with latitude. Although most of the destruction of methane by OH radicals takes place in the tropical troposphere, a bias in the OH field (*Lawrence et al.*, 2001), possibly caused by strong emissions of non-methane hydrocarbons from the tropical rainforest in the dry season (*Kesselmeier et al.*, 2002), cannot explain the discrepancy either: A model simulation in which all OH over the tropical rainforest was removed caused an increase in methane concentrations of 0.7% at most, showing that an error in OH could explain only a very small fraction of the discrepancy.

4.6.3 Supporting Figures/Tables

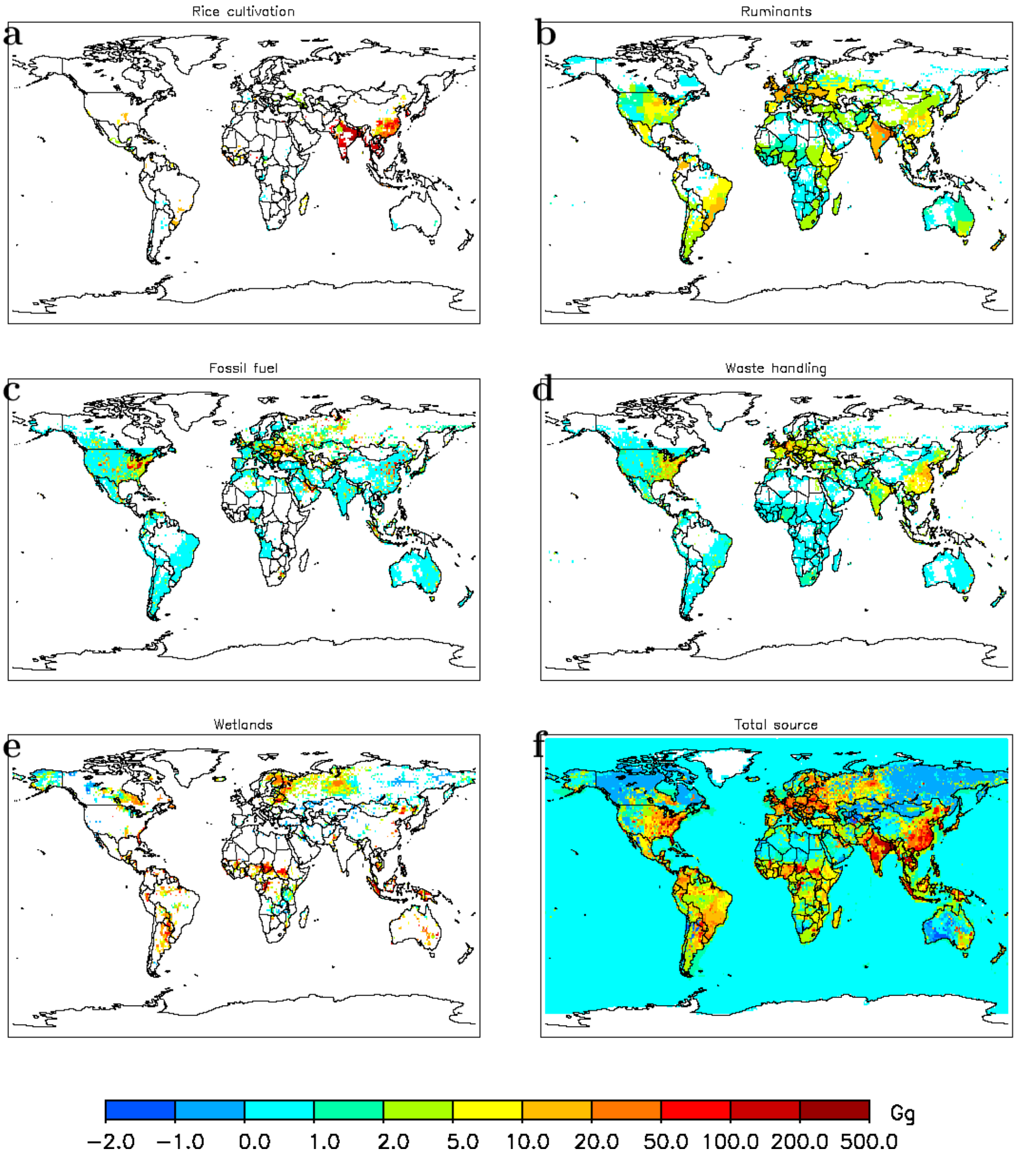

Figure 4.4: Spatial distributions of the main methane sources as used in the TM3 model run (brackets contain the total strengths - in Tg CH_4 - from August through November, and over the whole year, respectively): (a) rice cultivation (42, 80), (b) ruminants (31, 93), (c) fossil-fuel production and transmission (30, 89), (d) waste handling (22, 65), (e) wetlands (48, 145), and (f) total source (192, 540). The emissions have been summed over the period August through November, and are shown on a 1°x1°- grid in units of Gg CH_4 per grid cell.

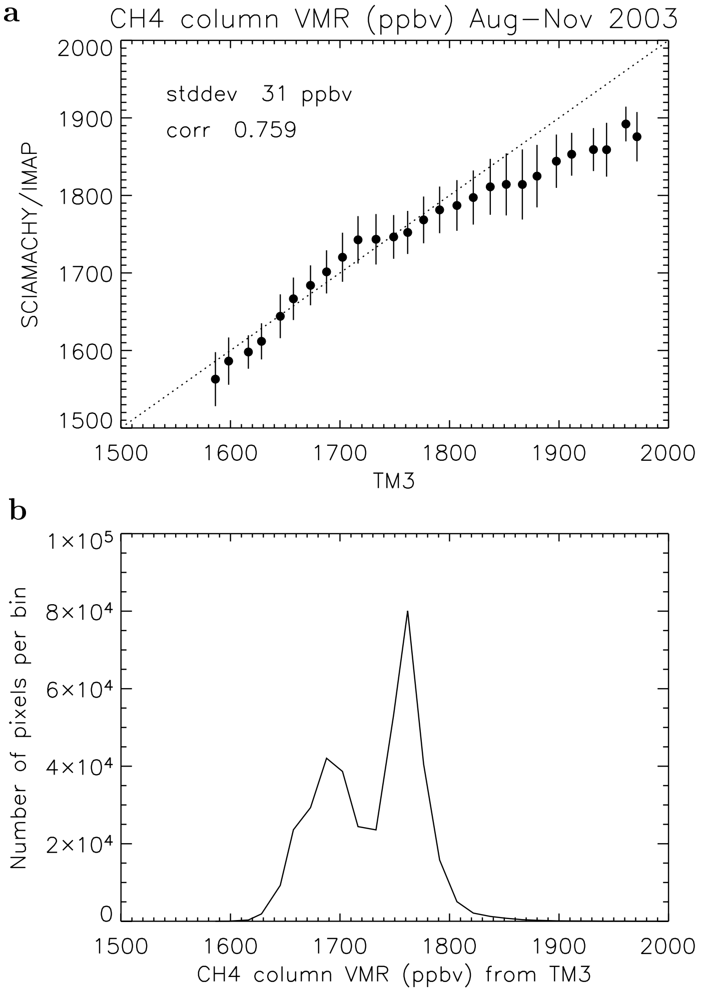

Figure 4.5: Panel (a): Comparison of measured and modelled column-averaged VMR. The TM3 data have been averaged over bins of 15 ppbv. Corresponding SCIAMACHY averages over these bins are shown together with the ±1-sigma spread within each bin. The dotted line corresponds to the unit gradient line. Values of the standard deviation of the measurement-model difference, and of the linear (Pearson) correlation coefficient are given in the plot. The agreement between measurement and model is generally very good. In particular, the spread of measured concentrations relative to modelled ones is small (below 2%). Note that the relatively large mismatch at the highest concentrations represents only a small number of pixels (10-1000 for the highest 10 bins). However, there appear to be two clear explanations for this discrepancy. First, the extreme model values are all sampled in South-East Asia, where the model presumably has a high bias due to an overestimation of the rice emissions. Second, the satellite pixel can contain some clouds, so that a fraction of the methane in the boundary layer may be shielded. This effect is largest when there is a lot of boundary-layer methane, i.e. in regions with large sources. Panel (b): Number of pixels per VMR−bin.

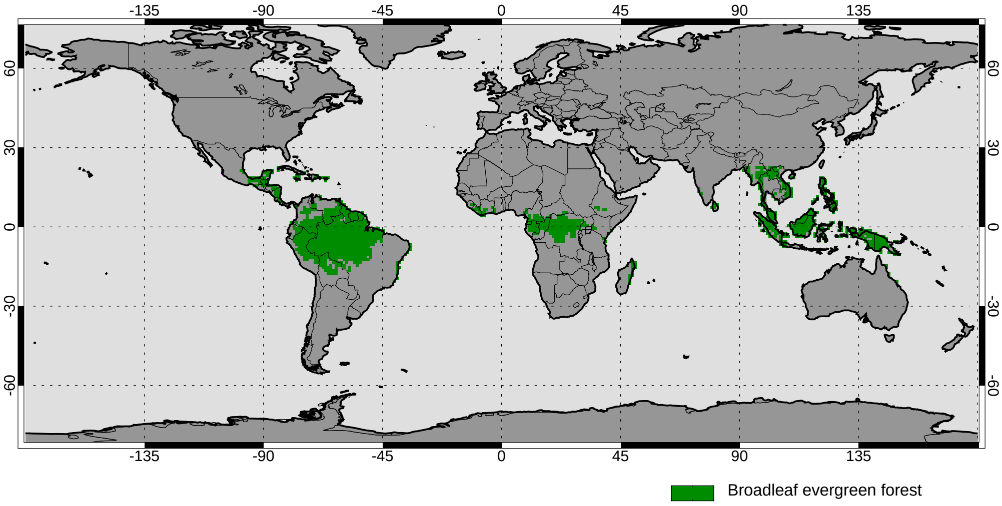

Figure 4.6: Broadleaf evergreen forest is indicated in green (22)

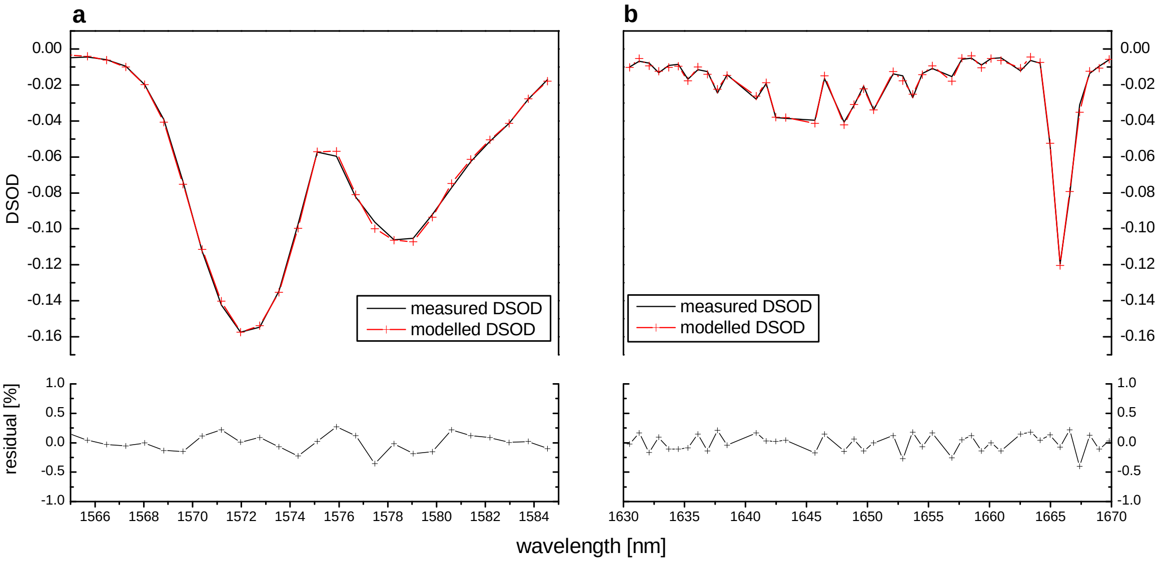

Figure 4.7: Typical modelled and measured differential slant optical densities (DSOD) in the CO_2 (a) and CH_4 (b) fit windows are shown here. In panel (a), CO_2 contributes most to the depicted total DSOD, while there are also faint absorptions by water vapour. In panel (b), absorptions by CO_2 and H2O marginally add to the strong CH_4 signal. In both panels, all species are fitted simultaneously and make up the total DSOD using a gaussian slit function with 1.35 nm full width at half maximum.

Table 4.1: Methane emissions (Tg CH_4) per source category as used in the TM3 model for the period August through November 2003 and for the whole year (between brackets). The sources are given for six different regions: the whole globe, the tropics (15°S - 15°N), tropical Africa (30°W-65°E), tropical Indonesia (90°E-180°E), tropical South-America (180°W-30°W), and the Amazon basin (here taken as the area 15°S-4°N and 76°W-50°W).

Category	**Globe**	**Tropics**	**Trop. Africa**	**Trop. Indon.**	**Trop. S-Amer.**	**Amazon**
Fossil fuel production	29.8 (89.3)	1.3 (3.8)	0.2 (0.6)	0.7 (2.1)	0.4 (1.1)	0.0 (0.0)
Ruminants	31.1 (93.0)	5.2 (15.5)	2.2 (6.5)	0.6 (1.7)	2.0 (5.9)	0.3 (1.0)
Rice cultivation	41.5 (80.0)	5.9 (15.8)	0.7 (1.8)	3.7 (11.0)	0.3 (0.8)	0.0 (0.1)
Waste handling	21.7 (64.9)	1.6 (4.7)	0.5 (1.4)	0.5 (1.4)	0.5 (1.4)	0.0 (0.1)
Biomass burning	8.4 (29.0)	5.3 (16.7)	1.7 (7.9)	0.9 (2.2)	2.7 (6.5)	1.9 (3.6)
Biofuel burning	6.7 (20.0)	2.2 (6.6)	1.0 (3.1)	0.7 (2.1)	0.2 (0.7)	0.0 (0.1)
Other anthropogenic	1.7 (5.2)	0.0 (0.1)	0.0 (0.0)	0.0 (0.0)	0.0 (0.1)	0.0 (0.0)
Wetlands	47.7 (145.1)	23.5 (68.5)	12.0 (28.7)	7.1 (25.1)	4.3 (14.6)	1.9 (7.7)
Termites	6.7 (20.0)	4.2 (12.5)	2.1 (6.4)	0.5 (1.4)	1.5 (4.6)	0.9 (2.8)
Other natural	7.9 (23.5)	2.3 (6.8)	0.4 (1.2)	1.1 (3.2)	0.7 (2.2)	0.1 (0.3)
Soil sink	-11.0 (-30.0)	-3.5 (-10.1)	-1.9 (-5.5)	-0.4 (-1.3)	-1.2 (-3.2)	-0.6 (-1.5)
Total	192.2 (540.0)	47.8 (140.9)	18.9 (52.2)	15.3 (48.9)	11.5 (34.6)	4.6 (14.2)

Satellite chartography of atmospheric methane from SCIAMACHY onboard ENVISAT: Analysis of the years 2003 and 2004

C. Frankenberg[1], J.F. Meirink[2], P. Bergamaschi[3], A.P.H. Goede[2], M. Heimann[4], S. Körner[4], U. Platt[1], M. van Weele[2], and T. Wagner[1]

[1]Institute of Environmental Physics, University of Heidelberg, INF 229, 69120 Heidelberg, Germany

[2]Royal Netherlands Meteorological Institute, Section of Atmospheric Composition, P.O.Box 201, 3730 AE De Bilt, The Netherlands

[3]European Commission Joint Research Centre, Ispra, Italy

[4]Max Planck Institute for Biogeochemistry (MPI-BGC), Jena, Germany

Journal:	Journal of Geophysical Research
Status:	Submitted: 26 May 2005
	Revised: 14 September 2005

Chapter 5

Satellite chartography of atmospheric methane from SCIAMACHY onboard ENVISAT: Analysis of the years 2003 and 2004

C. Frankenberg, J.F. Meirink, P. Bergamaschi, A.P.H. Goede, M. Heimann, S. Körner, U. Platt, M. van Weele, and T. Wagner

The UV/Vis/near infrared spectrometer SCIAMACHY onboard the European ENVISAT satellite enables total column retrieval of atmospheric methane with high sensitivity to the lower troposphere. The vertical column density of methane is converted to column averaged mixing ratio by using carbon dioxide retrievals as proxy for the probed atmospheric column. For this purpose, we apply concurrent total column measurements of CO_2 in combination with modeled column-averaged CO_2 mixing ratios. Possible systematic errors are discussed in detail while the precision error is 1.8% on average. This paper focuses on methane retrievals from January 2003 through December 2004. The measurements with global coverage over continents are compared with model results from the chemistry–transport model TM4. In the retrievals, the north-south gradient as well as regions with enhanced methane levels can be clearly identified. The highest abundances are found in the Red Basin of China, followed by northern South America, the Gangetic plains of India and central parts of Africa. Especially the abundances in northern South America and the Red Basin are generally higher than modeled. Further, we present the seasonal variations within the investigated time period. Peak values in Asia due to rice emissions are observed from August through October. We expand earlier investigations that suggest underestimated emissions in the tropics. It is shown that these underestimations show a seasonal behavior that peaks from August through December. The global measurements may be used for inverse modeling and are thus an important step towards better quantification of the methane budget.

5.1 Introduction

Methane (CH_4) is, after carbon dioxide, the second most important anthropogenic greenhouse gas, contributing directly 0.48 W m^{-2} to the total anthropogenic radiative forcing of 2.43 W m^{-2} by well-mixed greenhouse gases (*IPCC*, 2001, and references therein). In addition, it exhibits an indirect effect of about 0.13 W m^{-2} through formation of other greenhouse gases, most notably tropospheric ozone and stratospheric water vapor (*Lelieveld et al.*, 1998). In contrast to these abundance based radiative forcing estimates, *Shindell et al.* (2005) calculated the overall forcing based on emissions, thereby accounting for all indirect effects. From the emissions-based viewpoint, they conclude that the impact of anthropogenic methane on radiative forcing is larger than previously estimated, namely about 0.8 W m^{-2}.

Since the beginning of industrialization, methane abundances in the atmosphere have more than doubled (*Etheridge et al.*, 1998) albeit with decreasing growth rate (*Dlugokencky et al.*, 1998) during the past two decades and considerable inter-annual variations (*Dlugokencky et al.*, 2001). Furthermore, there is evidence that natural methane emissions have a positive feedback from rising temperatures (*Worthy et al.*, 2000; *Gedney et al.*, 2004; *Shindell et al.*, 2004), leading to expectations of a further increase in methane abundances. Reduction of methane emissions could at present be a cost-effective and feasible strategy for reducing positive radiative forcing (*Hansen et al.*, 2000; *Hansen and Sato*, 2004). Hence, better knowledge of methane distribution and emissions is indispensable for a correct assessment of its impact on climate as well as on the chemical composition of the atmosphere (*Dentener et al.*, 2005) through, e.g., a reduction of the OH radical concentrations at higher methane abundances. Also the Kyoto protocol calls for an independent global quantification and monitoring of emissions (*IPCC*, 2000; *Bergamaschi et al.*, 2004). According to current emission inventories, approximately 70% of global methane emissions are anthropogenic (*Lelieveld et al.*, 1998). The largest contributors are fossil fuel production, ruminants, waste handling and rice cultivation (*Olivier and Berdowski*, 2001). Wetlands constitute the most important natural source.

Although the global annual source strength of methane (550 ± 50 Tg yr^{-1}) is comparatively well constrained, considerable uncertainties still exist in regard to the partitioning amongst sources and their spatial and temporal distribution. "Bottom-up" approaches use local flux measurements and statistical data for upscaling to global totals. This upscaling, however, may inherit large uncertainties, especially for sources with large spatial or temporal variability (e.g. CH_4 from wetlands). In contrast, "top-down" approaches use atmospheric measurements and inverse atmospheric models in order to derive estimates of sources (and sinks) (*Hein et al.*, 1997; *Houweling et al.*, 1999; *Bergamaschi et al.*, 2000; *Fletcher et al.*, 2004b; *Dentener et al.*, 2003; *Chen*, 2003; *Butler et al.*, 2004; *Fletcher et al.*, 2004a; *Bergamaschi et al.*, 2005b). A major limitation of present top-down estimates is the limited number of atmospheric observation sites. Hence, additional a priori information from bottom-up estimates is usually required in order to overcome the underdetermination of the inverse problem. As a consequence, large uncertainties still exist, especially for regions ill-sampled by the current atmospheric network, e.g. large parts of the tropics (see, for instance, the Climate Monitoring and Diagnostics Laboratory (CMDL) of the US. National Oceanic & Atmospheric Administration (NOAA): http://www.cmdl.noaa.gov/).

Satellites offer the unique possibility of sensing methane globally, retrieving methane abundances in remote areas where ground based measurements might be complicated or even impossible due to infrastructural or political obstacles. The atmospheric lifetime of methane, mainly determined by oxidation due to OH radicals, is relatively long, viz. about 8 years (*IPCC*, 2001; *Lelieveld et al.*, 1998). Consequently, methane is well mixed and its variations in time and space are rather small, demanding unprecedented precision (1-2%) for space based total column retrievals that can be employed in top-down inversions. Methane columns have been measured from space by the IMG instrument on board ADEOS (*Clerbaux et al.*, 2003) and, more recently, by the SCIAMACHY instrument on board ENVISAT (*Buchwitz et al.*, 2005a; *Frankenberg et al.*, 2005c; *Buchwitz et al.*, 2005b). The IMG measurements were made by mid-infrared emission spectroscopy, being sensitive to methane in the free troposphere but suffering a substantially reduced sensitivity near the Earth's surface. SCIAMACHY retrievals are based on absorption spectra of solar radiation in the near-infrared. The recorded photons have traversed the entire atmospheric column twice, thereby exhibiting high sensitivity, including toward the surface. In the future, both measurement types could be combined synergistically.

Frankenberg et al. (2005c) presented methane column retrievals from SCIAMACHY for the period August-November 2003, reporting a good overall agreement of these retrievals with model simulations. However, substantial differences were found over large parts of the continental tropics, which were attributed to an underestimation of tropical methane emissions in the model.

In this work, we extend the analysis in *Frankenberg et al.* (2005c) by presenting methane retrievals for the entire years 2003 and 2004. Possible systematic errors and retrieval precision are discussed in detail. Further, considerable improvements in the retrieval and in computing a modeled column averaged mixing ratio that is directly comparable to SCIAMACHY retrievals have been elaborated.

5.2 The SCIAMACHY instrument

SCIAMACHY (SCanning Imaging Absorption spectroMeter for Atmospheric CHartographY) (*Bovensmann et al.*, 1999) onboard the European Space Agency's environmental research satellite ENVISAT consists of 8 individual grating spectrometer channels (1 through 8) measuring in the ultraviolet, visible and near infrared wavelength regions (240 nm–2380 nm) of the solar spectrum. The satellite operates in a near polar, sun-synchronous orbit at an altitude of 800 km with a local equator crossing time of approximately 10:00 am. The instrument alternates between limb and nadir modes of measurement. In the latter mode, a swath of 960 km gives full global coverage every six days (14 orbits per day). The typical ground pixel size of SCIAMACHY is 30 km (along-track, i.e. approximately north-south) times 60 to 120 km (across-track, i.e. approx. east-west). SCIAMACHY is an advanced successor of GOME (Global Ozone Monitoring Experiment) onboard ERS-2, the smaller footprint being one of its major improvements. Both GOME and SCIAMACHY are equipped with UV/Vis spectrometers, enabling global detection of NO_2, BrO, $OClO$, H_2O, SO_2, O_3, CH_2O, O_2 and O_4 as well as providing information on clouds and aerosols (*Burrows et al.*, 1999; *Wagner et al.*, 2002).

In addition to GOME, SCIAMACHY features three near infrared spectrometers (ch. 6: 1000-

1750 nm, ch. 7: 1940-2040 nm, and ch. 8: 2265-2380 nm) that enable global measurements of total columns of CH_4, CO_2, N_2O and CO by means of differential optical absorption spectroscopy (DOAS) (*Platt*, 1994). First results from these near infrared channels are now available from two other groups (*Buchwitz et al.*, 2004, 2005a; *Gloudemans et al.*, 2004, 2005; *Buchwitz et al.*, 2005b), using different retrieval algorithms to retrieve methane column densities from channel 8 of SCIAMACHY. Following *Frankenberg et al.* (2005c), we only used spectra from channel 6 to avoid problems due to an ice layer on the detectors of channels 7 and 8 (*Gloudemans et al.*, 2005). In addition, channel 6 exhibits a better signal-to-noise ratio and spatial resolution (60x30 km compared to 120x30 km in channel 8) than the other near infrared channels. The only major drawback is the lower spectral resolution (FWHM approx. 1.35 nm) compared to channels 7 and 8 (FWHM approx. 0.24 nm).

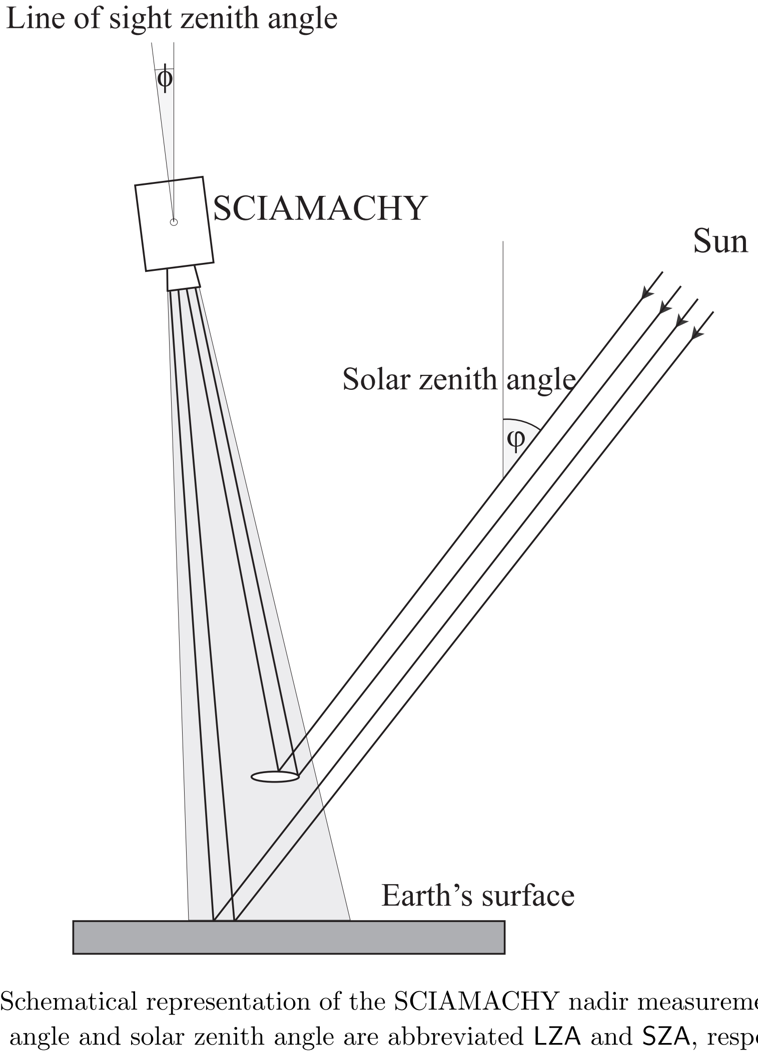

Figure 5.1: Schematical representation of the SCIAMACHY nadir measurement geometry. Line of sight zenith angle and solar zenith angle are abbreviated LZA and SZA, respectively.

Figure 5.1 illustrates the SCIAMACHY measurement geometry in the nadir mode. Line of sight zenith angles (LZA) are off-nadir by up to 30°. In addition to these earthshine radiance measurements, direct solar irradiance measurements are performed each day.

5.3 Retrieval methods

5.3.1 Retrieval of vertical column densities

We applied the iterative maximum a posteriori (IMAP) DOAS algorithm (*Frankenberg et al.*, 2005a) to retrieve vertical column densities (VCD or simply V, concentration integrated vertically from the surface to the top of atmosphere) of CH_4 and CO_2. A simplified radiative transfer scheme that ignores scattering is used to model a spectra that SCIAMACHY would measure given the a priori abundances of all absorbers. In our case we model optical densities, i.e. the negative logarithm of the ratio of the nadir radiance and the solar irradiance spectra. The algorithm basically performs a non-linear constrained least squares fit (based on the Optimal Estimation approach introduced by *Rodgers* (1976)), directly iterating a low order polynomial and the vertical column densities of the absorbers of interest until the modeled total optical densities fit the measurement.

The algorithm and an extensive sensitivity analysis are described in detail in *Frankenberg et al.* (2005a). A retrieval simulation was performed to study various effects with potential impact on the retrieval, for instance pressure and temperature variations in the atmosphere. These errors were shown to be mostly below 1%.

The algorithm has been successfully applied to retrieve carbon monoxide (*Frankenberg et al.*, 2005b) and methane (*Frankenberg et al.*, 2005c). In contrast to previous methane retrievals (*Frankenberg et al.*, 2005c), we use the latest edition of HITRAN (**hi**gh-resolution **tran**smission molecular absorption database, *Rothman et al.* (2005)) for the calculation of reference spectra. It comprises substantial updates especially for CO_2 lines residing in the fitting window applied in this study.

Further fit parameters employed for the retrieval of the dataset presented in this study are summarized in Table 5.1. Although we perform a total column retrieval, the vertical column densities of CH_4 and CO_2 are divided into three separate layers, where the upper two layers (from 3-12 km and 12-120 km) are tightly constrained via the a priori covariance matrix (see *Rodgers* (2000) for details). Only the constraints for the lowermost layer are noncommittal. Since the information content of the measurements is too low to retrieve different height layers independently, tight constraints for all but one layer are needed to avoid numerical instabilities.

The retrieved total column, i.e. the sum of the vertical columns of all height layers, is still sensitive to variations in higher atmospheric layers but treats them as if they occurred in the lowest layer. This has important implications for the sensitivity of the retrieval with respect to concentration changes in different height layers. In our application, the averaging kernel is defined as the sensitivity of the total column retrieval to concentration perturbations with respect to the a priori at different height layers. Given the true changes in each height layer, the vertical column as retrieved by SCIAMACHY can be approximated by:

$$\hat{V} = V_a + \sum_i A^i \cdot (V^i - V_a^i)\,, \tag{5.1}$$

where

$\hat{V}$ = retrieved total VCD
V_a = a priori total VCD
V^i = true VCD of height layer i
V_a^i = a priori VCD of height layer i
A^i = averaging kernel of height layer i.

For weak absorbers, radiative transfer alone determines the averaging kernels; Thus, they should be equal at all heights if scattering is neglected. For strong absorbers such as CH_4 and CO_2, the sensitivity also depends on the shape of the individual absorption lines and thereby, due to pressure broadening, also on height (*Frankenberg et al.*, 2005a). This implies that the averaging kernels depend on the choice of the state vector (vector containing the quantities to be retrieved, see *Rodgers* (2000) and *Frankenberg et al.* (2005a)).

Figure 5.2 shows the averaging kernels for our CH_4 and CO_2 retrievals. Since the a priori covariance is noncommittal only for the lowest atmospheric layer, averaging kernels are close to unity in this layer. Thus, perturbations in this height layer are reproduced accurately and,

Table 5.1: Fit parameters as used for the CH_4 and CO_2 retrieval

Fit parameter	height layer [km]	a priori	a priori σ [a]
		CH_4 fit[b]	
CH_4 (I)	0-3	$1.127 \cdot 10^{19}$ [molec/cm^2]	$1.127 \cdot 10^{19}$ [molec/cm^2]
CH_4 (II)	3-12	$1.83 \cdot 10^{19}$ [molec/cm^2]	$1.83 \cdot 10^{15}$ [molec/cm^2]
CH_4 (III)	12-120	$5.98 \cdot 10^{18}$ [molec/cm^2]	$5.98 \cdot 10^{14}$ [molec/cm^2]
CH_4 climatology[c]	0-120	0 [-]	5 [-]
H_2O	0-120	$4.773 \cdot 10^{22}$ [molec/cm^2]	$4.773 \cdot 10^{22}$ [molec/cm^2]
H_2O climatology[c]	0-120	0 [-]	5 [-]
CO_2	0-120	$7.98 \cdot 10^{21}$ [molec/cm^2]	$7.98 \cdot 10^{21}$ [molec/cm^2]
CO_2 climatology[c]	0-120	0 [-]	5 [-]
		CO_2 fit[d]	
CO_2 (I)	0-3	$2.453 \cdot 10^{21}$ [molec/cm^2]	$2.453 \cdot 10^{21}$ [molec/cm^2]
CO_2 (II)	3-12	$3.995 \cdot 10^{21}$ [molec/cm^2]	$3.995 \cdot 10^{17}$ [molec/cm^2]
CO_2 (III)	12-120	$1.534 \cdot 10^{21}$ [molec/cm^2]	$1.534 \cdot 10^{17}$ [molec/cm^2]
CO_2 climatology[c]	0-120	0 [-]	5 [-]
H_2O	0-120	$4.773 \cdot 10^{22}$ [molec/cm^2]	$4.773 \cdot 10^{22}$ [molec/cm^2]
H_2O climatology[c]	0-120	0 [-]	5 [-]

---

[a] σ as given in the a priori covariance matrix, assuming zero off-diagonal elements (*Rodgers*, 2000; *Frankenberg et al.*, 2005a).

[b] fit window: 1630.5-1669.9 nm; 2 iterations; Slit function: Gaussian, 1.35 nm FWHM; degree of polynomial: 2

[c] as climatological fit parameter the difference between the US standard atmosphere and a midlatitude winter atmosphere was taken. For details concerning the implementation see *Frankenberg et al.* (2005a)

[d] fit window: 1562.6-1584.6 nm; 2 iterations; Slit function: Gaussian, 1.35 nm FWHM; degree of polynomial: 2

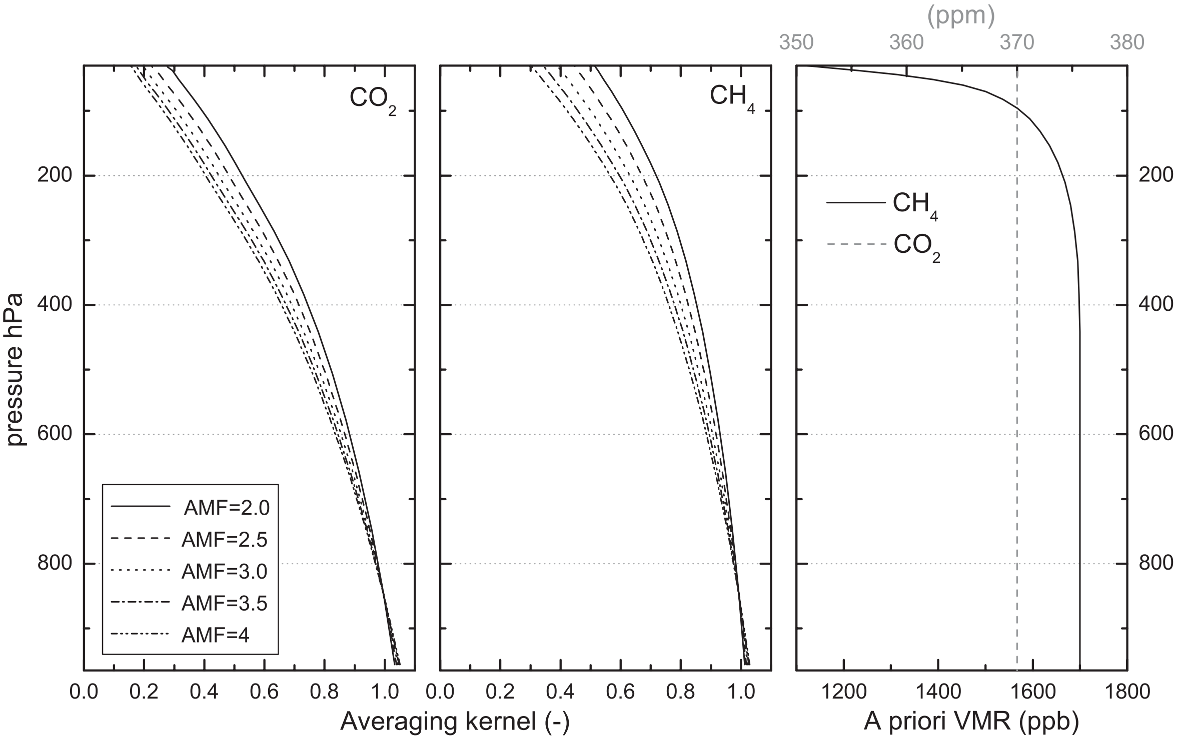

Figure 5.2: Averaging kernels of the IMAP DOAS retrieval of CH_4 and CO_2 for different air-mass factors ($\approx 1/\cos(\mathsf{LZA})+1/\cos(\mathsf{SZA})$). The right panel shows the corresponding a priori profiles for which the averaging kernels have been computed (profiles from US standard atmosphere provided by *Kneizys et al.* (1996)).

most importantly, with equal sensitivity to both species. Deviations from the a priori in higher atmospheric layers are still retrieved, albeit with less sensitivity.

5.3.2 Converting vertical column densities to column averaged mixing ratios

If vertical column densities are to be converted to column averaged mixing ratios, we need to know the probed total atmospheric column, which, in turn, depends on pressure and light path distribution. One of the main advantages of the near infrared spectral regions is that Rayleigh scattering as well as thermal emissions can be safely ignored. In the absence of clouds and aerosols, we can thus exactly derive the path of the photons that constitute the measurement by simple geometric considerations of the measurement geometry, i.e. considering the line of sight zenith angle (LZA) and the solar zenith angle (SZA) (see Figure 5.1). In this simple case, we could directly convert vertical column densities to column averaged mixing ratios of CH_4 and CO_2 by scaling with the probed vertical column of all atmospheric constituents (strictly speaking without water vapor), a quantity that can be derived from surface pressure.

Aerosols and clouds (as apparent in Figure 5.1) in the field of view complicate the retrieval (*Buchwitz et al.*, 2000; *Buchwitz and Burrows*, 2003; *O'Brien and Rayner*, 2002; *Rayner et al.*, 2002) since they substantially alter the light path and thereby the probed total column. This renders a simple scaling by surface pressure insufficient. The deviations induced by these changes in the light path are generally not large in the near infrared but the precision requirements for a meaningful retrieval of CH_4 are so strict (1-2%) that these effects have to be considered. In typical conditions, the effect of aerosols is below 2% if the surface albedo exceeds 5% (*Buchwitz and Burrows*, 2003; *Houweling et al.*, 2005). In extreme cases, as in dust storms in the Sahara, which exhibit high optical densities even in the near infrared, the errors in the retrieved vertical columns are up to 10% and strongly depend on surface albedo (*Houweling et al.*, 2005). Partial cloud cover further complicates the retrieval since clouds shield the atmospheric layers underneath. Since SCIAMACHY has large footprints, most pixels are partially covered by clouds, and the majority of the measurements would be rejected if strict constraints on cloud coverage were imposed.

In order deal with aerosols and partial cloud cover, we have to apply a proxy for the total column of the probed atmosphere. This total vertical column of dry air (V_{air}) depends on both pressure and light path distribution. Using proxy X, V_{air} reads

$$V_{\mathsf{air}} = \frac{V(X)}{\overline{VMR}(X)}, \tag{5.2}$$

where $\overline{VMR}(X)$ denotes the column averaged mixing ratio and $V(X)$ the vertical column density of species X. Usually, spectroscopic O_2 or O_4 measurements are used as proxy (*Pfeilsticker et al.*, 1998b; *Wagner et al.*, 2003) as their averaged mixing ratios are precisely known and exhibit negligible variations. However, these species absorb in very different wavelength regions (e.g. O_2 : 760 nm) and are thus not directly representative for the light path distribution in the near infrared. In contrast, CO_2 is retrieved in a spectrally neighboring fitting window ensuring very similar light path distributions. In addition to the prerequisite of identical light paths, the sensitivity of the measurement to the species of interest and its proxy for the total air column has to be very similar at height levels where the largest deviations from the expected light path occur. The choice of the state vector as described above ensures nearly equal averaging kernels in the lowermost atmospheric layer. In terms of radiative transfer properties, CO_2 is thus an ideal proxy. A complication is that CO_2 exhibits variations in the column averaged mixing ratio, albeit generally below 3% (*Olsen and Randerson*, 2004a). In *Frankenberg et al.* (2005c), CO_2 retrievals were introduced as proxy for the probed column assuming a globally constant mixing ratio. Here we greatly improve this approach by considering modeled column averaged mixing ratios of carbon dioxide (see section 5.4.2) to diminish the systematic errors induced by variations in CO_2. The column averaged mixing ratio of methane is thus obtained by

$$\overline{VMR}(\mathsf{CH_4}) = \frac{V_{\mathsf{meas}}(\mathsf{CH_4})}{V_{\mathsf{meas}}(\mathsf{CO_2})} \cdot \overline{VMR}(\mathsf{CO_2}), \tag{5.3}$$

where $\overline{VMR}(CO_2)$ is the modeled column averaged mixing ratio of CO_2. Although the CO_2 model might not exactly represent the true value, the strongest variations, i.e. the seasonal cycle, are well reproduced.

The measurements exhibit a small positive bias compared to the model simulations. To facilitate the comparison, we scale $\overline{VMR}(CH_4)$ by a constant factor (0.982). In comparison to *Frankenberg et al.* (2005c), this factor changed due to updates in applied CO_2 line parameters.

5.3.3 Error analysis

The derived column averaged mixing ratio is affected by statistical errors in the retrieval of the column densities of methane and carbon dioxide, errors in the modeled $\mathsf{CO_2}$ column abundances and possible systematic differences in the light-path distribution between the two spectral fitting windows.

Precision error of the retrieval algorithm

The retrieved vertical columns exhibit a precision error in the least squares fit due to instrumental noise. The statistical fit error shows substantial variations since it strongly depends on the signal-to-noise ratio of the recorded spectra and thereby on surface albedo. On average, the standard deviation of this error term is about 1.5 and 1% for $\mathsf{CH_4}$ and $\mathsf{CO_2}$, respectively. Since both errors are uncorrelated, the relative uncertainty in the ratio reads

$$\sigma_{\mathsf{rel}}\left(\frac{V(\mathsf{CH_4})}{V(\mathsf{CO_2})}\right) = \sqrt{\sigma^2_{\mathsf{rel}}(V(\mathsf{CH_4})) + \sigma^2_{\mathsf{rel}}(V(\mathsf{CO_2}))}\,, \tag{5.4}$$

which is about 1.8% (corresponding to roughly 30 ppb) on average in our retrievals. We find typical standard deviations between modeled and measured column averaged mixing ratios of 30 ppb, being consistent with our uncertainty estimates.

As single retrievals are not very precise, we rely on spatial and temporal averages that are constituted by a preferably high number of retrievals. Averaging over N independent retrievals in space and/or time, the precision error in the mean ratio reads

$$\sigma_{\mathsf{rel}}\overline{\left(\frac{V(\mathsf{CH_4})}{V(\mathsf{CO_2})}\right)} = \sqrt{\frac{\overline{\sigma^2_{rel}\left(\frac{V(\mathsf{CH_4})}{V(\mathsf{CO_2})}\right)}}{N}}\,. \tag{5.5}$$

In the following, retrieval uncertainty refers to the estimated 1-σ-error in the averaged ratio (scaled with $\overline{VMR}(\mathsf{CO_2})$).

Errors in the modeled carbon dioxide column

Errors in the modeled $\mathsf{CO_2}$ column and differences in the light path affect the accuracy and are harder to quantify. However, errors in the modeled $\mathsf{CO_2}$ column can be assumed to be mostly well below 1%. Biomass burning events, for instance, lead to typical carbon monoxide column abundances of up to $4 \cdot 10^{18}$ molec/cm^2 in the seasonal average (*Bremer et al.*, 2004). Assuming an emission ratio of 1:10 for carbon monoxide, the total $\mathsf{CO_2}$ column would be enhanced by $4 \cdot 10^{19}$ molec/cm^2, which is only 0.5% of its background value of $8 \cdot 10^{21}$ molec/cm^2. Also strong diurnal $\mathsf{CO_2}$ variations near the ground perturb the total column by only 0.5% (*Olsen and Randerson*, 2004a). The strongest variations in the $\mathsf{CO_2}$ column due to uptake and release mechanisms of the biosphere show a seasonal dependence and are well reproduced by the model.

Errors due to differences in the light path distributions

Small differences might exist between the light path distribution of the CH_4 and CO_2 retrievals, which are spectrally about 80 nm apart. These difference can be induced by changes in surface albedo, cloud albedo or aerosol optical properties.

Clouds mostly shorten the light path. For cloud detection, we applied the approach of *Frankenberg et al.* (2005c), discarding measurements with an effective cloud top height (assuming that the entire ground pixel is homogeneously cloudy) of more than 1 km. Surface and cloud albedo determine which fractions of the recorded photons are scattered back from the earth's surface and cloud top, respectively (see Figure 5.1). If these albedos do not change between the spectral range of the two fitting windows (1563-1585 and 1631-1670 nm for CO_2 and CH_4, respectively), the light path distribution in both spectral ranges is identical. A problem arises if surface and/or cloud albedo change substantially in our wavelength range. First sensitivity studies suggest that, if cloud or surface albedo change by 25% in this spectral range, the bias could rise to ±3%, though it mostly lies between 0.5 and 2%. This potential bias increases if the cloud filter is less restrictive (e.g. allowing an effective cloud top height of 2 km) and is largest when high clouds are present.

A similar consideration holds for aerosols. We analyzed retrievals over the Sahara (here: 20-30° N/0-20° E) to quantify the effect of aerosols which was found to be much larger in this region (*Houweling et al.*, 2005) than elsewhere. The Sahara is ideally suited for retrieval since it is mostly cloud free, exhibits a high surface albedo in the near infrared and is devoid of local methane sources. For the Sahara, we found a standard deviation of less than 10 ppb in modeled methane column abundances from January 2003 through December 2004. To analyze the effect of aerosols, we applied two approaches to convert retrieved vertical columns to column averaged mixing ratios: In the first, we scaled with the total vertical column of air (estimated from surface pressure) and in the second approach, we used concurrent CO_2 retrievals as a proxy for the probed column.

Figure 5.3 shows a histogram of the retrieved column averaged mixing ratios over the entire time period (2003-2004) using the two different approaches. It is obvious that the variations obtained using surface pressure are much larger than those obtained using CO_2 as a proxy. Also, the shape of the distribution is substantially different for both methods; using surface pressure, the distribution is not Gaussian but exhibits high frequencies at the upper tail. While clouds mostly shorten the light path, *Houweling et al.* (2005) have shown that aerosols have disparate effects on the retrieval: Depending on surface albedo and aerosol types, the light path can as well be strongly enhanced (overestimated vertical columns) as also shortened. This effect is reflected in the retrieval distribution using a simple surface pressure scaling. Most of the spread in the simple scaling approach is attributable to aerosols, clouds and, to a smaller amount, also to variations in sea level pressure and water vapor concentrations, which have not been considered in this comparison.

The application of CO_2 as proxy reduces the standard deviation of the retrieved mixing ratios from 37 to 18 ppb and results in a Gaussian distribution. The effects of aerosols and clouds, uncertainties in surface pressure and water vapor column are largely eliminated. The lowest panel of Figure 5.3 depicts the time dependent, relative 1-σ spread of CO_2 and CH_4 VCDs scaled with surface pressure, respectively. Further, the relative spread in the ratio is shown.

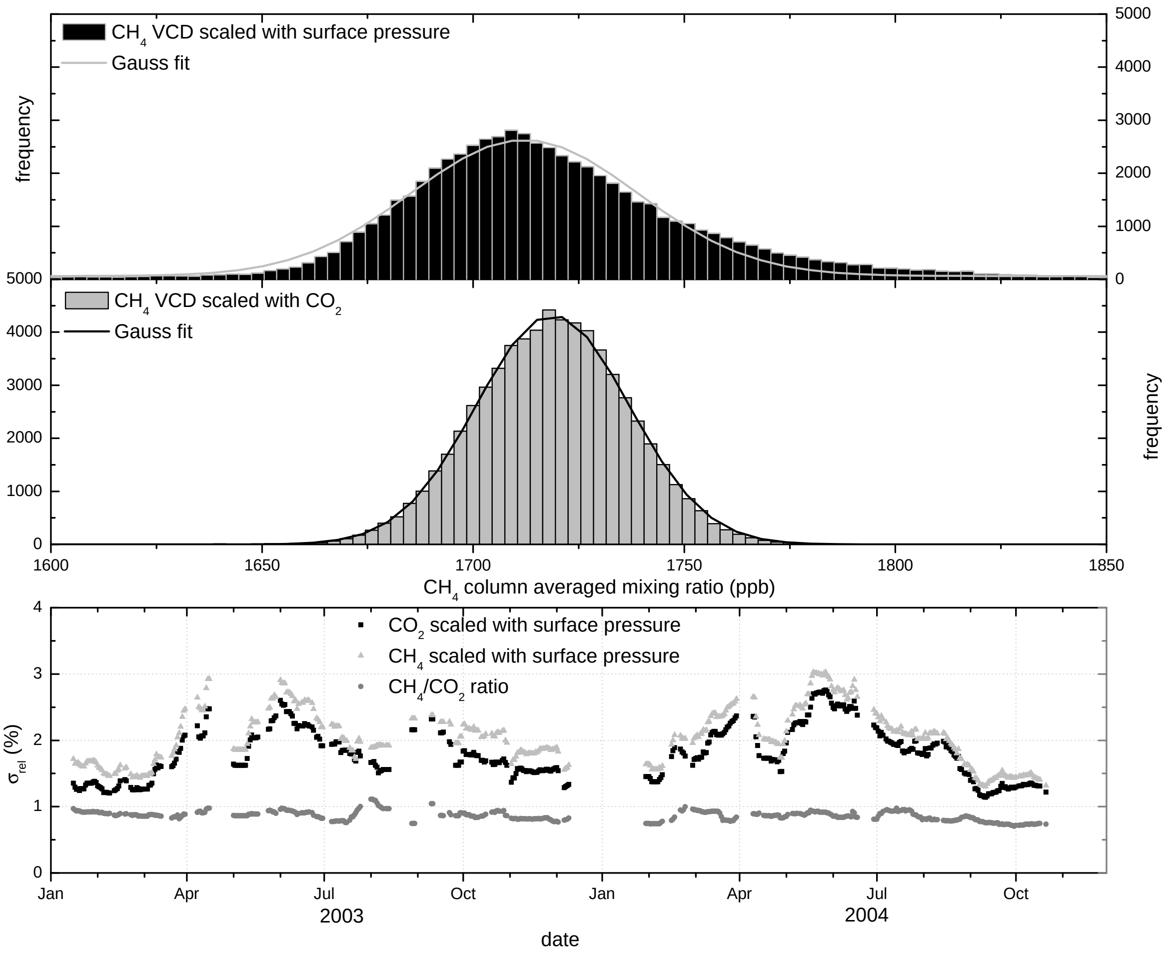

Figure 5.3: The effect of aerosols and clouds on SCIAMACHY retrievals over the Sahara. The upper panel shows histograms and corresponding Gaussian fits of CH_4 column-averaged concentrations over the Sahara (all retrievals from 2003 through 2004 within 20-30° N/0-20° E) derived by scaling the retrieved CH_4 VCD either by surface pressure (estimated from surface elevation, assuming a mean-sea-level pressure of 1013 hPa and an exponential pressure profile with a scale height of 8.5 km) or by the retrieved CO_2 VCD, equation (3). The lowest panel shows the standard deviation (relative in percent) of retrieved CO_2 and CH_4 VCDs scaled with surface pressure as a function of time. In addition, the relative standard deviation of the CH_4/CO_2 ratio is depicted. The same geographical area but a 30-day box filter has been used. This figure is based on all retrievals with an effective cloud-top height of less than 1 km (see text).

One can clearly see that the spread of the CH_4 and CO_2 retrievals scaled by surface pressure are correlated and exhibit substantial variations, most likely due to partial cloud cover and changes in the aerosol optical depth and height distribution (see *Houweling et al.* (2005) for a discussion on the influence of aerosols on SCIAMACHY CO_2 retrievals). The ratio of CH_4/CO_2, however, exhibits a low spread throughout the time period under consideration; The effect of aerosols is effectively neutralized in the ratio. Furthermore, the relative 1-σ spread (mostly about 0.9%) is consistent with our estimate of the retrieval precision, which is about 15 ppb over the Sahara due to the high surface albedo.

5.3.4 Outlook

Future space missions, such as the Orbiting Carbon Observatory (OCO, Jet Propulsion Laboratory, see *Crisp et al.* (2004)) or the Greenhouse gases Observing SATellite (GOSAT, Japan Aerospace Exploration Agency), will have far smaller ground pixel sizes for which the measurement scene can be considered to be more homogenous. This should largely resolve the problem of partial cloud cover. A substantially higher spectral resolution will yield both a higher measurement precision and additional information on aerosols. Hence, these instruments are expected to facilitate the use of proxies in wavelength regions that may be spectrally distant.

5.4 Atmospheric models

We use two atmospheric chemistry transport models to simulate total column abundances of methane and carbon dioxide.

5.4.1 Methane modeling with TM4

The model results presented in this paper are based on simulations with the global chemistry–transport model TM4, the successor of TM3 (*Dentener et al.*, 2003, and references therein). The model has a regular longitude–latitude spatial grid, and hybrid σ–pressure layers in the vertical. It is driven by six-hourly meteorological fields from the European Centre for Medium Range Weather Forecast (ECMWF) operational data. These fields include global distributions for horizontal wind, surface pressure, temperature, humidity, liquid and ice water content, cloud cover and precipitation. Key processes included are mass-conserved tracer advection, convective tracer transport, boundary-layer diffusion, photolysis, dry and wet deposition as well as tropospheric chemistry including non-methane hydrocarbons to account for chemical loss by reaction with OH (*Houweling et al.*, 1998). Except for methane, anthropogenic emissions are based on *Van Aardenne et al.* (2001), which in turn is based on the widely used EDGAR (Emission Database for Global Atmospheric Research) data base (*Olivier et al.*, 1999), while natural emissions are as in *Houweling et al.* (1998).

The model version employed here differs from *Dentener et al.* (2003) in a number of aspects:

- The spatial resolution is 3×2 degrees, with 25 vertical levels up to 0.1 hPa.
- A mass-conserving pre-processing of the meteorological input is applied according to *Bregman et al.* (2003).
- The stratospheric destruction of methane by reaction with OH, Cl and $O(^1D)$ is taken into account by applying correction factors to the model-calculated destruction rate based on a 2D-model (G. Velders, personal communication).
- Furthermore, CH_4 concentrations above 50 hPa are nudged to the monthly-mean zonal HALOE/CLAES climatology from UARS (*Randel et al.*, 1998).

- The emissions of methane are as described in Table 5.2. Modifications with respect to *Frankenberg et al.* (2005c) are: (1) EDGAR version 3.2 is used instead of 2.0; (2) biomass burning emissions are based on *Olivier et al.* (2003) instead of *Hao et al.* (1991); (3) emissions have been scaled to different global totals for a number of source categories, most notably total rice emissions have been reduced from 80 to 60 Tg yr^{-1}, in agreement with *Olivier et al.* (1999).

The model has been run for the period 2000 through 2004. The simulated methane burden is approximately in steady-state at 4850 Tg during this period, with a tropospheric (below 100 hPa) lifetime of around 9.4 years. Modeled concentrations are generally in good agreement with surface measurements from the NOAA-CMDL network (e.g., *Dlugokencky et al.*, 2003), although the interpolar difference is overestimated by around 30 ppb. So far, it is unclear whether these discrepancies are due to errors in transport, OH fields or emission inventories.

5.4.2 Carbon dioxide modeling with TM3 3.8

TM3-MPI 3.8 (*Heimann and Körner*, 2003) is a three-dimensional global atmospheric transport model for an arbitrary number of active or passive tracers. In this study, we use meteoro-

Table 5.2: CH_4 emissions applied in the TM model.

Source category	Reference	Emission (Tg CH_4 yr^{-1})
Anthropogenic		
Domestic ruminants	EDGAR[a]	89
Fossil fuel production	EDGAR[a]	87
Waste treatment	EDGAR[a,b]	73
Rice cultivation	*Matthews et al.* (1991)	60
Biomass burning	*Olivier et al.* (2003)[c]	35
Biofuel	EDGAR[a]	14
Minor sources	EDGAR[a]	5
Natural		
Wetlands	*Walter et al.* (2001)[d]	155
Termites	*Sanderson* (1996)	20
Ocean	*Houweling et al.* (1999)	15
Wild animals	*Houweling et al.* (1999)	5
Volcanoes	*Houweling et al.* (1999)	4
Soil sink	*Ridgwell et al.* (1999)	-30
Total		532

---

[a] EDGAR version 3.2, year 1995.

[b] landfills scaled to 40 Tg yr^{-1}.

[c] 5-year average of the period 1997–2001, with total forest burning scaled to 20 Tg yr^{-1} and savanna burning to 15 Tg yr^{-1}

[d] 15-year mean field.

logical reanalysis fields from the National Centre for Environmental Prediction (NCEP/DOE AMIP-II). The model was run with a resolution of 1.8°×1.8° and 28 height layers. The ocean as source or sink for atmospheric CO_2 was implemented according to *Takahashi et al.* (2002) using monthly mean fluxes without interannual variations. Anthropogenic emissions are derived from the EDGAR 3.2 database (*Olivier and Berdowski*, 2001) by temporal extrapolation of the annual mean fluxes of 1990 and 1995. Those mainly include agricultural activities and biomass burning. The CO_2 fluxes from the natural biosphere were modeled by the BIOME-BGC ecosystem model using the same temporally resolved meteorology as the atmospheric transport. The biosphere fluxes follow a diurnal cycle. To obtain realistic spatial gradients, the model was run over a spin-up time of 10 years with a coarser resolution, starting from a globally constant CO_2 mixing ratio. The years 2002 and 2003 were modeled with the final resolution.

Verification of the transport properties of the model was performed by *Heimann and Körner* (2003). Especially for CO_2, comparison of TM3 results with in-situ atmospheric measurements from various aircraft campaigns and ground based measurements shows that the model simulates realistic mixing ratio distributions not only at the surface but also in upper parts of the troposphere (Peylin et al., LSCE Paris, manuscript in preparation).

So far, only model results of the year 2003 were applied. These were also used for the correction of the seasonal CO_2 variations in 2004.

5.4.3 Comparing models with SCIAMACHY retrievals

The atmospheric models provide mixing ratios in different height layers. These can be converted to the vertical column of each height layer (V_i). In principle, the (mass weighted) column averaged mixing ratio of the model output could then be computed as the ratio of the sum of all vertical sub-columns of the trace gas species of interest to the total vertical column of all atmospheric constituents. For comparison of model output to SCIAMACHY measurements, this simple approach is no more valid as it does not take instrument sensitivity into account. The averaging kernels (Figure 5.2) show that perturbations, especially in higher atmospheric layers, are generally underestimated by the SCIAMACHY retrieval by up to 50%. In order to have a comparable modeled mixing ratio, the model output has to be converted to the column averaged mixing ratio that SCIAMACHY would measure if the model represented the exact methane profile. This conversion has been applied to the modeled methane abundances using equation 5.1, a considerable improvement to *Frankenberg et al.* (2005c) where the modeled column averaged mixing ratios were computed without taking instrument sensitivity into consideration.

The basic effect of this conversion is that perturbations in the model from the a priori sub-column are damped by the factor given in the averaging kernel at the respective height. Thus, the strongest effect of this conversion to SCIAMACHY sensitivity is to curb stratospheric methane variations. In most cases, tropical regions exhibit higher methane mixing ratios (compared to the a priori level) in the upper troposphere and lower stratosphere (UTLS), whereas polar regions show lower abundances (see stratospheric methane climatology from the HALOE instrument onboard the UARS satellite: http://haloedata.larc.nasa.gov/home/index.php). Adjusting column averaged mixing ratios derived from the model to SCIAMACHY sensitivity thus implies a reduction in the tropics and an increase in polar regions (compared with a simple computation of the modeled column averaged mixing ratios).

When interpreting the results presented in this study, care has to be taken not to confuse column averaged mixing ratios with tropospheric or even surface mixing ratios. Since methane is depleted in the stratosphere, the VMRs presented in this study are generally lower than pure tropospheric mixing ratios.

5.5 Results

We present the column averaged mixing ratios of methane as a 2-year average as well as seasonal averages.

5.5.1 2-year average maps of methane abundances

Figure 5.4a depicts the two-year average VMR of methane. A simple cloud filter discarding retrievals with an effective cloud top height of over 1 km was applied. The overall variations are rather small, most deviations from the global mean being well below 5%. The most striking feature is the clear north-south gradient caused by higher natural and anthropogenic methane emissions in the northern hemisphere. The entire Australian continent as well as southern parts of Africa and South America show very low methane abundances compared to the mid-latitudes. Moreover, there is little scatter on smaller scales, i.e. most pixels show a strong spatial correlation to surrounding areas. This is mostly due to the relatively long lifetime of methane, leading to extended areas of enhancement even for point sources. We restrict the long-term average plots to landmasses since a reasonable retrieval over the ocean requires either low lying clouds, sun glint or a very rough ocean surface to exhibit a sufficiently high albedo. Thus, long-term maps over the ocean would be strongly biased to certain seasons. In addition, the statistical uncertainties (1-σ) in the SCIAMACHY averages (as defined in section 5.3) are shown in Figure 5.4c. Higher uncertainties are mainly due to low sampling frequency or low surface albedo (e.g. parts of Russia and Canada as well as retrievals at coastlines). Figure 5.4b shows the corresponding TM4 model output. Both the north-south gradient and the main regions with enhancements predicted by the model are on the whole consistent with the measurements. In northern South America and central Africa, however, the retrievals reflect higher methane abundances than the model. As already mentioned, disparities in the light path due to high-frequency spectral structures in surface or cloud albedo are a possible source of bias. This bias would therefore also depend on the surface type and albedo. However, there is no indication for such behavior in the two-year average: The retrievals vary smoothly over different surface types.

Figure 5.5 depicts the same SCIAMACHY retrievals as in Figure 5.4a but with a less strict cloud filter (effective cloud top height below 2.5 km) and without discarding retrievals over the ocean. Thereby we achieve full global coverage. The north-south gradient can also be well observed over the ocean. Most methane abundances, surprisingly, are higher than in Figure 5.4a. However, the absolute values have to be interpreted with care because, as discussed in section 5.3, clouds are a potential source of bias, especially if no strict cloud filter is applied. At the continent-ocean border, the frequency of reasonable retrievals changes abruptly (less

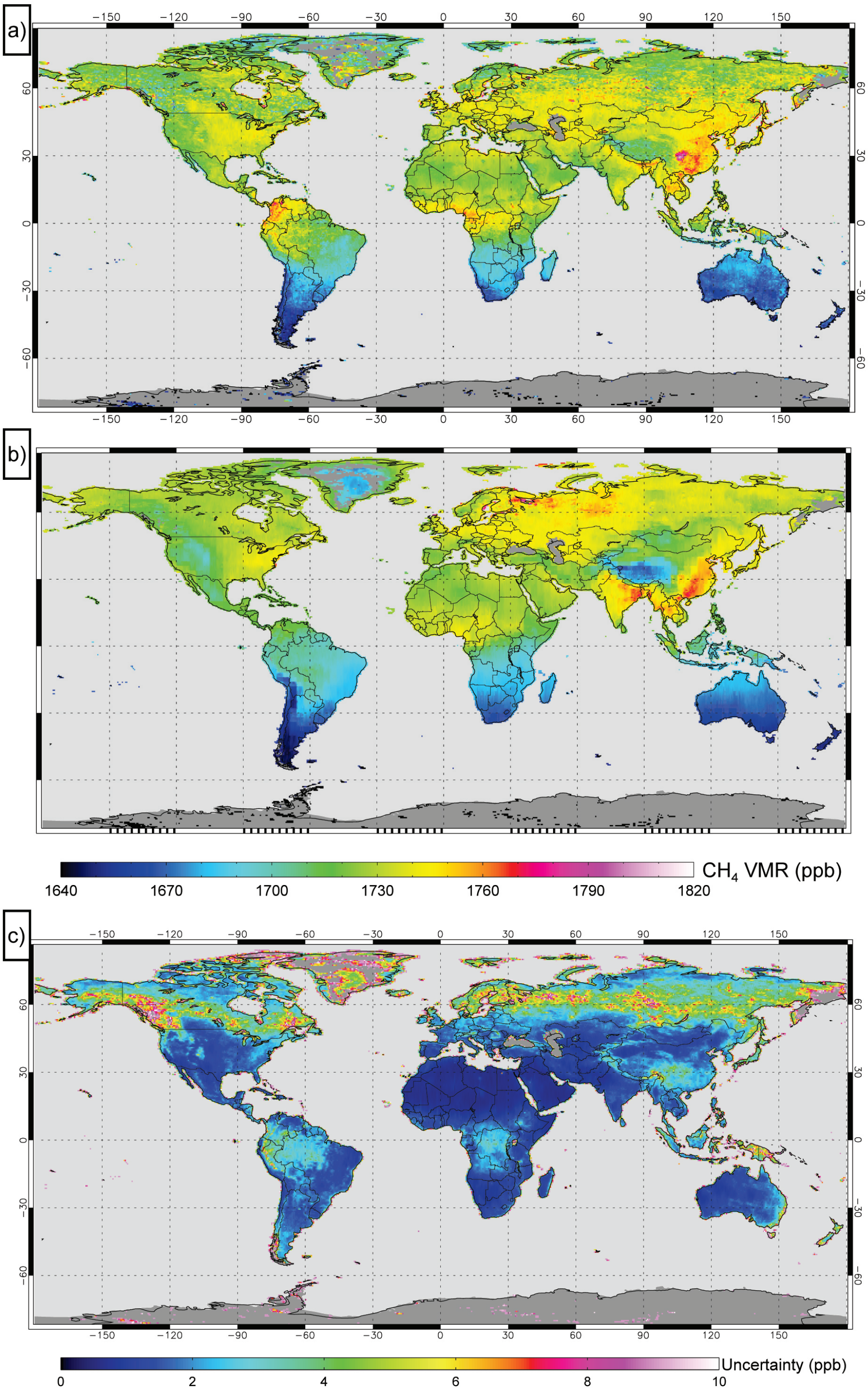

Figure 5.4: Panel a) shows the two-year average of column averaged mixing ratios (in ppb) of methane retrieved from SCIAMACHY from January 2003 through December 2004. The measurements have been gridded with a spatial resolution of 0.5° longitude times 0.5° latitude. Panel b) shows the corresponding (i.e. sampled at the exact place and time of the measurements) TM4 model results while panel c) depicts the estimated statistical uncertainty associated with the SCIAMACHY retrieval (see section 5.3.3 for details).

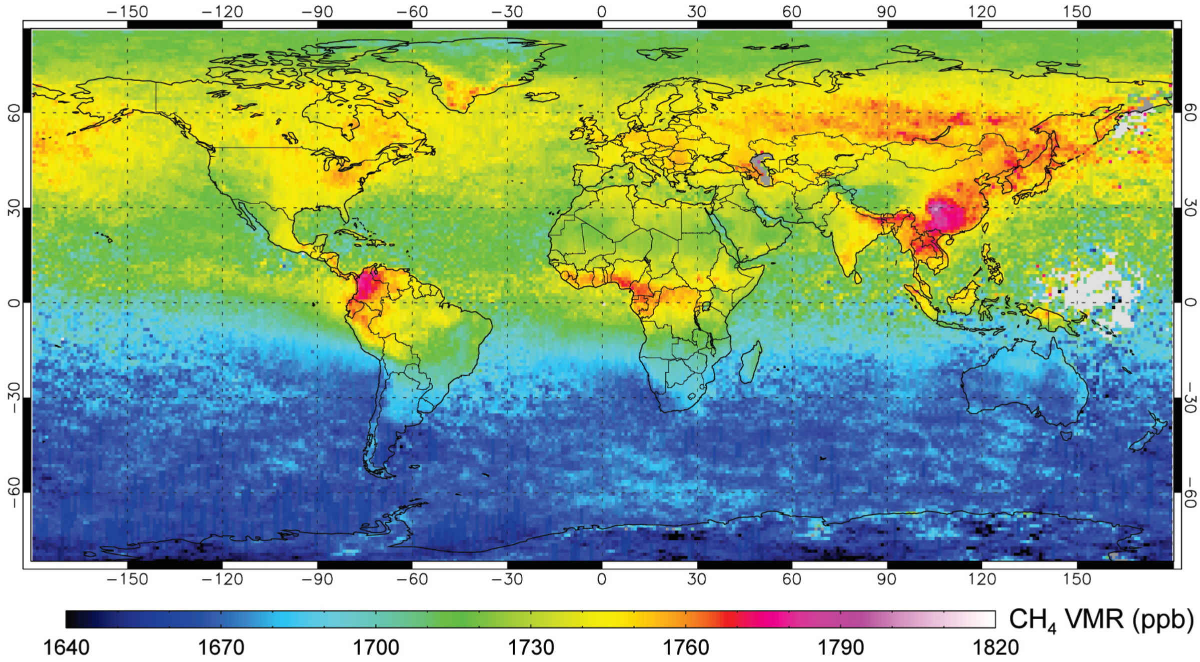

Figure 5.5: Two-year average of methane VMR as retrieved by SCIAMACHY with less strict cloud filter (effective cloud top height less than 2.5 km) and gridded on 1° longitude times 1° latitude.

reliable measurements over the ocean), often resulting in a rather steep gradient in the observed mean of methane abundances. We see that clouds do not always hinder a reasonable retrieval, contributing, on the contrary, to meaningful measurements if a suitable proxy for the light-path is applied. In the future, the combination of information on effective cloud top height and cloud fraction as well as surface and cloud albedos will facilitate the quantification of the effect of clouds. At present, we minimize the errors induced by partial cloud cover by confining our analysis to retrievals that comply with the strict cloud filter criteria.

In Figure 5.4a, various regions with enhanced methane abundances (on larger spatial scales) can be detected. Retrieved VMRs in Russia show substantial variation and are hard to interpret due to the absence of strong spatial correlation of high methane abundances to surrounding pixels and a relatively high uncertainty in the retrievals (mostly due to low surface albedo, see Figure 5.4c). Thus, we focus on regions where uncertainties in the average are low and signals from methane emissions strong.

There are regions with substantially enhanced CH_4 VMRs indicating strong regional methane emissions. The most outstanding region is the Red Basin in China showing the highest mean abundances on the entire globe (please note that the highest values are depicted in white). Further, there are high VMRs in northern parts of South America (not in line with the modeled abundances in Figure 5.4a), central Africa and also slight enhancements in the U.S.A.. A zoom into these regions with a narrower color-scale is shown in Figure 5.6.

In the United States (Figure 5.6a), the highest abundances are observed south of the Great lakes. According to the EDGAR base (*Olivier and Berdowski*, 2001), emissions from coal mining are very strong in this regions, but other anthropogenic activities also play a significant role. The Rocky mountains show lower VMRs partly due to high surface elevation that results directly in a reduced column averaged VMR (due to the relatively stronger weight of the

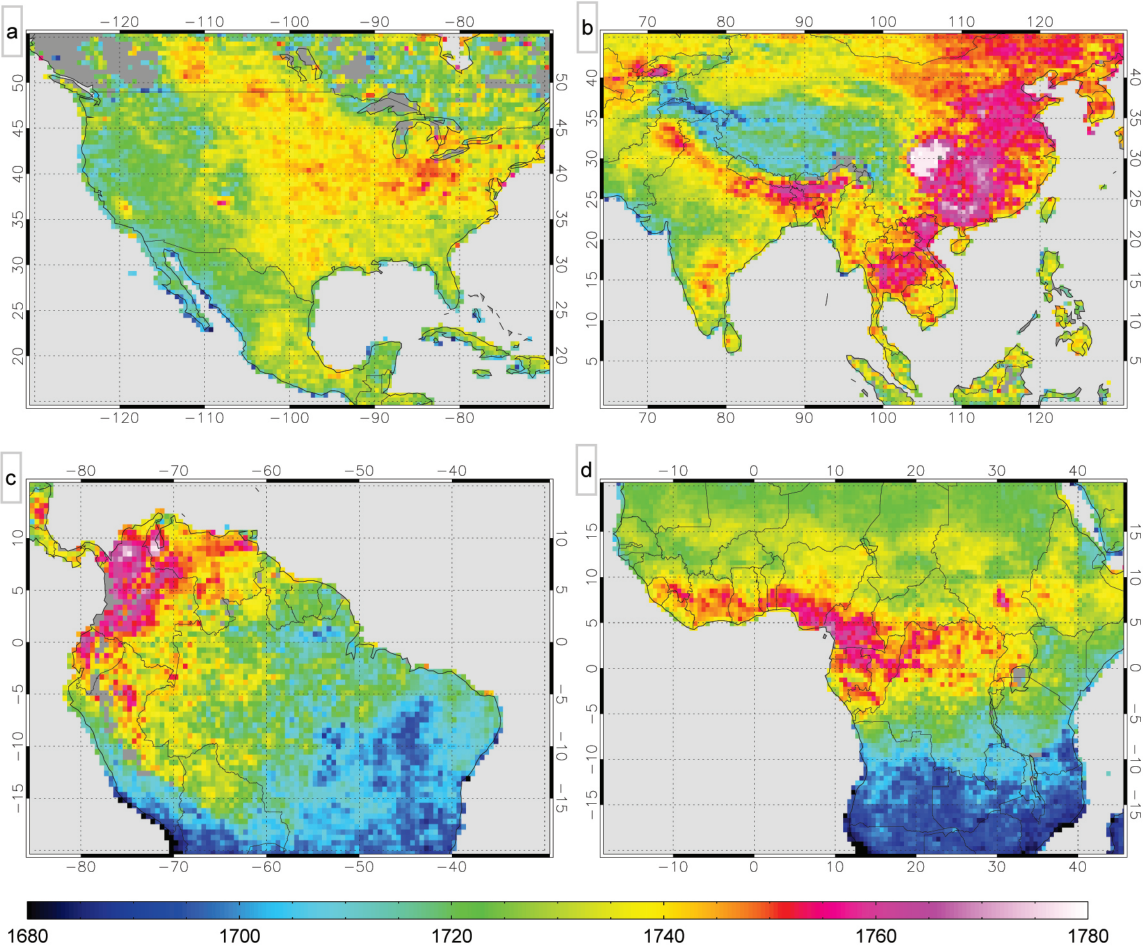

Figure 5.6: Global methane mean column averaged mixing ratios (in ppb). The same time period and spatial resolution as in Fig. 5.4a is used but with a different color scale and with focus on four specific geographical regions, viz. USA (a), Asia (b), South America (c) and Africa (d). Note that the highest abundances are shown in white whereas pixels with missing data (e.g. over ocean) are shown in gray. Only pixels with a maximum statistical error of 8 ppb are depicted.

stratosphere in case of low surface pressure). Also, this region exhibits few sources of methane. Strong variations in coastal areas may be related to an overall higher uncertainty in the averaged mixing ratios in these regions (see Figure 5.4c) due to lower albedos or a smaller number of measurements within these pixels. The same could hold for the peculiar enhancement in New Mexico at approximately 36.75° N and 108° W, but further investigations are necessary to ascertain the cause of the enhancement.

In Asia (Figure 5.6b), the highest methane abundances by far are found, particularly in the Red Basin (major cities: Chengdu and Chongqing) and regions further south-east. Rice paddies, coal mining, domestic ruminants and waste handling can be assumed to constitute the main sources. In India, the entire Gangetic plains (rice paddies, domestic ruminants) show higher methane VMRs than the surrounding areas. Also in Thailand, Laos and Vietnam, substantial enhancements are observed. Inverse modeling is required to attribute the emissions quantitatively to different sources. In Southeast Asia, rice paddies, wetlands, landfills and domestic ruminants are the strongest sources according to *Olivier and Berdowski* (2001).

In South America (Figure 5.6c), the highest abundances are found in Venezuela (close to Lake

Maracaibo), Columbia, Ecuador and parts of Peru. Also parts of Brazil in the Amazon basin show high VMRs. Particularly surprising are the high values in Venezuela and Columbia: The observed VMRs are much higher than those modeled by TM4 (based on the emission inventories in Table 5.2). In Colombia, the major part of emissions is supposed to be attributable to digestive processes of dairy and meat cattle (*Gonzalez and Rodriguez*, 2000; *Olivier and Berdowski*, 2001). However, these sources are not expected to exhibit the strong seasonal variations that we observe in methane abundances over Colombia (see section 5.5.2). One might argue that high CH_4 concentrations may be transported into this region. However, the effect of emissions on atmospheric concentrations would be expected to diminish away from source regions. Since the CH_4 abundances are highest in Colombia/Venezuela, they have to be caused mainly by local emissions, while transport can only explain part of the enhancements.

In Africa (Figure 5.6d), rather homogenous enhancements between 4° S and 8° N (west of 40° E) are found. Below 8° S, methane is clearly depleted. In Sudan, a region with distinctively high methane emissions from wetlands is apparent in the SCIAMACHY retrievals as predicted by wetland models (*Walter et al.*, 2001). Surprisingly, on the other hand, there are also enhanced VMRs in Ethiopia.

5.5.2 Seasonal variations in global methane abundances

Seasonal variations in methane abundances may be induced due to several factors apart from emissions with strong seasonal patterns such as rice emissions or biomass burning. Variations in predominant wind fields caused by ITCZ movements, for instance, or changes in OH fields can also cause strong seasonal variations in methane abundances. For a first quantitative analysis of the time dependence of the methane distribution, we developed time series in different geographic locations. For the SCIAMACHY retrieval and the TM4 model results, we applied a 30 day box filter (± 15 days) to smooth the data.

In Figure 5.7, the temporal behavior over Asia (20-30° N/80-120° E), tropical Africa (10° S-15° N/20° W-60° E) and tropical South America (10° S-15° N/40-90° W) are shown. In Asia, the main seasonality is caused by rice emissions, which are very intense during a relatively short time period. As can be seen in the upper panel of Figure 5.7, methane enhancements due to rice emissions (peak months are August through October) seem to occur approximately 1 month earlier than given in the model, although the magnitude is very similar (given 60 Tg yr^{-1} rice emissions in the model). Higher methane abundances are also seen to decline earlier, resulting in markedly lower SCIAMACHY retrievals in November as compared to the model. These results are consistent with the findings of *Chen* (2003) who also found a time shift in methane emissions with respect to current emission inventories. The start of the rice emissions is also reflected in an enhanced standard deviation of the SCIAMACHY retrievals since local sources induce large scatter.

Especially for modeling purposes, the temporal evolution of sources is of primary importance. These emissions largely determine methane abundances in the entire Asian region and are also transported towards Africa (*Frankenberg et al.*, 2005c) or North America. Different regions can be affected depending on predominant wind fields during the time of peak emissions.

Also in tropical Africa, we observe a phase shift between SCIAMACHY retrievals and model simulations. The absolute abundances are in general on the same order but the measure-

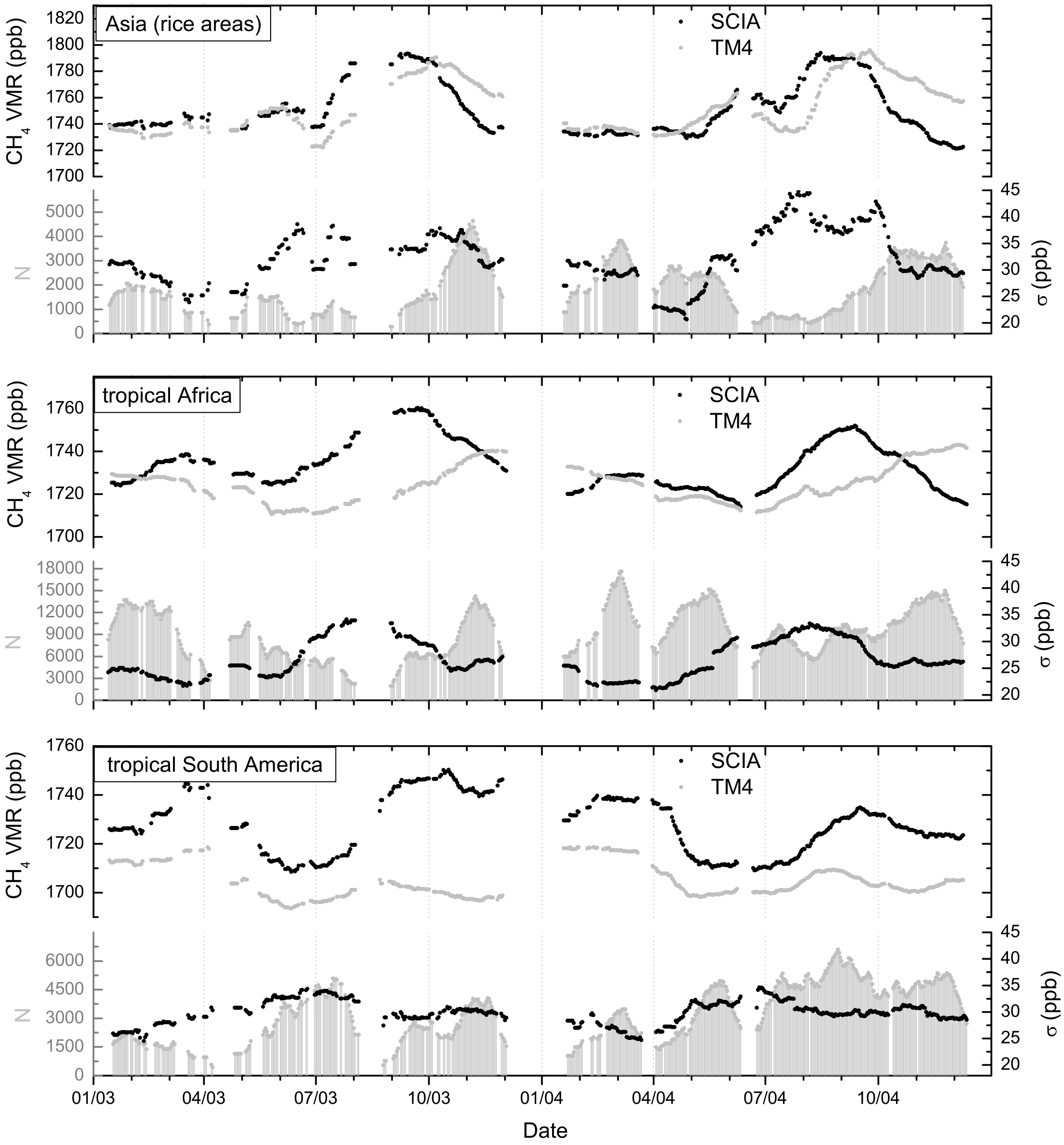

Figure 5.7: Timeseries of SCIAMACHY measurements in different geographic locations smoothed in time with a 30 day box filter (+/- 15 days). In the upper panels, the SCIAMACHY retrieval (corrected with model CO_2 fields) and the TM4 model results (using averaging kernel correction) are depicted. The respective bottom panels show the total number of SCIAMACHY retrievals (in gray) and their standard deviation (black dots, not to be confused with the 1-σ precision error) as used for the calculation of the 30-day running average. For the averaging, only retrievals in areas with less than 1 km surface elevation are considered. The exact geographic locations of the areas are 20-30° N/80-120° E for Asia, 10° S-15° N/20° W-60° E for tropical Africa and 10° S-15° N/40-90° W for tropical South America. Gaps in the timeseries are caused by missing SCIAMACHY data (Due to the ice layer on channels 7 and 8, SCIAMACHY switches to the decontamination mode from time to time).

ments show higher mixing ratios starting already in July/August. In tropical South America, measurements are higher than the model throughout the year. However, as in *Frankenberg et al.* (2005c), the largest discrepancies are found from August through December, especially in 2003. For the rest of the year, the temporal evolution of measurement and model is very similar apart from an offset of ≈ 15-30 ppb at any given time. August through September is the typical biomass burning season in tropical South America as is evident in observations of increased carbon monoxide abundances (*Bremer et al.*, 2004; *Frankenberg et al.*, 2005b). Depending on vegetation and fire type, molar emission ratios (CH_4/CO_2) of biomass burning range from 0.4% to 1.3% (*Andreae and Merlet*, 2001) with indications of even higher ratios in tropical rainforest areas (*Alvala and Kirchhoff*, 1998). If the emission ratio of methane is exactly the same as the ratio of the background concentrations (≈ 0.5%), the methane emissions would be indiscernible to us if the particular biomass burning event is not correctly included in the CO_2 model. Thus, biomass burning can be a source of differences between model and measurements, especially in direct proximity of the fires.

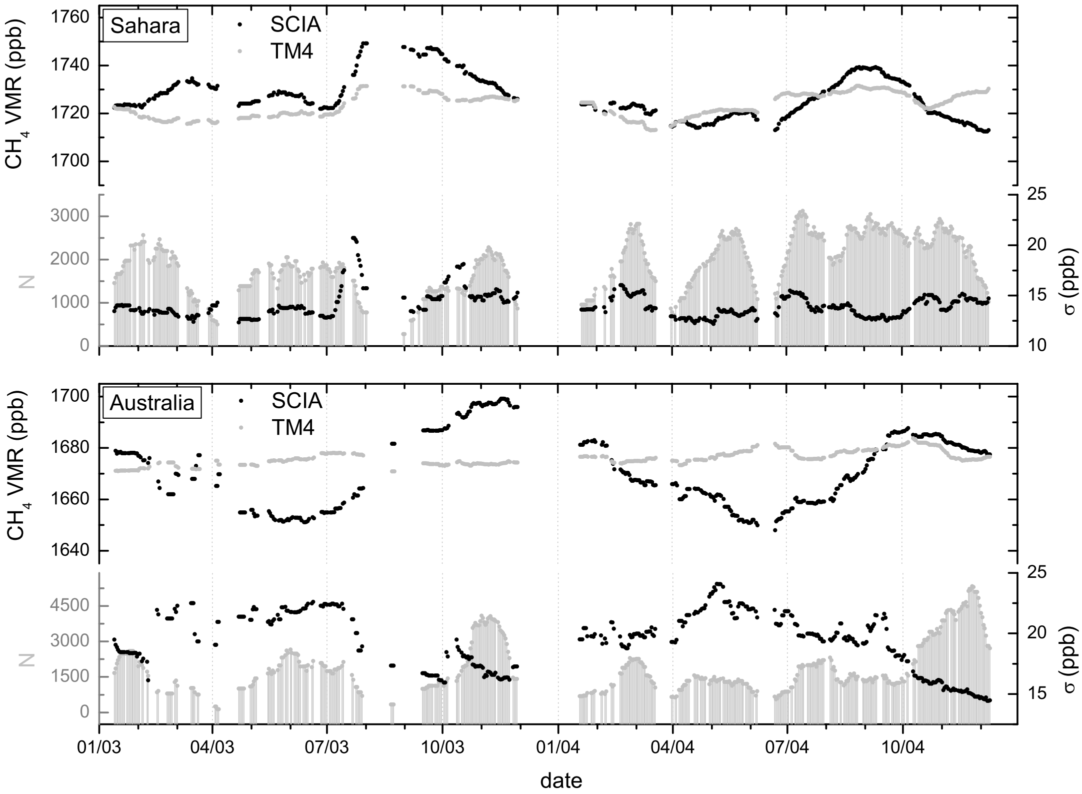

Figure 5.8: Timeseries of SCIAMACHY measurements over the Sahara and Australia. The same criteria as in Figure 4 apply. The exact geographic locations of the areas are 20-30° N/0-20° E for the Sahara and 20°-30° S for the complete Australian continent. The latitudinal bins have been chosen to have comparable solar zenith angles (with a phase shift of 6 months) for both regions. The respective bottom panels depict the total number of SCIAMACHY retrievals and their standard deviation as used for the calculation of the 30day running average.

Figure 5.8 shows time series for the Sahara and Australia. In general, the retrieval over the Sahara does not show large discrepancies compared to the model. Both capture enhanced methane abundances starting in July 2003 but with a higher magnitude in the measurement. These enhancements are accompanied by a relatively high standard deviation in the measurements. Because of the lack of local sources, this suggests that the enhancements are induced by transport, either from Europe or from Asia.

In Australia, there are systematic differences between model and measurement. The SCIAMACHY retrieval shows seasonal variations that are not predicted by the model. The model simulations show close agreement with NOAA-CMDL surface measurements at Cape Grim, Samoa and Easter Island, and are also consistent with FTIR CH_4 column measurements at Wollongong. The sinusoidal variations in time have a minimum in June and a maximum in December, albeit with a relatively low amplitude (± 1.2%). A retrieval dependence on solar zenith angle cannot explain the variations as this should result in a similar behavior over the Sahara (with a 6-month phase shift), which is not the case (Figure 5.8). Potential alternative explanations are unaccounted variations in CO_2 or a hitherto unknown retrieval bias.

A global view of the seasonal cycle gives a better overview of the seasonal cycles in different geographic locations. Figure 5.9 shows seasonal plots of retrieved and simulated global methane VMRs. The associated CO_2 model fields that were used to scale the measurements are depicted in Figure 5.10. It should be noted that the retrievals in the seasonal mean are sometimes only single snapshots of the methane distribution. Especially over the ocean, only few valid measurements are available due to the low ocean albedo in the near infrared, causing, in most cases, an unacceptably reduced signal-to-noise ratio. Hence, care has to be taken in interpreting the seasonal means and, the 1-σ uncertainties given in Figure 5.9i-l have to be considered. Enhanced methane VMRs south of Iceland appear in the June/July/August average. From the model simulation we could infer that the enhancement is largely due to a transport event on 18-20 July 2003.

The most pronounced feature we observe is due to the temporal variation of methane emissions from rice paddies in Southeast Asia with typical maxima from August through October, resulting in higher VMRs in the periods June-August and September-November. The differences between model and measurement in this case partly result from the deviation of the observed from the modeled temporal evolution (see Figure 5.7). In Africa, the highest methane abundances are situated towards the south in Dec/Jan/Feb, while they are strongest and situated further northward in Sep/Oct/Nov. This, on the whole, corresponds well to the temporal evolution and spatial distribution of wetland emissions (*Shindell et al.*, 2004).

In South America, the highest abundances are found from January through April, in line with current wetland distributions. However, in northern parts of South America the highest abundances appear from September through November, as also evident in the two-year mean (see Figure 5.6c). The current emission inventory for Colombia and Venezuela (together 4.9 Tg yr^{-1} given by the EDGAR (Emission Database for Global Atmospheric Research) database (*Olivier and Berdowski*, 2001)) can hardly explain such abundances. The seasonality of the signal calls for an exclusion of more or less constant sources such as energy related emissions or cattle breeding. The total rice production in Colombia is only 2% of that in India (see Food and Agriculture Organization of the United Nations http://apps.fao.org) and thus unlikely to be the source of such high methane abundances. Other possible tropical sources are biomass burning and termites. However, in northern South America no substantial biomass burning was detected in the July-November period (*Bremer et al.* (2004), Tropospheric Emission Monitoring Internet Service http://www.temis.nl), while termites are not expected to exhibit strong seasonality in their methane emissions (*Zimmermann et al.*, 1982; *Sanderson*, 1996). Thus, the origin of these high abundances still remains unclear.

A more detailed discussion and rigorous comparison with atmospheric models using different emission inventories will be presented in a subsequent publication (*Bergamaschi et al.*, 2005a).

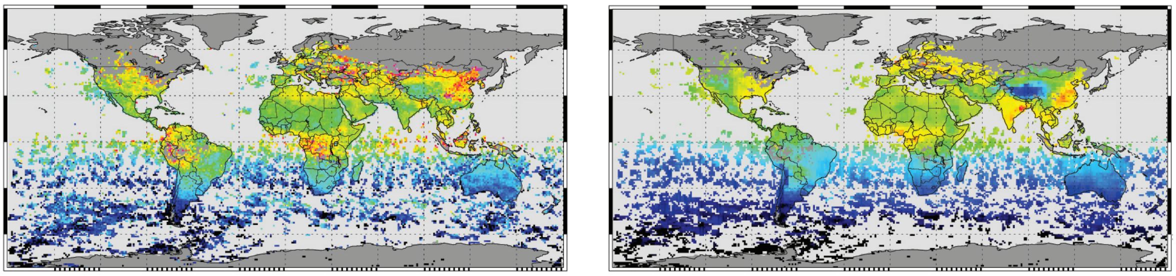

(a) DJF SCIAMACHY (b) DJF TM4

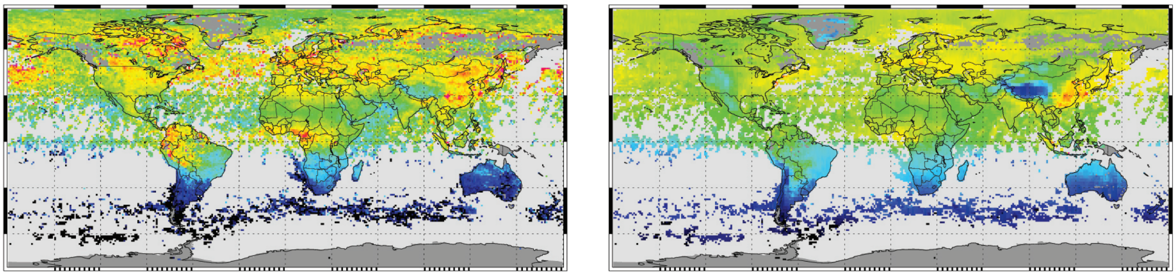

(c) MAM SCIAMACHY (d) MAM TM4

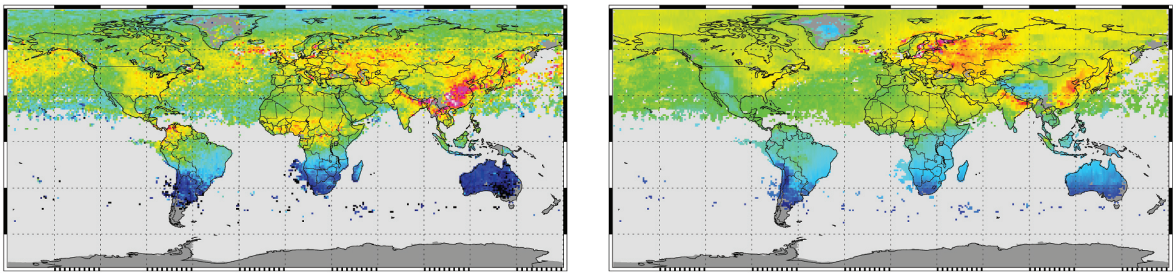

(e) JJA SCIAMACHY (f) JJA TM4

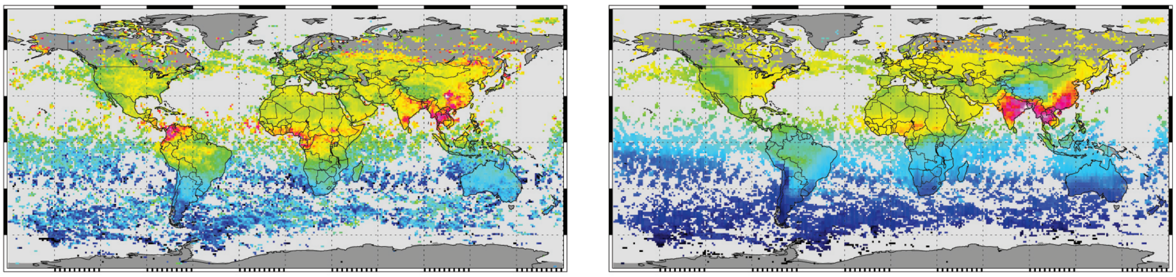

(g) SON SCIAMACHY (h) SON TM4

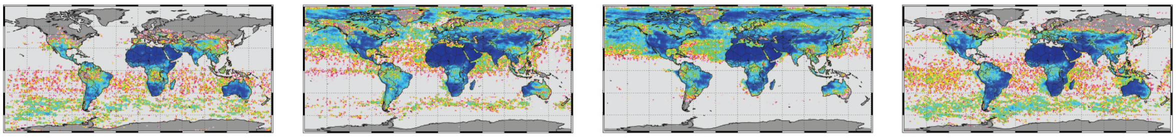

(i) DJF (j) MAM (k) JJA (l) SON

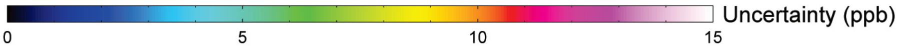

Figure 5.9: Seasonal plots (December/January/February, March/April/May, June/July/August and September/October/November) as retrieved by SCIAMACHY in the the years 2003 and 2004 (averaged over 1° longitude and 1° latitude). For comparison, the TM4 model results for the same time periods are depicted on the right hand side. Only pixels with an estimated statistical error below 15 ppb are depicted. The statistical retrieval uncertainties in the SCIAMACHY averages are shown in the lower panels (i-l).

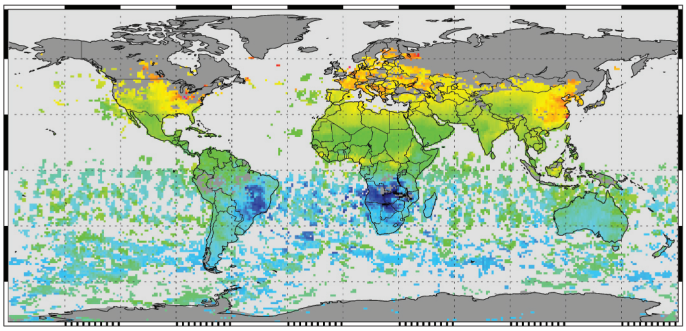

(a) DJF TM3 CO_2

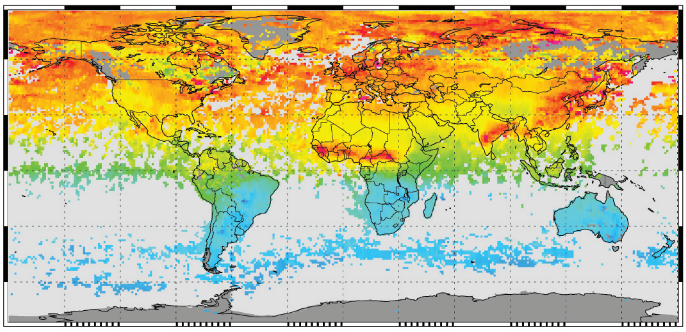

(b) MAM TM3 CO_2

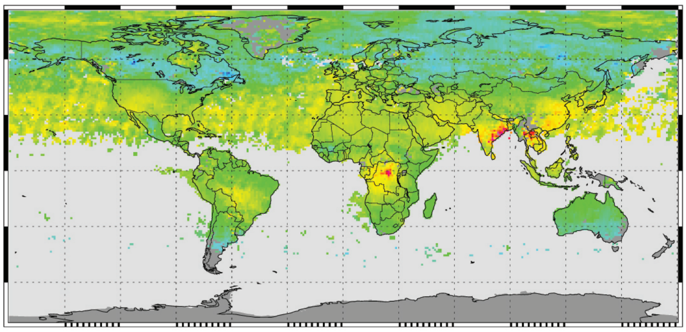

(c) JJA TM3 CO_2

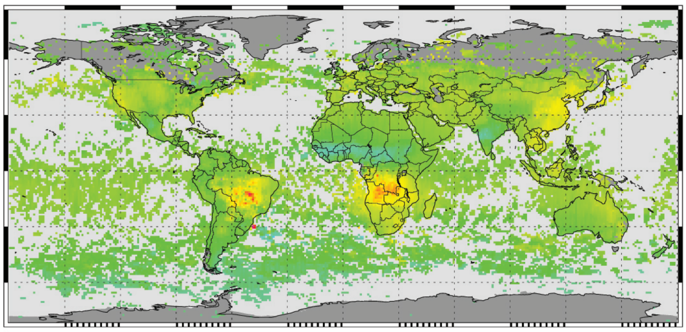

(d) SON TM3 CO_2

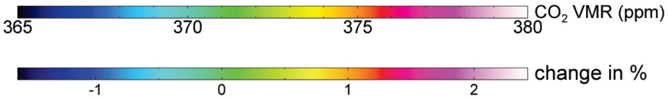

Figure 5.10: Seasonal plots (December/January/February, March/April/May, June/July/August and September/October/November, derived from TM3-MPI) of the modeled column averaged CO_2 mixing ratio as used for the calculation of the mixing ratio of CH_4.

5.6 Conclusions

The space-borne spectrometer SCIAMACHY onboard ENVISAT now enables first precise measurements of atmospheric methane from space with high sensitivity including toward the ground and global coverage over continents. In this paper, we investigate available SCIAMACHY data in the years 2003 and 2004 and derive maps of the methane distribution as well as the corresponding methane abundances modeled with the atmospheric chemistry transport model TM4. We use CO_2 as a proxy for the probed atmospheric column to convert methane total columns to column averaged mixing ratios. For this purpose, concurrent retrievals of the total column of CO_2 are used in combination with modeled CO_2 abundances. Since variations in the CO_2 column abundances are far smaller than those in methane, we retrieve precise maps of the column averaged mixing ratio of methane.

In these maps, the north-south gradient can be clearly identified. In the two-year average, we found the most pronounced enhancements of methane in the Red Basin of China and in large areas of Asia in general, followed by northern parts of South America and central Africa. In particular, the high mixing ratios in Columbia and Venezuela are surprising, and much higher than our TM4 simulations. This indicates higher CH_4 emissions in this region than given by the CH_4 inventories used in our study. The largest seasonal variations are caused by rice emissions in Asia, which are very intense during a relatively short time period. Our measurements indicate that these emissions already start towards the end of July and decline sharply in November, which is earlier than predicted by the model based on the inventory by *Matthews et al.* (1991). This is of primary importance for the modeling of global methane abundances.

Confirming our previous analysis (*Frankenberg et al.*, 2005c), we found strong deviations between observed and modeled CH_4 abundances in tropical regions, hinting at so far underestimated tropical emissions. The analysis of the two-year period reveals that these discrepancies between measurements and model are highest in the time period from August through December, especially in the year 2003.

Over Australia, we found unexpected seasonal variations (± 1.2%) in the measured CH_4/CO_2 ratio. To date, the origin of this behavior remains unclear and needs further investigations to exclude a measurement bias.

In the long term, however, the correlation with atmospheric models is very good and the standard deviation between model and measurement is about 30 ppb (*Frankenberg et al.*, 2005c), which corresponds to a retrieval precision of 1.8% for a single measurement. Thus, the measurements represent an enormous potential for verifying or correcting current methane emission inventories. A more detailed comparison with the atmospheric models TM4 and TM5 (*Krol et al.*, 2005), including the analysis of different emission inventories and application of high-resolution atmospheric models (*Krol et al.*, 2005; *Bergamaschi et al.*, 2005b) for source regions of special interest, will be part of a subsequent publication (*Bergamaschi et al.*, 2005a).

Acknowledgments

Most importantly the authors would like to thank all scientists and engineers involved in the European Space Agency's ENVISAT/SCIAMACHY mission, especially John Burrows and his team from the University of Bremen. If they had not fought shadows, SCIAMACHY would not have been possible. We also thank the national space agencies of Germany (DLR), the Netherlands (NIVR) and Belgium (BUSOC). The SCIAMACHY level-1 data used in this paper was made available by ESA and processed by DLR. We thank the Netherlands SCIAMACHY Data Center, in particular Ankie Piters and John van de Vegte from KNMI, for their invaluable assistance in transferring the data set to Heidelberg. We thank Tim Deutschmann for writing C libraries to access SCIAMACHY data and Suniti Sanghavi for proofreading the manuscript. We wish to acknowledge the European Commission for supporting the 5th Framework Programme RTD project EVERGREEN (contract number EVG1-CT-2002-00079). We further acknowledge exchange of information within the EU 6^{th} FP Network of Excellence ACCENT (http://www.accent-network.org/).

Discussion & Appendix

Chapter 6

General Discussion and Outlook

6.1 Absorption Spectroscopy

In chapter 2 (*Frankenberg et al.*, 2005a), an algorithm for trace gas retrieval in the near infrared was developed. Under the assumption of a non-scattering atmosphere, the algorithm was extensively tested using artificial measurements. It has been shown that the temperature profile can have a substantial impact on the retrieval if a precision of within a few percent is desired (see Appendix C.3.2 for a more comprehensive treatment of the impact of temperature). A climatological fit parameter was introduced to minimize a bias induced by temperature variations. It was shown that, if strong absorbers are to be retrieved, the sensitivity of the measurement depends on the ambient pressure, and thus on height. This effect, which is introduced by the broadening of the absorption lines at higher pressure, is of special importance when interpreting results as elaborated in chapter 5 (*Frankenberg et al.*, 2005d). Since most variations in the atmosphere (e.g. due to mountains clipping part of the atmosphere, actual emissions at the surface or high aerosol loading in the boundary layer affecting the light path) occur in lower layers close to the ground, the fit parameters for higher atmospheric layers were constrained according to the optimal estimation theory by *Rodgers* (2000). This method forces the fit algorithm to permit strong variations only in the lowermost atmospheric layers. However, the method is flexible enough for the constraints to be easily adjusted (*Rodgers*, 2000) if, for instance, higher spectral resolution enables mutually independent retrieval of different height layers. In regard to DOAS methods in general, optimal estimation can also be easily used to constrain nonlinear parameters such as spectral shift and squeeze. Not constraining these parameters often leads to unstable solutions. Furthermore, the effect of overlapping absorbers (see Sect. A.4 and *Frankenberg et al.* (2005a) for details) and the I_0 effect (*Aliwell et al.*, 2002) can be effectively avoided by the developed algorithm. Thus, *IMAP-DOAS* is not only of interest for special applications in the near infrared but also as a flexible framework for absorption spectroscopy in general.

The algorithm developed in chapter 2 enabled the retrieval of carbon monoxide as shown in chapter 3.

So far, the algorithm ignores scattering processes in the atmosphere. However, even in the near infrared, aerosols and partial cloud cover can alter the light path substantially. If precision requirements are on the order of 1-3% (as in the case of methane), a proxy for the light path is indispensable. Hence, chapters 4 introduced concurrent total column retrievals of CO_2 as proxy to convert total column measurements of methane into column averaged mixing ratios that are independent on aerosol loadings, partial cloud cover and surface pressure variations. Since the mixing ratio of CO_2 exhibits variations, it cannot be considered an ideal proxy such as O_2. Thus, chapter 5 further refined the computation of column averaged mixing ratios of methane by applying modeled CO_2 abundances.

Theoretically, O_2 would be the best proxy to convert total column retrievals to column averaged mixing ratios. However, it turned out that O_2 is suitable as proxy only to a limited extent since the radiative transfer properties in the wavelength region at about 760 nm (where O_2 is retrieved) differ from those in the near infrared (for a more detailed analysis of the impact of aerosols see, for instance, Appendix B or *Houweling et al.* (2005); *van Diedenhoven et al.* (2005)). This can be illustrated by the optical properties of aerosols in different wavelength regions.

Figure 6.1 shows the scattering properties of a typical industrial aerosol at wavelengths of special interest for the retrievals in the near infrared. The bulk phase functions at 1580 and 1670 nm strongly resemble each other and also the aerosol optical depth changes only by 6% in this wavelength range. At 760 nm, where the proxy O_2 is usually retrieved, phase function and optical depth show substantial differences and thereby aggravate a comparison of the light path distribution with other wavelength ranges. Additional information could be retrieved if measurements in the 2.3 µm range are also considered.

With prior knowledge on aerosol microphysical properties and their height distribution in the field of view, one could determine their influence on the light path distribution in different spectral regions and thus still use O_2 as proxy for the light path. For SCIAMACHY retrievals, the aerosol properties in the field of view are not yet well known but a better characterization of these will help overcome the difficulties induced by the differences in light path distributions in spectrally disparate fitting windows. However, due to the large ground pixel size of SCIAMACHY (60 times 30 km), the field of view can neither be considered homogenous in surface albedo nor in aerosol or cloud distribution. The effects of scene inhomogeneities are not yet well understood and need to be further analyzed. Partial cloud cover especially is hard to discriminate from aerosols. Thus, a synergistic combination with imaging spectrometers having high spatial resolution (such as MERIS http://envisat.esa.int/instruments/meris/) would be desirable in order to obtain more accurate information on the distribution of aerosols and clouds within the field of view of SCIAMACHY (having high spectral but poor spatial resolution). This is of utmost importance where CO_2 retrievals are concerned since these strictly rely on concurrent O_2 measurements as proxy. The extent to which uncertainties in aerosol properties (such size and height distribution and refractive index) translate into uncertainties in the retrieval of CO_2 or CH_4 with O_2 used as proxy is not yet well quantified. This aspect certainly requires further studies if precision requirements of better than 1% for CO_2 mixing ratios are to be met. Some first investigations of the impact of aerosols on the light path distribution in the O_2 and CO_2 fitting windows are shown in Appendix B.

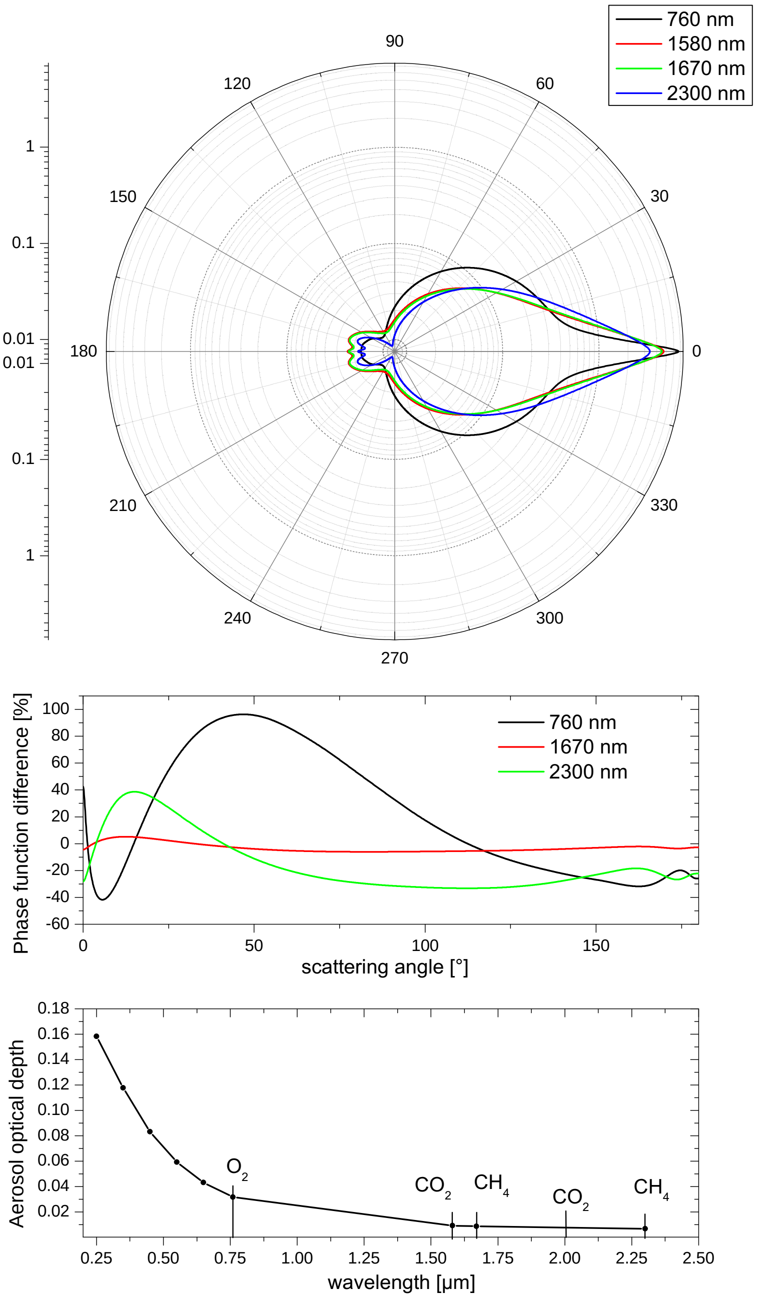

Figure 6.1: Microphysical properties of a typical industrial aerosol (bimodal log-normal number density distribution with mean radii 0.078 and 0.497 µm and standard deviations of 1.49 and 2.16, respectively. The fraction of the coarse mode is $4.36 \cdot 10^{-4}$ and the refractive index is $1.4 + 0.04i$. Data provided by S. Sanghavi using the Mie Theory). The upper panel shows the bulk phase function at three different wavelengths. The middle panel shows the relative differences with respect to the phase function at 1580 nm (in percent). The lower panel depicts the spectral behavior of the aerosol optical thickness.

6.2 Present shortcomings and future potential

As already indicated, SCIAMACHY suffers shortcomings that will hopefully be overcome by future, dedicated space missions. The ice layer on the detectors of channels 7 and 8 forced the employment of channel 6 spectra, despite the coarser spectral resolution (≈ 1.35 nm). As a result, the retrieval sensitivity and hence also the retrieval precision are reduced. On average, the estimate of the 1-σ precision error in the CH_4 VMR is about 30 ppb. Further, as described in chapter 5 (*Frankenberg et al.*, 2005d), partial cloud cover can induce retrieval biases of up to 3%. For SCIAMACHY, a precise determination of the partial cloud cover and cloud top height would be desirable, ideally at very high spatial resolution as obtained by instruments like MERIS. The errors can also be reduced by improving spectral and spatial resolution of the spectrometer. Future, more dedicated, space missions such as OCO (from NASA; see http://oco.jpl.nasa.gov/ and GOSAT (from JAXA, the Japanese Aerospace Exploration Agency; see http://www.jaxa.jp/missions/projects/sat/eos/gosat/index_e.html) are expected to implement these improvements, thereby obtaining a higher retrieval precision and accuracy. It has to be noted that SCIAMACHY is not a dedicated greenhouse gas mission but a pioneer in space-borne near-infrared sounders. In that respect, the results are remarkable, making SCIAMACHY a milestone in greenhouse gas retrieval from space and an ideal test-bed for future missions.

At the current stage of this work, the following measures bear the potential of further improving the retrieval accuracy:

- Inclusion of a surface elevation database as a priori knowledge,
- Inclusion of ECMWF temperature and pressure profiles as a priori knowledge,
- Inclusion of modeled stratospheric methane abundances as a priori knowledge,
- Synergistic use of sounders with high spatial resolution (for cloud and aerosol detection),
- Creation of a global surface reflectance database for all wavelength windows.

As shown in chapter 2 (*Frankenberg et al.*, 2005a), the atmospheric temperature profile can have an influence on the CO_2 retrieval in channel 6, especially if the surface temperature is very low (see Figure 2.8). At surface temperatures below 270 K, the CH_4/CO_2 ratio will thus exhibit a positive bias. The inclusion of ECMWF pressure and temperature profiles as a priori knowledge would minimize this potential bias. This requires an on-line computation of reference spectra at high spectral resolution for each height layer given by the ECMWF model (for each fit). As this is computationally expensive, it calls for a pre-computed spectral database.

The 1-2% precision error that was achieved in this work cannot be further improved using channel 6 spectra. For the methane retrieval, the task is now to characterize accurately all factors affecting the accuracy.

6.3 Carbon dioxide retrievals

If mixing ratios of CO_2 are to be retrieved, a very high precision (about 0.5-1%) is needed (*Rayner and O'Brien*, 2001; *Rayner et al.*, 2002) to obtain an added value to the existing ground based measurements. For SCIAMACHY it is not yet clear whether these requirements can be met but the experience gained from SCIAMACHY is certainly of great value for future missions. In this thesis, CO_2 retrievals have mainly been used to avoid the problems inherent in the uncertainties of light path distribution. The primary problem of retrieving CO_2 abundances is the lack of a suitable proxy for the probed atmospheric column. Radiative transfer properties in the O_2A band ($\approx 760\,\mathrm{nm}$) differ strongly from those in the near infrared, rendering a comparison of the light path distributions difficult (cf. Appendix B). Only a detailed knowledge of the aerosol type (including all microphysical properties) and height distribution would allow a reasonable comparison of the light paths and thereby the application of O_2 as proxy for the probed atmospheric column at different wavelengths. The prerequisite for this approach would be a homogeneous field of view, which is hardly fulfilled by SCIAMACHY. Using a multiple scattering radiative transfer model, *Houweling et al.* (2005) shows that the impact of aerosols on the light path can indeed by quite large, far larger and more complex than previous estimates of *O'Brien and Rayner* (2002) and *Dufour and Breon* (2003), which only take single scattering into account. Due to their spectral proximity, the CH_4/CO_2 ratio is affected only to a small (not measurable) extent but the impact on CO_2 retrievals using O_2 as proxy is not yet well quantified. A precise and bias-free CO_2 retrieval from space is thus certainly an extremely challenging objective, even for future space missions. However, the potential scientific results certainly warrant these efforts.

6.4 Carbon monoxide retrieval

The retrieval of carbon monoxide was severely hindered by instrumental effects such as the ice layer on channels 7 and 8, the high dark current and dark current variabilities as well as the increasing number of dead and bad pixels (for an overview on the instrumental aspects of SCIAMACHY see the SCIAMACHY calibration web page http://www.sron.nl/∼SCIA_CAL/).

However, an extensive analysis and correction of these effects allowed retrievals that clearly reveal global biomass burning patterns (see chapter 3 (*Frankenberg et al.*, 2005b)) and emissions attributable to industrial activities.

Figure 6.2 shows new results obtained after use of an updated version of the HITRAN database (*Rothman et al.*, 2005), which provides substantial refinements of water line parameters within the CO fitting window. The impact of the ice layer on the detector has not yet been considered in this analysis. However, even in the long term mean regions with strikingly enhanced total columns can be identified, namely the biomass burning area in South America and Africa as well as regions in China (probably due to industrial activities).

Since a detailed analysis of the instrumental characteristics of channels 7 and 8 has been performed only recently (*Gloudemans et al.*, 2005), the results presented in this study can be seen as a stepping stone towards a more precise and reliable carbon monoxide analysis. Furthermore, after several extended decontamination periods, the build-up of an ice layer

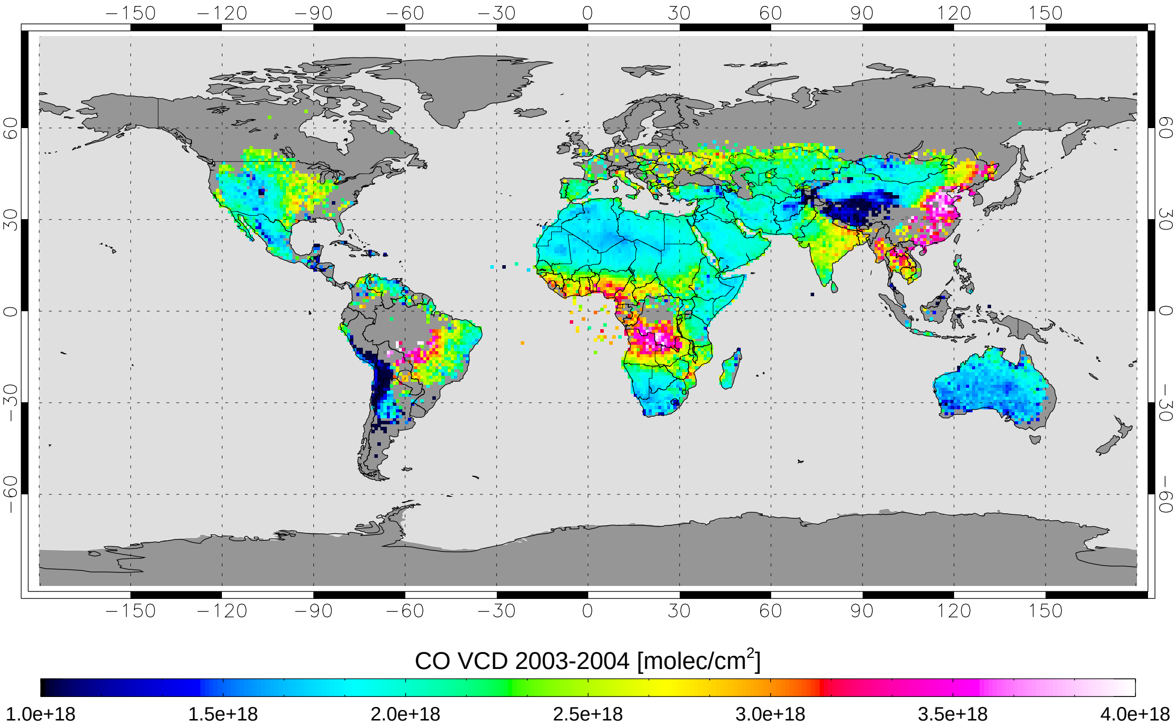

Figure 6.2: CO mean VCD 2003-2004. The retrievals are depicted here using a 1°x1° grid.

on the detectors is now substantially reduced (see http://www.sron.nl/∼SCIA_CAL/), thus promising better results from future retrievals.

Fig. 6.3 illustrates the problem due to the ice layer on channels 7 and 8. Photons are scattered within the ice layer before impinging on the detector. The additional scattering leads to a broadening of the slit function. Uncertainties in the slit function can have severe implications. First, a systematic bias in the retrieval can be introduced and second, systematic residuals could hinder the retrieval of a weak absorber (such as CO) due to overlapping absorptions of strong absorbers (such as H_2O or CH_4, see Appendix A.4 for details). Hence, the application of a time-dependent slit function is planned for future retrievals. According to the convolution theorem (cf. D.1), the scattering within the ice layer could be modeled via an additional convolution, requiring only the basis instrumental line shape (without scattering) to be multiplied with a time varying line shape (accounting for the ice) in the Fourier space.

Since one of the main sources of CO is oxidation of methane, both species are interlinked and of importance for the global carbon cycle. CO retrievals can also be used as proxy for the amount of carbon released by biomass burning because it is then, in contrast to CO_2 and CH_4, substantially enhanced compared to background abundances. In conjunction with information from space borne sounders that retrieve fire counts, fire temperature and total affected area, better constraints on the time and extent of fires are obtained and help modeling the abundances not only of CO but also of CO_2 and CH_4.

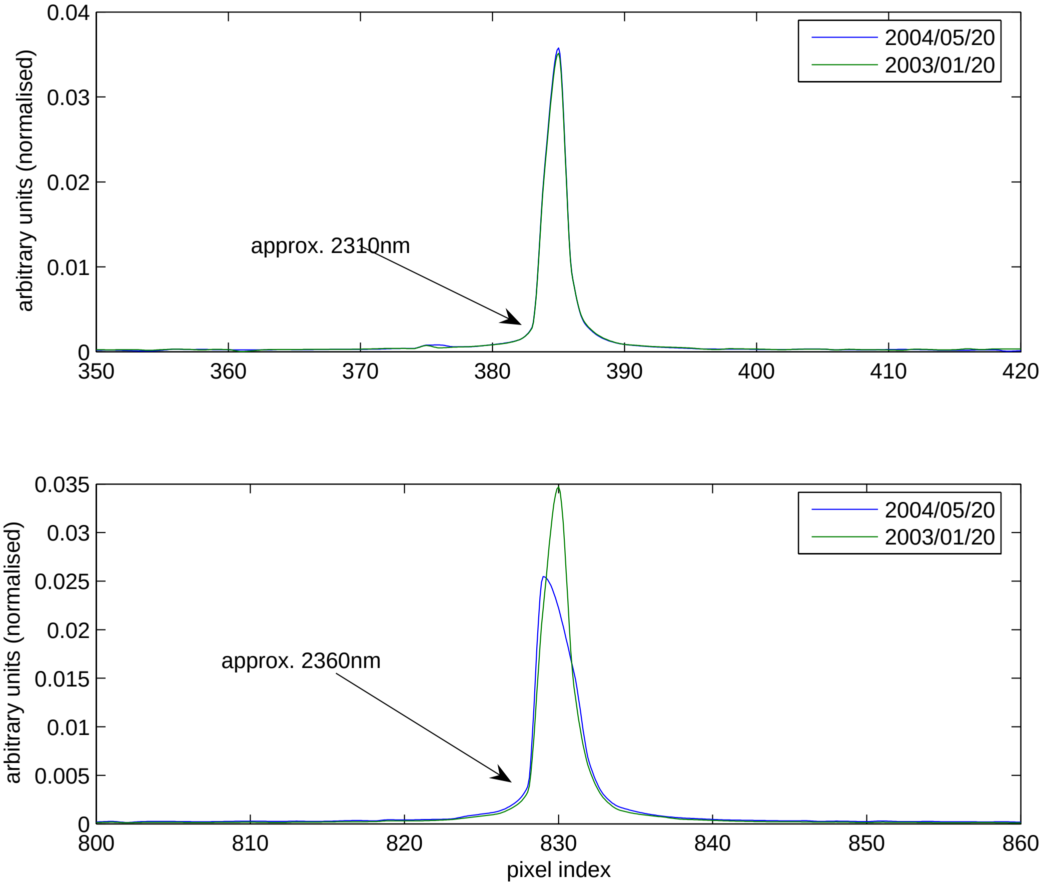

Figure 6.3: Slit function variations in channel 8 (total number of pixels: 1024). It can be seen that the effect of the ice layer on the slit function is not the same throughout the channel, at the beginning of channel 8 (2310 nm), the slit function remains nearly undisturbed while at 2360 nm, there is a substantial broadening between the two dates. The slit functions have been determined using the in-flight measurements from SCIAMACHY's Spectral Light Source (SLS).

6.5 Methane retrieval

The retrievals of methane performed in this work are unprecedented and of paramount value in the assessment of the global methane budget. Especially in the tropics, where ground based measurements are scarce or simply non existent, large discrepancies between measurement and models based on current methane emission inventories were found. SCIAMACHY, from its vantage point in space, now allows to fill the gaps inherent in ground-based point measurements. Despite its moderate precision compared to in-situ measurements, SCIAMACHY methane retrievals offer a unique data-set that can be applied in top-down source inversions using atmospheric models.

This thesis (chapter 4 (*Frankenberg et al.*, 2005c)) suggests the existence of a hitherto unknown methane source in the tropics. Recent investigations of methyl chloride emissions from plants (*Hamilton et al.*, 2003) led to the discovery of in-situ CH_4 formation of methane in plants (*Keppler et al.*, 2005). *Keppler et al.* (2005) show that plants can indeed be a major direct source of methane and not only a transport medium for methane released by bacteria. These new findings could help resolve the observed discrepancies in the tropics. Although further investigations and, most importantly, ground based validations are needed, there are now strong indications that the current state of knowledge of the methane budget requires considerable revision, especially in the tropics. Due to the sparsity of ground based measurements and the strong convective processes in tropical regions, total column retrievals (not influenced by local vertical transport processes) as presented in this study are indispensable to unravel the tropical methane budget.

In order to infer sources and sinks from the retrieved columns, an inverse problem has to be solved using an atmospheric transport model (often referred to as inverse modeling). Atmospheric inverse modeling using satellite data should allow us to go far beyond statistical means of several years of data for large geographical regions, as was done in the past. Instead, it offers the prospect of unambiguously tracing the causes of the observed variability of CO and CH_4 on inter-annual or even shorter time scales. *Meirink et al.* (2005) describe the application of an inverse modeling approach based on four-dimensional variational (4D-var) data assimilation. Using synthetic SCIAMACHY measurements, they conclude that the retrievals at their estimated precision of 1.5 to 2% will contribute considerably to reducing the uncertainty associated with monthly, subcontinental ($\sim$ 500 km) methane source strengths. Hence, atmospheric modeling should be considered as important as retrieval itself: Without models it is hard to interpret the retrieved columns, not to mention the estimation of source strengths. However, without global measurements, source inversion using models would not be unambiguously, especially if high spatial and temporal resolution in source determination is desired.

6.5.1 High resolution modeling

As atmospheric modeling is indispensable for the deduction of actual emissions from total column retrievals, the quality and resolution of the model is important. The atmospheric model TM5 (*Krol et al.*, 2005) allows definition of *zoom regions* where a higher spatial resolution (so far up to 1°x 1°) is applied. Especially in regions with high variability of sources or divergent wind fields, high resolution modeling promises a more accurate description of the distribution of atmospheric methane.

Figures 6.4 and 6.5 show three-weekly averages of measurements and modeled values (high resolution) in Asia from August through October 2003. The correlation between measurements and modeled values is very good at large. Small scale variations seem to be resolved well by both model and measurements. Only in Burma and Thailand, measurements are found to be higher than predicted by the model. Since even regional (or country to country) differences can be resolved, SCIAMACHY measurements could be used to assess the impact of mitigation strategies aimed at reducing methane emissions by rice paddies (see Sect. 6.6). Further, given additional measurements such as soil temperature, soil water content and precipitation rate, these measurements could help to establish a process oriented model of methane emissions as done by *Walter and Heimann* (2000). Using zoom models for regions of special interest with respect to the global methane budget promises to significatntly reduce uncertainties in the methane budget, thereby providing emission estimates that are well resolved in time and space.

An illustrative example of how SCIAMACHY retrievals help evaluate emission inventories is shown in Figures 6.6 and 6.7. The figures show modeled and retrieved column averaged mixing ratios of methane over South America, averaged from January through March 2003. Current emission inventories state wetlands as the main source in this region (according to *Keppler et al.* (2005), direct plant emissions might actually contribute significantly to tropical emissions). A direct visual comparison reveals that the wetland inventory by Kaplan et al. (2005, personal communication) results in modeled column averaged mixing ratios that are in close agreement with the retrievals. In contrast, the application of the inventory by *Walter et al.* (2001) results in differences of 10-30 ppb between model and retrieval in the vicinity of the equator. Hence, methane emissions around the equator are much higher than estimated by *Walter et al.* (2001). Whether wetlands or direct methane emissions from plants (*Keppler et al.*, 2005) constitute the major source in this region cannot be unambiguously asserted by the SCIAMACHY retrievals. Future measurements of the isotopic signature of methane in the tropical region (unfortunately not possible by SCIAMACHY) might help to discriminate between different methane sources.

These examples only give a first idea of the potential of the methane retrievals resulting from this work. The full potential will be exploited when inverse modeling techniques are employed.

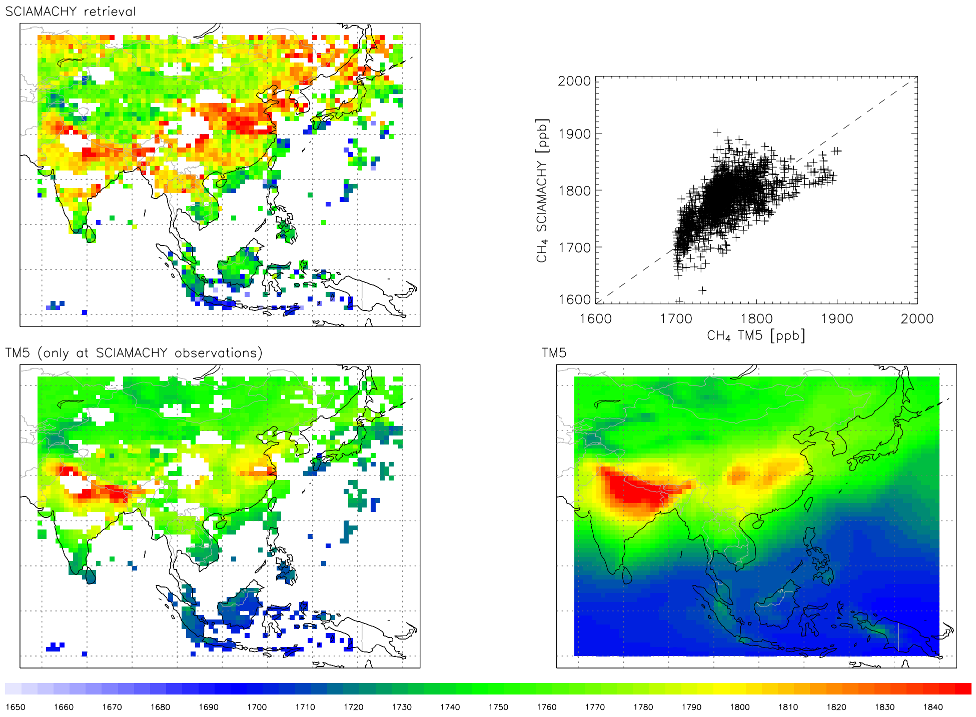

(a) 01.08.2003-21.08.2003

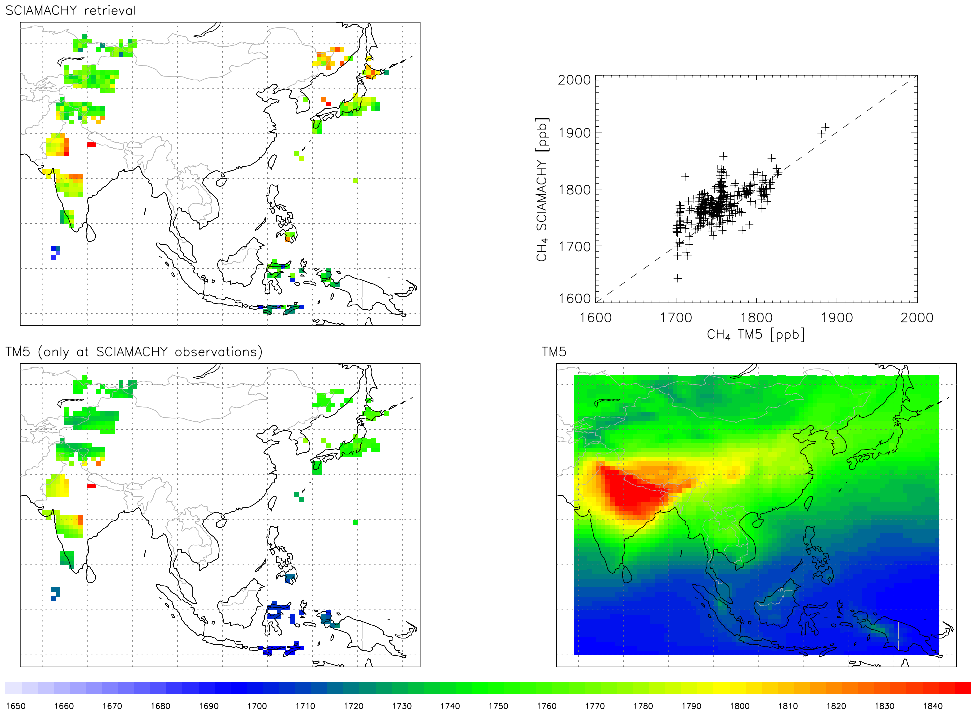

(b) 22.08.2003-11.09.2003

Figure 6.4: Comparison between SCIAMACHY measurements and modeled abundances using the TM5 model at high resolution mode (I). The lower right panel shows the TM5 model results averaged over the entire time period whereas the lower left panel is only averaged over modeled values that correspond (in space and time) to available SCIAMACHY measurements (depicted in the upper left panel). The upper right panel shows correlation plots of all measurement points that contribute to the averaged maps.

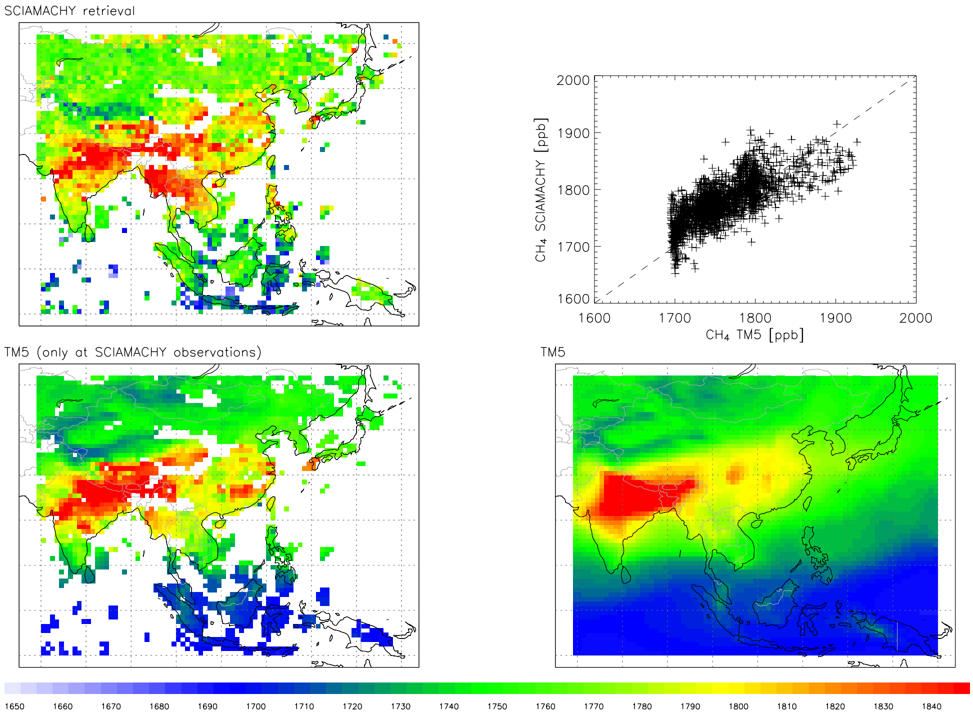

(a) 12.09.2003-02.10.2003

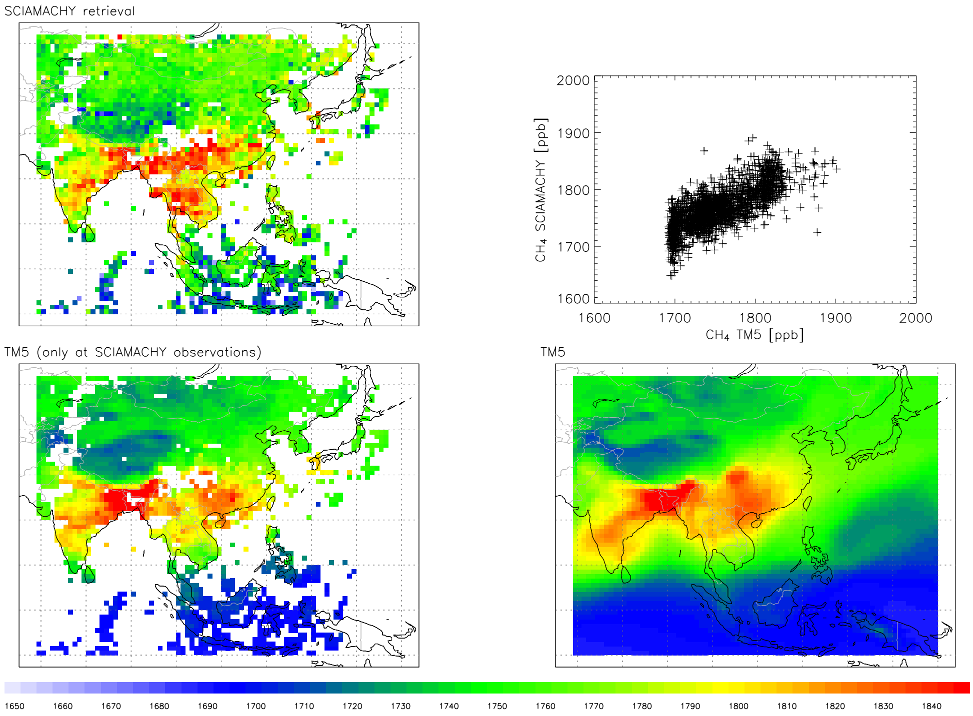

(b) 03.10.2003-23.10.2003

Figure 6.5: Comparison between SCIAMACHY measurements and modeled abundances using the TM5 model at high resolution mode (II). For details see 6.4.

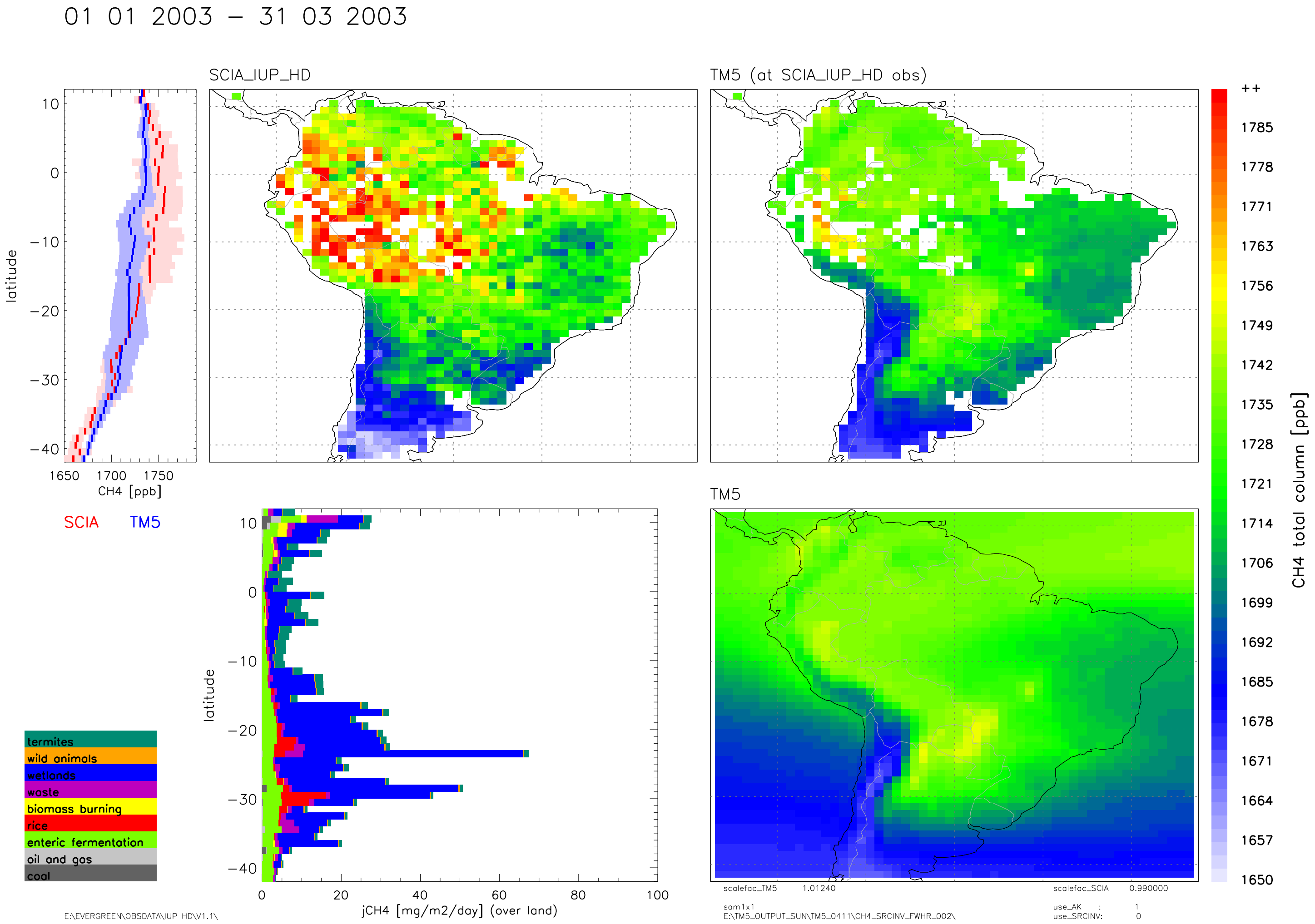

Figure 6.6: Comparison between SCIAMACHY measurements and modeled abundances using the TM5 model at high resolution mode over South America applying the wetland inventory of *Walter et al.* (2001). The plots show methane column averaged mixing ratios averaged from January through March 2003. The lower left panel shows the latitudinal distribution of the sources used in the model. The upper panels depict the average latitudinal methane abundances from the model and the retrieval, respectively. The plot was kindly provided by Peter Bergamaschi (JRC, Italy) using the SCIAMACHY data elaborated in this study and TM5 model results.

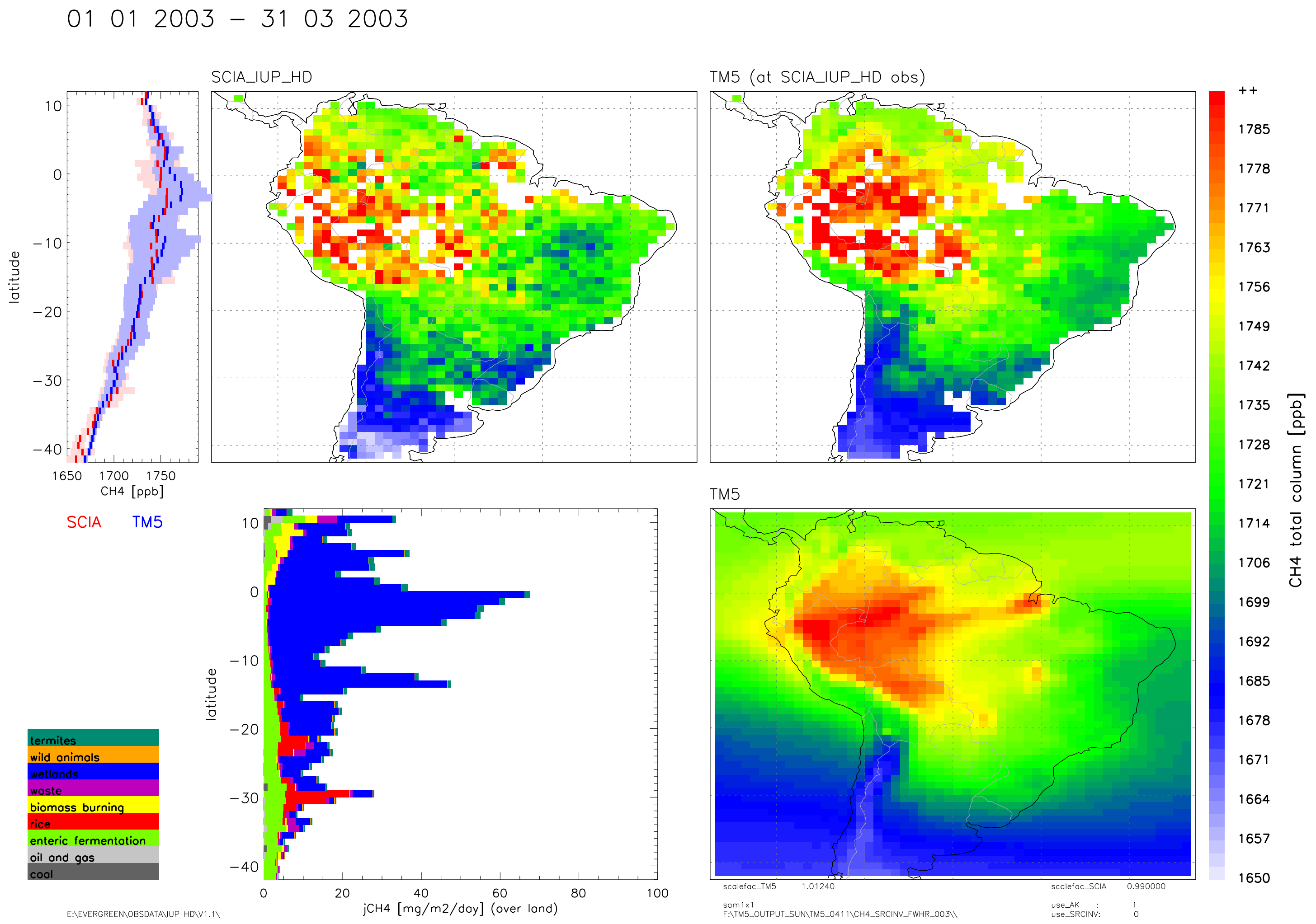

Figure 6.7: Comparison between SCIAMACHY measurements and modeled abundances using the TM5 model at high resolution mode over South America applying the wetland inventory of Jed O. Kaplan (Kaplan et al. manuscript in preparation). The different panels are the same as in Figure 6.6. The plot was kindly provided by Peter Bergamaschi (JRC, Italy) using the SCIAMACHY data elaborated in this study and TM5 model results.

6.6 Climate change issues

With regard to global change, methane is of particular interest since it is currently the second strongest anthropogenic greenhouse gas but bears the potential of being more easily curbed than carbon dioxide. After having suggested an alternative scenario of methane growth rates (*Hansen et al.*, 2000) (compared to the IPCC reference scenarios (*IPCC*, 2001)), *Hansen and Sato* (2004) postulate that feasible reversal of the growth of atmospheric CH_4 and other trace gases would provide a vital contribution toward averting dangerous anthropogenic interference with global climate. Although natural methane sources are expected to have a positive feedback on rising temperatures (*Worthy et al.*, 2000; *Gedney et al.*, 2004; *Shindell et al.*, 2004), there are viable measures that can be taken to substantially reduce anthropogenic methane production.

Rice cultivation is probably the largest anthropogenic source of methane. Methane release depends on cultivar choice (*van der Gon*, 2000), irrigation management (*Sass et al.*, 1992), and fertilization (*Schimmel*, 2000). Mitigation strategies are one focus in literature (cf. *Sass et al.* (1991, 1992); *Cai et al.* (2000); *Denier van der Gon et al.* (2002)) and include, for instance, changes in water management (*Li et al.*, 2005). Methane emissions by ruminants can be reduced via dietary adjustments (*McGrabb et al.*, 1997). Similarly, CH_4 escaping from landfills, coal mining and oil and natural gas systems can be reduced or captured (*Hogan et al.*, 1991; *de la Chesnaye F. et al.*, 2001), with economic benefits that can offset the costs. The intricacy of the problem lies in the fact that the largest share in methane reductions is feasible in developing countries, i.e. in regions where energy consumption (and thereby CO_2 emissions) is expected to rise strongly in the coming decades. However, developing countries do not have to comply with the Kyoto Protocol and financial incentives for reducing emissions are lacking.

Methane, ozone, carbon monoxide and NO_x are intricately coupled via atmospheric chemistry. Amongst them, only methane and ozone are direct greenhouse gases. *Shindell et al.* (2005) finds that a 100% reduction in anthropogenic methane emissions would reduce radiative forcing by $0.79\ Wm^{-2}$, a value that is larger than the abundance based radiative forcing estimates of *IPCC* (2001) ($0.61\ Wm^{-2}$). The main reason for the discrepancies with respect to the *IPCC* (2001) estimates is that, in the absence of other ozone precursor emissions, methane emissions alone would have lead to more methane than is currently present (*Shindell et al.*, 2005). Interestingly, due to the chemical coupling, a possible reduction in NO_x emissions would, although desirable, lead in turn to an increase in methane abundances and thereby global warming.

To summarize, reducing anthropogenic methane emissions is a viable measure to mitigate global warming but future scenarios strongly depend on developing countries. While economic prosperity often goes hand in hand with higher consumption of fossil fuels (see *Aldhous* (2005) for the unprecedented example of China's booming economy), methane, carbon monoxide and black carbon emissions (*Ramanathan et al.*, 2005) can be substantially reduced having higher industrial standards. Monitoring changes in atmospheric abundances of the species of interest (and thereby emissions) on a global scale is indispensable for a better understanding of the budgets and assessment of possible mitigation measures. Further, global maps as derived in this study are a direct and easily understandable proof of, e.g., methane emissions by rice paddies. Slightly unscientifically spoken, global maps of trace gas distributions derived from actual measurements (and not models) are supposed to be more accessible (and convincing) to policymakers and might have more public outreach than complicated graphs.

…

Appendix A

Absorption Spectroscopy of Atmospheric Trace Gases

This section provides a slightly more detailed overview over absorption spectroscopy and radiative transfer in the near infrared. Hence, some issues are repeated.

A.1 The Beer-Lambert Law

It is found experimentally that the extinction of radiance by matter depends linearly on the incident radiance and the amount of absorbing matter along the beam. Thus, the extinction of light along an infinitesimal path ds and a single absorber can be described by the well known *Beer-Lambert Law*:

$$dI(\lambda) = -I(\lambda)c(s)\sigma(\lambda, p, T)ds \,. \tag{A.1}$$

Here σ denotes the wavelength dependent absorption cross section (also depending on temperature T and pressure p, cf. Sec. C) and $c(s)$ denotes the number concentration of the absorbing species ($\mathsf{molecules/m^3}$).

Integration of equation A.1 yields the relationship between the incident intensity $I_0(\lambda)$ at $s = 0$ and the transmitted intensity $I(\lambda)$:

$$I(\lambda) = I_0(\lambda) \exp\left(-\tau\right) \,, \tag{A.2}$$

where

$$\tau(\lambda) = \int \sigma(\lambda, p, T)c(s)ds \,. \tag{A.3}$$

The dimensionless quantity τ is called optical density, opacity or optical depth. In case of multiple absorbers, equation A.2 has to take into account optical densities of several absorbing species:

$$I(\lambda) = I_0(\lambda) \exp\left(-\sum_i \tau_i\right) \,, \tag{A.4}$$

where τ_i denotes the optical density of absorber i.

In most cases, the DOAS approach simplifies equation A.3 by assuming that σ does not strongly depend on temperature and pressure or that pressure and temperature along the path ds are constant:

$$\tau_i(\lambda) = \int \sigma_i(\lambda, p, T) c_i(s) ds \ \approx \sigma_i(\lambda) \int c_i(s) ds \, . \tag{A.5}$$

The integration of the number concentration $c_i(s)$ of species i along the light path can be further summarized to the slant column density SCD:

$$SCD_i = \int c_i(s) ds \, . \tag{A.6}$$

Theoretically, each measurement integrates over a variety of light paths. Especially in the UV spectral region, or in the presence of aerosols or clouds, multiple scattering complicates the determination of a *typical* light path. *Marquard et al.* (2000) have shown that especially in the case of scattered radiation there is a nonlinear relationship between the absorption cross section and the total optical depth because the strength of the absorption influences the light path distribution. If strong absorbers are involved, the distribution of the light paths will therefore be a function of the absorption cross section.

Considering the near infrared region, it is far easier to determine the light path since atmospheric scattering is nearly negligible. Even in the case of strong absorbers like $\mathsf{CH_4}$ or $\mathsf{H_2O}$ the relative amount of scattered radiation is very small. Nevertheless, aerosols could influence the radiative transfer even in the near infrared.

A.2 Differential Optical Absorption Spectroscopy (DOAS)

Solving equation A.4 for the optical density linearizes the problem with respect to the optical densities for each absorber:

$$\sum_i \tau_i \ = -\ln\left(\frac{I(\lambda)}{I_0(\lambda)}\right) \, . \tag{A.7}$$

The difficulty is that not only the atmospheric species of interest are absorbing. Rayleigh and Mie scattering also contribute to the total extinction within the atmosphere. Since the absorptions due to transitions (electronic, vibrational or rotational) of atmospheric molecules are strongly varying with wavelength, it is fairly easy to discriminate between *high frequency* absorptions of atmospheric molecules and *low frequency* absorptions due to, e.g., scattering processes. The low frequency extinction can be simply modeled by a low order polynomial.

Thus, the total optical density τ_{tot} consists of the sum of optical densities of each absorber (including the so-called Ring spectrum accounting for inelastic scattering that leads to a filling-in of strong Fraunhofer lines) and a low order polynomial of degree n attributed to low frequency extinction processes (such as scattering in general or absorption by the earth's surface):

$$-\ln\left(\frac{I(\lambda)}{I_0(\lambda)}\right) = \tau_{tot}(\lambda) = \sum_i SCD_i \cdot \sigma_i(\lambda) + \sum_{x=0}^{n} a_x \lambda^x \, . \tag{A.8}$$

The parameter vectors $\overrightarrow{SCD}$ and $\overrightarrow{a}$ are then retrieved by minimizing χ^2 (the squared euclidian norm $\|\cdot\|_2$ of the residual vector):

$$\chi^2(\overrightarrow{SCD}, \overrightarrow{a}) = \left\| \ln\left(\frac{I(\lambda)}{I_0(\lambda)}\right) + \sum_i SCD_i \cdot \sigma_i(\lambda) + \sum_{x=0}^{n} a_x \lambda^x \right\|_2^2 \rightarrow min\,. \tag{A.9}$$

The linear least squares approach is suitable in this case since the system of equations is strongly overconstrained (number of spectral points $\gg$ parameters to be retrieved). Usually also a spectral shift and squeeze of the wavelength grid is allowed. This results in a nonlinear problem that has to be solved by using e.g. the Levenberg-Marquardt algorithm (*Levenberg*, 1944; *Marquardt*, 1963).

A detailed description of the fitting routine is given by *Platt* (1994), *Leue et al.* (2001) or *Wenig* (2001).

A.3 The Forward Model

Based on the inverse theory of *Rodgers* (2000), this section describes the forward radiative transfer model, determining the dependence of the measurement on the quantities to be retrieved. Since the measurement depends on the spectrometer as well, the instrumental function is included in the forward model. The forward model has to be evaluated with a relatively fine wavelength grid in order to account properly for high frequency absorptions. This grid is usually much finer than the resolution of the instrument (typically about 0.001 nm).

A.3.1 Simplified Radiative Transfer

For the nadir viewing geometry of remote sensing instruments like SCIAMACHY, the modelling of the radiation is substantially simplified if scattering as a source term can be neglected. In the near infrared spectral region this simplification is appropriate in the absence of aerosols.

Using this simplification, the reflected upwelling radiance I^+ from the earth's surface (assumed to be a lambertian reflector) measured by a space-borne satellite in a plane parallel atmosphere is simply

$$I^+ = F\frac{A}{\pi}\mu_0 \exp\left(-\frac{\tau_{tot}}{\mu_0}\right) \exp\left(-\frac{\tau_{tot}}{\mu}\right) , \tag{A.10}$$

where

A = Lambertian albedo$[0 \ldots 1]$
F = solar irradiance
μ_0 = cosine of the solar zenith angle
μ = cosine of the line of sight zenith angle
τ_{tot} = total vertical optical depth of the atmosphere.

The logarithm linearizes the equation with respect to the optical density:

$$\ln\left(\frac{I^+}{F}\right) = \underbrace{\ln\left(\frac{A}{\pi}\mu_0\right)}_{const} - \underbrace{\left(\frac{1}{\mu_0} + \frac{1}{\mu}\right)}_{AMF_{\mathsf{geom}}} \tau_{tot} \tag{A.11}$$

The total vertical optical depth can be described as the sum of the respective optical densities of each trace gas and extinction due to low frequency scattering and absorption (extinction = absorption+scattering), which can be parameterized by a low order polynomial:

$$\tau_{tot} = \sum_i \underbrace{\left[\int_{z=0\mathsf{km}}^{z_{\mathsf{max}}} \sigma_i(\lambda, p(z), T(z)) c_i(z) dz\right]}_{\tau_i} + \underbrace{\sum_{x=0}^{n} a_x \lambda^x}_{\tau_{ex}} , \tag{A.12}$$

with z denoting the height above the earth's surface and z_{max} the top of atmosphere (a rather arbitrary definition). The absorption cross sections strongly depend on temperature and pressure. Hence the total optical density of an absorber cannot be given by a single absorption cross section. The integral in eq. (A.12) describing the total vertical optical density of species i can be approximated by the sum of the optical density of individual height layers j of height Δz_j in which temperature and pressure are assumed to be nearly constant:

$$\tau_i \approx \sum_j \sigma_i(\lambda, p(z_j), T(z_j)) \cdot c_i(z_j) \cdot \Delta z_j \tag{A.13}$$

Neglecting scattering, the slant optical density is simply the total vertical optical density multiplied with the geometric air mass factor (AMF_{geom}, see eq. (A.11)). If scattering processes are considered, the air mass factor can depend on height and box air mass factors should be introduced (see e.g. *Friedeburg* (2003)):

$$\tau_i^{\mathsf{slant}} \approx \sum_j AMF_j \cdot \sigma_i(\lambda, p(z_j), T(z_j)) \cdot c_i(z_j) \cdot \Delta z_j \tag{A.14}$$

Thus, the influence of scattering processes can be easily implemented in the retrieval scheme. Since Rayleigh scattering can be neglected in the near infrared, only the impact of aerosols and clouds on the box air mass factors warrants further investigations.

So far, each box has been weighted equally. This simplification is, however, not always valid, especially at high solar zenith angles. Even if scattering is neglected, the curvature of the earth and refraction lead to different air mass factors at different heights. However, at high solar zenith angles, the uncertainties are, in general, much higher and these values will probably be omitted in the evaluation if high accuracy has to be achieved.

In this study, the profiles of temperature, pressure and mixing ratios are taken from standard profile catalogues as the U.S. standard atmosphere, provided by the source code of the radiative transfer models LOWTRAN/MODTRAN (*Kneizys et al.*, 1996).

A.3.2 Instrumental Function

A grating spectrometer like SCIAMACHY smoothes the incoming radiation $I(\lambda)$ by convoluting $I(\lambda)$ with the instrumental slit function $g(\lambda)$:

$$I_{meas}(\lambda) =< I(\lambda) >\equiv \frac{\int\limits_{-\infty}^{\infty} I(\lambda')g(\lambda-\lambda')d\lambda'}{\int\limits_{-\infty}^{\infty} g(\lambda-\lambda')d\lambda'} \,. \tag{A.15}$$

For the sake of simplification in the following the application of the instrumental slit function is denoted by the symbol $< \cdot >$. The shape of the instrumental slit function is often described by a gaussian function. Especially the near infrared channels of SCIAMACHY seem to have a broader slit function at the wings. This can be described by a Voigt function (see eq. (C.5)) with two parameters, namely the Lorentzian halfwidth γ_L and the Gaussian halfwidth γ_G. These parameters are also often described in terms of the Full Width at Half Maximum ($FWHM_L$ and $FWHM_G$). Generally, the width of the slit function is broader than the spectral distance between the detector pixels. This means that the slit function maps the actual signal at a certain wavelength to different detector pixels. The sampling rate is often below the Nyquist-sampling frequency, hence undersampled (often only 2 pixels per $FWHM$, c.f. *Chance et al.* (2005)).

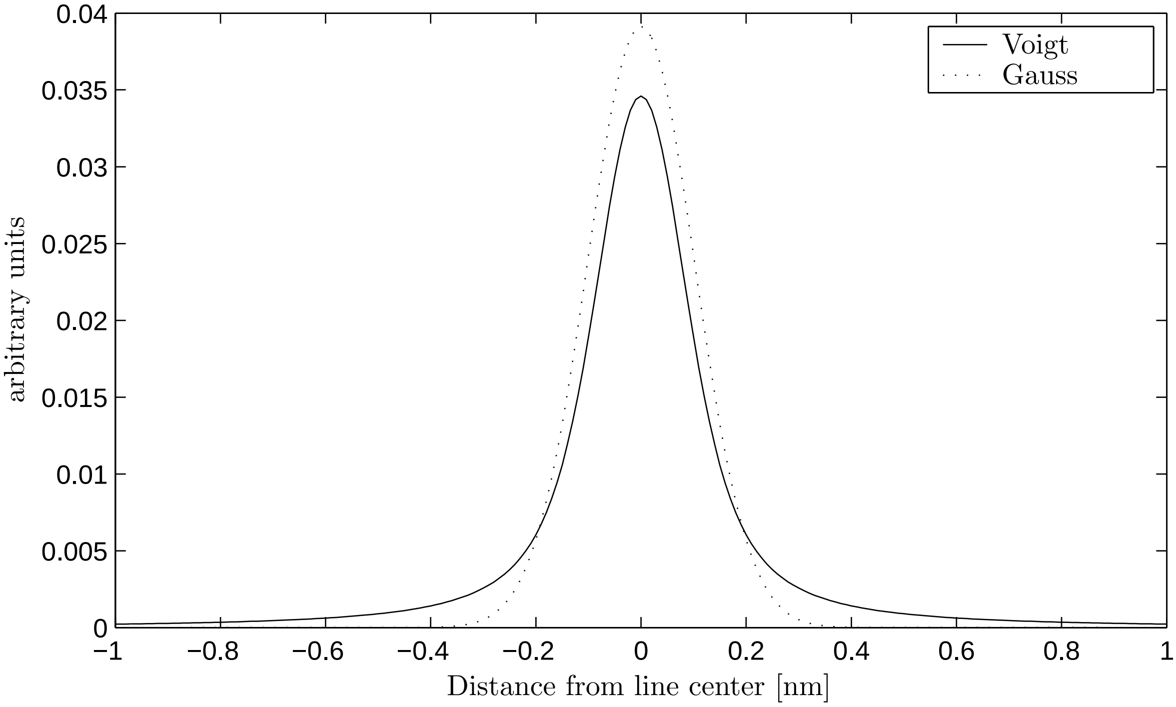

Figure A.1: Gaussian and Voigt slit function. The gaussian slit function has a $FWHM$ of 0.24 nm and the Voigt function a gaussian $FWHM$ of 0.075 nm and a lorentzian $FWHM$ of 0.065 nm.

A.3.3 Nonlinearity due to the instrumental function

If strong absorbers are present, the slit function plays a crucial role in the analysis, because the problem becomes nonlinear if the width of the high frequency absorption lines is not fully resolved by the spectrometer. In other words, the convolution and exponentiation cannot be interchanged

$$< I_0 \exp(-\tau_{tot}) > \neq I_0 \exp(< -\tau_{tot} >) \,, \tag{A.16}$$

which has no strong impact if τ is small. Hence, this inequality is often neglected in UV/Vis DOAS applications because the optical depths of absorbers are relatively small ($\tau \ll 1$).

This nonlinearity can be quantified by simulating, using simplified assumptions, a SCIAMACHY measurement in one of the near infrared channels. For instance, the measurement of the optical density of water vapor was simulated by scaling a reference optical density τ^{ref} with a factor $x : \{0.0 \dots 3.0\}$. The reference optical density is simply the theoretical slant optical density of water vapor at a solar zenith angle of 60° assuming a U.S. standard atmosphere. The convolution of the high resolution transmission was performed with a gaussian function of 0.24 nm $FWHM$ and a spectral resolution of 0.001 nm. The theoretically measured optical density is simply

$$\tau^{meas}_{\mathsf{H_2O}}(x) = -\ln\Big(< \exp(-x \cdot \tau^{ref}) >\Big) \,. \tag{A.17}$$

The standard DOAS approach assumes that the measured optical density depends linearly on the factor x. If we look at the theoretically obtained optical density of a single detector pixel (considering the value of τ^{meas} only at one wavelength in the center of an absorption line) it is striking that the measured signal does not depend linearly on the factor x. This behavior is depicted in Fig. A.2. It should be mentioned that this is only an idealized modeled response of a single detector pixel but describes the general effect. The nonlinearity of the response of other pixels may be different. However, this idealized modeled measurement enables us to underline the need for a modified iterative DOAS method for trace gas retrieval.

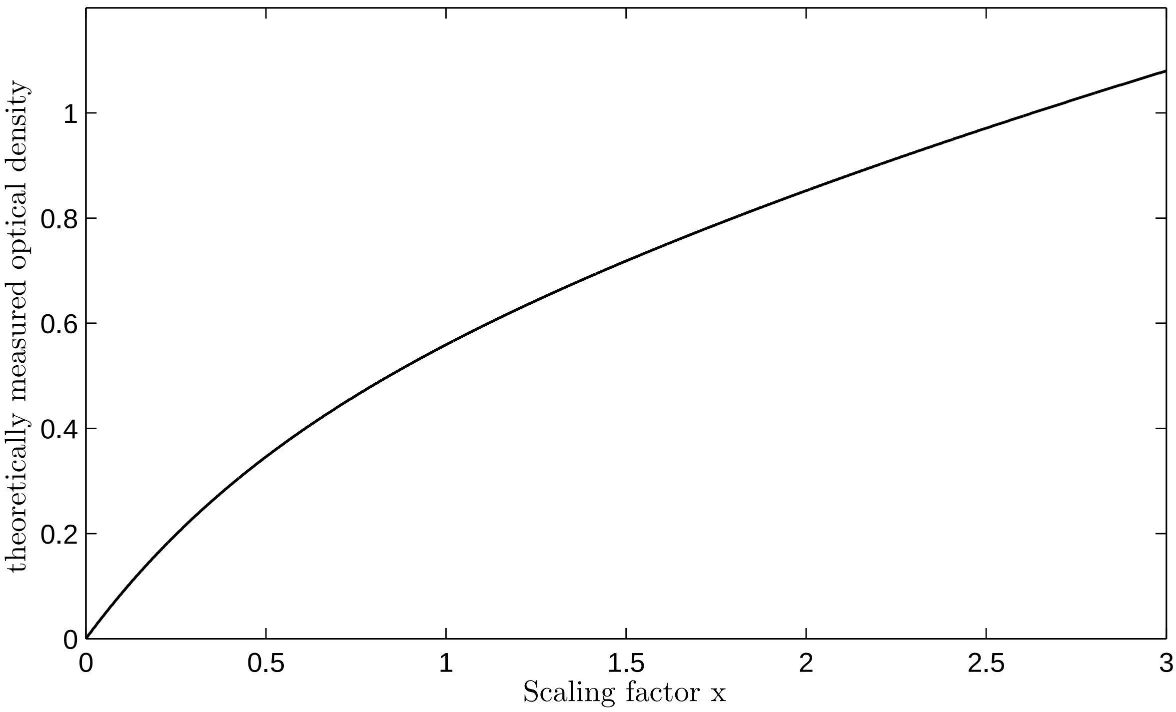

Figure A.2: Theoretical response of a SCIAMACHY detector pixel due to a concentration change (factor x times a standard concentration)

A.4 Effects of overlapping strong absorbers and its implications on the CO retrieval

CO is a relatively weak absorber in the near-infrared spectral region from 2320-2380 nm. Within this region there are several strong absorption features of CH_4 and H_2O. In Fig. A.3 the slant optical densities of the respective absorbers are depicted (note the different y-scale of the CO absorptions). As can be seen the absorptions of methane and water are far stronger than the CO absorptions. Hence, the task is to model the absorptions of the two strong absorbers properly in order to detect the CO absorptions.

The classical DOAS approach would fit the convoluted reference spectra to the measured optical density. Let $< \cdot >$ denote the convolution operation with the instrumental slit function (assumed to be gaussian or voigt). Since we are dealing with strong absorber, interchanging of exp and convolution is not allowed:

$$\exp\left(< -\sum_i \tau_i >\right) \neq < \exp\left(-\sum_i \tau_i\right) > . \tag{A.18}$$

In order to avoid this problem, one usually fits a modelled convoluted optical density τ_i^{mod} to the measurement:

$$\tau_i^{mod} = -\ln(< \mathrm{e}^{-\tau_i} >) . \tag{A.19}$$

These optical densities can also be seen in Fig. A.3 as black lines (in grey the original optical densities in high resolution (as seen by the atmosphere). Assuming that the modelled optical density is exactly the measured one there should be no error term (this is accomplished by an iterative DOAS scheme).

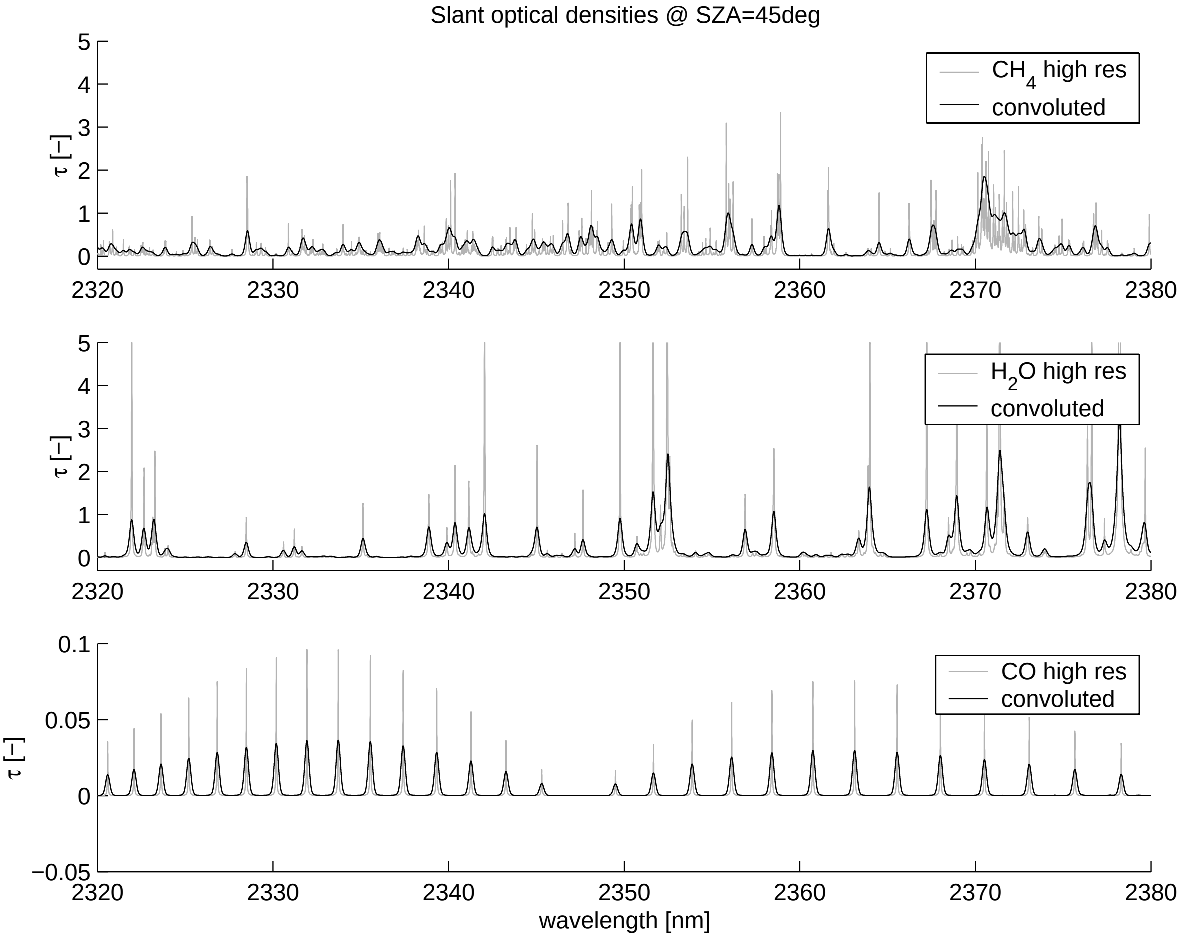

Figure A.3: Slant optical densities of $\mathsf{H_2O}$, $\mathsf{CH_4}$ and CO. Convolution has been performed in the intensity space.

However, we are dealing with two different strong absorbers in this spectral region. The respective optical densities are now denoted by $\tau_{\mathsf{CH_4}}$ and $\tau_{\mathsf{H_2O}}$. The (idealized) radiation seen by the detector is

$$< I_0 \exp\left((-\tau_{CH_4} - \tau_{\mathsf{H_2O}} - \sum_j b_j \right) > . \tag{A.20}$$

b_j is the low frequent polynomial associated with Raleigh, Mie and other broadband extinction processes. The convolution do not strongly affect the low frequent structures, hence

$$< I_0 \exp\left(-\tau_{\mathsf{CH_4}} - \tau_{\mathsf{H_2O}} - \sum_j b_j \right) >\approx I_0 \exp\left(-\sum_j b_j \right) < \exp(-\tau_{\mathsf{CH_4}} - \tau_{\mathsf{H_2O}}) > . \tag{A.21}$$

The optical density associated with methane was $\tau^{mod}_{\mathsf{CH_4}} = -\ln(< \mathsf{e}^{-\tau_{\mathsf{CH_4}}} >)$. In this case of two strong overlapping absorbers we have the problem that

$$< \exp(-\tau_{\mathsf{CH_4}} - \tau_{\mathsf{H_2O}}) > \neq - < \exp(-\tau_{\mathsf{CH_4}}) > - < \exp(-\tau_{\mathsf{H_2O}}) > . \tag{A.22}$$

This means that the absorptions of methane and water cannot be considered individually since they affect each other (similar to the saturation effect of a single absorber).

The error that will be made with respect to the modelled optical densities is

$$\triangle\tau = -\ln(<\exp(-\tau_{\mathsf{CH_4}}-\tau_{\mathsf{H_2O}})>)-(-\ln(<\exp(-\tau_{\mathsf{CH_4}})>)-\ln(<\exp(-\tau_{\mathsf{H_2O}})>))\ .\quad\text{(A.23)}$$

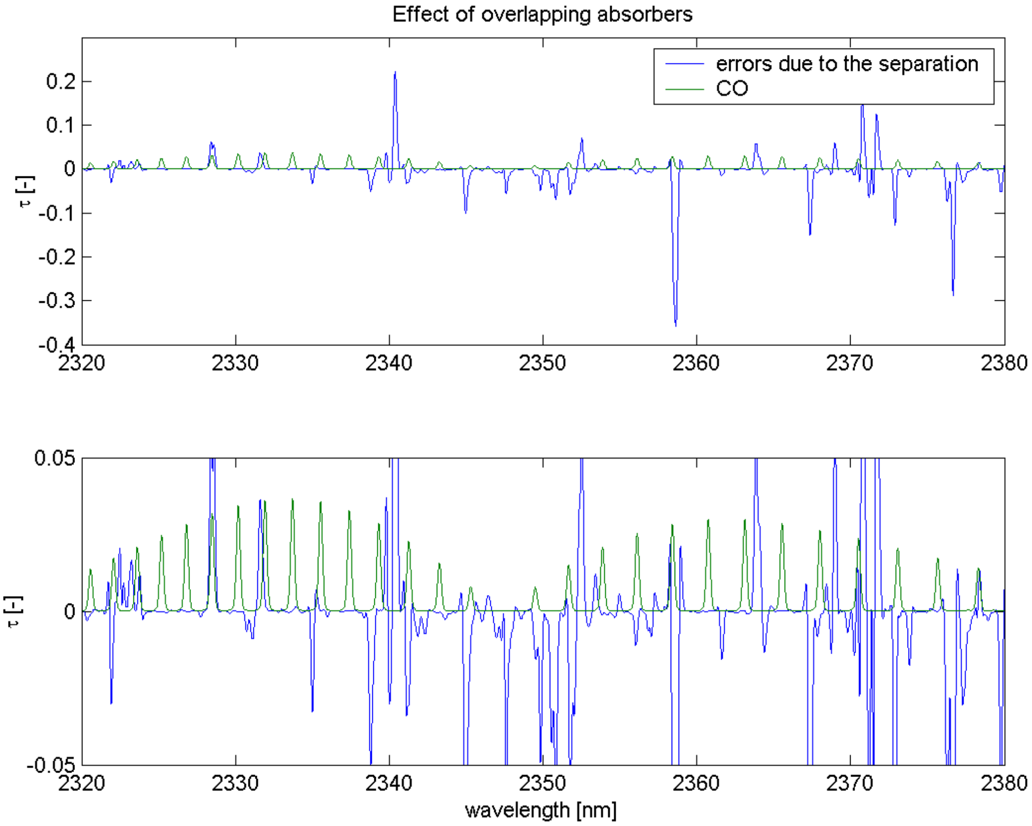

Figure A.4: $\triangle\tau$ in comparison with the CO absorptions (SZA=45°, US standard atmosphere)

In Fig.A.4 this error and the CO absorption features are shown. It is striking, that the error is far larger than the CO absorptions and thus cannot be neglected.

The only way to avoid this mistake is an iterative weighting function DOAS retrieval that uses $-\ln(<\mathsf{e}^{-\tau_{\mathsf{CH_4}}-\tau_{\mathsf{H_2O}}}>)$ as a linearization point.

Appendix B

Aerosol impact on the retrievals

So far, aerosols have been neglected in the retrieval of the total columns of CO_2 and CH_4. In the ratio, however, this effect largely canceled out. Here, I briefly describe how aerosols influence the light path distribution of a total column retrieval in different wavelength ranges. For that purpose, the radiative transfer model SCIATRAN 1.2 is applied (©University of Bremen, *Buchwitz et al.* (2000)). The aerosol optical properties in the model are mostly obtained from the software package OPAC (Optical Properties of Aerosols and Clouds, *Hess et al.* (1998)).

The air mass factor for a specific trace gas i can be defined as

$$AMF_i(\lambda) = \frac{1}{VOD_i(\lambda)} \ln\left(\frac{I^*(\lambda)}{I^\dagger(\lambda)}\right) , \tag{B.1}$$

where

$AMF_i(\lambda)$ = wavelength dependent air mass factor for species i,
$VOD_i(\lambda)$ = vertical optical density of species i,
$I^*(\lambda)$ = measured intensity if trace gas i is not present,
$I^\dagger(\lambda)$ = measured intensity if trace gas i is present.

Without scattering, the air mass factor does not depend on wavelength. This situation will change even in the near infrared if aerosols cannot be neglected any more. In the center of strong absorption lines, the relative fraction of light scattered back from aerosols within the atmosphere will be higher than on the wings or between absorption lines. Further, spectral changes in surface albedo and aerosol scattering properties induce a wavelength dependence of the air mass factor. If lines of different species overlap, there will be also a interdependency of the air mass factors of different molecules.

For the simulations two aerosol scenarios are applied. In the lowermost atmospheric layer up to 2 km height, a typical urban aerosol (OPAC definition) and between 2 and 10 km an average continental aerosol is chosen. The vertical profile of the two scenarios is depicted in Figure B.1. The only difference is that the aerosol load in the lowermost atmosphere is strongly enhanced in the *high* aerosol loading scenario.

Figure B.2 shows the impact of aerosols on the air mass factor of O_2 and CO_2. The O_2 air mass factor exhibits a strong wavelength dependency due to two reasons: first, the absorption lines are very strong and second, the aerosol optical density is substantially higher than in the CO_2 fitting window. Thus, the O_2 retrieval is quite sensitive to aerosols, especially at low

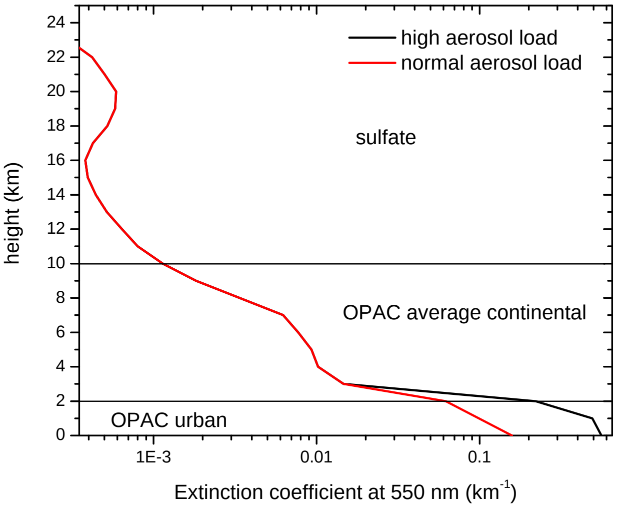

Figure B.1: Extinction coefficient profile of the two aerosol scenarios applied in the simulations. In addition, the aerosol type in the respective height layers is shown.

albedos. However, the strong wavelength dependence could also be used to derive information on aerosols. Depending on surface albedo, the mean air mass factor can be both higher and lower than the geometric one. In contrast to Rayleigh scattering, aerosol phase functions often exhibit a strong forward peak and only a small fraction of the incident radiation is scattered back. This has important implications for the light path distribution. If the surface albedo is high, the fraction of light scattered back from aerosols before impinging on the earth's surface is negligible. The aerosol phase function often only leads to an expansion of the angle of the light hitting the surface. Due to the nonlinearity of the air mass factor with respect to the incident angle, the air mass factor is thereby enhanced in comparison to a geometric one. If, however, the surface albedo is low, the backscatter fraction from the aerosols is gaining relative importance and the air mass factor is lower than the geometric one.

The challenging task is accurately characterize the impact of aerosol size distribution, height distribution and refractive index on the retrieval of O_2, CO_2 and CH_4. The most important question remains: to what precision can O_2 be applied as proxy for the light path distribution at distinct wavelengths? Large discrepancies between the light paths already exist in this tentative example using only two scenarios. At low albedos, for instance, we observe already the opposite effect of enhanced aerosol loadings for the air mass factors of O_2 (enhanced) and CO_2 (reduced). The general situation in the atmosphere will be far more complicated, uplifted aerosol layers might exist alongside with boundary layer aerosol of complex nature. Simple (single-scattering) radiative transfer codes fail to quantify these complex effects accurately. Only recently, scientific focus shifted to these issues, for instance in *van Diedenhoven et al.* (2005) and *Houweling et al.* (2005). For methane retrievals, these problems could be largely obviated by using CO_2 retrievals in a neighboring spectral window as proxy. For CO_2 itself, not only the precision requirements are more stringent but a suitable proxy in direct spectral proximity is also missing.

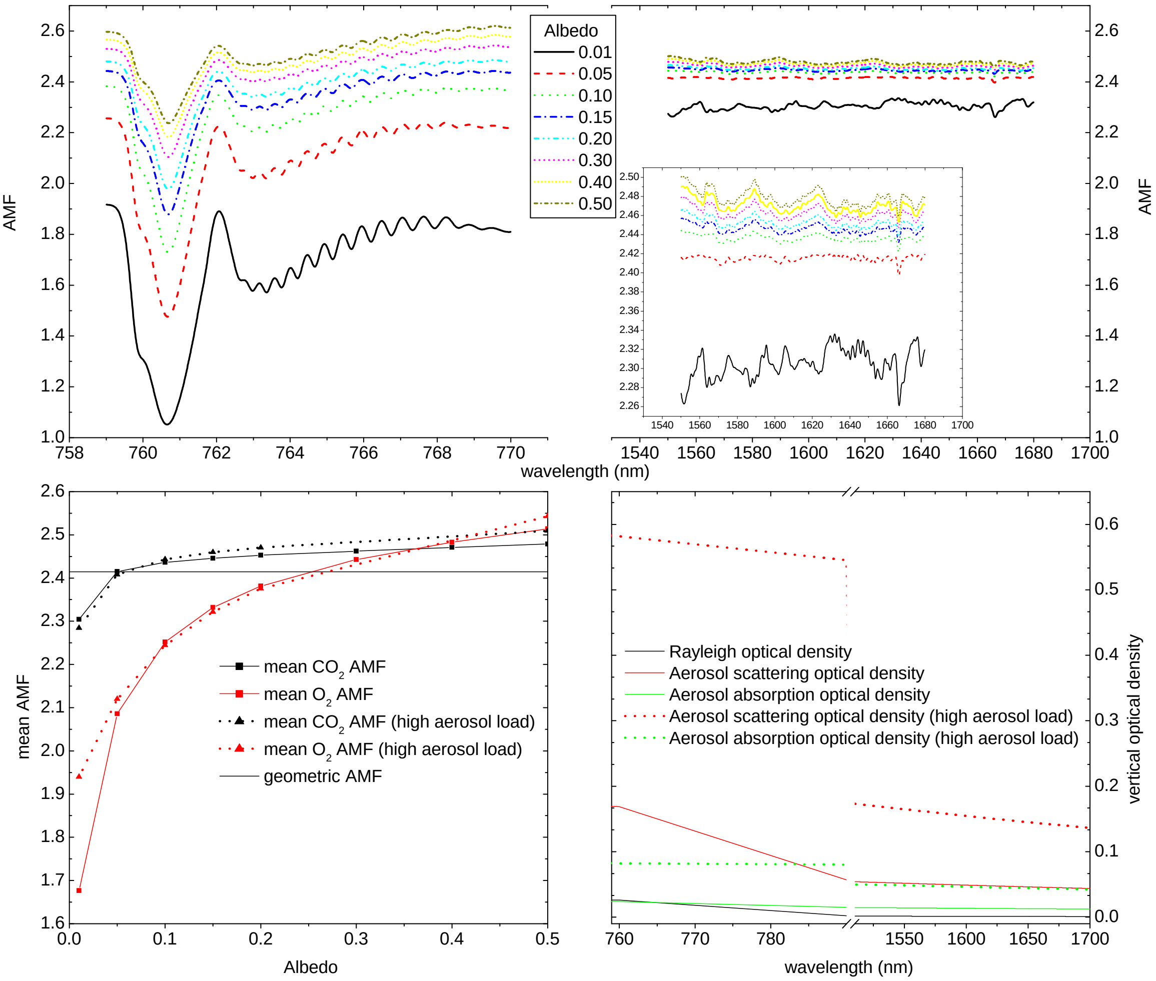

Figure B.2: Impact of aerosols and surface albedo on the air mass factor in the near infrared. A nadir measurement at a solar zenith angle of 45° has been simulated with SCIATRAN. The upper two panels show the air mass factors for O_2 (left) and CO_2 (right), respectively for different surface albedos and a *normal* aerosol load. The high resolution air mass factors haven been convolved (weighted with intensity) with a Gaussian slit function (FWHM=0.35 nm for O_2 and 1.35 nm for CO_2). The lower left panel shows the mean air mass factor of O_2 and CO_2 as a function of surface albedo for two different aerosol scenarios, the aerosol optical density of which is depicted in the lower right panel.

Appendix C

Calculation of Reference Cross Sections

In contrast to the UV/Vis spectral region, absorption of light by molecules in the near infrared region is mainly due to vibrational and rotational transitions whose ground state population distribution is strongly temperature dependent. Hence, their respective cross sections strongly depend on temperature and pressure. A single cross section can therefore not be used as reference for the entire atmosphere. A common approach to overcoming this problem is to divide the atmosphere into several height layers and calculate vertical optical densities of the respective layers according to an assumed profile of pressure, temperature and mixing ratio (see e.g. *Buchwitz et al.* (2000)). For weak absorbers, as is often the case in the UV/Vis spectral region, the shape of the absorption lines does not have a strong influence on the retrieval, although there is often a substantial dependence on temperature and also pressure (see, for instance, *Nizkorodov et al.* (2004) who analyze the pressure and temperature dependence of NO_2 cross sections). Temperature determines the population of the lower states and is also often considered in UV/Vis DOAS.

Weighting each height layer equally the total vertical optical density is simply the sum of the respective optical densities of each height layer.

The task is now to compute optical densities or cross sections according to the temperature and pressure conditions prevailing in the respective layer. This chapter mainly describes the processes impacting intensity and shape of the absorption, hence also the retrieval. A more comprehensive and theoretical overview of the processes involved in the transitions can be found in *Herzberg* (1950) or *Thomas and Stamnes* (1999). Charlie Zender provides Freely Available Community Texts (FACTs) also on radiative transfer, including a detailed treatment of line shapes (http://dust.ess.uci.edu/facts/).

C.1 General Description of Absorption Cross Sections

In the case of Local Thermodynamic Equilibrium (LTE), where frequent inelastic collisions of the molecules maintain the distribution of the ground states in thermodynamic equilibrium (also called a *thermal bath* for the absorbers), the absorption cross section of a single transition line $\sigma_i(\nu)$ can be written as the product of the line intensity S_i and a frequency dependent part determining the line shape $\Phi_i(\nu)$ (*Thomas and Stamnes*, 1999):

$$\sigma_i(\nu) = S_i \Phi_i(\nu) \,. \tag{C.1}$$

The total absorption cross section of the molecule $\sigma_{tot}(\nu)$ or simply $\sigma(\nu)$ considering all transitions can then be described as the sum of all individual cross sections:

$$\sigma_{tot}(\nu) = \sum_i \sigma_i(\nu) \,. \tag{C.2}$$

Strictly speaking, eqn. (C.2) is only valid when each transition can be treated separately (i.e. as isolated lines). If lines are overlapping e.g. due to pressure broadening, this simple summation is not valid any more. However, this effect, called *collisional narrowing*, has been neglected so far. Since we are dealing with absorptions close to saturation, the actual line shape influences the degree of saturation and, in turn, the sensitivity of the retrieval.

Considering nadir measurements, most of the absorption takes place in the troposphere where optical collisions between molecules result in a lifetime of the upper state that is much longer than the radiative lifetime. Thus, LTE can be assumed which simplifies the calculation of state populations (see Sec. C.3). Considering, for instance, mesospheric limb measurements, this assumption might not be valid and non-LTE thermodynamic has to be considered. The same holds for the O_2 band at 1.27 mym where the relatively short radiative lifetime of 2.7 s (*Brasseur and Solomon*, 1996) results in air-glow at low ambient pressure.

C.2 Line Broadening

The line transitions do not take place at discrete spectral positions but at a broadened interval around the line center ν_0. One reason for this is the uncertainty in the knowledge of the lifetime Δt of the energy state (*Thomas and Stamnes*, 1999). According to Heisenberg's Uncertainty Principle, this leads to an uncertainty in the energy of the transition, hence leading to an uncertainty of the transition frequency. This process is called *natural broadening.* Assuming that the uncertainty in the lifetime is proportional to the lifetime t_r itself ($\Delta t \propto t_t$), a reduction of the lifetime leads to an increased broadening (since $\Delta E \Delta t \approx \frac{h}{2\pi}$).

C.2.1 Pressure Broadening

The natural lifetime of an energy state is often too long to have a substantial impact on the line-broadening process. Optical collisions between molecules effectively reduce the lifetime of the upper state (*Thomas and Stamnes*, 1999). As in the case of natural broadening, pressure broadening of lines is governed by a Lorentz line shape

$$\Phi_L(\nu) = \frac{\gamma_L}{\pi[(\nu - \nu_0)^2 + \gamma_L^2)]} \,, \tag{C.3}$$

with γ_L denoting the Lorentzian halfwidth of the broadened line.

The width depends linearly on the collision frequency with other molecules, hence it is proportional to the mean velocity of the molecules and inverse proportional to the mean free path. In theory, pressure broadening is thus proportional to pressure and inverse proportional to the square root of the temperature. The dependence as calculated in this study is briefly described in Sec. C.3.2.

C.2.2 Doppler Broadening

The relative speed of the absorbing molecules with respect to the incident light source leads to a small doppler shift of the absorbed (and emitted) frequency. Considering the one-dimensional Maxwell-Boltzmann distribution with the mean velocity $\overline{|v|}$ ($\overline{|v|} = \sqrt{2k_BT/m}$) it can be shown that the line shape of a purely doppler broadened line can be described by a Gaussian function (*Thomas and Stamnes*, 1999; *Goody and Yung*, 1989):

$$\Phi_D(\nu) = \frac{1}{\sqrt{\pi}\gamma_D} e^{-(\nu-\nu_0)^2/\gamma_D^2}\,, \tag{C.4}$$

with

$$\begin{aligned} \gamma_D &= \frac{\nu_0}{c}\overline{|v|} = \frac{\nu_0}{c}\sqrt{2k_BT/m} \\ m &= \text{molecular weight}\,. \end{aligned}$$

C.2.3 Combined Doppler and Pressure Broadening

Assuming that the processes of doppler and pressure induced broadening are completely independent, the resulting combined line shape is described by a so called *Voigt* profile (*Thomas and Stamnes*, 1999; *Goody and Yung*, 1989):

$$\Phi_V(\nu) = \frac{y}{\pi^{3/2}\gamma_D} \int_{-\infty}^{\infty} \frac{\exp(-t^2)}{(x-t)^2 + y^2}\,, \tag{C.5}$$

with y denoting the ratio γ_L/γ_D and x the distance from the line center in units of the Lorentzian halfwidth ($x = (\nu - \nu_0)/\gamma_D$).

Since the integral cannot be solved analytically, it has to be computed numerically. In literature, many computationally efficient methods are described. Most of them are based on the method of *Humlíček* (1982) and in this study, the new implementation by *Kuntz* (1997) was implemented in a C++ program. For the sake of computational efficiency, a wing cutoff is normally chosen as the maximum distance from the line center that is considered in the computation of Φ_V. In this study a wing cutoff of 20cm^{-1} was chosen.

C.2.4 Discussion

The Lorentz line shape described before is based on certain simplifications. Hence, the resulting actual shape of the line may differ from the computed one. Especially the shape of the far wings is sometimes only poorly described by a Voigt line shape. Considering only pressure broadening, the absorption coefficient at frequencies with a large displacement from the line center is proportional to the pressure (c.f. *Goody and Yung* (1989, Chap. 3.3)). Especially when the line centers are in saturation (optical densities $\gg 1$) the line wings play a more important role in the DOAS analysis because they contribute most to the weighting functions when the line center is already in saturation. Furthermore, line broadening due to collisions with water vapor can have a different influence than collisions with other molecules. This effect is so far not quantified.

The aforementioned problems and the fact that the exact shape of the far wings is generally not known exactly will result in errors in the DOAS analysis of absorbers in saturation. Thus, care has to be taken in the choice of an appropriate spectral window. At least some lines not in saturation should reside in the fitting window. Furthermore, the signal to noise ratio of pixels close to saturation strongly deteriorates. Hence, a suitable weighting of the respective pixels has to be chosen.

For a more comprehensive treatment of line shapes, the reader may be referred to *Goody and Yung* (1989); *Fano* (1963) and references therein.

C.3 The HITRAN Spectral Database

The HITRAN (HIgh-resolution TRANsmision) spectral database (*Rothman et al.*, 1998, 2003, 2005) provides information about spectroscopic line parameters of several molecules and their isotopes. All HITRAN data have been scaled to a temperature of 296K and a pressure of 1013.25mb. The parameters used in this study are summarized in table C.1. Furthermore, HITRAN provides estimations of the uncertainties of the respective parameters.

Table C.1: spectral line parameters provided by HITRAN

line parameter	description
$\nu_{\eta\eta'}$	line transition frequency [$\mathsf{cm^{-1}}$]
$S_{\eta\eta'}$	spectral line intensity [$\mathsf{cm^{-1}/(molec \cdot cm^{-2})}$] at $\mathsf{T_{ref}}$
γ_{air}	air-broadened halfwidth at half maximum [$\mathsf{cm^{-1}/atm}$] at $\mathsf{T_{ref}}$
γ_{self}	self-broadened halfwidth at half maximum [$\mathsf{cm^{-1}/atm}$] at $\mathsf{T_{ref}}$
E_η	lower state energy of the transition [$\mathsf{cm^{-1}}$]
n	coefficient of temperature dependence of γ_{air}
δ	air-broadened pressure shift [$\mathsf{cm^{-1}/atm}$]

C.3.1 Temperature correction of line intensity

Since HITRAN only provides data at standard temperature of 296K, the line strength has to be corrected when using different temperatures. Assuming local thermodynamic equilibrium (LTE), the population of the states can be described by Boltzmann statistics. The correction of the line intensity with respect to temperature is given by (*Rothman et al.*, 1998)

$$S_{\eta\eta'}(T) = S_{\eta\eta'}(T_{ref}) \frac{Q(T_{ref})}{Q(T)} \frac{\exp(-c_2 E_\eta/T)}{\exp(-c_2 E_\eta/T_{ref})} \frac{[1-\exp(-c_2\nu_{\eta\eta'}/T)]}{[1-\exp(-c_2\nu_{\eta\eta'}/T_{ref})]} \tag{C.6}$$

with

$$\begin{aligned} Q(T) &= \text{total internal partition function} \\ c_2 &= \text{second radiation constant} = hc/k = 1.4399\mathsf{cm/K}\,. \end{aligned}$$

The total internal partition is approximated by the product of the vibrational and rotational partition sums (*Thomas and Stamnes*, 1999):

$$Q(T) \approx Q_v(T)Q_r(T)\,. \tag{C.7}$$

The vibrational and rotational partition sums are the total, probability-weighted number of available vibrational and rotational states, respectively. In this study the total internal partition sum is parameterized as a fourth order polynomial of the temperature T (*Gamache et al.*, 1990). The polynomial coefficients are adapted from HITRAN.

The fourth term of the right hand side of equation C.6 is due to stimulated emission which is normally quite small in comparison to the Boltzmann term (third term). Hence the sensitivity of the line intensity with respect to temperature mainly depends on the lower state energy E_η. Neglecting spontaneous emission, equation C.6 can be written as

$$S_{\eta\eta'}(T) = S_{\eta\eta'}(T_{ref})\underbrace{\frac{Q(T_{ref})}{Q(T)}\frac{\exp(-c_2E_\eta/T)}{\exp(-c_2E_\eta/T_{ref})}}_{CF(E_\eta,T)} \tag{C.8}$$

summarizing the second and third terms of the right side as a correction factor $CF(E_\eta,T)$ depending on temperature and lower state energy. Taking a closer look at the correction factor CF in Fig. C.1, it is striking that it has an important influence on the line intensity. As expected, states exhibiting low energies are strongly preferred at low temperatures while states with relatively high energies are more densely populated at higher temperatures. The sensitivity of the correction factor can be described by the derivative of CF with respect to temperature. The relative change of CF given a temperature deviation of $1K$ is depicted in Fig. C.2. Especially at relatively high temperatures and high lower state energies the influence of the temperature appears to be strong (e.g. a temperature change of 10K at 290K and a lower state energy of 1800 cm^{-1} induces a change of $\approx 25\%$ of the line intensity). This has an important impact on the DOAS retrieval, since, if every line in the DOAS fitting window were to have the same lower state energy, one would not be able to distinguish between a change in concentration or simply a change in temperature. Especially in the case of long lived greenhouse gases, requiring high accuracy, this plays a major role.

Taking a closer look at the impact of the temperature on the line intensities exhibiting lower state energies about $\mathsf{200-300cm^{-1}}$ (Fig. C.3), it is striking that the impact of the temperature is relatively low and sometimes even negligible. In the spectral region from 2330 to 2370 nm, where also the CO absorption features are located, there are two overlapping strong absorbers, namely methane and water vapor. The transition lines of these two absorbers have significantly different lower state energies in that wavelength region. The resulting vertical optical density (assuming US standard atmosphere) and the lower state energies of the strongest absorption lines are shown in Fig. C.4. Since the lower state energies of water are generally far higher than those of methane, the sensitivity to temperature of water absorptions is stronger. This could result in uncertainties of the estimated vertical optical depth, for neither the VMR profile nor the temperature profile is known exactly. Regarding methane, one has to mention that

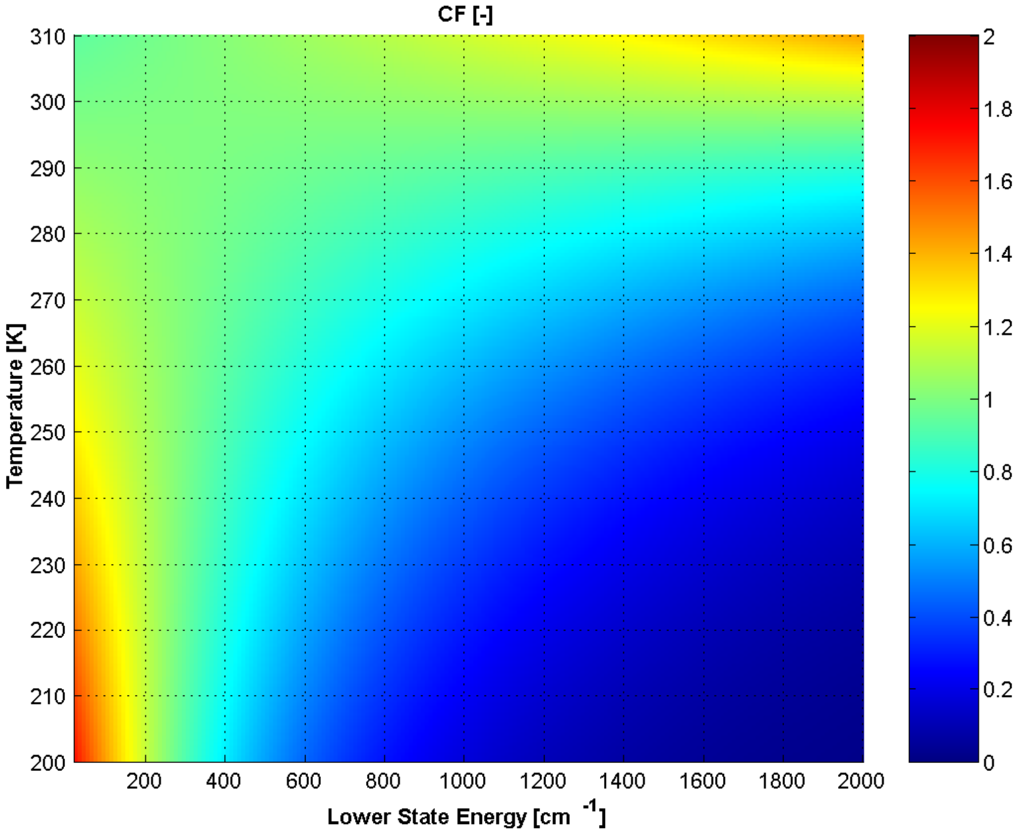

Figure C.1: Correction factor *CF* of methane as a function of temperature and lower state energy

the lower state energies are only given at discrete values (low accuracy, uncertainty about 50cm^{-1}). This can result in errors in the corrected line intensity and in the response to temperature changes.

Considering the stratosphere with the prevalent low temperatures, some water lines are strongly diminished (a correction factor approaching zero at about 1800 cm^{-1} and 220K). In the nadir viewing mode this has no strong impact on the measurements because the stratospheric absorptions are nearly negligible.

In order to attain exact results, one has to choose fitting windows where the lower state energies of the line transitions are strongly different, i.e. each line exhibits a different response to a temperature change. In this way, one can avoid the weighting functions becoming nearly linearly dependent, which hinders a sensible retrieval. In the case of a grating spectrometer like SCIAMACHY, this gets even more complicated since the instrumental slit function sometimes maps the signal of many absorption lines into a single detector pixel.

The temperature of the atmosphere is strongly varying in the troposphere, especially in the boundary layer, the region where most of the absorption takes place. Thus, the assumed temperature profile has an important influence on the retrieval to be quantified.

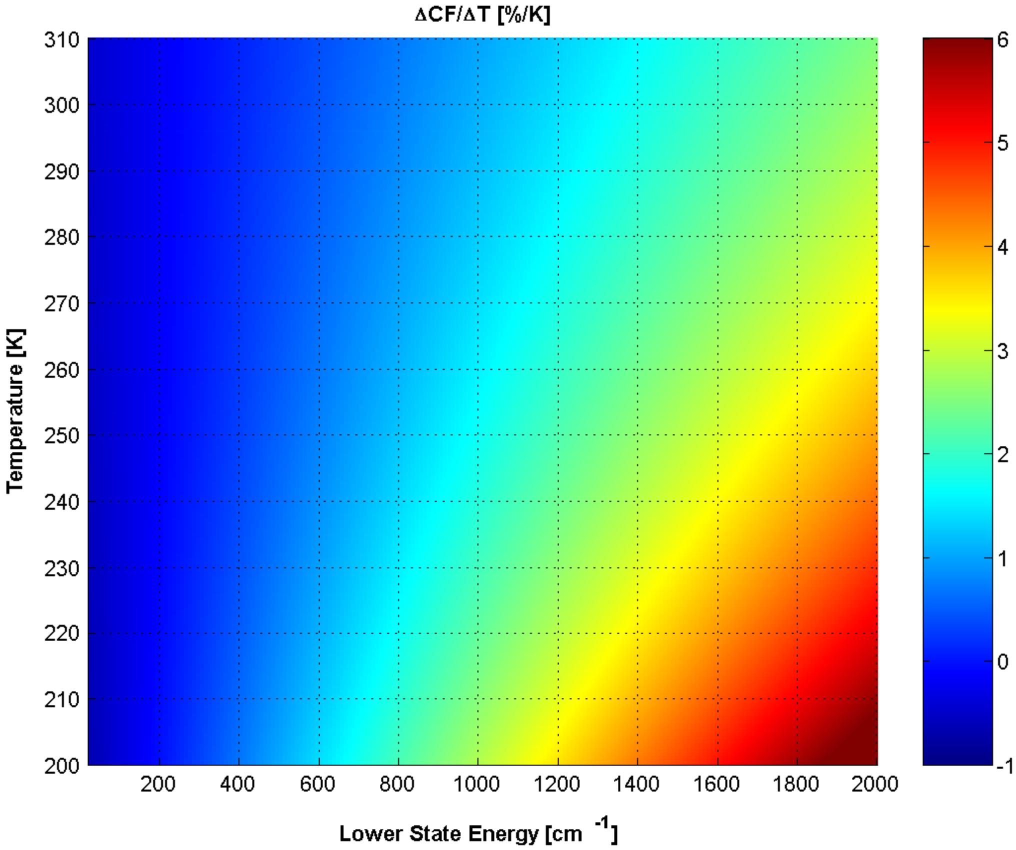

Figure C.2: Derivative of the correction factor CF of water vapor with respect to temperature from $20 - 2000\mathrm{cm}^{-1}$ (change given in percentage per Kelvin)

C.3.2 Temperature and pressure correction of line halfwidth and line position

According to *Rothman et al.* (1998) the effective pressure broadened halfwidth $\gamma_L(p,T)$ of a molecule at a partial pressure p_s [atm] is calculated as

$$\gamma_L(p,T) = \left(\frac{T_{ref}}{T}\right)^n \gamma_L^{air}(p_{ref},T_{ref})\frac{(p-p_s)}{p_ref} + \gamma_L^{self}(p_{ref},T_{ref})\frac{p_s}{p_ref} \,. \tag{C.9}$$

As described in Sec. C.2.1, the broadening depends on the collisions between molecules. Therefore, one has to distinguish between collisions of identical molecules (generally having a stronger effect, γ_L^{self}) and collisions with non-identical molecules (γ_L^{air}). In the case of trace gases with low partial pressures, self broadening can be neglected and the equation simplifies to

$$\gamma_L(p,T) = \frac{p}{p_{ref}} \cdot \left(\frac{T_{ref}}{T}\right)^n \gamma_L^{air}(p_{ref},T_{ref}). \tag{C.10}$$

Considering for instance O_2, this simplification might be crucial. In this study, self broadening was always considered. As already mentioned, the broadening coefficient due to water vapor might be different but is not quantified.

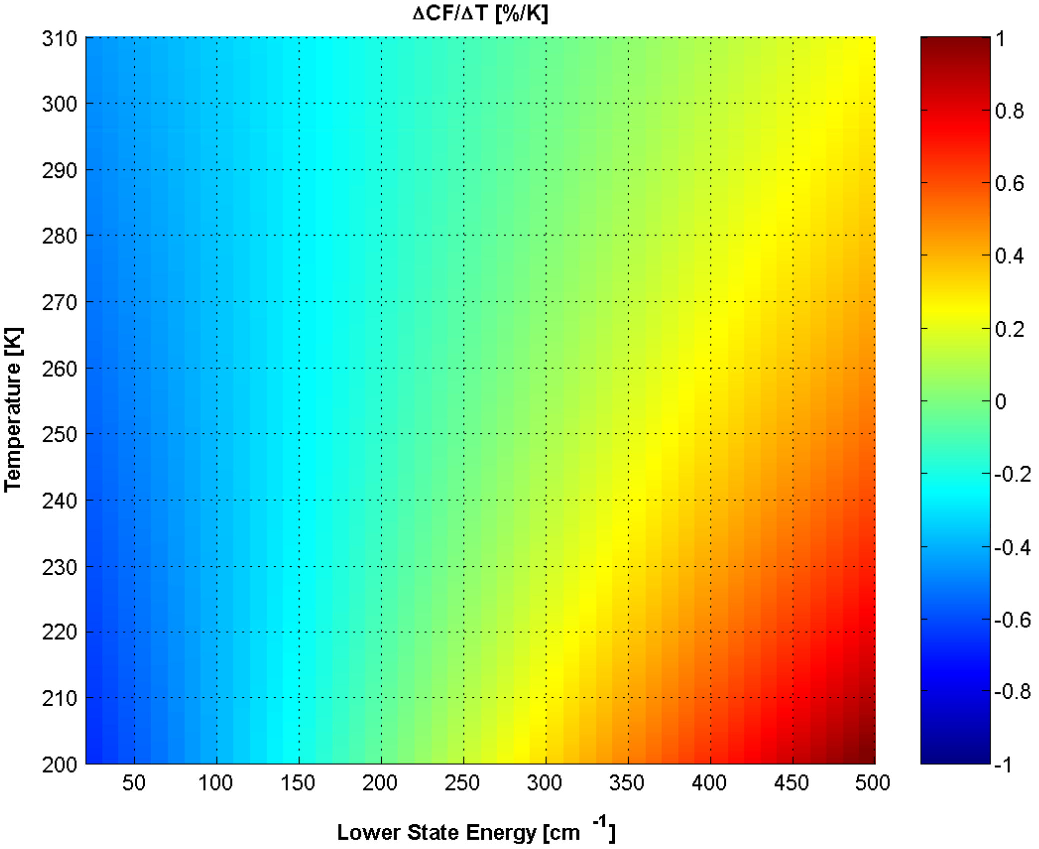

Figure C.3: Derivative of the correction factor CF of water vapor with respect to temperature from $20 - 500\text{cm}^{-1}$(change given in percentage per Kelvin)

As the line positions $\nu_{\eta\eta'}$ are given at vacuum, a pressure shift has to be included to compute the line centers at different ambient pressures (*Rothman et al.*, 2003; *Fano*, 1963):

$$\nu^*_{\eta\eta'} = \nu_{\eta\eta'} + \delta(p_{ref})p\,. \tag{C.11}$$

This effect is usually negligible in the UV/VIS spectral region because the effect in units of wavelength is rather small ($\Delta\nu/\Delta\lambda = 10^{-7}\lambda^{-2}$). In the near infrared region this could have an effect also due to the strong absorptions. Hence, it is implemented in the computing routines.

C.3.3 Uncertainties in transition parameters

HITRAN also provides error codes for the given parameters. In one of the most important wavelength regions (namely between 2320–2380 nm), the uncertainties in all parameters of water vapor are very high (all parameters have an error code of 0, see table C.2). This may account for systematic residuals in the DOAS fitting procedure. Furthermore, errors in the spectral parameters of the strong absorbers (i.e. of water and methane) can hinder a sensible retrieval of minor absorbers as CO, because the uncertainties can result in errors in the optical densities of the strong absorbers that are larger than the absorptions of the minor absorber itself. This is of special importance when the spectral lines are strongly overlapping.

For water, HITRAN provides only a single general pressure broadening coefficient of 0.64 in

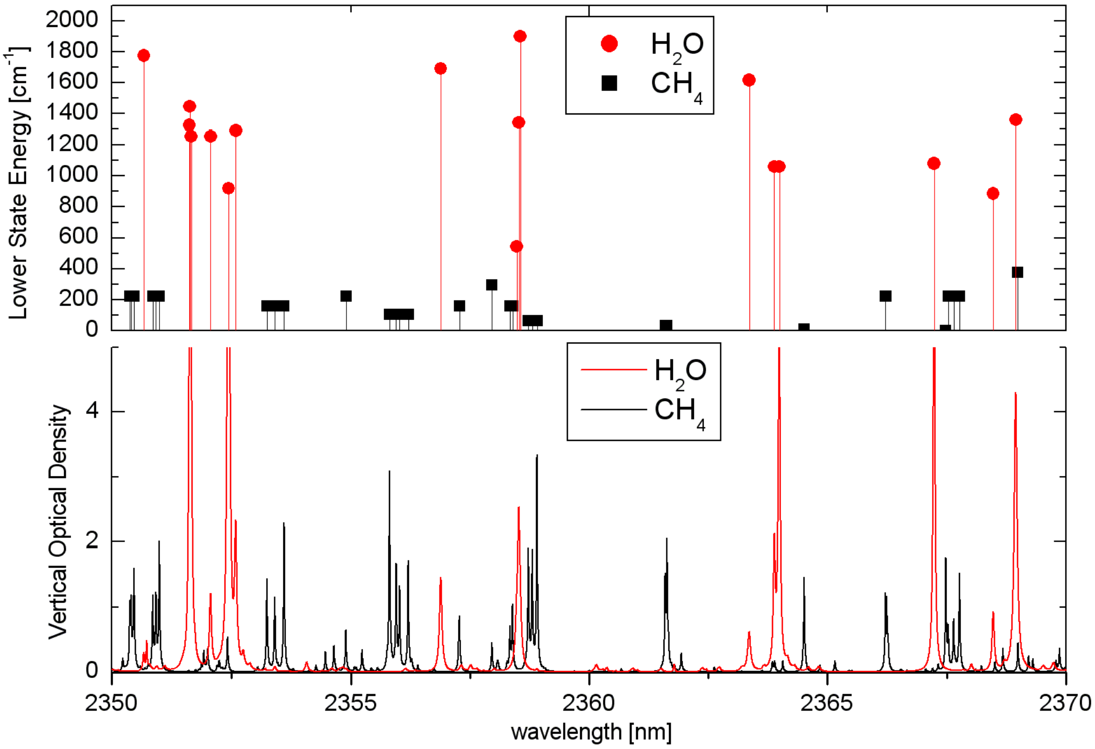

Figure C.4: Vertical optical densities and corresponding lower state energies of water vapor and methane. Only the lower state energies of the strongest lines (water: $\mathsf{S} > 10^{-24}\mathsf{cm/molec}$, methane: $\mathsf{S} > 10^{-21}\mathsf{cm/molec}$) are depicted.

the aforementioned region. As can be seen in Fig. C.5 the pressure broadening coefficient could have a strong influence on the resulting vertical optical depth. For this comparison, the pressure broadening coefficients were artificially scaled as 1.2 and 0.8. The coefficient of every transition line has been scaled with the same factor. The lower panel shows the variation of the resulting vertical optical densities computed with different coefficients.

In this case, the high resolution spectra were convoluted with a Gaussian instrumental slit function ($FWHM$=0.24 nm). A greater pressure broadening coefficient leads to a reduced saturation of the strong lines, hence to a stronger absorption after convolution (and vice versa for the reduced pressure broadening coefficient). The deviations of the resulting VOD's are, of course, similar to the VOD's itself. The VOD's of the respective simulations are now denoted as $\mathsf{VOD_x}$, x being the scaling factor of the pressure broadening coefficient. Performing a linear least squares fit of the pairs $(\mathsf{VOD_1};\mathsf{VOD_{1.2}})$ and $(\mathsf{VOD_1};\mathsf{VOD_{0.8}})$, the following results are obtained:

$$\mathsf{VOD_{1.2}} = \mathsf{0.9266} \cdot \mathsf{VOD_1}$$

$$\mathsf{VOD_{0.8}} = \mathsf{1.0961} \cdot \mathsf{VOD_1}$$

Thus, an uncertainty in the pressure broadening coefficient could result in a fit error of ≈ 10%. This uncertainty can also induce stable residuals that are depicted in Fig. C.6. As an example the residuals of the $(\mathsf{VOD_1};\mathsf{VOD_{1.2}})$ fit are shown ($RES = \mathsf{0.9266} \cdot \mathsf{VOD_{1.2}} - \mathsf{VOD_1}$). The variance of the residual is $\approx 1.3 \cdot 10^{-4}$.

Table C.2: Uncertainty Codes Used in HITRAN Database

Wavenumber and Pressure shift (cm^{-1})		**Intensity, Halfwidths, and Temperature-dependence**	
Code	Uncertainty Range	Code	Uncertainty Range
0	$\geq$ 1. cm^{-1} or Unreported	0	Unreported or Unavailable
1	$\geq$ 0.1 and $<$ 1.cm^{-1}	1	Default or Constant
2	$\geq$ 0.01 and $<$ 0.1cm^{-1}	2	Average or estimate
3	$\geq$ 0.001 and $<$ 0.01cm^{-1}	3	$\geq$ 20%
4	$\geq$ 0.0001 and $<$ 0.001cm^{-1}	4	$\geq$ 10% and $<$ 20%
5	$\geq$ 0.00001 and $<$ 0.0001cm^{-1}	4	$\geq$ 5% and $<$ 10%
6	Better than 0.000001 cm^{-1}	6	$\geq$ 2% and $<$ 5%
		7	$\geq$ 1% and $<$ 2%
		8	$<$ 1%

C.3.4 Discussion

The precise knowledge of the actual transition parameters is indispensable if minor absorbers are to be retrieved within a fit window that contains strong absorbers. The uncertainties in the line parameters of strong absorbers not only result in a systematic error, but also induce stable residual structures which can be of the order of the optical density of minor absorbers. If these residuals are not completely linearly independent of the absorption lines of minor absorbers, it will hinder a sensible retrieval.

Since the transition parameters provided by HITRAN in the wavelength range between 2200 and 2400 nm are of a relatively poor accuracy (recently updated in the latest version of HITRAN: *Rothman et al.* (2005)), further improvements in the quality of these parameters would be of substantial importance for the proper retrieval of CO. Another source of uncertainty is the actual vertical profile of temperature and water vapor concentration. As shown in Sec. C.3.1, the temperature has a strong impact on the line strength of water vapor. In the case of water vapor the actual vertical concentration profile as well as the temperature at the respective altitudes can vary strongly, which leads to uncertainties in the actual optical density of water vapor.

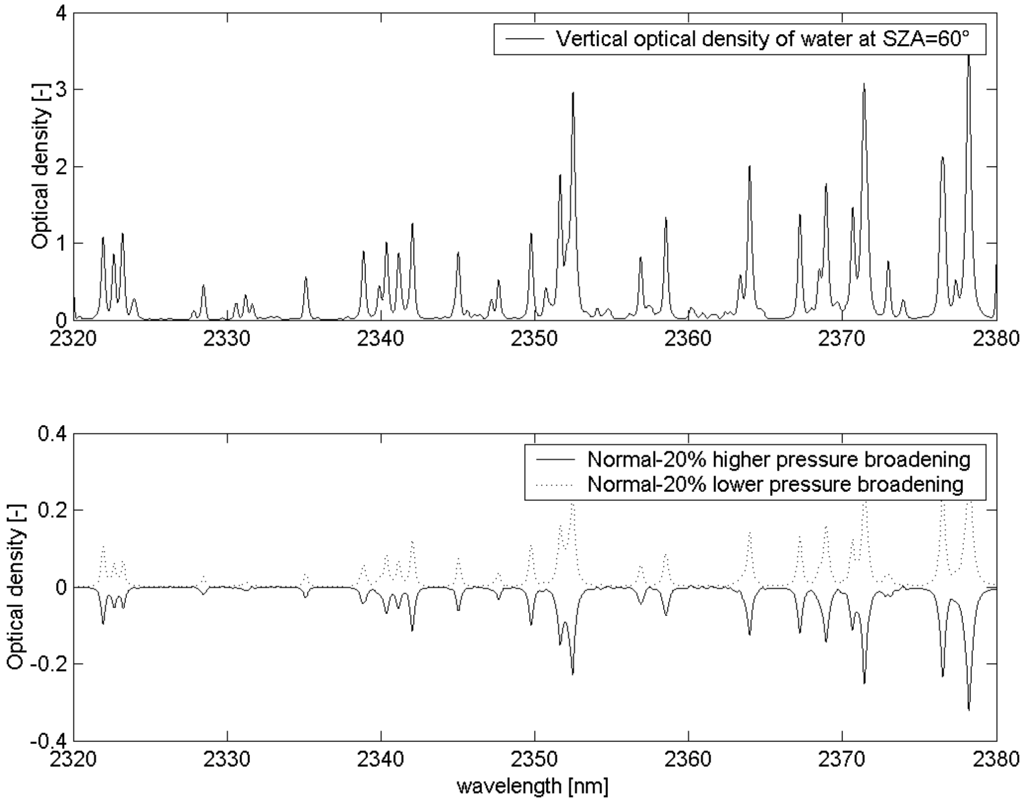

Figure C.5: Impact of a variation in the pressure broadening coefficient. An US standard atmosphere and a SZA of 60° is chosen. The slit function is gaussian with a FWHM of 0.24nm.

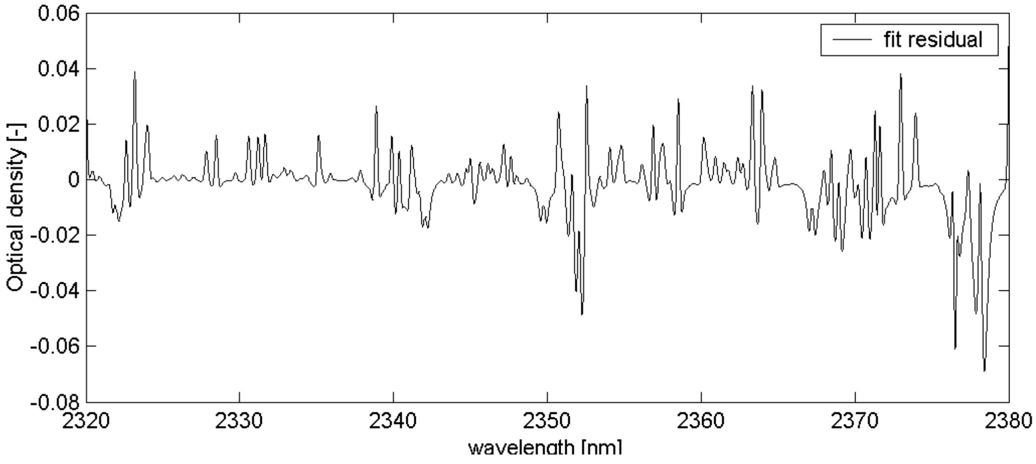

Figure C.6: Residual of the $(\mathsf{VOD}_1; \mathsf{VOD}_{1.2})$ fit

C.4 Minor absorbers in the near infrared

In addition to the strong absorbers methane, carbon dioxide and water, there are many other absorbers that are currently not being measured. Figure C.7 gives an overview of cross sections in the near infrared (from 700 to 2500 μm).

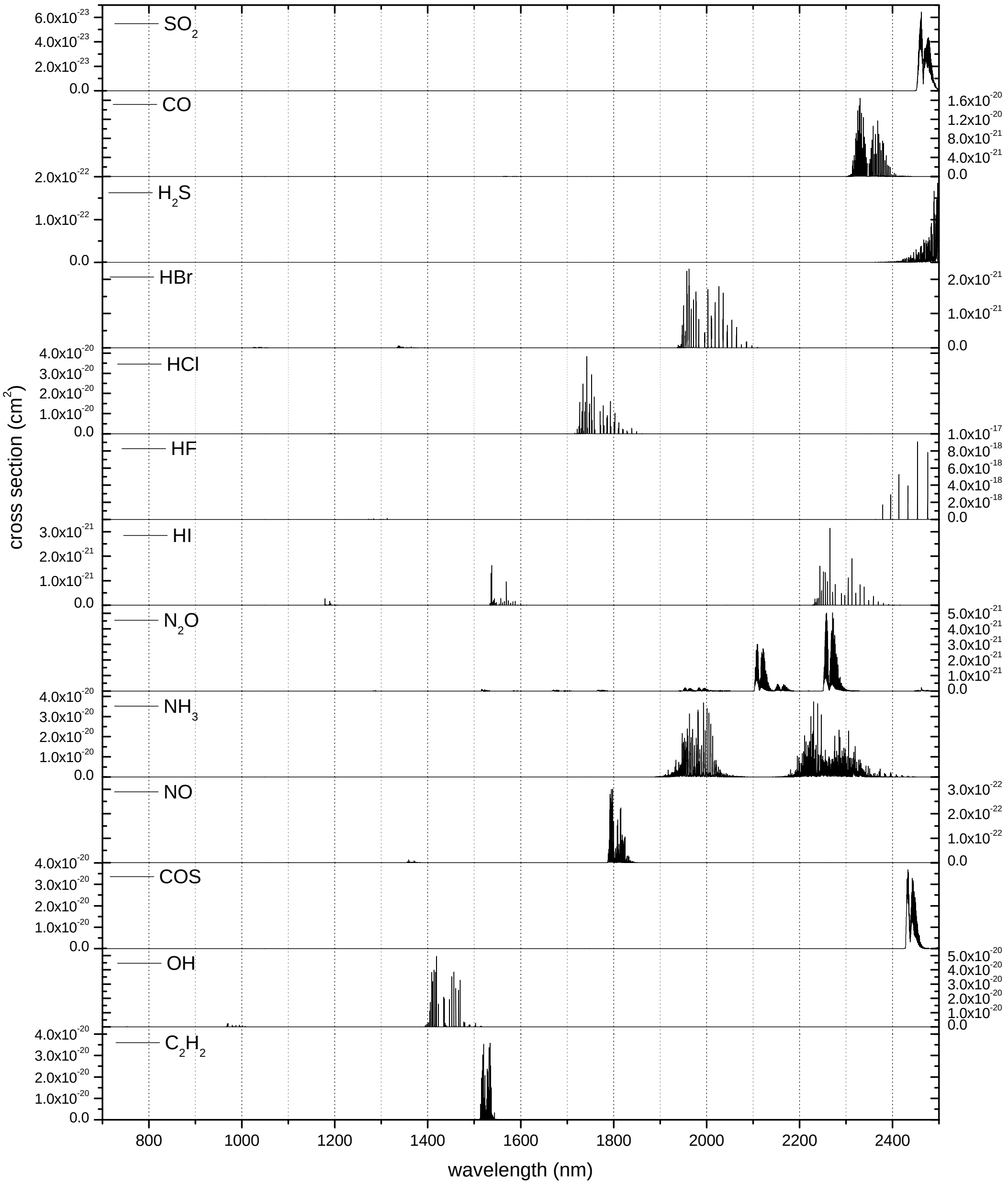

Figure C.7: Cross sections (at 298K and 1013 hPa) in the NIR according to the HITRAN 2005 database

Appendix D

Programming

Retrieval algorithms using satellite measurements have to be very efficient since an enormous amount of data is to be processed. Each day, SCIAMACHY measures about 100000 spectra in each channel and the the raw data adds up to about 5Gb per day. Hence, the retrieval algorithm has to be embedded in data access routines to avoid unnecessary data transformation (such as ASCII exports) and to speed up data access and processing. Within this thesis, a framework for easy data access and fast retrievals has been written in the computing language C++. The code bases on access routines to the binary SCIAMACHY data format (PDS) written by Tim Deutschmann. Since the complete source comprises several thousand lines, a detailed description is inappropriate. The solution to the nonlinear least squares problem is solved in a numerically efficient way according to *Rodgers* (2000, p. 96; Eq. (5.43)). The Gnu Scientific Library (GSL) is used to solve the problem by QR decomposition with pivotting. In the following, I will describe some of the routines of the retrieval algorithm in more detail.

D.1 Convolution

Mathematically, the spectra recorded by a spectrometer are a convolution of the actual (before entering the spectrograph) spectra (I) with the instrumental line shape (ILS or here denoted by $\phi_I(\lambda)$):

$$(I * \phi)(\lambda) = \int_{-\infty}^{\infty} I(\lambda') \cdot \phi_I(\lambda - \lambda') d\lambda' \tag{D.1}$$

Solving the integral numerically is computationally expensive and cannot be performed when a fast retrieval algorithm is desired. In this thesis, two different approaches were applied to solve the integral in a fast way: Via the Fast Fourier Transformation (FFT) and via multigrid binomial filters.

D.1.1 Convolution via Fast Fourier Transformation

According to the Convolution Theorem, the convolution is simply a multiplication in the Fourier space:

$$\mathcal{F}[(I * \phi)(\lambda)] = \mathcal{F}[(I(\lambda)] \cdot \mathcal{F}[\phi(\lambda)]\,, \tag{D.2}$$

where the transformation in the Fourier space reads

$$\mathcal{F}[f(x)](k) = \int_{-\infty}^{\infty} f(x) \cdot \exp(-2\pi ikx) dx\,. \tag{D.3}$$

In a discrete space, the convolution can then be solved in a neat and fast way via the Fast Fourier Transformation (*Duhamel and Vetterli*, 1990). Here, I implemented the convolution by using FFT algorithms provided by the Gnu Scientific Library (GSL). The C++ code reads as follows:

```
 void convolve_fft2(valarray<double>& data, /**! data which has to be convolved */
      double* response,     // response function (already convolved, has to be of length 2^n
      long power)           // length of the response function */
{
    long i;
    int n = data.size();

    double *data2 = new double[power];
    double *convolved = new double[power];

        for(i=0; i<power; i++)
        {
            if(i<n)
                        data2[i]=data[i];
            else
                        data2[i] = 0;  //zero padding at the end in order to avoid tailing effects
        }

        //FFT of the zero padded data
        gsl_fft_real_radix2_transform(data2, 1, power);

        //complex multiplication*************************************************************

        convolved[0] = data2[0]*response[0];
        for(i=1; i<power/2; i++)
        {
            convolved[i] = data2[i]*response[i] - data2[power-i]*response[power-i];
            convolved[power-i] = data2[i]*response[power-i]+data2[power-i]*response[i];
        }
        convolved[power/2] = data2[power/2]*response[power/2];

        //*********************************************************************************

        // inverse fourier transformation*************************************************
        gsl_fft_halfcomplex_radix2_inverse(convolved, 1, power);

        for(i=0; i<n; i++)
                data[i] = convolved[i];

        free(data2);
        free(convolved);
}
```

D.1.2 Convolution via multigrid binomial filters

If the instrumental line shape is Gaussian, the convolution can be performed even faster with multigrid binomial filters (see *W. Wells* (1986) as well as *Jähne* (2002) and references therein). In this simple code, the binomial filter $\mathcal{B}^2 = 1/4[1\,2\,1]$ is applied in a multistep approach. The binomial filter is applied to the data array (data) and finally interpolated on the desired grid (grid) via GSL spline routines. Depending on the number of iterations (s), the effective width of the mask (in terms of grid resolution) reads (*Jähne*, 2002)

$$\sigma^2 = \frac{1}{6}(4^s - 1)\,. \tag{D.4}$$

The Full Width at Half Maximum (FWHM) is then

$$FWHM = \frac{\sigma}{2 \cdot \sqrt{2 \cdot \log(2)}}\,. \tag{D.5}$$

Assuming the ILS to be of Gaussian shape with a FWHM of 0.25 nm (like channel 8), 10 iterations are necessary if the (highly resolved) grid resolution is 0.0014 nm.

```
void convolve_bin2(valarray<double> data, int iterations, valarray<double> highGrid,
   valarray<double> grid, valarray<double>& results)
{
        float a1,a2;
        a1=0;
        a2=0;

        int stride=0;
        int expo=pow(4,iterations);

        //apply the binomial filter [1 2 1] on a variable grid:
        for(int j=0;j<iterations;j++)
        {
                stride = pow(2,j);
                for(int i=0;i<data.size()-stride;i+=stride)
                {
                        a2 = data[i];
                        data[i] = (a1+data[i+stride]+data[i]+data[i]);
                        a1 = a2;
                }
         }

         int size = data.size()/stride;

         double *xa = new double[size];
         double *ya = new double[size];

         cout.precision(8);
         for(int i=0,r=0;i<data.size()-stride;i+=stride,r++)
         {
                 xa[r] = highGrid[i];
                 ya[r] = data[i]/expo;
         }

         gsl_interp_accel *acc = gsl_interp_accel_alloc ();
         gsl_spline *spline = gsl_spline_alloc (gsl_interp_cspline, size);

```

```
        gsl_spline_init (spline, xa, ya, size);

        for (i = 0; i < grid.size(); i ++)
                results[i]=gsl_spline_eval (spline, grid[i], acc);

        gsl_spline_free (spline);
        gsl_interp_accel_free(acc);
        free(xa);
        free(ya);
}
```

Header file

```
#include <valarray>
#include <gsl/gsl_errno.h>
#include <gsl/gsl_fft_halfcomplex.h>
#include <gsl/gsl_spline.h>
#include "math.h"
#include <iostream>

using namespace std;
```

List of Figures

List of Tables

References

Aldhous, P. (2005), Energy: China's burning ambition, *Nature*, *435*, 1152–1154, doi:10.1038/4351152a.

Aliwell, S., P. Johnston, A. Richter, M. V. Roozendael, T. Wagner, D. Arlander, J. Burrows, D. Fish, R. Jones, K. K. Tørnkvist, J.-C. Lambert, K. Pfeilsticker, and I. Pundt (2002), Analysis for BrO in zenith-sky spectra: An intercomparison exercise for analysis improvement, *J. Geophys. Res.*, *107*(D14), 4199, doi:10.1029/2001JD000329.

Alvala, P., and V. Kirchhoff (1998), Observations of atmospheric methane and carbon monoxide in brazil: SCAR-B mission, *J. Geophys. Res.*, *103*(D24), 31,101–32,105.

Andreae, M., and P. Merlet (2001), Emission of trace gases and aerosols from biomass burning, *Global Biogeochem. Cycles*, *15*, 955–966.

Bergamaschi, P., M. Bräunlich, T. Marik, and C. Brenninkmeijer (2000), Measurements of the carbon and hydrogen isotopes of atmospheric methane at izaña, tenerife: Seasonal cycles and synoptic-scale variations, *J. Geophys. Res.*, *105*(D11), 14,531 – 14,546, doi:10.1029/1999JD901176.

Bergamaschi, P., R. Hein, C. A. M. Brenninkmeijer, and P. J. Crutzen (2000a), Inverse modeling of the global CO cycle, 2. Inversion of $^{13}C/^{12}C$ and $^{18}O/^{16}O$ isotope ratios, *J. Geophys. Res.*, *105*(14), 1929–1946, doi:10.1029/1999JD900819.

Bergamaschi, P., R. Hein, M. Heimann, and P. J. Crutzen (2000b), Inverse modeling of the global CO cycle, 1. Inversion of CO mixing ratios, *J. Geophys. Res.*, *105*(14), 1909–1928, doi:10.1029/1999JD900818.

Bergamaschi, P., H. Behrend, and A. Jol (2004), Inverse modelling of national and EU greenhouse gas emission inventories - report of the workshop "Inverse modelling for potential verification of national and EU bottom-up GHG inventories" under the mandate of the Monitoring Mechanism Committee WG-1 23-24 October 2003, JRC, Ispra.

Bergamaschi, P., C. Frankenberg, S. Körner, M. Heimann, U. Platt, T. Wagner, M. van Weele, and J. Meirink (2005a), Satellite cartography of atmospheric methane from SCIAMACHY onboard ENVISAT: (II) Comparison with atmospheric chemistry transport models, *J. Geophys. Res.*, in preparation.

Bergamaschi, P., M. Krol, F. Dentener, A. Vermeulen, F. Meinhardt, R. Graul, M. Ramonet, W. Peters, and E. J. Dlugokencky (2005b), Inverse modelling of national and European

CH_4 emissions using the atmospheric zoom model TM5, *Atmos. Chem. Phys. Discuss.*, *5*, 1007–1066.

Bovensmann, H., J. P. Burrows, M. Buchwitz, J. Frerik, S. Noël, V. V. Rozanov, K. V. Chance, and A. Goede (1999), SCIAMACHY - mission objectives and measurement modes, *J. Atmos. Sci.*, *56*, 127–150.

Brasseur, G., and S. Solomon (1996), *Aeronomy of the Middle Atmosphere: Chemistry and Physics of the Stratosphere and Mesosphere*, Kluwer Academic Publishers.

Bregman, B., A. Segers, M. Krol, E. Meijer, and P. van Velthoven (2003), On the use of mass-conserving wind fields in chemistry–transport models, *Atmos. Chem. Phys.*, *3*, 447–457.

Bremer, H., J. Kar, J. R. Drummond, F. Nichitu, J. Zou, and J. Liu (2004), Spatial and temporal variation of MOPITT CO in Africa and South America: A comparison with SHADOZ ozone and MODIS aerosol, *J. Geophys. Res.*, *109*, D12,304, doi:10.1029/2003JD004234.

Buchwitz, M., and J. Burrows (2003), Retrieval of CH_4, CO, and CO_2 total column amounts from SCIAMACHY near–infrared nadir spectra: Retrieval algorithm and first results, in *Remote Sensing of Clouds and the Atmosphere VIII*, *Proceedings of SPIE*, vol. 5235, edited by K. Schäfer, A. Comeron, M. Carleer, and R. Picard, pp. 375–388.

Buchwitz, M., V. Rozanov, and J. Burrows (2000), A near-infrared optimized DOAS method for the fast global retrieval of atmospheric CH_4, CO, CO_2, H_2O, and N_2O total column amounts from SCIAMACHY Envisat-1 nadir radiances, *J. Geophys. Res.*, *105*(D12), 15,231–15,245.

Buchwitz, M., V. V. Rozanov, and J. P. Burrows (2000), A correlated-k distribution scheme for overlapping gases suitable for retrieval of atmospheric constituents from moderate resolution radiance measurements in the visible/near-infrared spectral region, *J. Geophys. Res.*, *105*(14), 15,247–15,262, doi:10.1029/2000JD900171.

Buchwitz, M., R. Beek, K. Bramstedt, S. Noël, H. Bovensmann, and J. Burrows (2004), Global carbon monoxide as retrieved from SCIAMACHY by WFM-DOAS, *Atmos. Chem. Phys. Discuss.*, *4*, 2805–2837.

Buchwitz, M., R. de Beek, J. P. Burrows, H. Bovensmann, T. Warneke, J. Notholt, J. F. Meirink, A. P. H. Goede, P. Bergamaschi, S. Körner, M. Heimann, and A. Schulz (2005a), Atmospheric methane and carbon dioxide from SCIAMACHY satellite data: Initial comparison with chemistry and transport models, *Atmos. Chem. Phys.*, *5*, 941–962.

Buchwitz, M., R. de Beek, S. Noel, J. Burrows, H. Bovensmann, H. Bremer, P. Bergamaschi, S. Koerner, and M. Heimann (2005b), Carbon monoxide, methane and carbon dioxide columns retrieved from SCIAMACHY by WFM-DOAS: Year 2003 initial data set, *Atmos. Chem. Phys. Disc.*, *5*, 1943–1971.

Burrows, J.P., M. Weber, M. Buchwitz, V. Rozanov, A. LadstÃ¤dter-Weissenmayer, A. Richter, R. de Beek, R. Hoogen, K. Bramstedt, K.-U. Eichmann, M. Eisinger, and D. Perner (1999), The Global Ozone Monitoring Experiment (GOME): Mission concept and first scientific results, *J. Atm. Sciences*, *56*, 151–175.

Butler, T. M., I. Simmonds, and P. J. Rayner (2004), Mass balance inverse modelling of methane in the 1990s using a chemistry transport model, *Atmos. Chem. Phys.*, *4*, 2561–2580.

Cai, Z., H. Tsuruta, and K. Minami (2000), Methane emission from rice fields in China: Measurements and influencing factors, *J. Geophys. Res.*, *105*(D13), 17,231–17,242.

Cantrell, C., R. Shetter, A. McDaniel, J. Calvert, J. Davidson, D. Lowe, S. Tyler, R. Cicerone, and J. Greenberg (1990), Carbon kinetic isotope effect in the oxidation of methane by hydroxyl radicals, *J. Geophys. Res.*, *95*, 22,455–22,462.

Chance, K., T. P. Kurosu, and C. E. Sioris (2005), Undersampling correction for array detector-based satellite spectrometers, *Applied Optics*, *44*(7), 1296–1304.

Chen, Y.-H. (2003), Estimation of methane and carbon dioxide surface fluxes using a 3-d global atmospheric chemical transport model, *Tech. Rep. Report No. 73*, Center for Global Change Science Department of Earth, Atmospheric and Planetary Sciences MI.

Chevallier, F. (2001), Sampled databases of 60-level atmospheric profiles from the ECMWF analyses, *Research. rep. no. 4*, EUMETSAT/ECMWF.

Clerbaux, C., J. Hadji-Lazaro, S. Turquety, G. Mégie, and P.-F. Coheur (2003), Trace gas measurements from infrared satellite for chemistry and climate applications, *Atmos. Chem. Phys.*, *3*, 1495–1508.

Clough, S., F. Kneizys, and R. Davies (1989), Line shape and the water vapor continuum, *Atmos. Res.*, *23*, 229–241.

Crisp, D., R. Atlas, F.-M. Breon, L. Brown, J. Burrows, P. Ciais, B. Connor, S. Doney, I. Fung, D. Jacob, C. Miller, D. O'Brien, S. Pawson, J. Randerson, P. Rayner, R. Salawitch, S. Sander, B. Sen, G. Stephens, P. Tans, G. Toon, P. Wennberg, S. Wofsy, Y. Yung, Z. Kuang, B. Chudasama, G. Sprague, B. Weiss, R. Pollock, D. Kenyon, and S. Schroll (2004), The Orbiting Carbon Observatory (OCO) mission, *Advances in Space Research*, *34*(4), 700–709.

de la Chesnaye F., H. R., K. D., and L. J.A. (2001), Cost-effective reductions of non-CO_2 greenhouse gases, *ENERGY POLICY*, *29*(14), 1325–1331.

Deeter, M. N., L. K. Emmons, G. L. Francis, D. P. Edwards, J. C. Gille, J. X. Warner, B. Khattatov, D. Ziskin, J.-F. Lamarque, S.-P. Ho, V. Yuding, J.-L. Attie, D. Packman, J. Chen, D. Mao, and J. R. Drummond (2003), Operational carbon monoxide retrieval algorithm and selected results for the MOPITT instrument, *J. Geophys. Res.*, *108*, 4399–4409.

DeFries, R., and J. Townshend (1994), NDVI-derived land cover classifications at a global scale, *Int. J. Remote Sensing*, *15*, 3567–3586.

deMore, W. (1993), Rate constant ratio for the reactions of OH with CH_3D and CH_4, *J. Phys. Chem.*, *92*, 8564–8566.

Denier van der Gon, H. A. C., M. J. Kropff, N. van Breemen, R. Wassmann, R. S. Lantin, E. Aduna, T. M. Corton, and H. H. van Laar (2002), From the Cover: Optimizing grain yields reduces CH_4 emissions from rice paddy fields, *Proc. Nat. Acad. Sci. USA*, *99*(19), 12,021–12,024.

Dentener, F., M. van Weele, M. Krol, S. Houweling, and P. van Velthoven (2003), Trends and inter-annual variability of methane emissions derived from 1979-1993 global CTM simulations, *Atmos. Chem. Phys.*, *3*, 73–88.

Dentener, F., D. Stevenson, J. Cofala, R. Mechler, M. Amann, P. Bergamaschi, F. Raes, and R. Derwent (2005), The impact of air pollutant and methane emission controls on tropospheric ozone and radiative forcing: CTM calculations for the period 1990-2030, *Atmos. Chem. Phys.*, *5*, 1731–1755.

Devol, A. H., J. E. Richey, B. R. Forsberg, and L. A. Martinelli (1990), Seasonal dynamics in methane emissions from the Amazon River floodplain to the troposphere, *J. Geophys. Res.*, *95*(14), 16,417–16,426.

Dicke, R. (1953), The effect of collisons upon the doppler width of spectral lines, *Phys. Rev.*, *89*(2), 472.

Dlugokencky, E., K. Masarie, P. Lang, and P. Tans (1998), Continuing decline in the growth rate of the atmospheric methane burden, *Nature*, *393*, 447–450.

Dlugokencky, E. J., B. P. Walter, K. A. Masarie, P. M. Lang, and E. S. Kasischke (2001), Measurements of anomalous methane increase during 1998, *Geophys. Res. Lett.*, *28*(3), 499–502.

Dlugokencky, E. J., S. Houweling, L. Bruhwiler, K. A. Masarie, P. M. Lang, J. B. Miller, and P. P. Tans (2003), Atmospheric methane levels off: Temporary pause or a new steady-state?, *Geophys. Res. Lett.*, *30*(19), doi: 10.1029/2003GL018,126.

Dufour, E., and F. Breon (2003), Spaceborne estimate of atmospheric CO_2 column by use of the differential absorption method: error analysis, *Appl. Opt.*, *42*, 3595–3609.

Duhamel, P., and M. Vetterli (1990), Fast fourier transforms: A tutorial review and a state of the art, *Signal Processing*, *19*, 259–299.

Ehrlich, H. L. (1990), *Geomicrobiology*, 3rd ed., Marcel Dekker, Inc., New York.

Etheridge, D., L. Steele, R. Francey, and R. Langenfels (1998), Atmospheric methane between 1000 A.D. and present: Evidence of anthropogenic emissions and climate variability, *J. Geophys. Res.*, *103*(D13), 15,979–15,993.

Fano, U. (1963), Pressure broadening as a prototype of relaxation, *Phys. Rev.*, *131*(1), 259–268.

Fletcher, M., S. Mikaloff, P. Tans, L. Bruhwiler, J. Miller, and M. Heimann (2004a), CH_4 sources estimated from atmospheric observations of CH_4 and its $^{13}C/^{12}C$ isotopic ratios: 2. Inverse modeling of CH_4 fluxes from geographical regions, *Global Biogeochem. Cycles*, *18*(4), GB4005, doi:10.1029/2004GB002224.

Fletcher, M., S. E. Mikaloff, P. Tans, L. Bruhwiler, J. B. Miller, and M. Heimann (2004b), CH_4 sources estimated from atmospheric observations of CH_4 and its $^{13}C/^{12}C$ isotopic ratios:

1. Inverse modeling of source processes, *Global Biogeochem. Cycles*, *18*(4), GB4004, doi: 10.1029/2004GB002223.

Frankenberg, C., U. Platt, and T. Wagner (2005a), Iterative maximum a posteriori (IMAP)-DOAS for retrieval of strongly absorbing trace gases: Model studies for $\mathsf{CH_4}$ and $\mathsf{CO_2}$ retrieval from near infrared spectra of SCIAMACHY onboard ENVISAT, *Atmos. Chem. Phys.*, *5*, 9–22.

Frankenberg, C., U. Platt, and T. Wagner (2005b), Retrieval of CO from SCIAMACHY onboard ENVISAT: detection of strongly polluted areas and seasonal patterns in global CO abundances, *Atmos. Chem. Phys.*, *5*, 1639–1644.

Frankenberg, C., J. F. Meirink, M. van Weele, U. Platt, and T. Wagner (2005c), Assessing Methane Emissions from Global Space-Borne Observations, *Science*, *308*(5724), 1010–1014, doi:10.1126/science.1106644.

Frankenberg, C., J. Meirink, P. Bergamaschi, A. Goede, M. Heimann, S. Körner, U. Platt, M. van Weele, and T. Wagner (2005d), Satellite cartography of atmospheric methane from SCIAMACHY onboard ENVISAT: Analysis of the years 2003 and 2004, *J. Geophys. Res.*, revised version submitted.

Friedeburg, C. v. (2003), Derivation of trace gas information combining differential optical absorption spectroscopy with radiative transfer modelling, Ph.D. thesis, Institut für Umweltphysik, University of Heidelberg.

Gamache, R., R. Hawkins, and L. Rothman (1990), Total internal partition sums in the temperature range $70 - 3000$ k: atmospheric linear molecules, *J. Mol. Spectrosc.*, *142*, 205–219.

Gedney, N., P. Cox, and C. Huntingtonford (2004), Climate feedback from wetland methane emissions, *Geophys. Res. Lett.*, *32*(L20503), doi:10.1029/2004GL020919.

Gierczak, T., S. Herndon, G. Vaghjiani, and A. Ravishankara (1997), Rate coefficients for the reactions of hydroxyl radicals with methane and deuterated methanes, *J. Phys. Chem.*, *101*, 3125–3134.

Gloudemans, A., H. Schrijver, A. Straume, I. Aben, A. Maurellis, M. Buchwitz, R. de Beek, C. Frankenberg, and T. Wagner (2004), $\mathsf{CH_4}$ and CO total columns from SCIAMACHY: comparisons with TM3 and MOPITT, in *Proceedings ACVE2, 3-7 May, Frascati, Italy (ESA SP-562)*.

Gloudemans, A. M. S., H. Schrijver, Q. Kleipool, M. M. P. van den Broek, A. G. Straume, G. Lichtenberg, R. M. van Hees, I. Aben, and J. F. Meirink (2005), The impact of SCIAMACHY near-infrared instrument calibration on $\mathsf{CH_4}$ and CO total columns, *Atmos. Chem. Phys. Disc.*, *5*, 1733–1770.

Gonzalez, F., and H. Rodriguez (2000), Greenhouse-gas emissions in Colombia 1998-2010, *Tech. rep.*, Colombian Academy of Sciences, Santafé de Bogotá,.

Goody, R., and Y. Yung (1989), *Atmospheric Radiation*, Oxford University Press, New York.

Gupta, M., M. McGrath, R. Cicerone, F. Rowland, and M. Wolfsberg (1997), $^{12}\mathsf{C}/^{1}\mathsf{3C}$ kinetic isotope effects in reactions of $\mathsf{CH_4}$ with OH and Cl, *Geophys. Res. Lett.*, *24*, 2761–2764.

Gurney, K., R. Law, A. Denning, P. Rayner, D. Baker, P. Bousquet, L. Bruhwiler, Y. Chen, P. Ciais, S. Fan, I. Fung, M. Gloor, M. Heimann, K. Higuchi, J. John, T. Maki, S. Maksyutov, K. Masarie, P. Peylin, M. Prather, B. Pak, J. Randerson, J. Sarmiento, S. Taguchi, T. Takahashi, and C. Yuen (2002), Towards robust regional estimates of $\mathsf{CO_2}$ sources and sinks using atmospheric transport models, *Nature*, *415*, 626–630.

Hamilton, J. T. G., W. C. McRoberts, F. Keppler, R. M. Kalin, and D. B. Harper (2003), Chloride Methylation by Plant Pectin: An Efficient Environmentally Significant Process, *Science*, *301*, 206–209, doi:10.1126/science.1085036.

Hansen, J., and M. Sato (2004), Greenhouse gas growth rates, *Proc. Nat. Acad. Sci. USA*, *101*(46), 16,109–16,114.

Hansen, J., M. Sato, R. Ruedy, A. Lacis, and V. Oinas (2000), Global warming in the twenty-first century: An alternative scenario, *Proc. Nat. Acad. Sci. USA*, *97*(18), 9875–9880.

Hansen, J., M. Sato, R. Ruedy, L. Nazarenko, A. Lacis, G. A. Schmidt, G. Russell, I. Aleinov, M. Bauer, S. Bauer, N. Bell, B. Cairns, V. Canuto, M. Chandler, Y. Cheng, A. D. Genio, G. Faluvegi, E. Fleming, A. Friend, T. Hall, C. Jackman, M. Kelley, N. Kiang, D. Koch, J. Lean, J. Lerner, K. Lo, S. Menon, R. Miller, P. Minnis, T. Novakov, V. Oinas, J. Perlwitz, J. Perlwitz, D. Rind, A. Romanou, D. Shindell, P. Stone, S. Sun, N. Tausnev, D. Thresher, B. Wielicki, T. Wong, M. Yao, and S. Zhang (2005), Efficacy of climate forcings, *J. Geophys. Res.*, *110*, D18,104, doi:10.1029/2005JD005776.

Hao, W. M., M. H. Liu, and P. J. Crutzen (1991), Estimates of the annual and regional releases of CO_2 and other trace gases to the atmosphere from fires in the tropics based on the FAO statistics for the period 1975-1980, in *Fire in the tropical biota*, edited by J. Goldhammer, pp. 440–462, Springer, New York.

Heimann, M., and Körner (2003), The Global Atmospheric Tracer Model TM3, Model Description and Users Manual Release 3.8a, *Tech. Rep. 5*, Max Planck Institute for Biogeochemistry (MPIBGC), Jena, Germany.

Hein, R., P. J. Crutzen, and M. Heimann (1997), An inverse modeling approach to investigate the global atmospheric methane cycle, *Global Biogeochem. Cycles*, *11*(1), 43 – 76, doi:10.1029/96GB03043.

Herzberg, G. (1950), *Molecular Spectroscopy and Molecular Structure: I. Spectra of Diatomic Molecules*, van Nostrand, Princeton.

Hess, M., P. Koepke, and I. Schult (1998), Optical Properties of Aerosols and Clouds: The Software Package OPAC., *Bull. Am. Met. Soc.*, *79*, 831–844.

Hogan, K. B., J. S. Hoffman, and A. M. Thompson (1991), Methane on the greenhouse agenda, *Nature*, *354*, 181–182, doi:10.1038/354181a0.

Holloway, T., H. L. II, and P. Kasibhatla (2000), Global distribution of carbon monoxide, *J. Geophys. Res.*, *105*, 12,123–12,147.

Houweling, S. (1999), Global modeling of atmospheric methane sources and sinks, Ph.D. thesis, Institute for Marine and Atmospheric research Utrecht, University of Utrecht, ISBN 90-393-2296-1.

Houweling, S., F. J. Dentener, and J. Lelieveld (1998), The impact of non-methane hydrocarbon compounds on tropospheric photochemistry, *J. Geophys. Res.*, *103*, 10,673–10,696.

Houweling, S., T. Kaminski, F. Dentener, J. Lelieveld, and M. Heimann (1999), Inverse modeling of methane sources and sinks using the adjoint of a global transport model, *J. Atmos. Res.*, *104*(D21), 26,137–26,160.

Houweling, S., F. Dentener, J. Lelieveld, B. Walter, and E. Dlugokencky (2000), The modeling of tropospheric methane: How well can point measurements be reproduced by a global model?, *J. Geophys. Res.*, *105*(14), 8981–9002, doi:10.1029/1999JD901149.

Houweling, S., W. Hartmann, I. Aben, H. Schrijver, J. Skidmore, G.-J. Roelofs, and F. M. Breon (2005), Evidence of systematic errors in SCIAMACHY-observed CO_2 due to aerosols, *Atmos. Chem. Phys. Discuss.*, *5*, 3313–3340.

Humlíček, J. (1982), Optimized computation of the Voigt and complex probability functions, *J. Quant. Spectrosc. Radiat. Transfer*, *82*, 472.

IPCC (2000), Good practice guidance and uncertainty management in national greenhouse gas inventories.

IPCC (2001), *Climate Change 2001: The Scientific Basis. Contribution of Working Group I to the Third Assessment Report of the Intergovernmental Panel on Climate Change*, 881 pp., Cambridge University Press, Cambridge, United Kingdom and New York, NY, USA.

Jacob, D. J. (1999), *Introduction to atmospheric chemistry*, Princeton University Press.

Jähne, B. (2002), *Digital Image Processing*, 5th ed., Springer, Berlin.

Kasting, J. (1993), Earth's early atmosphere, *Science*, *259*, 5097.

Kasting, J., and J. Siefert (2002), Life and the evolution of earth's atmosphere, *Science*, *296*, 5570.

Keppler, F., J. T. Hamilton, M. Braß, and T. Röckmann (2005), An overlooked major source of atmospheric methane: In situ formation in plants, *Nature*, submitted.

Kesselmeier, J., U. Kuhn, S. Rottenberger, T. Biesenthal, A. Wolf, G. Schebeske, M. O. Andreae, P. Ciccioli, E. Brancaleoni, M. Frattoni, S. T. Oliva, M. L. Botelho, C. M. A. Silva, and T. M. Tavares (2002), Concentrations and species composition of atmospheric volatile organic compounds (VOCs) as observed during the wet and dry season in Rondônia (Amazonia), *J. Geophys. Res.*, *107*(D20), 8053, doi:10.1029/2000JD000267.

Kleipool, Q. (2003a), Algorithm specification for dark signal determination, *Tech. rep. SRON-SCIA-PhE-RP-009*, SRON.

Kleipool, Q. (2003b), Recalculation of OPTEC5 non-linearity. report containing the NL correction to be implemented in the data processor, *Tech. rep. SRON-SCIA-PhE-RP-013*, SRON.

Kleipool, Q. (2004), SCIAMACHY: Orbital variation of dark signal, *Tech. rep. SRON-SCIA-PhE-RP-18*, SRON.

Kneizys, F. X., L. W. Abreu, G. P. Anderson, J. H. Chetwynd, E. P. Shettle, D. C. Robertson, P. Acharya, L. Rothman, J. E. A. Selby, W. O. Gallery, and S. A. Clough (1996), The MODTRAN 2/3 report and LOWTRAN 7 model, *Tech. rep.*, Phillips Laboratory, Geophysics Directorate, Hanscom AFB.

Kobayashi, H., A. Shimota, K. Kondo, E. Okumura, Y. Kameda, H. Shimoda, and T. Ogawa (1999), Development and evaluation of the interferometric monitor for greenhouse gases: a high throughput fourier transform infrared radiometer for nadir earth observations, *Appl. Opt.*, *38*, 6801–6807.

Krol, M., S. Houweling, B. Bregman, M. van den Broek, A. Segers, P. van Velthoven, W. Peters, F. Dentener, and P. Bergamaschi (2005), The two-way nested global chemistry-transport zoom model TM5: algorithm and applications, *Atmos. Chem. Phys.*, *5*, 417–432.

Kuntz, M. (1997), A new implementation of the Humlíček algorithm for the calculation of the Voigt profile function, *J. Quant. Spectrosc. Radiat. Transfer*, *57*(6), 819–824.

Lawrence, M., P. Jöckel, and R. von Kuhlmann (2001), What does the global mean OH concentration tell us?, *Atmos. Chem. Phys. Disc.*, *1*, 37–49.

Lelieveld, J., P. J. Crutzen, and F. J. Dentener (1998), Changing concentration, lifetime and climate forcing of atmospheric methane, *Tellus*, *50*(B), 128–150.

Leue, C., M. Wenig, T. Wagner, O. Klimm, U. Platt, and B. Jähne (2001), Quantitative analysis of NO_x emissions from GOME satellite image sequences, *J. Geophys. Res.*, *106*, 5493–5505.

Levenberg, K. (1944), A method for the solution of certain non-linear problems in least squares, *Quart. Appl. Math.*, *2*, 164–168.

Levin, I., P. Ciais, R. Langenfelds, M. Schmidt, M. Ramonet, K. Sidorov, N. Tchebakova, M. Gloor, M. Heimann, E. Schulze, N. Vygodskaya, O. Shibistova, and J. Lloyd (2002), Three years of trace gas observations over the eurosiberian domain derived from aircraft sampling - a concerted action, *Tellus*, *54B*, 696–712.

Li, C., S. Frolking, X. Xiao, B. M. III, S. Boles, J. Qiu, Y. Huang, W. Salas, , and R. Sass (2005), Modeling impacts of farming management alternatives on CO_2, CH_4, and N_2O emissions: A case study for water management of rice agriculture of China, *Gobal Biogeochem. Cycles*, *19*, GB3010, doi:10.1029/2004GB002341.

Livingston, W., and L. Wallace (1991), An atlas of the solar spectrum in the infrared from 1850 to 9000 cm^{-1} (1.1 to 5.4 μm), *Tech. rep. 91-001*, National Solar Observatory.

Lu, Y., and R. Conrad (2005), In Situ Stable Isotope Probing of Methanogenic Archaea in the Rice Rhizosphere, *Science*, *309*(5737), 1088–1090.

Ma, Q., and R. Tipping (1999), The averaged density matrix in the coordinate representation: Application to the calculation of the far-wing line shapes for H_2O, *J. Comp. Phys.*, *111*(13), 5909.

Marquard, L., T. Wagner, and U. Platt (2000), Improved air mass factor concepts for scattered radiation differential optical absorption spectroscopy of atmospheric species, *J. Geophys. Res.*, *105*(D1), 1315–1327.

Marquardt, D. W. (1963), An algorithm for least-squares estimation of nonlinear parameters, *J. Soc. Indust. Math.*, *11*, 431–441.

Matthews, E., I. Fung, and J. Lerner (1991), Methane emission from rice cultivation: Geographic and seasonal distribution of cultivated areas and emissions, *Global Biogeochem. Cycles*, *1*, 61–86.

Maurellis, A., R. Lang, and W. van der Zande (2000), A new doas parameterization for retrieval of trace gases with highly-structured absorption spectra, *Geophys. Res. Lett.*, *27*(24), 4069–4072.

McGrabb, G., K. Berger, T. Magner, C. May, and R. Hunter (1997), Inhibiting methane production in brahman cattle by dietary supplementation with a novel compound and the effects on growth, *Aust. J. Agric. Res.*, *48*(3), 323–329.

Meirink, J. F., H. J. Eskes, and A. P. H. Goede (2005), Sensitivity analysis of methane emissions derived from SCIAMACHY observations through inverse modelling, *Atmos. Chem. Phys. Discuss.*, accepted.

Melack, J., L. Hess, M. Gastill, B. Forsberg, S. Hamilton, I. Lima, and E. Novo (2004), Regionalization of methane emissions in the Amazon Basin with microwave remote sensing, *Global Change Biology*, pp. 530–544, doi:10.1111/j.1529-8817.2003.00763.x.

Morrissey, L. A., and G. P. Livingston (1992), Methane emissions from Alaska Arctic tundra - An assessment of local spatial variability, *J. Geophys. Res.*, *97*(16), 16,661.

Nizkorodov, S., S. Sander, and L. Brown (2004), Temperature and Pressure Dependence of High-Resolution Air-Broadened Absorption Cross Sections of $\mathsf{NO_2}$ (415-525 nm), *J. Phys. Chem. A*, *108*, 4864–4872.

O'Brien, D. M., and P. J. Rayner (2002), Global observations of the carbon budget 2. $\mathsf{CO_2}$ column from differential absorption of reflected sunlight in the 1.61 $\mu\mathsf{m}$ band of $\mathsf{CO_2}$, *J. Geophys. Res.*, *107*(D18), 4354, doi:10.1029/2001JD000617.

Olivier, J., and J. Berdowski (2001), *Global emissions sources and sinks, In: Berdowski, J., Guicherit, R. and B.J. Heij (eds.) The Climate System*, 33-78 pp., A.A. Balkema Publishers Swets & Zeitlinger Publishers, Lisse, The Netherlands.

Olivier, J., J. Peters, C. Granier, G. Pétron, J. F. Müller, and S. Wallens (2003), Present and future surface emissions of atmospheric compounds, *POET Report 2, EU project EVK2-1999-00011.*

Olivier, J. G. J., A. F. Bouwman, J. J. M. Berdowski, C. Veldt, J. P. J. Bloos, A. J. H. Visschedijk, C. W. M. Van der Maas, and P. Y. J. Zandveld (1999), Sectoral emission inventories of greenhouse gases on a per country basis as well as 1×1, *Env. Sci. Policy*, *2*, 241–263.

Olsen, S. C., and J. T. Randerson (2004a), Differences between surface and column atmospheric CO_2 and implications for carbon cycle research, *J. Geophys. Res.*, *109*(D02301), doi:10.1029/2003JD003968.

Olsen, S. C., and J. T. Randerson (2004b), Differences between surface and column atmospheric CO_2 and implications for carbon cycle research, *J. Geophys. Res.*, *109*(D02301), doi:doi:10.1029/2003JD003968.

Pavlov, A. A., J. F. Kasting, L. L. Brown, K. A. Rages, and R. Freedman (2000), Greenhouse warming by CH_4 in the atmosphere of early Earth, *jgr*, *105*(14), 11,981–11,990, doi:10.1029/1999JE001134.

Pfeilsticker, K. (1999), First geometrical path lengths probability density function derivation of the skylight from spectroscopically highly resolving oxygen a-band observations. 2. derivation of the levy-index for the skylight transmitted by mid-latitude clouds, *J. Geophys. Res.*, *104*, 4101–4116.

Pfeilsticker, K., F. Erle, O. Funk, H. Veitel, and U. Platt (1998a), First geometrical pathlengths probability density function derivation of the skylight from spectroscopically highly resolving oxygen a-band observations: 1. measurement technique, atmospheric observations, and model calculations, *J. Geophys. Res.*, *103*, 11,483–11,504.

Pfeilsticker, K., F. Erle, O. Funk, H. Veitel, and U. Platt (1998b), First geometrical pathlengths probability density function derivation of the skylight from spectroscopically highly resolving oxygen A-band observations: 1. Measurement technique, atmospheric observations, and model calculations, *J. Geophys. Res.*, *103*, 11,483–11,504.

Pine, A. (1997), N_2 and ar broadening and line mixing in the p and r branches of the ν_3 band of CH_4, *J. Quant. Spectrosc. Radiat. Transfer*, *57*, 157–176.

Platt, U. (1994), *Differential optical absorption spectroscopy (DOAS), in Air Monitoring by Spectroscopic Techniques*, John Wiley, New York.

Platt, U., W. Allen, and D. Lowe (2004), Hemispheric average Cl atom concentration from $^{13}C/^{12}C$ ratios in atmospheric methane, *Atmos. Chem. Phys.*, *4*, 2393–2399.

Press, W., S. Teukolsky, W. Vetterling, and B. Flannery (2002), *Numerical Recipes in C/C++ - The Art of Scientific Computing*, 3rd ed., Cambridge University Press, Cambridge.

Ramanathan, V., C. Chung, D. Kim, T. Bettge, L. Buja, J. T. Kiehl, W. M. Washington, Q. Fu, D. R. Sikka, and M. Wild (2005), Inaugural Article: Atmospheric brown clouds: Impacts on South Asian climate and hydrological cycle, *PNAS*, *102*(15), 5326–5333.

Randel, W., F. Wu, J. Russell III, A. Roche, and J. Waters (1998), Seasonal cycles and QBO variations in stratospheric CH_4 and H_2O observed in UARS HALOE data, *J. Atmos. Sci.*, *55*, 163–185.

Rayner, P. J., and D. M. O'Brien (2001), The utility of remotely sensed CO_2 concentration data in surface source inversions, *Geophys. Res. Lett.*, *28*(1), 175–178.

Rayner, P. J., R. M. Law, D. M. O'Brien, T. M. Butler, and A. C. Dilley (2002), Global observations of the carbon budget 3. Initial assessment of the impact of satellite orbit, scan geometry, and cloud on measuring $\mathsf{CO_2}$ from space, *J. Geophys. Res.*, *107*(D21), 4557, doi: doi:10.1029/2001JD000618.

Reichle Jr., H. G., B. E. Anderson, V. S. Connors, T. C. Denkins, D. A. Forbes, B. B. Gormsen, R. L. Langenfels, D. O. Neil, S. R. Nolf, P. C. Novelli, N. S. Pougatchev, M. M. Roell, and L. P. Steele (1999), Space shuttle based global CO measurements during april and october 15 1994, MAPS instrument, data reduction, and data validation, *J. Geophys. Res.*, *104*, 21 443–21 454.

Ridgwell, A. J., S. J. Marshall, and K. Gregson (1999), Consumption of atmospheric methane by soils: A process-based model, *Global Biogeochem. Cycles*, *13*, 59–70.

Rodgers, C. (1976), Retrieval of atmospheric temperature and composition from remote measurements of thermal radiation, *Rev. Geophys. Space Phys.*, *14*, 609–624.

Rodgers, C. D. (2000), *Inverse Methods for Atmospheric Sounding*, World Scientific, London.

Rothman, L., C. P. Rinsland, A. Goldman, S. Massie, D. P. Edwards, J.-M. Flaud, A. Perrin, C. Camy-Peyret, V. Dana, J.-Y. Mandin, J. Schroeder, A. McCann, R. R. Gamache, R. B. Wattson, K. Yoshino, K. Chance, K. Jucks, L. Brown, V. Nemtchinov, and P. Varanasi (1998), The HITRAN Molecular Spectroscopic Database and HAWKS (HITRAN Atmospheric Workstation): 1996 Edition, *J. Quant. Spectroscopy and Rad. Transfer*, *60*, 665–710.

Rothman, L., A. Barbe, D. C. Benner, L. Brown, C. Camy-Peyret, M. Carleer, K. Chance, C. Clerbaux, V. Dana, V. Devi, A. Fayt, J.-M. Flaud, R. Gamache, A. Goldman, D. Jacquemart, K. Jucks, W. Lafferty, J.-Y. Mandin, S. Massie, V. Nemtchinov, D. Newnham, A. Perrin, C. Rinsland, J. Schroeder, K. Smith, M. Smith, K. Tang, R. Toth, J. V. Auwera, P. Varanasi, , and K. Yoshino (2003), The HITRAN molecular spectroscopic database: edition of 2000 including updates through 2001, *J. Quant. Spectrosc. Radiat. Transfer*, *82*, 5–44.

Rothman, L., D. Jacquemart, A. Barbe, D. C. Benner, M. Birk, L. Brown, M. Carleer, J. C. Checkerian, K. Chance, L. Coudert, V. Danai, V. Devi, J.-M. Flaud, R. Gamache, A. Goldman, J.-M. Hartmann, K. Jucks, A. Maki, J.-Y. Mandin, S. Massie, J. Orphal, A. Perrin, C. Rinsland, M. Smith, J. Tennyson, R. Tolchenov, R. Toth, J. V. Auwera, P. Varanasi, and G. Wagner (2005), The HITRAN 2004 molecular spectroscopic database, *J. Quant. Spectrosc. Radiat. Transfer*, *96*(2).

Sanderson, M. (1996), Biomass of termites and their emissions of methane and carbon dioxide: A global database., *Global Biogeochem. Cycles*, *10*, 543–557.

Sass, R., F. Fisher, F. Turner, and P. Harcombe (1991), Mitigation of Methane Emissions from Rice Fields: Effects of Incorporated Rice Straw, *Global Biogeochem. Cycles*, *5*, 275–287.

Sass, R., F. Fisher, Y. Wang, F. Turner, and P. Harcombe (1992), Methane Emission from Rice Fields: The Effect of Flood Water Management, *Global Biogeochem. Cycles*, *6*, 249–262.

Schimmel, J. (2000), Global change - Rice, microbes and methane, *Nature*, *403*, 375.

Schrijver, H. (1999), Retrieval of carbon monoxide, methane and nitrous oxide from SCIAMACHY measurements, pp. 285–294, Estec, Nordwijk, The netherlands.

Shindell, D., B. Walter, and G. Faluvegi (2004), Impacts of climate change on methane emissions from wetlands, *Geophys. Res. Lett.*, *32*(L2120224), doi:10.1029/2004GL021009.

Shindell, D. T., G. Faluvegi, N. Bell, , and G. A. Schmidt (2005), An emissions-based view of climate forcing by methane and tropospheric ozone, *Geophys. Res. Lett.*, *32*, L04,803, doi:10.1029/2004GL021900.

Slijkhuis, S. (2001), SCIAMACHY level 0 to 1c processing algorithm theoretical baseline document, *ATBD: ENV-ATB-DLR-SCIA-0041*, DLR.

Snover, A. K., P. D. Quay, and W. M. Hao (2000), The d/h content of methane emitted from biomass burning, *Global Biogeochem. Cycles*, *14*(1), 11–24.

Solomon, S., H. L. Miller, J. P. Smith, R. W. Sanders, G. H. Mount, A. L. Schmeltekopf, and J. F. Noxon (1998), Atmospheric NO_3, 1. Measurement Technique and the Annual Cycle, *J. Geophys. Res.*, *94*, 11 041–11 048.

Strow, L., and D. Reuter (1988), Effect of line mixing on atmospheric brightness temperatures near 15μm, *Appl. Opt.*, *27*, 872–878.

Takahashi, T., S. C. Sutherland, C. Sweeney, A. Poisson, N. Metzl, B. Tilbrook, N. Bates, R. Wanninkhof, R. A. Feely, C. Sabine, J. Olafsson, , and Y. Nojiri (2002), Global sea-air CO_2 flux based on climatological surface ocean pCO_2, and seasonal biological and temperature effects, *Deep-Sea Res.*, *49*, 1601–1622.

Tans, P., P. Bakwin, and D. Guenther (1996), A feasible global carbon cycle observing system: a plan to decipher today's carbon cycle based on observations, *Global Change Biol.*, *2*, 309–318.

Thomas, G. E., and K. Stamnes (1999), *Radiative Transfer in the Atmosphere and Ocean*, Cambridge University Press, Cambridge.

Van Aardenne, J. A., F. J. Dentener, C. G. M. Klein Goldewijk, J. Lelieveld, and J. G. J. Olivier (2001), A 1×1 degree resolution data set of historical anthropogenic trace gas emissions for the period 1890–1990, *Global Biogeochem. Cycles*, *15*, 909–928.

van der Gon, D. (2000), Changes in CH_4 emission from rice fields from 1960 to 1990s - 1. Impacts of modern rice technology, *Gobal Biogeochem. Cycles*, *14*(1), 61–72.

van Diedenhoven, B., O. Hasekamp, and I. Aben (2005), Surface pressure retrieval from SCIAMACHY measurements in the O_2A Band: validation of the measurements and sensitivity on aerosols, *Atmos. Chem. Phys.*, pp. 2109–2120.

Volkamer, R., T. Etzkorn, A. Geyer, and U. Platt (1998), Correction of the oxygen interference with uv spectroscopic (doas) measurements of monocyclic aromatic hydrocarbons in the atmosphere, *Atmos. Environ*, *32*, 3731–3747.

W. Wells, I. (1986), Efficient synthesis of gaussian filters by cascaded uniform filters, *IEEE Trans. Pattern Anal. Mach. Intell.*, *8*(2), 234–239.

Wagner, T., and U. Platt (1999), Satellite mapping of enhanced BrO concentrations in the troposphere, *Nature*, *395*, 486–490.

Wagner, T., S. Beirle, C. v.Friedeburg, J. Hollwedel, S. Kraus, M. Wenig, W. Wilms-Grabe, S. Kühl, and U. Platt (2002), Monitoring of trace gas emissions from space: tropospheric abundances of BrO, NO_2, H_2CO, SO_2, H_2O, O_2, and O_4 as measured by GOME, in *Air Pollution 2002*, vol. 10, pp. 463–472, WIT Press.

Wagner, T., J. Heland, M. Zöger, and U. Platt (2003), A fast H_2O total column density product from GOME - validation with in-situ aircraft measurements, *Atmos. Chem. Phys.*, *3*, 651–663.

Walter, B., M. Heimann, and E. Matthews (2001), Modeling modern methane emissions from natural wetlands 1. Model description and results, *J. Geophys. Res.*, *105*(D24), 34,189–34,206.

Walter, B. P., and M. Heimann (2000), A process-based, climate-sensitive model to derive methane emissions from natural wetlands: Application to five wetland sites, sensitivity to model parameters, and climate, *Global Biogeochem. Cycles*, *14*(3), 745–766.

Washenfelder, R., P. Wennberg, and G. Toon (2003), Tropospheric methane retrieved from ground-based near-ir solar absorption spectra, *Geophys. Res. Lett.*, *30*(23), 2226, doi:10.1029/2003GL017969.

Wenig, M. (2001), Satellite measurement of long-term tropospheric trace gas distributions and source strengths - algorithm development and data analysis, Ph.D. thesis, Institut für Umweltphysik, University of Heidelberg.

Worthy, D., I. Levin, F. Hopper, M. Ernst, and N. Trivett (2000), Evidence for a link between climate and northern wetland methane emissions, *J. Geophys. Res.*, *105*, 4031–4038, doi:10.1029/1999JD901100.

Xiao, Y., N. Tanaka, and A. Lasaga (1997), An evaluation of hydrogen kinetic isotope effect in the reaction of CH_4 with OH free radical (abstract), in *EOS Trans., AGU, 74 (16), Spring Meet. Suppl., 71.*

Zimmermann, P., J. Greenberg, S. Wandiga, and P. Crutzen (1982), Termites: A potentially large source of atmospheric methane, carbon dioxide and molecular hydrogen, *Science*, *218*, 563–565.

Danksagung/Acknowledgements

Als erstes möchte ich mich bei meinem Doktorvater Prof. Ulrich Platt sowie Thomas Wagner bedanken. Sie haben mich freundlich in Heidelberg aufgenommen, mir eine interessante Themenstellung gegeben, anregende Diskussionen geliefert und mir die Unterstützung und wissenschaftliche Freiheit gegeben, welche ich nach anfänglichem Stochern im Dunkeln nur geniessen konnte.

Weiterhin danke ich Prof. Jos Lelieveld für die freundliche Übernahme der Begutachtung der Arbeit.

Der Satellitengruppe in Heidelberg danke ich für eine anspornende, kreative und doch gleichzeitig entspannte Zeit. Eine Auflistung unvergesslicher Momente würde den Rahmen dieser Arbeit sprengen. Barbara, Fahim, Janis, Jens, Michael, Roman, Steffen, Suniti, Thierry, Thomas, Tim, Sven, Walburga, DANKE!!

Tim Deutschmann danke ich zusätzlich für die Programmierung der Bibliotheken zum Zugriff auf SCIAMACHY Daten.

Der neu entstandenen Fussballgruppe am IUP danke ich für die zwar körperlich anstrengenden aber geistig entspannenden Schlachten, welche ein wenig von der wissenschaftlichen Arbeitswelt ablenkten.

Michael Buchwitz, Rüdiger de Beek und dem NIR Team von SRON danke ich für die anregende und doch kollegiale *Konkurrenz*. Ohne diesen Druck hätte ich zwar weniger Stress während meiner Doktorarbeit, dafür aber umso mehr beim Zusammenschreiben selbiger gehabt.

I thank Jan Fokke Meirink (KNMI) for a very fruitful cooperation. Not only started I to trust my own retrievals when we first compared SCIAMACHY with the TM3 model, our discussions also gave me a deeper insight into modeling and methane in general. Similar holds for Peter Bergamaschi (JRC). Shortly after the beginning of the collaboration with Jan Fokke and Peter, the value of models became immediately evident to me.

I thank Ankie Pieters and John van de Vegte (KNMI) for their invaluable assistance in transferring the SCIAMACHY data to our group. What is a group without data?

I thank all scientists and engineers involved in the European Space Agency's ENVISAT/SCIAMACHY mission, especially John Burrows and his team from the University of Bremen. If they had not fought shadows, SCIAMACHY (and this thesis) would not have been possible.

I thank Suniti for being there, for opening my eyes to the world, for her emotional support even when I was in a grouchy mood, and for helping me with my written and spoken English. सबकुछ् के लिये धन्यवाद्।

Letztlich möchte ich meinen Eltern danken. Ihr habt mir nicht nur Wege geebnet sondern mir auch selbstlos alle richtungsweisenden Entscheidungen überlassen.